Field-Induced Phase Transition of Lead-Free Antiferroelectric Niobates

Feldinduzierter Phasenübergang von bleifreien antiferroelektrischen Niobaten

Fachbereich Material- und Geowissenschaften, Technische Universität Darmstadt

Dissertation zur Erlangung des akademischen Grades Doktor der Naturwissenschaften (Dr. rer. nat.)
von Mao-Hua Zhang

Erstgutachter: Assist. Prof. Dr. Jurij Koruza
Zweitgutachter: Prof. Dr. Wolfgang Donner

Darmstadt, Mai 2022

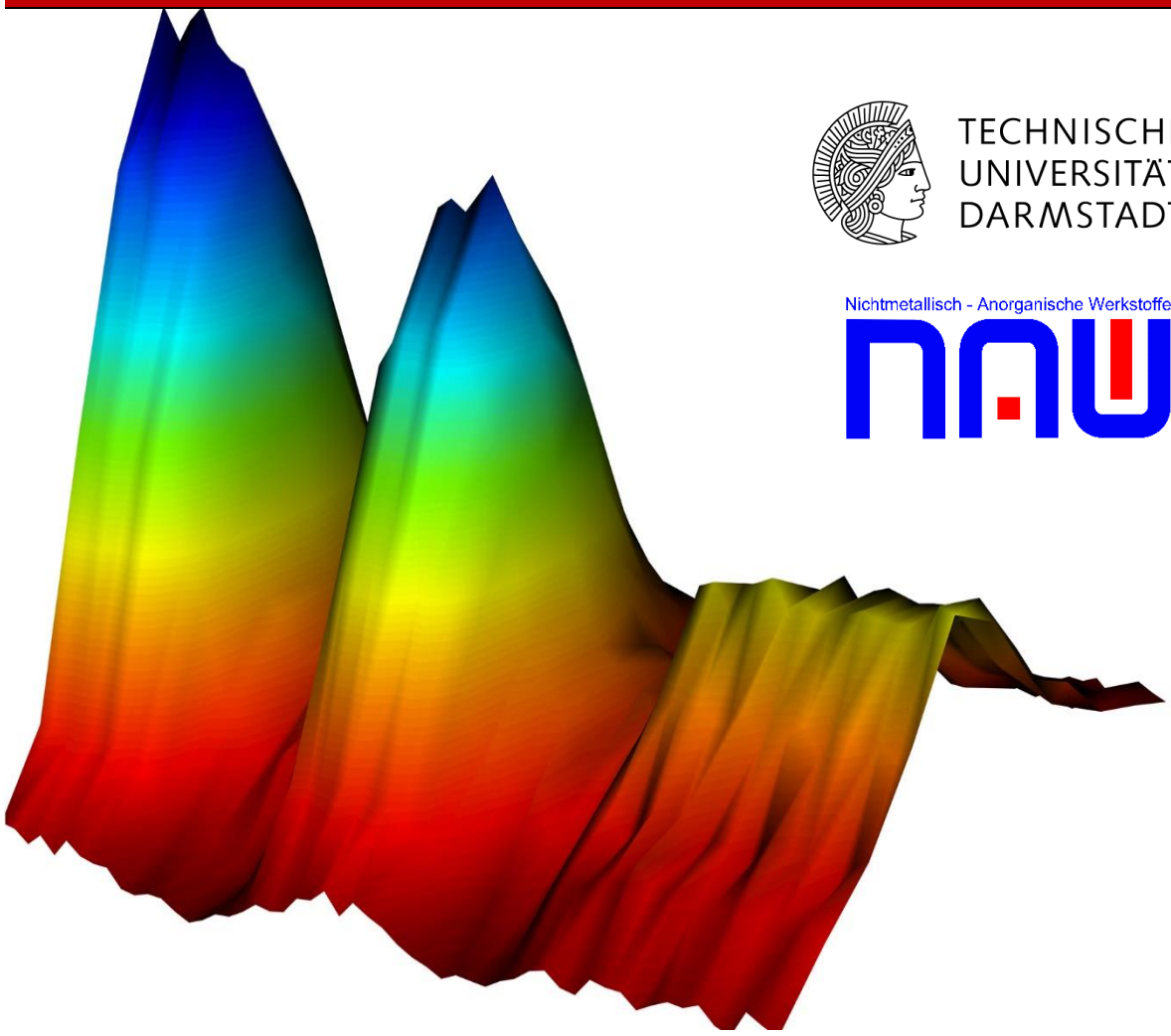

TECHNISCHE UNIVERSITÄT DARMSTADT

Nichtmetallisch - Anorganische Werkstoffe

Dissertation

Field-Induced Phase Transition of Lead-Free Antiferroelectric Niobates

von Mao-Hua Zhang, M. Eng.

geboren in 1993 in Zunyi.

Erstgutachter: Assist. Prof. Dr. Jurij Koruza

Zweitgutachter: Prof. Dr. Wolfgang Donner

Beisitzer: Prof. Dr. Andreas Klein

Beisitzer: Prof. Dr. Ralf Müller

Tag der Prüfung: 10. Mai 2022

Darmstadt, Technische Universität Darmstadt

Year thesis published in TUprints 2022

Bitte zitieren Sie dieses Dokument als:

URN: urn:nbn:de:tuda-tuprints-214208

https://tuprints.ulb.tu-darmstadt.de/21420

Dieses Dokument wird bereit gestellt von tuprints,

E-Publishing-Service der TU Darmstadt

Declaration of Authorship

Thesis Statement pursuant to § 22 paragraph 7 and § 23 paragraph 7 of APB TU Darmstadt

I hereby formally declare that I, Mao-Hua Zhang, have written the submitted thesis independently pursuant to §22 paragraph 7 of APB TU Darmstadt. I did not use any outside support except for the quoted literature and other sources mentioned in the thesis. Furthermore, I state that all passages which have been taken out of publications of all means or unpublished material either whole or in part, in words or ideas, have been marked as quotations in the relevant passage. This thesis has not been handed in or published before in the same or similar form.

In the submitted thesis the written copies and the electronic version for archiving are pursuant to § 23 paragraph 7 APB identical in content.

Darmstadt, DATUM

Darmstadt, 30.März 2022

_____

Mao-Hua Zhang

Content

Content I
Symbols and Abbreviations V
Abstract IX
Zusammenfassung XI
1 Introduction 1
2 Theoretical Background 4
2.1 Dielectric Materials 4
2.1.1 From Dielectrics to Ferroelectrics 7
2.1.2 Ferroelectric Materials 9
2.1.3 Antiferroelectric Materials 10
2.2 Theory of Ferroic Phase Transitions 12
2.2.1 Thermodynamic Theory of Ferroelectric Phase Transitions 12
2.2.2 Thermodynamic Theory of Antiferroelectric Phase Transitions 18
3 Antiferroelectrics: Materials and Status Quo 27
3.1 $PbZrO_3$ 27
3.1.1 History: Phenomenological Observations 27
3.1.2 Structure of $PbZrO_3$ 27
3.2 $(Pb,La)(Zr,Sn,Ti)O_3$ 29
3.2.1 Effect of La Doping 31
3.2.2 Effect of Sn Doping 32
3.2.3 Field-Induced Phase Transition 33
3.3 $NaNbO_3$ 39
3.3.1 Structure at Room Temperature 39
3.3.2 Temperature dependence of the Phase Transitions 41
3.3.3 Field-Induced Phase Transitions in Crystals 42
3.3.4 Phase Stability of $NaNbO_3$ Ceramics 43
3.4 $NaNbO_3$-Based Antiferroelectrics 44
4 Materials and Methods 49
4.1 Materials 49
4.1.1 $NaNbO_3$ 49
4.1.2 $(1-x)NaNbO_3$-$xSrSnO_3$ 49
4.1.3 Mn-Modified $0.95NaNbO_3$-$0.05SrSnO_3$ 50
4.1.4 Nb_2O_5 Precursor 50
4.2 Electrical Characterization 50
4.2.1 Polarization and Strain Measurements 51
4.2.2 Temperature and Field Dependence of the Dielectric Properties 51
4.2.3 Macroscopic Piezoelectricity d_{33} 51
4.2.4 TSDC Measurement 52
4.2.5 Latent Heat Measurement 52
4.3 Scanning Electron Microscopy (SEM) 52

4.4 X-ray Diffraction 52
4.4.1 Conventional Laboratory XRD 52
4.4.2 High-Energy XRD 53
4.5 Solid-State NMR Spectroscopy 53
4.6 Transmission Electron Microscopy 54
4.7 First-Principles Calculations 54
5 *Ex Situ* Study of the Field-Induced Transition in $NaNbO_3$ 57
5.1 Electrical Properties 57
5.1.1 Field-Induced Phase Transition at Room Temperature 57
5.1.2 Frequency Dependence of the Phase Transition 59
5.1.3 Temperature Dependence of the Phase Transition 61
5.1.4 Temperature Dependence of the Dielectric Properties 63
5.1.5 Field Dependence of the Dielectric Properties 66
5.2 Structure and Microstructure 69
5.2.1 XRD Characterization 69
5.2.2 TEM Study 71
5.2.3 NMR Study 73
5.3 Summary 75
6 *In Situ* Study of the Field-Induced Transition in $NaNbO_3$ 77
6.1 Refinement of the Structure at Zero Field 77
6.2 High-Energy XRD with Field 78
6.3 *In Situ* Characterization of Macroscopic Properties 80
6.4 Latent Heat Measurement 82
6.5 Cell Parameter Change 82
6.6 Macroscopic Volume Change 84
6.7 Discussion of the Decoupling Behavior 85
6.8 Summary 90
7 Design of New $NaNbO_3$-Based Antiferroelectric Compositions 93
7.1 Energy Difference Calculated by DFT 93
7.2 Global Structure 95
7.3 Local Structure 99
7.4 Electrical Properties 101
7.4.1 Field-Induced Phase Transition 101
7.4.2 Dielectric Properties 104
7.5 Mn-Modified NN5SS Composition 107
7.5.1 Field-Induced Phase Transition at Room Temperature 107
7.5.2 *In situ* Synchrotron XRD Characterization of the Phase Transition 110
7.5.3 Discussion of the Effect of Mn 116
7.5.4 Temperature Dependence of the Phase Transition 119
7.5.5 Energy Storage Properties 120
7.6 Summary 120
8 Conclusion and Outlook 123
Acknowledgement CXXV
List of Tables CXXVII

List of figures CXXIX
Bibliography CXXXIX
Curriculum Vitae CLIII

Symbols and Abbreviations

Techniques

CBED	Convergent Beam Electron Diffraction
DFT	Density Functional Theory
NMR	Nuclear Magnetic Resonance
PDF	Pair Distribution Function
SAED	Selected Area Electron Diffraction
SEM	Scanning Electron Microscopy
STMAS	Satellite Transition Magic Angle Spinning
TEM	Transmission Electron Microscopy
TSDC	Thermally Stimulated Depolarization Current
XRD	X-ray Diffraction
ZA	Zone Axis
3QMAS	Triple-Quantum Magic Angle Spinning

Chemical Formula

AN	$AgNbO_3$
NN	$NaNbO_3$
NN3SS	$0.97NaNbO_3$-$0.03SrSnO_3$
NN4SS	$0.96NaNbO_3$-$0.04SrSnO_3$
NN5SS	$0.95NaNbO_3$-$0.05SrSnO_3$
NN5SS_0.1Mn	$0.95NaNbO_3$-$0.05SrSnO_3$ + 0.1wt.% MnO_2
NN5SS_0.5Mn	$0.95NaNbO_3$-$0.05SrSnO_3$ + 0.5wt.% MnO_2
NN5SS_1.0Mn	$0.95NaNbO_3$-$0.05SrSnO_3$ + 1.0wt.% MnO_2
NN5SS_2.0Mn	$0.95NaNbO_3$-$0.05SrSnO_3$ + 2.0wt.% MnO_2
NN6SS	$0.94NaNbO_3$-$0.06SrSnO_3$
PLZT	$(Pb,La)(Zr,Ti)O_3$
PLZST	$(Pb,La)(Zr,Sn,Ti)O_3$
PNZST	$(Pb,Nb)(Zr,Sn,Ti)O_3$
PZ	$PbZrO_3$
PZT	$Pb(Zr,Ti)O_3$

Dielectric Properties

D	Dielectric displacement
χ_{ij}	Dielectric susceptibility
ε_{ik}	Dielectric permittivity
ε_0	Permittivity of vacuum
$\varepsilon_{33}/\varepsilon_0$	Relative permittivity of the investigated materials
ε'	Real part of the permittivity
ε''	Imaginary part of the permittivity
$\tan\delta$	Loss tangent

Other Electrical and Mechanical Properties

d_{ijk}	Piezoelectric tensor
d_{33}	Piezoelectric charge coefficient (Berlincourt)
E	Electric field
E_F	Critical field for the field-induced phase transition
E_c	Coercive field
P	Polarization
P_r	Remanent polarization
S_{33}	Longitudinal strain
S_{11}	Transverse strain
S_V	Volume strain
S_{neg}	Negative strain
ω_{stor}	Storage energy density
ω_{rec}	Recoverable energy density
η	Energy storage efficiency
σ_{jk}	Stress tensor
x_{ij}	Strain tensor
s_{ijkl}	Elastic stiffness constants (a fourth-rank tensor)

Energy, Enthalpy and Work

A	Helmholtz free energy
G	Gibbs function
G_1	Elastic Gibbs function
G_2	Electric Gibbs function
H	Enthalpy
H_1	Elastic enthalpy
H_2	Electric enthalpy
Q	Heat
U	Internal Energy
W	Work

Temperature

C	Curie Constant
RT	Room temperature
T	Temperature
T_0	Curie-Weiss temperature
T_c	Curie point
T_{max}	Temperature of dielectric maximum
T_{P-R}	$P-R$ phase transition temperature

Other Abbreviations

AFD	Antiferrodistortive
AFE	Antiferroelectric

APBs	Antiphase boundaries
FE	Ferroelectric
θ	Diffraction angle

Point Defects

V'_{Na}	Na vacancy
$V_{\ddot{O}}$	Oxygen vacancy
$h^{\bullet}$	Hole
e'	Electron

Abstract

Antiferroelectric materials represent a new generation of capacitor materials whose capacitance increases with increasing bias voltage. Such materials offer a new solution for the snubber and DC link capacitors of future power switches with wide bandgap semiconductors and are also needed in electric and hybrid vehicles. The functionality of antiferroelectrics is intimately related to their unique property of changing between the AFE and FE states using an electric field. However, very few AFE systems are known and the mechanisms of the field-induced phase transition in polycrystalline materials remain insufficiently understood. Here, we show how the irreversible AFE to FE phase transition in the lead-free AFE prototype, $NaNbO_3$, is tailored to be reversible via compositional modification and defect chemistry engineering. Several questions regarding the mechanisms of the field-induced phase transition process in $NaNbO_3$-based antiferroelectrics have been addressed in this work.

Pure polycrystalline $NaNbO_3$ ceramic material with 100% AFE phase was prepared, which is the basis to study the field-induced phase transition. The AFE−FE phase transition could be triggered by applying a sufficiently high electric field and the attending structural and microstructural changes were investigated by a combination of *ex situ* XRD, TEM, and NMR characterizations. Notably, the phase transition is of irreversible nature. To gain further insight into the phase transition process, *in situ* high-energy XRD was employed. A field-induced phase transition from AFE to FE first occurred without significant polarization and strain changes. Subsequently, a microstructural change and a large change in both electric charge and volume were recorded simultaneously, which hints at a domain switching process that is clearly decoupled from the phase transition. The presence of the two successive processes was also corroborated by the latent heat measurement.

To achieve a reversible phase transition, a solid solution based on $SrSnO_3$ was proposed with reference to lead-based antiferroelectrics and the Goldschmidt tolerance factor, and then validated by first-principles calculations. Based on this strategy, a series of $SrSnO_3$-substituted ceramic materials were prepared and double polarization hysteresis loops characteristic of a reversible phase transition were obtained. The recorded remanent polarization and energy storage density are lower by a factor of 3 and higher by a factor of 7, respectively, compared to pure $NaNbO_3$. The influence of a less distorted local structure of the sodium site and a lower orthorhombic lattice distortion on the reversibility of the phase transition is discussed. Despite the reversibility, the large remanence of the solid solution and the associated low electrical breakdown strength of the solid solution are not desirable for high density energy storage

applications. To this end, the system was modified with different amounts of MnO_2, resulting in 10-fold lower remanent polarization and 15-fold higher energy storage density compared to pure $NaNbO_3$. In addition, the excellent temperature stability up to 150 °C renders the system a potential candidate for high temperature capacitor applications. The addition of Mn is believed to suppress the formation of oxygen vacancies and thus the amount of mobile defects upon application of an electric field. The structural basis for the reversibility of the AFE−FE phase transition is revealed using *in situ* high-energy XRD. The rigid structures with almost 70% lower atomic displacement of sodium ions compared to pure $NaNbO_3$ are assumed to be the driving force for the restoration of the AFE order.

This study has laid the foundation for penetrating the intricate and delicate interplay of composition, crystal structure, microstructure, and defect chemistry to understand how it defines the functional properties of antiferroic materials. It is expected that the strategies and approaches contained in this work will open the door to a new paradigm for the development of next-generation AFE materials.

Zusammenfassung

Antiferroelektrische Materialien stellen eine neue Generation von Kondensatormaterialien dar, deren Kapazität mit steigender Vorspannung zunimmt. Materialien dieser Art sind ideale Bauteile für Snubber- und DC-Link-Kondensatoren in neu entwickelten Leistungsschaltern mit breiter Bandlücke. Zudem werden sie auch in Elektro- und Hybridfahrzeugen benötigt. Die Funktionalität von Antiferroelektrika beruht auf dem Wechsel zwischen dem AFE und dem FE Zustand unter Einfluss eines elektrischen Feldes. Allerdings sind nur sehr wenige AFE Systeme bekannt und die Mechanismen, die dem feldinduzierten Phasenübergang in polykristallinen Materialien zugrunde liegen, sind noch unzureichend verstanden. In der vorliegenden Arbeit wird gezeigt, wie der irreversible AFE-FE-Übergang im bleifreien Prototyp $NaNbO_3$ mittels gezielter Modifizierung der Zusammensetzung und der Defektchemie reversibel gemacht werden kann. Im Zuge dessen werden mehrere offene Fragen bezüglich der Mechanismen des feldinduzierten Phasenübergangs in $NaNbO_3$-basierten Antiferroelektrika adressiert.

Als Grundlage für die Untersuchung des feldinduzierten Phasenübergangs wurden reine polykristalline $NaNbO_3$-Keramiken dargestellt, die zu 100% in der AFE Phase vorlagen. Mittels eines ausreichend hohen elektrischen Feldes kann der AFE-FE-Phasenübergang ausgelöst werden. Die damit einhergehenden Veränderungen der Struktur und Mikrostruktur werden durch eine Kombination von *ex-situ* XRD-, TEM- und NMR-Messungen untersucht. Bemerkenswerterweise ist der Phasenübergang irreversibel. Mittels hochenergetischer Röntgenbeugung werden *in-situ* tiefere Einblicke in den Prozess des Phasenübergangs gewonnen. Ein feldinduzierter Phasenübergang von AFE zu FE erfolgt zunächst ohne signifikante Änderungen der Polarisation und der Dehnung. Erst danach werden sowohl eine Änderung der Mikrostruktur als auch eine starke Änderung der elektrischen Ladung und des Volumens festgestellt. Dies deutet darauf hin, dass das Schalten der Domänen klar vom Phasenübergang entkoppelt ist. Das Vorhandensein beider aufeinanderfolgender Prozesse wird auch durch die Messung der latenten Wärme bestätigt.

Bezugnehmend auf bleihaltige Antiferroelektrika und die Goldschmidtsche Regel wurde die Bildung einer festen Lösung mit $SrSnO_3$ vorgeschlagen, um einen reversiblen Phasenübergang zu erzielen. Diese Strategie wurde durch DFT-Berechnungen validiert. Anschließend wurde eine Mischkristallreihe $SrSnO_3$-substituierter Keramiken dargestellt und die für einen reversiblen Phasenübergang charakteristischen Doppelhystereseschleifen erhalten. Die remanente Polarisation und die Energiespeicherdichte sind im Vergleich zu reinem $NaNbO_3$ um den Faktor 3 niedriger bzw. um den Faktor 7 höher. Der Einfluss einer weniger verzerrten

Lokalstruktur der Natriumstelle und einer geringeren orthorhombischen Gitterverzerrung auf die Reversibilität des Phasenübergangs wird diskutiert. Allerdings sind die hohe Remanenz und die damit verbundene geringe Durchschlagfestigkeit des Mischkristalls nachteilig für die Energiespeicherdichte. Aus diesem Grund wurde das System mit MnO_2 in verschiedenen Konzentrationen modifiziert, was zu einer 10-fach niedrigeren Remanenz und einer 15-fach höheren Energiespeicherdichte im Vergleich zu reinem $NaNbO_3$ führte. Darüber hinaus ist die ausgezeichnete Temperaturstabilität bis zu 150 °C vorteilhaft für die Anwendung in Hochtemperatur-Kondensatoren. Es wird angenommen, dass die Zugabe von Mn die Bildung von Sauerstoff-Leerstellen unterdrückt und damit die Anzahl der beweglichen Defekte bei Anlegen eines elektrischen Feldes verringert. Die strukturelle Basis für die Reversibilität des AFE-FE-Phasenübergangs wird *in-situ* mittels hochenergetischer Röntgenbeugung aufgedeckt. Es wird vorgeschlagen, dass rigide Strukturen mit fast 70% geringerer Verschiebung der Natriumionen im Vergleich zu reinem $NaNbO_3$ die treibende Kraft für die Wiederherstellung der AFE Ordnung sind.

Zusammensetzung, Kristallstruktur, Mikrostruktur und Defektchemie bilden ein komplexes und empfindliches Zusammenspiel in den untersuchten Materialien. Mit dieser Studie wurde der Grundstein gelegt, dieses zu durchdringen und seinen Einfluss auf die funktionellen Eigenschaften von antiferroischen Materialien zu klären. Es ist zu erwarten, dass die in dieser Arbeit verwendeten Strategien und Ansätze den Weg für ein neues Paradigma in der Entwicklung von AFE Materialien der nächsten Generation ebnen werden.

1 Introduction

The origin and understanding of coupling phenomena between different physical properties is a central topic in solid state science. Much attention has been paid to ferroic materials: ferroelectrics, ferromagnetics, and ferroelastics. Understanding the cross-coupling between ferroic orders and external parameters presents both profound fundamental questions and great potential for innovative applications. However, the underlying mechanism of antiferroic materials and their potential for functionalization are less obvious because an antiferroic order parameter is not directly coupled to a macroscopic field as in the case of ferroics (electric field, magnetic field, and stress field), but to a microscopic staggered field that is related to the symmetry-related sublattice [1].

Due to the unique functionality of flipping forth and back between antiferroelectric and ferroelectric phases, antiferroelectric materials are gaining increasing attention for their potential applications in pulse power capacitors [2], DC-link capacitors for power electronics [3], high-energy density capacitors [4, 5], and solid-state electrocaloric cooling [6, 7].

The notion of antiferroelectricity was first raised by the theory of Kittel in 1951 [8]. Soon after, the perovskite lead zirconate, $PbZrO_3$, was found to be antiferroelectric [9] and is often considered the canonical antiferroelectric oxide. Nevertheless, the concept of antiferroelectricity is until today not well-defined. The formulation of a precise definition of antiferroelectricity is nontrivial, and the phenomenon is interpreted from different angles. Phenomenologically, an antiferroelectric crystal is a non-polar material that exhibits a double hysteresis loop of polarization as a function of field due to the field-induced phase transition. From an energetic point of view [10], the free energy of an antiferroelectric state is close to the ferroelectric state, so that the ferroelectric state can be induced in a non-polar crystal by applying an electric field. Moreover, the nature of antiferroelectricity is interpreted from both structural and energetic points of view: the structure of both antiferroelectric and ferroelectric materials is obtained through distortion of a non-polar high-symmetry reference phase; non-polar phases are antiferroelectric only if there is an alternative low-energy ferroelectric phase obtained by a polar distortion of the same high-symmetry reference structure, which promotes a small energy difference and ease of transformation between the two phases [1]. The fundamental physics of antiferroelectrics is still far from being systematically understood because of the weak connection between the microscopic aspects of crystal structure and energetics, and the macroscopic behavior.

In fact, antiferroelectric materials have overall received much less attention than ferroelectrics. Today, more than 1000 ferroelectric materials are known but only a few antiferroelectric systems have been thoroughly investigated. Among all antiferroelectric perovskite oxides, $PbZrO_3$-based antiferroelectrics are the most studied material systems. However, the toxicity of lead and environmental concerns have driven the search for lead-free antiferroelectric alternatives.

$NaNbO_3$ is arguably one of the most structurally-complicated perovskite system known to date. Not only is it characterized by a complex structure at room temperature, but it also exhibits a multiplex sequence of phases with temperature. At room temperature, the antiferroelectric order (*Pbcm* structure) competes with the ferroelectric order ($P2_1ma$ structure) and the phase stability is particularly sensitive to a variety of factors such as composition [11], starting chemicals [12], externally applied hydrostatic stress [13], epitaxial stress [14, 15] and grain size [16]. Tailoring the processing parameters to obtain polycrystalline $NaNbO_3$ with an antiferroelectric state is the first important task that forms the basis for studying the properties of $NaNbO_3$. On top of that, one important scientific question to be addressed is how the structure, microstructure and macroscopic functional properties change with the phase transition. For this, a combination of *ex situ* structural and electrical characterizations, and *in situ* synchrotron X-ray diffraction can provide better insight into the underlying mechanisms. Finally, the ultimate question is how to tune the phase transition to be reversible, as in the case of $PbZrO_3$-based antiferroelectrics. To this end, the existing literature provides some basic guidelines for the stabilization of the antiferroelectric order [17] and much of the reported work has been done on compositional modifications to tune the reversibility of the field-induced transition. A promising approach for the design and discovery of new antiferroelectric compositions is to combine them with first-principles calculations, which have proven successful in predicting the ground-state structure of $PbZrO_3$ [18]. First-principles calculations can help identify a desired material by establishing the relationship between antipolar and zone-center polar instability, while the latter produces a competing ferroelectric phase at low energy and is essential for triggering the field-induced phase transition.

The aim of the present work is to develop new lead-free antiferroelectric materials exhibiting double polarization hysteresis loops and to discuss and clarify fundamental issues related to the field-induced antiferroelectric−ferroelectric phase transition in polycrystalline $NaNbO_3$ ceramic materials. For this purpose, the prototype $NaNbO_3$ materials in the antiferroelectric state were processed and investigated with respect to its structural, microstructural, electric, and

electromechanical responses during the phase transition *ex situ* and *in situ*. Afterwards, new $NaNbO_3$-based compositions were developed with the guidance of first-principles calculations and studied with respect to their phase transition behavior and microstructural changes. Finally, the newly developed materials were modified for the purpose of reducing the hysteresis and obtaining an improved double polarization hysteresis loop via defect chemistry engineering. The presented discussion and understandings about the interplay of composition, crystal structure, microstructure, and defect chemistry and its influence on functional properties are expected to provide new insights into antiferroelectricity and support the development of next-generation antiferroelectric materials.

2 Theoretical Background

Before discussing the antiferroelectric materials, it is important to first clarify the concept of ferroelectricity and introduce the large family of dielectrics that also includes piezoelectrics, pyroelectrics, ferroelectrics, and of course antiferroelectrics. This section includes an introduction to the essential background of dielectric materials and their classification. Thermodynamic theory is discussed, with particular emphasis on ferroelectric and antiferroelectric phase transitions.

2.1 Dielectric Materials

Dielectric materials are insulators or poor conductors of electric current, due to a lack of charge carriers such as free electrons and holes that are mobile and can drift. When a dielectric is subjected to an externally applied electric field, the charges inside the material cannot move freely and polarization is developed. A dielectric in such a state is considered to be polarized. The macroscopic polarization, P_{i}, is defined as the assembly of electric dipole moments per unit volume.

$$P_{\mathrm{i}} = \frac{\sum p_{\mathrm{i}}}{V} \qquad 2\text{–}1$$

Different dielectric materials polarize to different degrees, which is determined by different mechanisms of polarization that are inherent in the material. In general, the stronger the field, the greater the macroscopic polarization P_{i}, which is coupled by the dielectric susceptibility, χ_{ij}.

$$P_{\mathrm{i}} = \varepsilon_0 \chi_{ij} E_{\mathrm{j}} \qquad 2\text{–}2$$

Here ε_0 is the permittivity of free space, which is 8.85×10^{-12} F/m and χ_{ij} is a second-order tensor, which is dimensionless. Note that equation 2–2 is valid under a low electric field, because nonlinearities in dielectrics are expected at high fields. Alternatively, equation 2–2 can be expressed as:

$$\begin{pmatrix} P_{\mathrm{x}} \\ P_{\mathrm{y}} \\ P_{\mathrm{z}} \end{pmatrix} = \varepsilon_0 \begin{pmatrix} \chi_{\mathrm{xx}} & \chi_{\mathrm{xy}} & \chi_{\mathrm{xz}} \\ \chi_{\mathrm{yx}} & \chi_{\mathrm{yy}} & \chi_{\mathrm{yz}} \\ \chi_{\mathrm{zx}} & \chi_{\mathrm{zy}} & \chi_{\mathrm{zz}} \end{pmatrix} \begin{pmatrix} E_{\mathrm{x}} \\ E_{\mathrm{y}} \\ E_{\mathrm{z}} \end{pmatrix} \qquad 2\text{–}3$$

The electric displacement, D_{i}, inside a dielectric material is contributed by the electric displacement in vacuum plus the polarization P_{i} of the material.

$$D_{\mathrm{i}} = \varepsilon_0 E_{\mathrm{i}} + P_{\mathrm{i}} = \varepsilon_0 E_{\mathrm{i}} + \varepsilon_0 \chi_{ij} E_{\mathrm{j}} = \varepsilon_0 \left(\delta_{ij} + \chi_{ij}\right) E_{\mathrm{j}} = \varepsilon_{ij} E_{\mathrm{j}} \qquad 2\text{–}4$$

Here ε_{ij} is the dielectric permittivity of the material and δ_{ij} is Kronecker's symbol ($\delta_{ij} = 1$ for $i = j$, $\delta_{ij} = 0$ for $i \neq j$). If isotropy condition is met:

$$\chi_{ij} = \chi\delta_{ij} \qquad 2\text{–}5$$

Equation 2–4 can be expressed as:

$$D_{\mathrm{i}} = \varepsilon_0\left(\delta_{ij} + \chi\delta_{ij}\right)E_{\mathrm{j}} = \varepsilon_0(1+\chi)\delta_{ij}E_{\mathrm{j}} = \varepsilon_0\varepsilon_{\mathrm{r}}E_{\mathrm{i}} \qquad 2\text{–}6$$

Here ε_{r} is the relative dielectric permittivity, which is the dielectric susceptibility plus 1. Linear dielectric, ferroelectric, and antiferroelectric materials are characterized by different field dependence of small-signal permittivity, as shown in Figure 2.1. In particular, an antiferroelectric material, e.g., (Pb,La)(Zr,Sn,Ti)O_3 and $AgNbO_3$ (AN), can exhibit increased permittivity with increasing bias field before the critical field at which the phase transition from the antiferroelectric to the ferroelectric phase occurs. From an application point of view, this phenomenon is of particular interest for power electronics, e.g., DC-link capacitors.

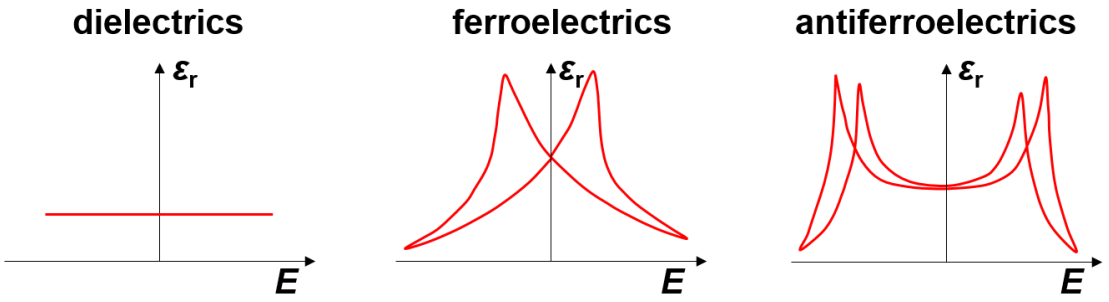

Figure 2.1: Representative electric field dependence of small-signal permittivity of linear dielectrics, ferroelectrics, and antiferroelectrics.

The macroscopic dielectric response of a dielectric is usually contributed by the following four mechanisms of polarization: electronic polarization, ionic polarization, orientation polarization, and space charge polarization, as shown in Figure 2.2. The electronic contribution arises from the displacement of the negatively charged electron shell relative to a positively charged nucleus and is present in all dielectrics. The ionic contribution refers to the displacement of cations with respect to anions, which is observed in ionic crystals. The orientation polarization describes the alignment of molecules (water, for example) with a permanent electric dipole moment driven by an electric field. The space charge polarization is an interfacial effect resulted from inhomogeneously accumulated charge carriers at structural interfaces, e.g., grain boundaries, phase boundaries, and domain walls. The spontaneous polarization in perovskite ferroelectrics, e.g., $BaTiO_3$, is a combination of different mechanisms, but is dominantly caused

by the ionic contribution, i.e., the off-centered displacement of the Ti atoms. The degree to which each mechanism contributes to the overall polarization of a dielectric material depends on the material type, form, and the frequency of the applied field [19].

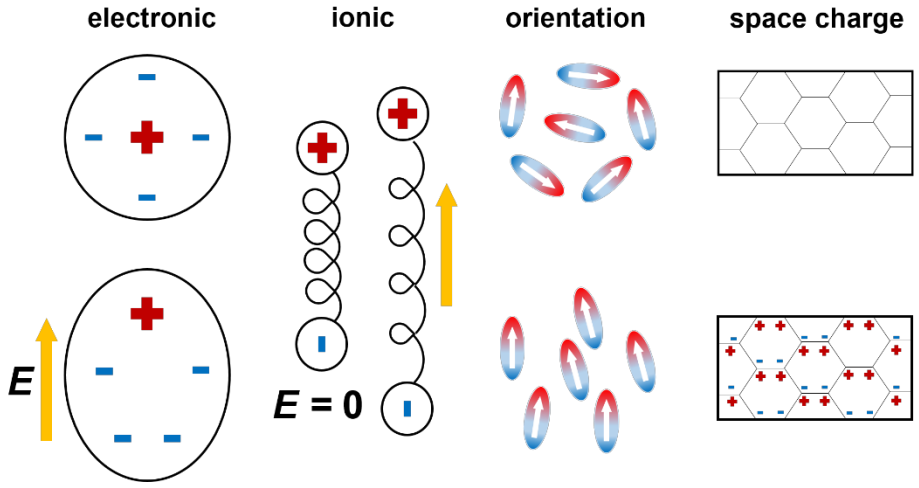

Figure 2.2: Four main polarization mechanisms under the application of an electric field: electronic polarization, ionic polarization, orientation polarization, and space charge polarization.

For the electronic polarization and ionic polarization, the behavior of the charges could be approximated as being bound to equilibrium positions by linear springs with the restoring force being proportional to the displacement [20]. The resonant frequency of electrons in atoms and of ions in ionic crystals is typically in the range of terahertz (THz) to (petahertz) PHz and (gigahertz) GHz to THz, respectively [19]. The behavior of orientation polarization and space charge polarization cannot be well described by the damped, forced harmonic motion but is characterized by a relaxation process. The space charge polarization can occur at a frequency range from mHz to megahertz (MHz), while the orientation polarization typically occurs at MHz to GHz frequencies. Due to the inherent lag between the changes in the polarization and electric field, the permittivity of a dielectric material shows a dependence on the frequency of the applied electric field, also known as dielectric dispersion. The attendant energy dissipation is the dielectric loss, which is especially high around the relaxation and resonance frequencies. The dielectric dispersion and the attendant energy dissipation are shown in Figure 2.3, where the permittivity drops as each polarization mechanism fails to follow the electric field at high frequencies. The dielectric permittivity can be described by a complex value:

$$\varepsilon = \varepsilon' + i\varepsilon'' \qquad 2\text{–}7$$

The dielectric loss is usually expressed as the loss tangent:

$$\tan\delta = \frac{\varepsilon''}{\varepsilon'} \qquad 2\text{–}8$$

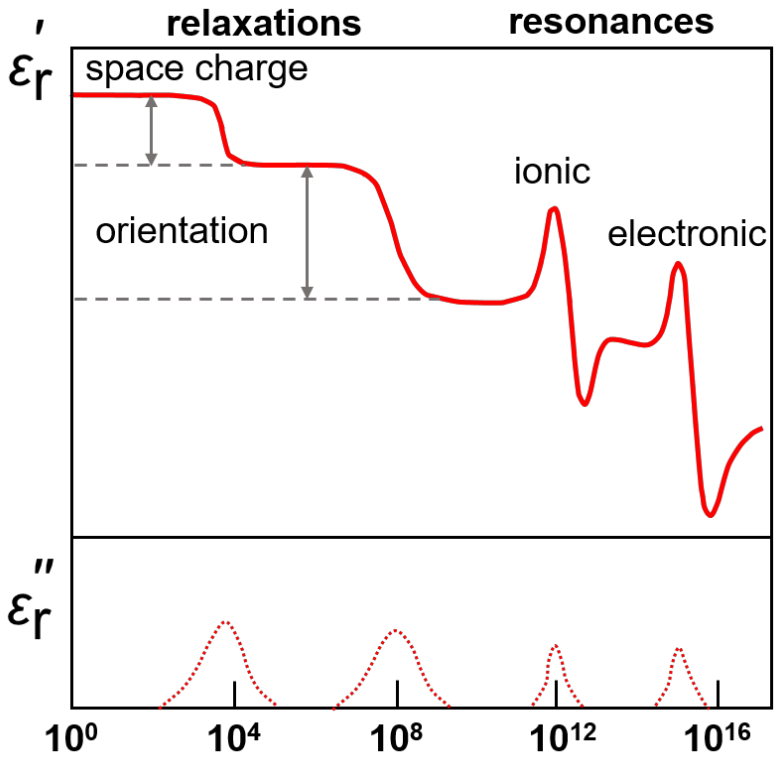

Figure 2.3: Real part ε_r' and imaginary part ε_r'' of the dielectric permittivity as a function of frequency. Space charge and orientation polarizations are relaxation processes and are strongly temperature dependent. Ionic and electronic polarizations are resonance processes and almost temperature independent.

2.1.1 From Dielectrics to Ferroelectrics

Piezoelectric materials are a subset of dielectrics in which polarization can be induced by mechanical force, known as the direct piezoelectric effect. The converse effect refers to the phenomenon that linear mechanical strain can be caused by an applied electric field. The phenomenon of piezoelectricity was discovered by Pierre and Jacques Curie in 1880 on a quartz crystal. The direct piezoelectric effect can be formulated as:

$$D_i = d_{ijk}^E \sigma_{jk} + \varepsilon_{ik}^\sigma E_k \qquad 2\text{–}9$$

where the dielectric displacement, D_i, is coupled to the stress, σ_{jk}, via the piezoelectric tensor, d_{ijk}^E.

The converse piezoelectric effect can be formulated as:

$$x_{ij} = d_{ijk}^\sigma E_k + s_{ijkl}^E \sigma_{kl} \qquad 2\text{–}10$$

where the strain x_{ij} is coupled to the electric field E_k via the piezoelectric tensor d_{ijk}^{σ}.

For a dielectric material to be piezoelectric, it is necessary for the crystal to have no center of symmetry, otherwise no polarization could be induced due to a full compensation of the charges. Depending on the symmetry of crystals with respect to a point, there are in total 32 crystal classes (point groups) and 21 of these have no center of symmetry (inversion center). With the exception of point group 432, which has a high symmetry and eliminates all non-zero piezoelectric coefficients, the remaining 20 point groups are piezoelectric materials. Of the 20 piezoelectric crystal classes, 10 are characterized by the presence of spontaneous polarization in the absence of an electric field. At a constant temperature, bound charges cannot be detected on the surface of the pyroelectric crystal because they are compensated by the flow of free charges within the crystal and accumulated charges in the surroundings. However, a change of the electric charges on the surface corresponding to the change of spontaneous polarization can be observed as temperature changes. This is the pyroelectric effect and these 10 polar classes are referred to as pyroelectric materials. A polar pyroelectric material is ferroelectric when its spontaneous polarization can be reoriented under the application of an external electric field. The classifications of dielectrics, piezoelectrics, pyroelectrics, and ferroelectrics are shown in Figure 2.4.

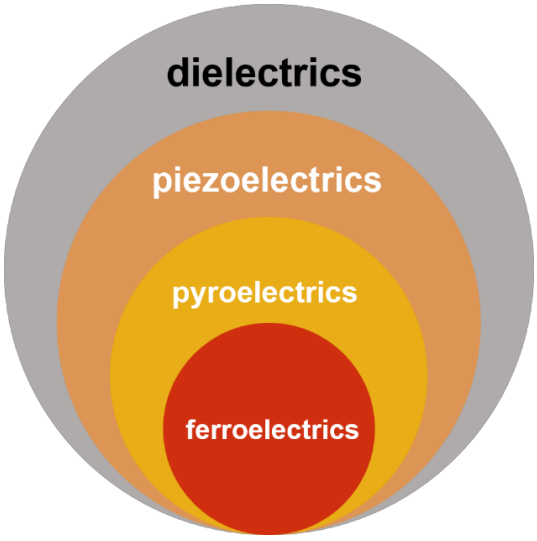

Figure 2.4: Piezoelectrics, pyroelectrics, and ferroelectrics are subgroups of dielectrics.

The 32 crystal classes are classified according to their crystal systems, centrosymmetry, and polarity, as listed in Table 2.1

Table 2.1: Overview of 32 point groups. Crystallographic classification according to their crystal systems, centrosymmetry and polarity [19]. Piezoelectrics are highlighted in bold.

	Centrosymmetric	Non-centrosymmetric	
	Non-polar (11)	Non-polar (11)	Polar (10)
Triclinic	$\bar{1}$		**1**
Monoclinic	2/*m*		**2, *m***
Orthorhombic	*mmm*	**222**	***mm2***
Rhombohedral	$\bar{3}m$, $\bar{3}$	**32**	**3, 3*m***
Tetragonal	4/*mmm*, 4/*m*	**422, $\bar{4}$2*m*, $\bar{4}$**	**4, 4*mm***
Hexagonal	6/*mmm*, 6/*m*	**622, $\bar{6}$*m*2, $\bar{6}$**	**6, 6*mm***
Cubic	*m*3*m*, *m*3	432, **$\bar{4}$3*m*, 23**	

2.1.2 Ferroelectric Materials

When ferroelectricity was first discovered in Rochelle salt ($KNaC_4H_4O_6 \cdot 4H_2O$), the origin of this "novel physical phenomenon" was unclear and was initially associated with hydrogen bonds. Later, ferroelectric properties were found in compounds with perovskite oxides, which nowadays represent an important group of ferroelectric materials. In addition, ferroelectric properties have also been found in pyrochlore, pseudo-ilmenite, and lead metaniobate, etc., whose structures are characterized by oxygen octahedra. So far, more than 1000 ferroelectric materials have been found. Historically, ferroelectric materials were generally divided into two groups. The first group refers to hydrogen bonded ferroelectrics and the second group refers to oxygen-octahedra ferroelectrics. The latter group is characterized by a number of common features. For example, oxygen-octahedra ferroelectrics are insoluble in water and can be easily synthesized in the form of polycrystalline ceramics. In addition, the spontaneous polarization of oxygen-octahedra ferroelectrics is usually an order of magnitude higher than that of hydrogen-bonded ferroelectrics. However, this classification has become increasingly unsatisfactory due to the appearance of new ferroelectric compounds whose structure and properties make it difficult to assign them to either of the above two groups. A satisfactory classification of ferroelectrics can be made on the basis of the mechanism of the occurrence of spontaneous polarization. The first type is characterized by displacive phase transition and the spontaneous polarization is caused by the displacement of a cation from the center of the surrounding oxygen octahedra. The orientation of the spontaneous polarization is either parallel or antiparallel to the displacement of the cation. The displacive phase transition is often

observed in oxygen-octahedra ferroelectrics. The second type is characterized by order-disorder phase transitions associated with the ordering of certain structural elements (e.g., protons in hydrogen bonds or radicals) that are disordered in the state before the transition. In the latter case, the process of generating polarization consists of the appearance of dipoles and the alignment of dipole moments in a parallel or antiparallel manner. The change in entropy during the ferroelectric transition is small for the displacive type and typically large for the order-disorder type. This feature can be used to distinguish one type of ferroelectrics from another. Note that only the oxygen octahedral ferroelectrics and antiferroelectrics are discussed in this thesis.

Ferroelectricity in perovskite oxides is subjected to a delicate balance between long-range Coulomb forces and short-range repulsions [21], with the former favoring the ferroelectric order and the latter favoring the non-polar cubic structure. In general, the origin of ferroelectricity in perovskite oxides is due to hybridization between the B-site cations and oxygen, which is essential for suppressing the short-range repulsions and stabilizing the ferroelectric order [22]. For example, in $BaTiO_3$ and $PbTiO_3$, the Ti is strongly distorted and hybridizes with the closer oxygen. Many ferroelectric oxide perovskites have B-site cations whose lowest unoccupied states are *d*-states that allow *d*-hybridization with oxygen, e.g., Nb^{5+}, Zr^{4+}, Ti^{4+} and so on.

2.1.3 Antiferroelectric Materials

Formulating a precise definition of antiferroelectricity is nontrivial, especially when compared to the definitions of ferroelectricity or piezoelectricity. It should be noted that our focus on antiferroelectricity in this thesis will be limited to oxides, and hydrogen-bonded antiferroelectric materials and antiferroelectric liquid crystals are beyond the scope of this work. According to Kittel´s model [8], arrays of ions are spontaneously polarized in an antiferroelectric crystal, while the direction of these polarizations is antiparallel in neighboring lines. To date, none of the known antiferroelectric oxides conforms to this collinear two-sublattice model. Nevertheless, Kittel pointed out the importance of individual unit cells for the definition of antiferroelectricity. To differentiate an antiferroelectric crystal from pyroelectric and ferroelectric materials, the spontaneous polarization of individual unit cells rather than that of the whole crystal should be considered. In ordinary pyroelectrics, all the unit cells exhibit spontaneous polarization that is uniform along one direction. In ferroelectrics, the spontaneous polarization within one domain is uniform along one direction, while neighboring domains

differ in the orientation of spontaneous polarization. In antiferroelectrics, although neighboring primitive cells can have different orientations of spontaneous polarization, the net spontaneous polarization is zero in a unit cell. A schematic illustration of the configurations of dipoles in neighboring unit cells of pyroelectrics, ferroelectrics and antiferroelectrics is shown in Figure 2.5. Ferrielectrics, though not very well studied, should be mentioned as a separate case. According to Kanzig *et al.*[23], ferrielectrics exhibit ferroelectric properties along certain crystallographic directions, while behaving like antiferroelectrics along other directions. Goldsmith [24] described an uncompensated antipolar structure in thiourea as "ferrielectricity". Ferrielectrics are also called "weak ferroelectrics", due to the observation of a small value of macroscopic polarization in these materials.

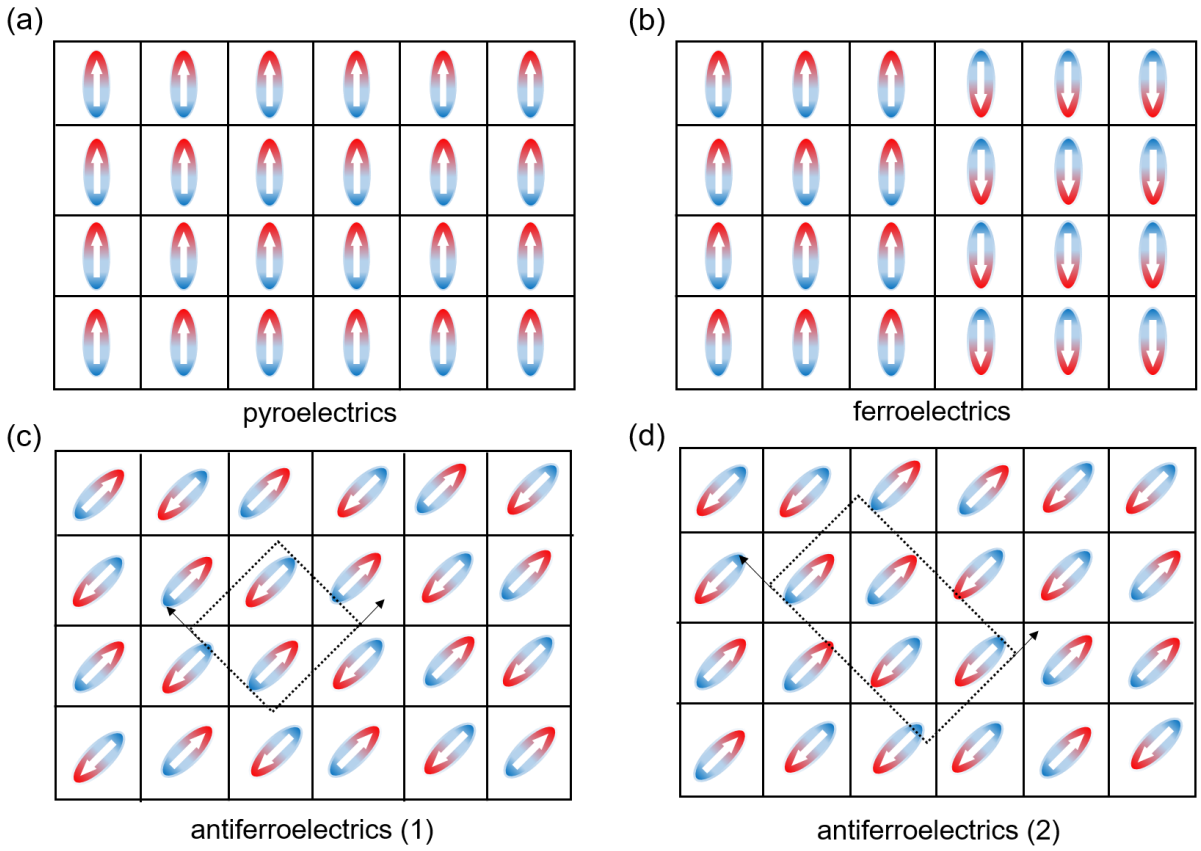

Figure 2.5: Schematic illustrations of the orientations of dipoles in neighboring unit cells of (a) pyroelectrics, (b) ferroelectrics, and (c-d) two cases of antiferroelectrics. The unit cells of antiferroelectrics are highlighted by dashed rectangle.

An antiferroelectric crystal is of particular interest when a phase transition from the antiferroelectric state to the ferroelectric state could be triggered by an applied electric field, since the functionalities of antiferroelectrics arise mostly from the changes in properties at the transition. Considering there is no universally accepted definition of antiferroelectricity and an

empirical definition of antiferroelectricity cannot be completely rigorous and exclusive, definitions of antiferroelectricity from various aspects are summarized as follows. From a practical point of view, an antiferroelectric crystal is a non-polar material that exhibits double polarization hysteresis loops. Moreover, the double loop should arise from a field-induced phase transition, otherwise the definition is problematic [25]. For example, a ferroelectric with first-order phase transition can exhibit a double loop at temperature slightly higher than T_c [26]. In addition, a double hysteresis loop can be induced by defect dipoles in a ferroelectric material at certain field frequencies. From an energetic point of view, an antiferroelectric state is an antipolar state, whose free energy is comparable to that of the ferroelectric modification of the same material and, thus, an antiferroelectric phase can be transformed to the ferroelectric state with the energy offered by the application of an electric field. A rather inclusive version of the definition was proposed by Rabe [1] from both structural and energetic points of view: "…an antiferroelectric is analogous to a ferroelectric in that their structures are obtained through distortion of a non-polar high-symmetry reference phase. The distortion is nonpolar for antiferroelectrics, while polar for ferroelectrics. However, not all non-polar phases obtained are antiferroelectric unless there is an alternative low-energy ferroelectric phase obtained by a polar distortion of the same high-symmetry reference structure, which allows a small energy difference and ease of transition between the two states." No matter along which path we are approaching the concept of antiferroelectricity, the competition between the ferroelectric order and the antiferroelectric order seems to be an intrinsic nature of antiferroelectrics [1].

2.2 Theory of Ferroic Phase Transitions

Mueller [27] was among the first to apply thermodynamic theory to ferroelectric material, in this case Rochelle salt. The free energy was written as an expansion in powers of polarization and strain and was used to link the parameters involved to experimentally measurable quantities. Interestingly, a phenomenological thermodynamic theory is able to link the macroscopic properties well, although a fundamental understanding of phase transition behavior, ionic or electronic displacements, long- or short-range interactions may be lacking.

2.2.1 Thermodynamic Theory of Ferroelectric Phase Transitions

If independent variables are specified, the equilibrium state of a homogeneous thermodynamic system can be described by a function, which is known as the thermodynamic characteristic

function. Landau's symmetry-based treatment of phase transitions [28] was first applied to ferroelectrics by Devonshire [29] and has been commonly accepted to describe and predict the ferroelectric phase transitions and the temperature dependence of material properties, also known as Landau-Devonshire theory.

According to the first law of thermodynamics, the change in the internal energy U of a system is:

$$dU = dQ + dW \qquad 2\text{–}11$$

where dQ is the heat gained by the system, dW is the work done on the system. For an elastic dielectric, dW is contributed by both mechanical and electrostatic energies:

$$dW = -X_{ij}dx_{ij} + E_m dD_m \qquad 2\text{–}12$$

where X_{ij} is the stress, x_{ij} is the strain, E_m is the electric field and D_m is the electric displacement. For a reversible process:

$$dQ = TdS \qquad 2\text{–}13$$

where T is the temperature and S is the entropy. Equation 2–11 could be rewritten as:

$$dU = TdS - X_{ij}dx_{ij} + E_m dD_m \qquad 2\text{–}14$$

Other potential functions in terms of the independent variables, including the internal energy U, entropy S, temperature T, etc., are summarized in Table 2.2.

Table 2.2: Summary of representative thermodynamic potential functions of elastic dielectrics.

Potential functions	Equations
Helmholtz free energy A	$A = U - TS$
Enthalpy H	$H = U + X_{ij}x_{ij} - E_m D_m$
Elastic enthalpy H_1	$H_1 = U + X_{ij}x_{ij}$
Electric enthalpy H_2	$H_2 = U - E_m D_m$
Gibbs function G	$G = H - TS$
Elastic Gibbs function G_1	$G_1 = H_1 - TS$
Electric Gibbs function G_2	$G_2 = H_2 - TS$

From the definitions summarized in Table 2.2, potential functions in the differential form could be derived and are summarized below:

Table 2.3: Summary of representative thermodynamic potential functions in the differential form.

Potential functions	Equations
Helmholtz free energy A	$dA = -SdT - X_{ij}dx_{ij} + E_m dP_m$
Enthalpy H	$dH = TdS - x_{ij}dX_{ij} - P_m dE_m$
Elastic enthalpy H_1	$dH_1 = TdS + x_{ij}dX_{ij} + E_m dP_m$
Electric enthalpy H_2	$dH_2 = TdS - X_{ij}dx_{ij} - P_m dE_m$
Gibbs function G	$dG = -SdT + x_{ij}dX_{ij} - P_m dE_m$
Elastic Gibbs function G_1	$dG_1 = -SdT + x_{ij}dX_{ij} + E_m dP_m$
Electric Gibbs function G_2	$dG_2 = -SdT - X_{ij}dx_{ij} - P_m dE_m$

Elastic Gibbs function G_1, which is expressed as a function of temperature, stress, and dielectric displacement, is the most convenient potential to use:

$$dG_1 = -SdT + x_{ij}dX_{ij} + E_m dP_m \qquad 2\text{–}15$$

given that temperature and stress are easily controlled in the laboratory and ferroelectrics are characterized by dielectric displacement or polarization.

If the system is in isothermal ($dT = 0$) and stress-free ($dX_{ij} = 0$) conditions, G_1 can be expanded in powers of the polarization. For simplicity, G_1 is expanded along one axis:

$$G_1 = G_{10} + \frac{1}{2}\alpha P^2 + \frac{1}{4}\beta P^4 + \frac{1}{6}\gamma P^6 \qquad 2\text{–}16$$

γ should be a non-negative value, otherwise G_1 is infinitely small as $P \rightarrow +\infty$. The order of the phase transition depends on the sign of β. The transition is of first order if β is negative while it is of second order if β is positive. Only α is assumed to be temperature dependent:

$$\alpha = \alpha_0(T - T_0) \qquad 2\text{–}17$$

here α_0 is a positive value and T_0 is the Curie-Weis temperature.

According to equations 2–15 and 2–16, the electric field E is:

$$E = \frac{\partial G_1}{\partial P} = \alpha P + \beta P^3 + \gamma P^5 \qquad 2\text{–}18$$

We can also have the second derivative of G_1:

$$\frac{\partial^2 G_1}{\partial P^2} = \frac{\partial E}{\partial P} = \frac{1}{\varepsilon} = \alpha + 3\beta P^2 + 5\gamma P^4 \qquad 2\text{–}19$$

When the system is in the paraelectric state ($P = 0$),

$$\frac{\partial E}{\partial P} = \frac{1}{\varepsilon} = \alpha \qquad 2\text{–}20$$

From equation 2–17:

$$\varepsilon = \frac{1}{\alpha_0 (T - T_0)} \qquad 2\text{–}21$$

Equation 2–21 is known as the Curie-Weiss law:

$$\varepsilon_r(0) = \varepsilon_r(\infty) + \frac{C}{(T - T_0)} \approx \frac{C}{(T - T_0)} \qquad 2\text{–}22$$

$$\alpha_0 = \frac{1}{\varepsilon_0 C} \qquad 2\text{–}23$$

2.2.1.1 Second-Order Phase Transitions

Second-order phase transitions are characterized by $\beta > 0$. From equation 2–18, G_1 gives a stationary point when $P = 0$. From equation 2–19, the second derivative of G_1 is always positive if α is positive and thus, G_1 has a minimum value when $P = 0$.

In the case where α is negative, when G_1 gives a stationary point ($E = 0$), the spontaneous polarization of the system can be obtained:

$$P^2 = \frac{\beta}{2\gamma}\left(-1 + \sqrt{1 - \frac{4\gamma\alpha_0(T - T_0)}{\beta^2}}\right) \qquad 2\text{–}24$$

From equation 2–19, the second derivative of G_1 is negative when $P^2 = 0$ and thus, G_1 has a local maximum when $P = 0$. A schematic plot of the elastic Gibbs function G_1 as a function of polarization at three different temperatures is shown in Figure 2.6.

i. When $T < T_0$, the two minimum points indicate that the system is in the ferroelectric state with two spontaneous polarization vectors that are equal in magnitude, but opposite in direction.

ii. The spontaneous polarization disappears at $T = T_0$, and the Curie point T_c is equivalent to the Curie-Weiss temperature T_0 for the second order phase transition.

iii. When $T > T_0$, the system is only stable when $P = 0$, i.e., in the paraelectric state.

The influence of higher order terms (P^6) can be neglected for the second-order phase transition. Therefore, the temperature dependence of spontaneous polarization can be derived. From equation 2–18,

$$P = \sqrt{\frac{\alpha_0(T_C - T)}{\beta}} \qquad 2–25$$

It can be seen that the spontaneous polarization of the second order phase transition decreases continuously with increasing temperature until the Curie point is reached and no latent heat will be detected.

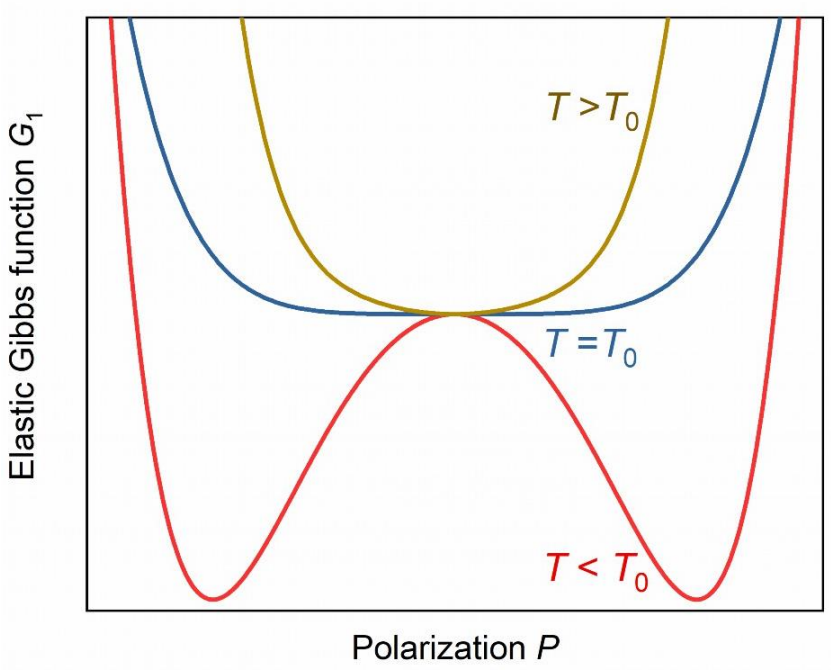

Figure 2.6: A schematic plot of the elastic Gibbs function G_1 of the second-order phase transition as a function of polarization at $T < T_0$, $T = T_0$, and $T > T_0$.

2.2.1.2 First-Order Phase Transitions

First-order phase transition appears when $\beta < 0$. In this case, the Curie-Weiss temperature T_0 and the Curie point T_c are different. T_0 is obtained experimentally by extrapolating the $\lambda(T)$ in the paraelectric regime and taking the intersection of the line with the temperature axis. At the Curie point T_c, from equation 2–16,

$$\frac{1}{2}\alpha_0(T_C - T_0)P_{Sc}^2 + \frac{1}{4}\beta P_{Sc}^4 + \frac{1}{6}\gamma P_{Sc}^6 = 0 \qquad 2–26$$

P_{Sc} is the spontaneous polarization at the Curie point.

From equation 2–18,

$$\frac{\partial G_1}{\partial P} = \alpha_0(T_c - T_0)P_{Sc} + \beta P_{Sc}^3 + \gamma P_{Sc}^5 = 0 \qquad 2–27$$

From equations 2–26 and 2–27,

$$P_{Sc}^2 = -\frac{3\beta}{4\gamma} \qquad 2–28$$

$$T_c = T_0 + \frac{3\beta^2}{16\alpha_0\gamma} \qquad 2–29$$

A ferroelectric system with a first-order phase transition exhibits different behavior near temperatures T_0 and T_c. A schematic representation of the elastic Gibbs function G_1 as a function of polarization at different temperatures is given in Figure 2.7.

i. Below T_0, G_1 has two minimum values when $P \neq 0$, indicating that the system is in the ferroelectric phase with two spontaneous polarizations that have equal values but opposite directions.

ii. At temperatures slightly higher than T_0, a new minimum value appears when $P = 0$. The value of G_1 for $P = 0$ is larger than that of G_1 at the other two minimum values and, hence, the paraelectric phase exists as a metastable state.

iii. As the temperature increases from T_0 to the Curie point T_c, the values of G_1 at the three minimum values are equivalent, indicating the energies of the ferroelectric and paraelectric states are equivalent.

iv. At temperatures slightly higher than T_c, G_1 has one minimum value when $P = 0$ and two other minimum values when $P \neq 0$. Since the value of G_1 when $P = 0$ is smaller, the system is in the paraelectric phase, but the ferroelectric phase exists as a metastable state.

v. A slight increase in temperature above T_c causes the two minimum values to disappear when $P \neq 0$, but two inflection points can still be observed. In this state, the ferroelectric phase can be induced by applying an electric field.

vi. A further increase in temperature above T_c causes the two inflection points at $P \neq 0$ to disappear and thus the ferroelectric phase can no longer be induced despite the application of an electric field.

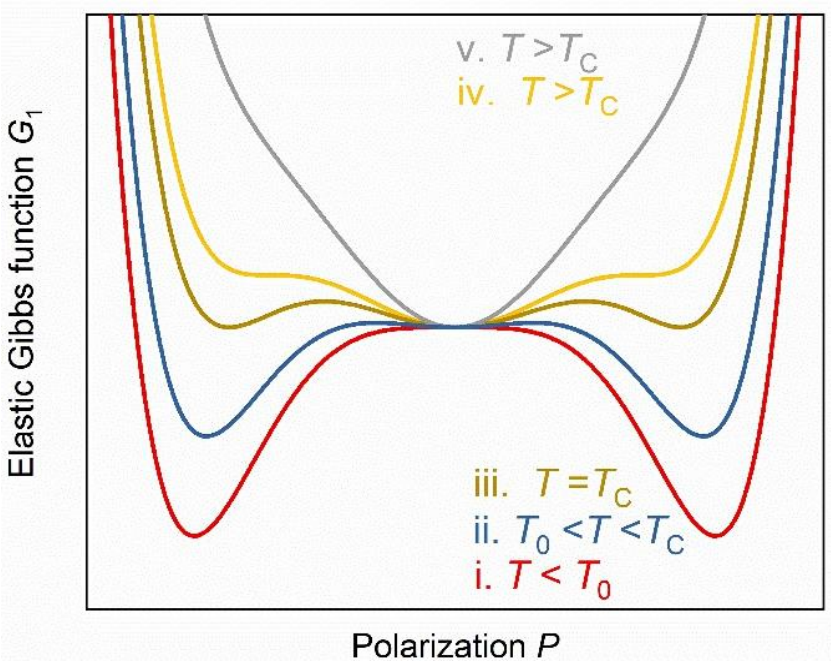

Figure 2.7: A schematic plot of the elastic Gibbs function G_1 of the first-order phase transition as a function of polarization at i. $T < T_0$, ii. $T_0 < T < T_c$, iii. $T = T_c$, iv. $T > T_c$, and v. $T > T_c$.

From Figure 2.7, we know that for the first-order phase transition the metastable ferroelectric phase can still exist at temperatures slightly above T_c upon heating, and T_0 is the lowest temperature the metastable paraelectric phase can exist upon cooling. As a result, the first-order phase transition is characterized by thermal hysteresis, i.e., the Curie point T_c experimentally measured during the heating run is always higher than that measured during the cooling run. Note that double polarization hysteresis loop, which is considered as an important experimental evidence for the identification of antiferroelectric−ferroelectric phase transition, can also be observed at temperatures slightly higher than T_c (the v. case in Figure 2.7) [26]. However, the double loop observed in this case cannot be taken as the evidence to prove the presence of antiferroelectricity. In other words, observation of double polarization hysteresis loops is not enough to prove the existence of antiferroelectric nature.

2.2.2 Thermodynamic Theory of Antiferroelectric Phase Transitions

Kittel [8] proposed the first theoretical model to describe the properties of an antiferroelectric system using a two-sublattice model, which is essentially a mixed microscopic description of polarization at the unit cell scale and a continuum description of the thermodynamics [2]. Each sublattice has its independent spontaneous polarization P_a and P_b. The system is in the

antiferroelectric state if $P_a = -P_b \neq 0$ and in the ferroelectric state if $P_a = P_b \neq 0$. Moreover, the system is in the ferrielectric state if $P_a \neq P_b \neq 0$. The Helmholtz free energy per unit volume of the system can be expanded as a function of the sublattice polarizations P_a and P_b.

2.2.2.1 Second-Order Phase Transition

First, the second-order phase transition is concerned ($h > 0$) and higher order terms (P^6) are neglected,

$$A = A_0 + f(P_a^2 + P_b^2) + g(P_a P_b) + h(P_a^4 + P_b^4) \quad 2–30$$

$$\frac{\partial A}{\partial P_a} = E = 2fP_a + gP_b + 4hP_a^3 \quad 2–31$$

The spontaneous polarization in the antiferroelectric state ($P_a = -P_b$) is obtained when $E = 0$.

$$P_{sa}^2 = \frac{g - 2f}{4h} \quad 2–32$$

If a small electric field is applied to the system in the antiferroelectric state, the macroscopic polarization $P = P_a + P_b$ can be obtained. Given 2–31:

$$\mathrm{d}E = 2f dP_a + g dP_b + 12hP_a^2 dP_a \quad 2–33$$

Similarly,

$$\mathrm{d}E = 2f dP_b + g dP_a + 12hP_b^2 dP_b \quad 2–34$$

From equations 2–33 and 2–34 ($P_a^2 = P_b^2$),

$$\begin{aligned} 2\mathrm{d}E &= 2fd(P_a + P_b) + gd(P_a + P_b) + 12hP_a^2 d(P_a + P_b) \\ &= 2fdP + gdP + 12hP_{sa}^2 dP \end{aligned} \quad 2–35$$

From equations 2–32 and 2–35,

$$\chi = \frac{dP}{dE} = \frac{1}{2(g - f)} \quad 2–36$$

At the Curie point, P_{sa}=0, $g = 2f$. On the antiferroelectric side,

$$\chi^- = = \frac{1}{g} \quad 2–37$$

In the paraelectric state, the fourth-power terms in 2–30 can be neglected,

$$\chi = \frac{2}{2f + g} \quad 2–38$$

At the Curie point ($g = 2f$),

$$\chi^{+} = \frac{1}{g} \qquad 2\text{–}39$$

Therefore, the dielectric susceptibility of an antiferroelectric system is continuous across the Curie point and does not necessarily have a high value. This is different from that of a ferroelectric system with a second-order phase transition.

Kittel [22] argued that f is related to the atomic polarizabilities and varies with temperature near the Curie point:

$$f = \frac{1}{2}g + \lambda(T - T_c) \qquad 2\text{–}40$$

From equation 2–32, when $T < T_c$

$$P_{sa}^2 = \frac{\lambda(T_c - T)}{2h} \qquad 2\text{–}41$$

From equation 2–36, when $T < T_c$,

$$\chi = \frac{1}{g - 2\lambda(T - T_c)} \qquad 2\text{–}42$$

From equation 2–38, when $T > T_c$,

$$\chi = \frac{1}{g + \lambda(T - T_c)} \qquad 2\text{–}43$$

Since the result of equation 2–41 must be positive, the antiferroelectric is on the low temperature side of the Curie point when λ is positive. Equation 2–42 shows that the dielectric susceptibility is at a maximum at the transition point. When λ is negative, the antiferroelectric state should occur on the high temperature side of the Curie point where the dielectric susceptibility has a minimum value.

2.2.2.2 First-Order Phase Transition

Now a first-order phase transition is concerned,

$$A = A_0 + f(P_a^2 + P_b^2) + g(P_a P_b) + h(P_a^4 + P_b^4) + j(P_a^6 + P_b^6) \qquad 2\text{–}44$$

$$\frac{\partial A}{\partial P_a} = E = 2fP_a + gP_b + 4hP_a^3 + 6jP_a^5 \qquad 2\text{–}45$$

In the antiferroelectric state ($E = 0$), $P_{sa} = -P_{sb}$,

$$6jP_{sa}^4 + 4hP_{sa}^2 + (2f - g) = 0 \qquad 2–46$$

At the Curie point, the free energy for this solution is equal to that for the paraelectric solution $P_a = P_b = 0$. From equation 2–44,

$$(2f - g) + 2hP_{sa}^2 + 2jP_{sa}^4 = 0 \qquad 2–47$$

From equations 2–46 and 2–47,

$$P_{sa}^2 = \frac{g - 2f}{h} \qquad 2–48$$

$$P_{sa}^4 = \frac{2f - g}{2j} \qquad 2–49$$

Similar to the treatment for the second-order phase transition, in the antiferroelectric state below the Curie point,

$$\chi^{-} = = \frac{1}{4f - g} \qquad 2–50$$

In the paraelectric state that is above the Curie point,

$$\chi^{+} = = \frac{2}{2f + g} \qquad 2–51$$

Therefore, the first-order antiferroelectric phase transition is characterized by a discontinuity in dielectric susceptibility at the Curie point.

The pioneering model of Kittel [8] is arguably of great importance for the phenomenological description of antiferroelectric phase transitions. However, the spontaneous polarization of sublattice is difficult to characterize experimentally and therefore of little practical value. Cross [30] and Okada [31] formulated a consistent continuum description of the thermodynamics of antiferroelectric phase transitions by restructuring the expression and introducing two vector order parameters related to the spontaneous polarization of the two-sublattice model, i.e., the antiferroelectric vector order parameter $\vec{q} = (\overrightarrow{P_a} - \overrightarrow{P_b})/2$ and the ferroelectric vector order parameter $\vec{q} = (\overrightarrow{P_a} + \overrightarrow{P_b})/2$. Such formulations allow better correlation between theoretical considerations and experimental data, and have been used to interpret experimental results in a qualitative way [32-34].

2.2.2.3 Tolédano's Model

Tolédano and Guennou [35] described antiferroelectric phase transitions using a modified Landau model, so that the status of the system (antiferroelectric, ferrielectric, or ferroelectric) can be directly evaluated by the value of the order parameters. A decoupling between the antiferroelectric order parameters, η, and the polarization, P, is induced when a nonpolar antiferroelectric system is subjected to an electric field. Two order parameters, including a single symmetry-breaking antiferroelectric order parameter η and the field-induced polarization P, are introduced into a Landau potential:

$$\Phi(\eta, P, T) = \Phi_0(T) + \frac{\alpha}{2}\eta^2 + \frac{\beta}{4}\eta^4 + \frac{\gamma}{6}\eta^6 + \frac{P^2}{2\chi_0} + \frac{\delta}{2}\eta^2 P^2 - EP \qquad 2\text{–}52$$

where $\alpha = (T - T_c)$, and the other phenomenological parameters are constant. This treatment expresses the property that a polar phase requires the mediation of the antiferroelectric order parameter to be stabilized under an electric field.

Minimizing Φ with respect to η and P,

$$\eta(\alpha + \beta\eta^2 + \gamma\eta^4 + \delta P^2) = 0 \qquad 2\text{–}53$$

$$P(1 + \delta\chi_0\eta^2) = \chi_0 E \qquad 2\text{–}54$$

Equations 2–53 and 2–54 yield four possible stable phases. At $E = 0$, the paraelectric phase ($\eta = 0$, $P = 0$) and the antiferroelectric phase ($\eta \neq 0$, $P = 0$) are stable. When $E \neq 0$, either a ferroelectric phase ($\eta = 0$, $P \neq 0$) or a ferrielectric phase ($\eta \neq 0$, $P \neq 0$) are stable, and a nonzero macroscopic polarization is present.

A theoretical temperature-electric field (T-E) phase diagram characterizing the paraelectric, antiferroelectric, and field-induced ferroelectric and ferrielectric phases is shown in Figure 2.8.

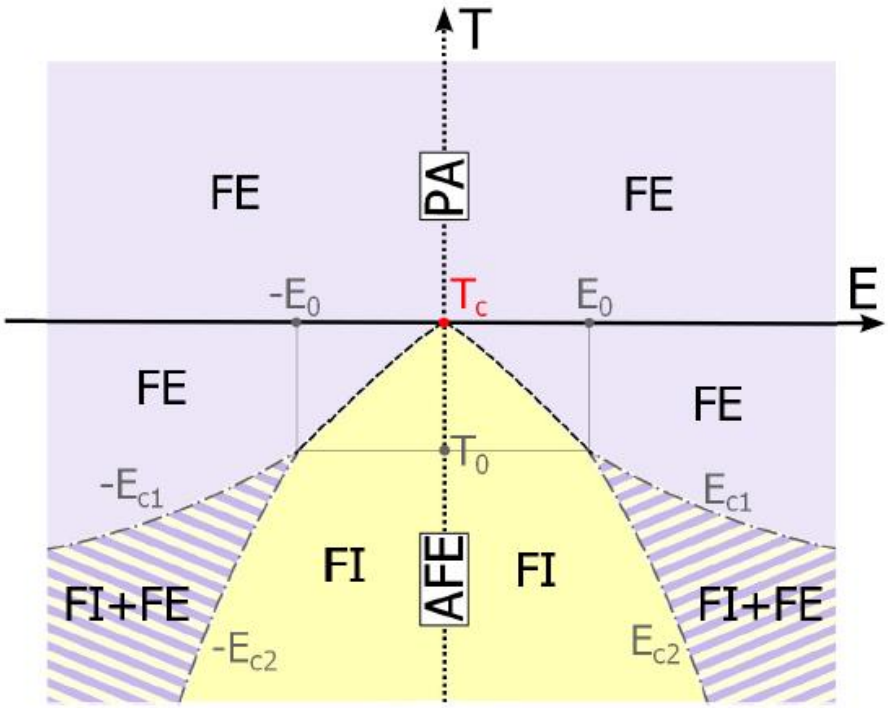

Figure 2.8: Theoretical temperature-electric field (*T*-*E*) phase diagram associated with the free energy given by equation 2–52 for $\beta > 0$ and $\delta > 0$. Hatched and hatched-dotted curves represent, respectively, second-order transition and limit of stability curves. Reprinted figure with permission from [35]. Copyright (2016) by the American Physical Society.

i. Above T_c, the paraelectric phase is stable when $E = 0$. The ferroelectric phase can be induced by applying an electric field.

ii. At $T_0 < T < T_c$, the antiferroelectric phase ($\eta \neq 0$, $P = 0$) is stable when $E = 0$. The antiferroelectric phase transforms into a ferrielectric phase when $E \neq 0$. The fourth-power terms in equation 2–53 can be neglected,

$$\eta^2 = -\frac{1}{\beta}(\alpha + \delta P^2) \qquad 2\text{–}55$$

From 2–53 and 2–54, P is a real root of the equation as follows,

$$\frac{\delta^2}{\beta}P^3 + \left(\frac{\alpha\delta}{\beta} - \frac{1}{\chi_0}\right)P + E = 0 \qquad 2\text{–}56$$

When the electric field is further increased, the ferrielectric phase transforms into the ferroelectric phase, indicating that the ferrielectric space group is a subgroup of the ferroelectric space group [35]. The transformation from the ferrielectric state to the ferroelectric state is a second-order phase transition, because there is no phase coexistence. The polarization becomes nonzero value ($P \neq 0$) during the phase transition, which is accompanied by the disappearance

of the decoupling order parameter (η = 0). From 2–53 and 2–54, the critical electric field at the phase transition can be derived,

$$E = \frac{P}{\chi_0} = \pm\frac{1}{\chi_0}\left(\frac{-\alpha}{\delta}\right)^{1/2} \qquad 2\text{–}57$$

iii. At $T < T_0$, the phase transition from the ferrielectric to the ferroelectric phase passes through the region of coexistence of the two phases and thus becomes a first-order transition characterized by discontinuous behavior. The limits of the region of coexistence, i.e. where the phase transition occurs, are given by the condition:

$$\frac{\partial^2\Phi}{\partial\eta^2}\cdot\frac{\partial^2\Phi}{\partial P^2} - \left(\frac{\partial^2\Phi}{\partial\eta\,\partial P}\right)^2 = (\alpha + 3\beta\eta^2 + \delta P^2)\left(\frac{1}{\chi_0} + \delta\eta^2\right) - 4\delta^2\eta^2P^2 = 0 \qquad 2\text{–}58$$

From 2–55 and 2–58,

$$\frac{3\delta^3}{\beta}P^4 + \delta P^2\left(\frac{4\delta\alpha}{\beta} - \frac{1}{\chi_0}\right) + \alpha\left(\frac{\delta\alpha}{\beta} - \frac{1}{\chi_0}\right) = 0 \qquad 2\text{–}59$$

The solutions of 2–59 with a positive value correspond to the electric fields E_{c1} and E_{c2}, where the ferrielectric−ferroelectric and ferroelectric−ferrielectric phase transitions occur, respectively.

The temperature dependence of the dielectric susceptibility at the paraelectric−antiferroelectric transition (P =0) can be derived from 2–54.

$$\chi = \frac{dP}{dE} = \frac{\chi_0}{1 + \delta\chi_0\eta^2} \qquad 2\text{–}60$$

For a second-order phase transition (β > 0), given 2–55 (P = 0),

$$\eta^2 = -\frac{\alpha}{\beta} \qquad 2\text{–}61$$

From 2–60 and 2–61,

$$\chi = \frac{dP}{dE} = \frac{\chi_0}{1 - \delta\chi_0\frac{\alpha}{\beta}} = \frac{\chi_0}{1 + \delta a\chi_0\frac{(T_c - T)}{\beta}} \qquad 2\text{–}62$$

Similar to the conclusion of the Kittel model (2–42), dielectric susceptibility passes through a maximum at the transition point. It is important to note that some antiferroelectric materials are characterized by increased dielectric permittivity with increasing electric field, which are highly desirable in high density power electronic applications [3]. Unfortunately, such behavior is not observed for all antiferroelectrics. Therefore, a qualitative prediction of how such enhanced permittivity can be achieved at the field-induced phase transition is provided: the Landau

potential parameters, which are also the material parameters, should be tuned in a way to approach the second-order line under the working conditions of the material. In Tolédano's model, the ferroelectric phase appears as a purely field-induced state that is subjected to symmetry requirements but is not present at zero field. The newly introduced order parameter, η, is considered as a structural mechanism responsible for the antiparallel dipole lattices [35]. The current model is related to Kittel's model in that η can be expressed in terms of strictly antiparallel dipoles, as assumed by Kittel.

3 Antiferroelectrics: Materials and Status Quo

The number of known perovskite antiferroelectric oxides is limited. Therefore, understanding the existing prototypical antiferroelectric systems is important for the development of new compositions. In this section, both lead-based and lead-free antiferroelectrics are reviewed, with particular emphasis on their composition, structure, and electrical properties.

3.1 $PbZrO_3$

In the search for new ferroelectrics, the similarity of the dielectric properties of $BaTiO_3$ and $PbZrO_3$ triggered great interest in the latter material, which is now generally recognized as an antiferroelectric prototype. The substitution of zirconium with a few atomic percent of titanium leads to the famous ferroelectric $Pb(Zr,Ti)O_3$ (PZT) [36], which exhibits versatile electromechanical properties and is still the most widely used piezoelectric system.

3.1.1 History: Phenomenological Observations

Roberts [37] reported that the temperature dependence of the dielectric properties of $PbZrO_3$ ceramics is very similar to that of $BaTiO_3$, i.e. the dielectric maximum of $PbZrO_3$ at 236 °C are reminiscent of the dielectric anomaly of ferroelectric systems at the Curie point. However, it was soon found that the field dependence of the dielectric response of $PbZrO_3$ is different from that of $BaTiO_3$. Shirane *et al.* [38] found that the Curie point of $BaTiO_3$ increases under a bias field, while that of $PbZrO_3$ decreases with increasing DC field. Since the off-centered atomic displacement in a ferroelectric system is favored by the application of an electric field, the Curie point should increase due to the stabilization of the ferroelectric order. The opposite observation in $PbZrO_3$ suggests that the dielectric anomaly of $PbZrO_3$ is of a different type of phase transition. Moreover, the characteristic ferroelectric polarization hysteresis loops could not be observed at room temperature. When the temperature approaches the Curie point, double polarization hysteresis loops were observed, indicating that $PbZrO_3$ is probably the first antiferroelectric material ever known.

3.1.2 Structure of $PbZrO_3$

The phase structure of $PbZrO_3$ is very complicated and has been studied from the 1940s to the present. The X-ray powder diffraction of $PbZrO_3$ was studied as early as 1946 by Megaw [39].

At the beginning, Megaw proposed that $PbZrO_3$ has a tetragonal symmetry at room temperature and the lattice parameters are a_T = 4.150 Å, c_T = 4.099 Å, with a c_T/a_T ratio of 0.988. Sawaguchi [9] studied the structure using an untwined $PbZrO_3$ crystal and found that the true symmetry is orthorhombic. The cell parameters are a = 5.87 Å ($\approx\sqrt{2}a_0$), b = 11.74 Å ($\approx 2\sqrt{2}a_0$), and c = 8.20 Å ($\approx 2a_0$), where a_0 is the cell parameter of the cubic phase. The unit cell contains 8 molecules (formula units) and the space group was assumed to be either centrosymmetric *Pbam* or non-centrosymmetric *Pba*2.

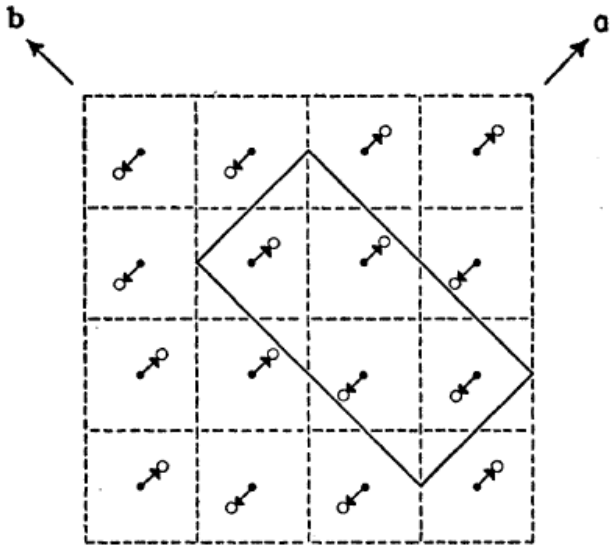

Figure 3.1: Schematic projection of the structure of $PbZrO_3$ on orthorhombic (001) plane. The black arrows represent the antiparallel atomic displacements of the Pb ions. The dashed lines delineate the pseudocubic subcells and the solid line shows the orthorhombic unit cell. Reprinted figure with permission from [9]. Copyright (1951) by the American Physical Society.

Fujishita *et al.* [40] reexamined the structure of $PbZrO_3$ and found that the positions of the Pb and Zr atoms agree well with previous studies by Sawaguchi [9] and Jona [41]. Both Pb and Zr experience only antiparallel shifts within the *ab* plane. Although three types of atomic displacements were found for the oxygen atoms, they exhibit only antiparallel displacements along the *c*-axis. Therefore, there should be no spontaneous polarization and Fujishita *et al.* therefore believed that the space group should be *Pbam*. The *Pbam* space group of $PbZrO_3$ at room temperature was subsequently confirmed by Tanaka *et al.* [42], Glazer *et al.* [43] and Corker *et al.* [44]. For example, Tanaka *et al.* performed conventional and convergent beam electron diffraction (CBED) on $PbZrO_3$ crystals and determined the structure as *Pbam* [42]. Glazer *et al.* [43] considered the possibility of disorder to explain the difficulty in determining

the true structure of $PbZrO_3$. The structure was found to be disordered with two substructure components connected by a shear of *c*/2. Possible differences in the structure of crystallites processed by different technological methods were discussed. Corker *et al.* [44] could not detect second harmonic generation in $PbZrO_3$, proving that the material is centrosymmetric.

With the advent of advanced techniques for structural characterization, the structure of $PbZrO_3$ has been further investigated at both low and high temperatures. Teslic and Egami [45] used a combination of the Rietveld refinement and atomic pair distribution function (PDF) analysis of pulsed neutron powder diffraction data to study the atomic structure as a function of temperature. In this way, both the average long-range structure and the local structure could be interpreted. Their Rietveld refinements showed that the large thermal factor for Pb increased faster above T = 200 K than below, which might be related to the anisotropic vibration of Pb atoms along the orthorhombic *c*-axis reported by Jona [41]. PDF analysis showed that in addition to the antiparallel displacements within the *ab* plane, the locally correlated displacements of Pb in the *c*-axis increased with increasing temperature, from 0.06 Å at room temperature to 0.14 Å at 473 K and 0.20 Å at 508 K. It seems that the study of Teslic and Egami supports that the ferroelectric order is present along the orthorhombic *c*-axis. However, although the Pb ions are locally displaced and correlated, and the Pb correlation length increases with increasing temperature, it is uncertain whether the long-range ferroelectric order is established in $PbZrO_3$.

In summary, a unified understanding of the structure of $PbZrO_3$ has not yet been achieved in the current literature, and the studies on its structure and phase transition behavior are still ongoing. Nevertheless, $PbZrO_3$ is probably the best model so far to approach the origin of antiferroelectricity.

3.2 $(Pb,La)(Zr,Sn,Ti)O_3$

The field-induced antiferroelectric−ferroelectric phase transition of $PbZrO_3$ can only be triggered near the Curie point [38], which makes the antiferroelectric prototype unsuitable for practical applications. Therefore, chemical modifications were made to $PbZrO_3$ in order to achieve an easily accessible phase transition at ambient conditions. The $(Pb,La)(Zr,Sn,Ti)O_3$ (PLZST) and $(Pb,Nb)(Zr,Sn,Ti)O_3$ (PNZST) systems are two major groups of $PbZrO_3$-based materials that have been most studied. The two systems can exhibit different macroscopic properties, e.g., antiferroelectric, ferroelectric, and even relaxor behavior with a slight change

in composition. More importantly, selected compositions readily exhibit a reversible AFE−FE phase transition at room temperature. Understanding the effects of composition, structure, microstructure and their interactions on the antiferroelectric properties of these two systems will be of great importance for the development of lead-free antiferroelectric materials.

Considering that the field-induced phase transition of $PbZrO_3$ was limited to a very limited temperature range, Jaffe [46] proposed two important criteria that should be satisfied for a AFE−FE phase transition to be triggered at a low electric field and be stable over an extended temperature range: (1) the sequence of phase transitions should be ferroelectric−antiferroelectric−paraelectric upon heating; (2) the maximum dielectric constant at the transition from the paraelectric state to the antiferroelectric state should be as high as possible. Jaffe argued that these two criteria ensure that the energy between the ferroelectric and antiferroelectric states is the same at the transition temperature, as is the energy between the antiferroelectric and paraelectric states at the Curie point. Berlincourt and Jaffe *et al.* have presented a $Pb(Zr,Sn,Ti)O_3$ system that meets these criteria [47]. This system is characterized by the presence of the ferroelectric state below the temperature range of the antiferroelectric state, which is not the case for $Pb(Zr,Ti)O_3$. Berlincourt *et al.* also reported the potential of antiferroelectric compositions $(Pb,Nb)(Zr,Sn,Ti)O_3$ (PNZST) and $(Pb,La)(Zr,Sn,Ti)O_3$ (PLZST) for energy conversion [47] and low-frequency transducers [48] applications. The phase diagrams of the versatile PNZST and PLZST systems have also been published [49]. The ternary phase diagram of the PLZST system is shown in Figure 3.2. The F_R region is the low-temperature rhombohedral region, the AFE_T and AFE_O regions are the antiferroelectric tetragonal and orthorhombic regions, respectively. The compositions near the phase boundary between antiferroelectric (AFE_T) and ferroelectric (F_R) phases are of particular interest and have been studied most frequently because the energies between the AFE and FE forms are so close that the transition between the two states can be achieved by an applied electric field. In contrast, the compositions in the AFE_O region are characterized by an ultrahigh electric field, which is impractical in real applications. The two material systems have attracted much attention and are still extensively studied today because the phase transition behavior can be easily tuned by composition, temperature change, electric field, and mechanical stress change [50].

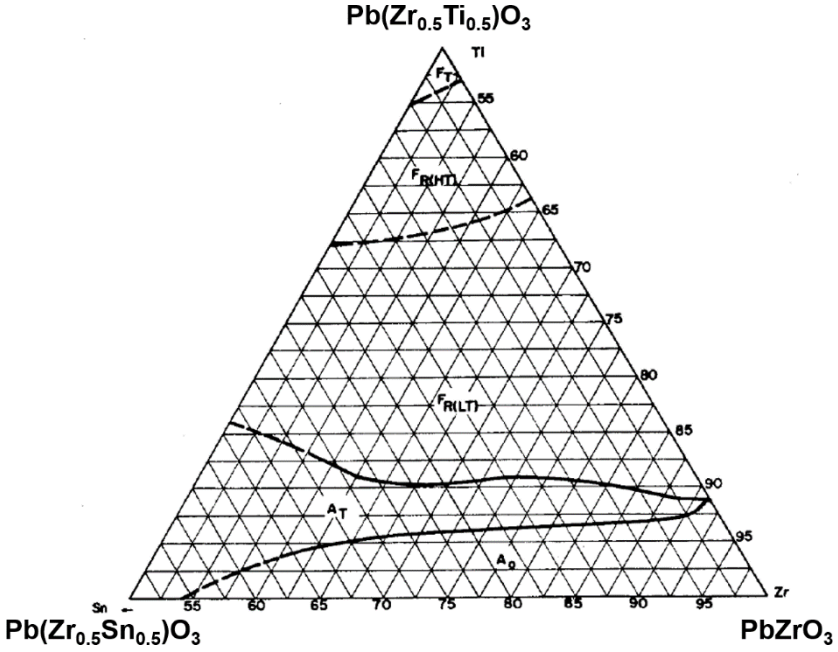

Figure 3.2: Phase diagram of $(Pb_{0.98}La_{0.02})(Zr, Ti, Sn)O_3$ systems. Copyright © 1966 IEEE, reprinted with permission from [49]. The compositions near the phase boundary between the antiferroelectric (AFE_T) and ferroelectric (F_R) phases are the most studied.

3.2.1 Effect of La Doping

Haertling and Land [51] studied the relaxor behavior of (Pb,La)(Zr,Ti)O_3 (PLZT) ceramics and found that the phase stability is very sensitive to the small variation in La content. When the La content increases, the antiferroelectric phase expands over the ferroelectric phase. The phase diagram of the PLZT system is shown in Figure 3.3, where the compositions within the shaded region exhibit a diffuse or smeared phase transition and are now referred to as slim ferroelectrics. Dai *et al.* [52] studied the effects of La content on the dielectric properties of a tetragonal $Pb(Zr_{0.40}Ti_{0.60})O_3$ ceramic. A low La content (0−8 at%) tended to diffuse the dielectric response at the phase transition temperature but no relaxor-like behavior was observed. For the sample with an intermediate La content (12 at%), a thermally induced transformation from a relaxor state to a normal ferroelectric state was observed upon cooling. A typical relaxor behavior was observed at a La content of 15−21 at%. Dai *et al.* [52] proposed that the coupling of oxygen octahedra is broken as a consequence of La doping and the resulting A-site vacancies, which is accompanied by the suppression of the long-range ferroelectric order and the formation of locally polarized regions. Viehland *et al.* investigated the electron diffraction patterns and microstructures of a series of La-modified Pb(Zr,Ti)O_3 with different La contents and Zr/Ti ratios using transmission electron microscopy (TEM) [53]. It was found that La substitution prevents the formation of normal micrometer-sized domains and favors the

formation of local polar moments. The ½[111] superlattice spots were found at temperatures above the onset of local polarization, suggesting that the local symmetry within the micro-sized polar regions is broken. Note that the appearance of the ½[111] superlattice spots is due to a doubling of the unit cell associated with the rotation of oxygen octahedra, indicating that the observation of superlattice reflections is not always related to antiferroelectricity. Based on their observations, Viehland *et al.* [53] proposed that a symmetry hierarchy exists in the PLZT system that is responsible for the complex pattern of disorder in the domain structure. Although the average symmetry at the macroscopic level is cubic, the average symmetry at the microscopic level appears to be the high-temperature rhombohedral state. Moreover, the average symmetry at the submicrometer level is the low-temperature rhombohedral state. The hierarchical symmetries may be the key to the slim polarization loops and the lower degree of hysteresis of the PLZT system, which can serve as a good reference for the development of hysteresis-free antiferroelectric materials.

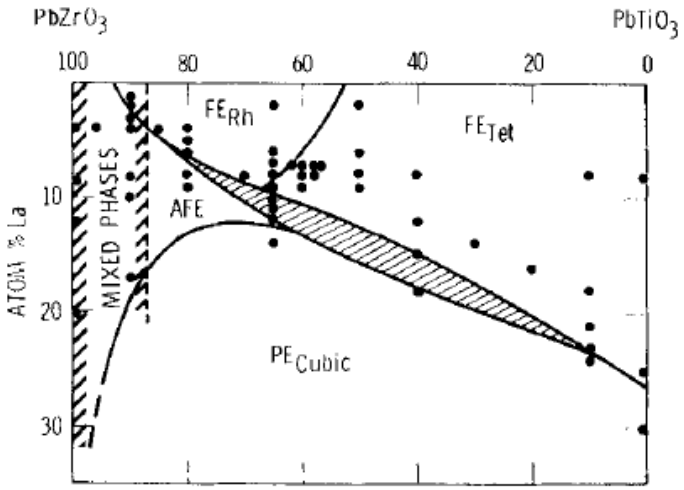

Figure 3.3: Phase diagram of (Pb,La)(Zr,Ti)O_3 system at room temperature, reprinted with permission from [51]. Copyright © John Wiley & Sons, Inc.

3.2.2 Effect of Sn Doping

The effects of Sn in the PLZST system can be seen from the phase diagram in Figure 3.2. The antiferroelectric tetragonal region expands greatly with increasing Sn content. Markowski *et al.* [54] investigated the effect of the ratio of Sn:Ti and Zr:Sn on the dielectric, polarization and strain properties of PLZST ceramics. It was found that the critical field increases with increasing Sn:Ti ratio as the compositions penetrate deeper into the AFE region. The degree of hysteresis, i.e. how narrow the loop is, is independent of the amount of Sn. Instead, the degree

of hysteresis shows a strong dependence on the temperature of the dielectric maximum, T_{max}, which remains almost unchanged with increasing Sn content. Viehland *et al.* [55] studied the dielectric properties of Sn-modified $Pb_{0.98}Nb_{0.02}[(Zr_{1-x}Sn_x)_{1-y}Ti_y]_{1-z}O_3$ ceramics as a function of Sn and Ti content. The strong deviation from the Curie-Weiss law was interpreted as evidence for the formation of local polar or antipolar couplings far above the dielectric maximum. At high temperatures the degree of deviation is weak and therefore no superlattice spots were observed. The degree of deviation and the intensity of the superlattice reflection increase with decreasing temperature, which is attributed to gradual increase in the magnitude of the local order parameter upon cooling and thus, the transition of the simple sinusoidal modulation at higher temperatures into antiphase boundaries (APBs). From the SAED patterns, a temperature dependence of the width of the APBs can be observed. Moreover, a strong suppression of the dielectric constant and a broadening of the dielectric maximum with increasing Sn content were observed, as shown in Figure 3.4, where the appearance of a plateau is explained by the existence of a "multicell" cubic state.

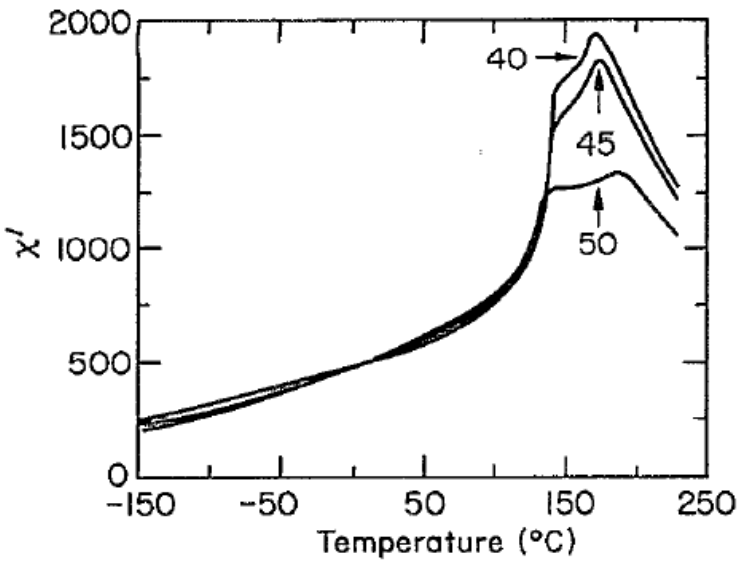

Figure 3.4: Temperature dependence of dielectric permittivity of Sn-modified PNZST ceramics as a function of Sn contents, measured at 10^5 Hz. Reprinted from [55], with the permission of AIP Publishing.

3.2.3 Field-Induced Phase Transition

In this section, the field-induced phase transition of the PLZST and PNZST systems are discussed, focusing on polarization, strain, and kinetics. The pioneering work of *in situ* XRD characterization of the field-induced phase transition is presented.

3.2.3.1 Strain

The specific volume of the cubic state is intermediate between those of the FE and AFE states [48]. One of the axes perpendicular to the antiparallel displacements is shorter than that in the cubic (reference) state in the AFE state, while the unit cell expands along the polar axis in the FE state. Therefore, for the same composition, the AFE form has a smaller cell volume than the paraelectric form, while the FE form has a larger lattice volume than the paraelectric form. Consequently, the field-induced phase transition from the AFE state to the FE state is accompanied by a large change in shape. For example, a field-induced longitudinal macroscopic strain of 0.87% has been reported for PLZST ceramics [56]. Interestingly, some antiferroelectric PLZST and PNZST systems show expansion not only in the longitudinal direction but also in the transverse direction during the AFE−FE phase transition [48, 57, 58], which is known as the "auxetic" behavior [59]. The transverse strain in ferroelectrics is negative, which attenuates the volume expansion caused by the longitudinal strain. Since the transverse strain in these antiferroelectrics is positive, the field-induced volume expansion can be quite large.

Previous studies on the temperature dependence of field-induced polarization and strain seem to indicate that strain is particularly sensitive to temperature changes. A thermodynamic analysis revealed that the volume change accompanying the field-induced transition is proportional to the scalar electrostrictive coefficient for the coupling between the two sublattices of the antiferroelectric phase [56]. The stronger the coupling between the two sublattices, the larger the volume change.

3.2.3.2 Decoupling of Polarization and Strain

An interesting decoupling phenomenon between polarization and longitudinal strain has been observed for $PbZrO_3$-based antiferroelectric compositions [60, 61]. For example, the longitudinal strain lags behind the polarization jump during the phase transition, and the longitudinal and volume strains still increase significantly after the polarization saturation [62]. However, the transverse strain and polarization appear to be synchronized during the phase transition [60]. Viehland *et al.* [63] suggested that it is possible to develop polarization without strain and conversely strain without polarization. In other words, the field-induced strain associated with the AFE−FE transition is only realized at an electric field well above that

required to saturate the polarization. The above results are in contradiction to the previously known mechanisms of electromechanical coupling in the sense that polarization and strain do not occur simultaneously [63, 64].

i. Electrostriction, where the strain is coupled to the square of the polarization via the electrostriction coefficient;

ii. Piezoelectric effect, where the strain is coupled to the electric field via the piezoelectric coefficient;

iii. Field-induced phase transition, where the strain is accompanied by the formation of the ferroelectric state.

The origin of the peculiar decoupling behavior observed in PLZST and PNZST systems is unclear [59, 65] because of complicated cases in different antiferroelectric compositions. Forst *et al.* [61] studied the influence of Sn content in $Pb(Zr,Sn,Ti)O_3$ and showed that the differences in the saturation behavior between the polarization and strain responses became more pronounced with increasing Sn content. Forst *et al.* believed that such behavior could be explained by the presence of multiple ferroelectric phases, which was reported previously [66]. An AFE−FE was initially triggered at a lower electric field, leading to saturation of the polarization. Significant strains were observed at higher electric fields, which was attributed to a secondary FE−FE phase transition from an intermediate orthorhombic phase to a rhombohedral phase.

3.2.3.3 Kinetics

The existence of a threshold field for the field-induced phase transition from the AFE state to the FE state is a universal phenomenon in many antiferroelectric systems. Below a critical field, not much polarization can be induced, while above the critical field, the induced polarization does not vary too much with the applied electric field [57]. Once the transition is induced, a sharp increase in polarization is observed and a large current must be supplied to ensure a non-delayed phase change. It should be noted that the critical field for the field-induced phase transition is always higher in the first cycle (the virgin state) than in the following cycles [49, 57].

Pan *et al.* studied the kinetics of the forward (antiferroelectric−ferroelectric) [56] and backward (ferroelectric-antiferroelectric) [67] phase transition of a PLZST system. The field-induced

phase transition is controlled by a phase nucleation process and the "switching" time is on the order of 1−2 μs when a field is high enough to induce the transition [57]. The activation field for the forward phase transition was determined to be 15−20 kV/mm [56], which is much higher than the value of 0.5−1.0 kV/mm for ferroelectric switching. This shows that nucleation of a new phase is more difficult than nucleation of new domains. For the backward phase transition, the "switching" time increases when the field of the transition from the FE state to the AFE state decreases. The difference between the field of the backward transition and the zero field is considered as the driving force for the recovery of the AFE state after removing the electric field. The higher the field, the larger the driving force for the backward transition and the shorter the "switching" time.

3.2.3.4 *In situ* XRD Study

Blue *et al.* [68] studied the field-induced phase transition of the $Pb_{0.98}La_{0.02}(Zr_{0.55}Sn_{0.33}Ti_{0.12})_{0.995}O_3$ ceramic using *in situ* XRD. The structure in the virgin state was identified as a single tetragonal phase with cell parameters a = 4.107 Å and c = 4.081 Å. A preferred domain structure was found for the ceramic sample exposed to an electric field, as shown in Figure 3.5, where the intensity of the (002) peak is significantly reduced compared to that of the powder. It was estimated that about 2/3 of the grains of the tetragonal phase are aligned with the c-axis planes tilted out of the sample plane, showing that the sample undergoes an irreversible change in microstructure after the application of an electric field, despite the maintained antiferroelectric state.

The XRD patterns of the sample at zero field and 2.6 kV/mm are shown in Figure 3.6. The profile of the tetragonal (111) reflection at zero field is significantly altered at 2.6 kV/mm, which fits well with the (111) and (−111) peaks of a rhombohedral structure with cell parameters a = 4.105 Å and θ = 89.85°. This suggests that the tetragonal phase transforms into the rhombohedral phase upon application of the electric field.

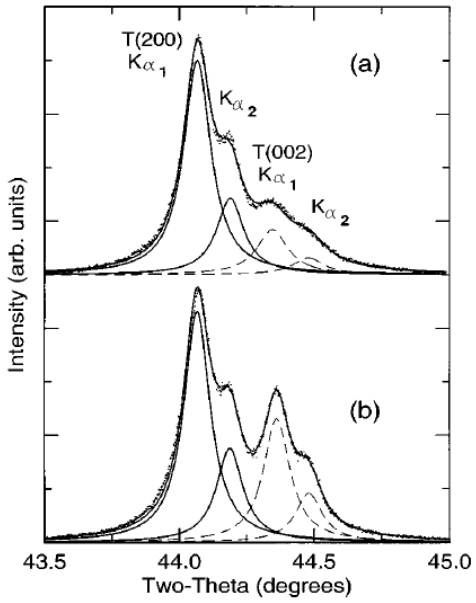

Figure 3.5: (200) and (002) reflection peaks of the PLZST sample at room temperature and zero field for (a) the ceramic sample to which an electric field was applied and (b) the same ceramic sample after it was ground to a powder. Reprinted from [68], with the permission of AIP Publishing.

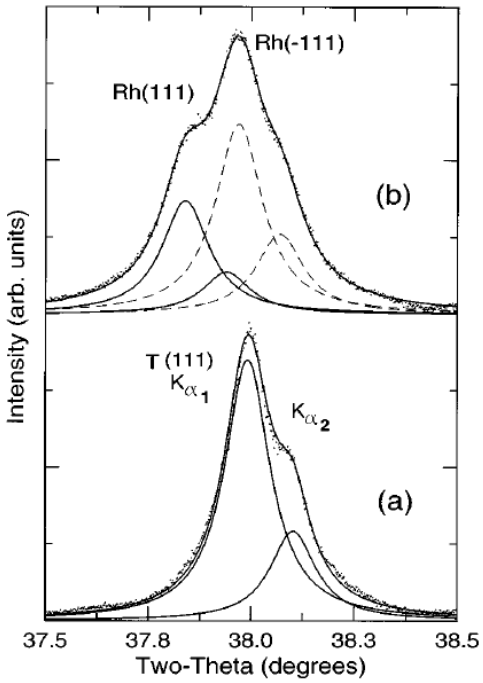

Figure 3.6: (111) reflection peaks of the PLZST ceramic sample at (a) zero field and (b) an applied electric field of 2.6 kV/mm. The profiles at zero field and 2.6 kV/mm can be fitted with a single tetragonal structure and a single rhombohedral structure, respectively. Reprinted from [68], with the permission of AIP Publishing.

Park *et al.* [62] studied the field-induced phase transition of a PLZST system and proposed a step-by-step sequence of the phase transition, as shown in Figure 3.7.

i. A virgin sample with randomly oriented antiferroelectric domains (Figure 3.7a) transforms into a preferentially oriented AFE state (Figure 3.7b) after the application of an electric field. Note that this process is irreversible without heating the sample above the Curie point.

ii. The phase transition from the AFE state to the FE state (Figure 3.7c) is induced, accompanied by a sudden increase in polarization. However, due to the presence of stress induced by volume expansion, a considerable degree of the alignment of polarization vectors is not achieved at this stage.

iii. The induced ferroelectric domains become polarized with the increase in electric field (Figure 3.7d). The alignment of the domains leads to an increase in polarization and longitudinal strain.

iv. The sample exhibits piezoelectric effect, i.e., the longitudinal strain continues to increase, while the transverse strain begins to decrease.

v. The FE state returns to the AFE state with preferred orientation. The random AFE state can be recovered only when the sample is heated above the Curie point.

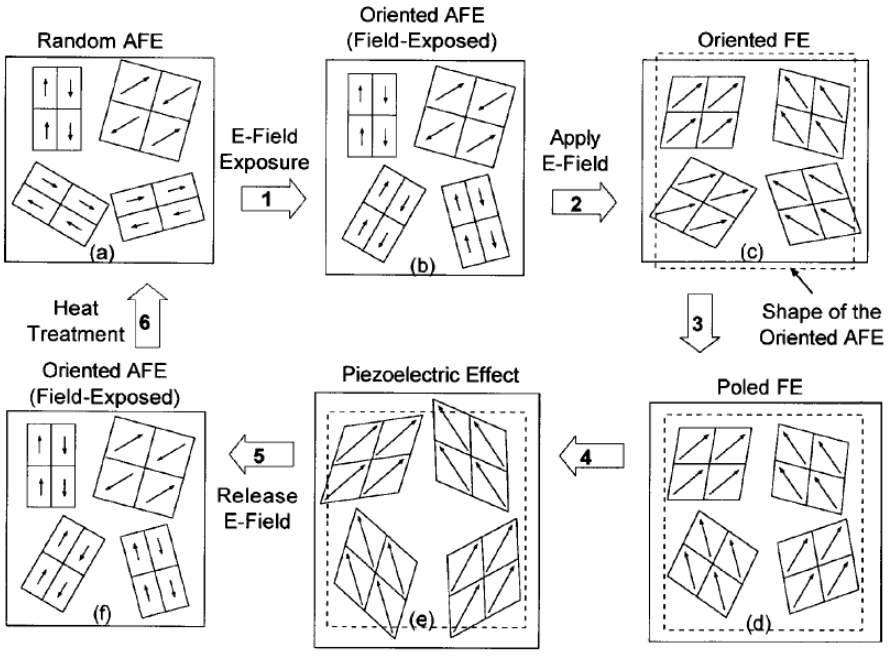

Figure 3.7: Schematic diagram of the AFE-FE phase transition procedure of the PLZST ceramic sample. Reprinted from [62], with the permission of AIP Publishing.

3.3 $NaNbO_3$

Similarly to $PbZrO_3$, $NaNbO_3$ was initially considered as one of the new ferroelectric materials because it exhibited an analogous temperature dependence of dielectric properties as expected in ferroelectric systems [69]. Matthias *et al.* [70] reported two dielectric anomalies with thermal hysteresis and the one at 480 °C was attributed to the Curie point of the system. However, the transition at 480 °C is only one of the complex and intriguing displacive phase transitions [71] exhibited by $NaNbO_3$, which possesses a complex phase diagram. Subsequently, $NaNbO_3$ has attracted considerable attention to understand the temperature- and field-induced structural changes and their effects on the functional properties. In this section, we review the development of scientific studies on $NaNbO_3$, with special attention to its structure and phase transitions.

3.3.1 Structure at Room Temperature

Vousden [72] performed detailed structural characterizations of $NaNbO_3$ crystals at room temperature using XRD and proposed that the space group is $P22_12$. Although this space group is different from *Pbcm* (alternatively *Pbma*), which is the widely accepted structure of $NaNbO_3$ today, Vousden's structural model is very close to the current understanding of $NaNbO_3$. It was found that the niobium ions are shifted by 0.11 Å with respect to the positions in the ideal perovskite structure in an antiparallel manner and therefore the structure is macroscopically nonpolar. This contradicted to the view at the time that $NaNbO_3$ is a ferroelectric system. In order to reconcile the non-polar structure with the observed ferroelectric properties, Vousden [73] suggested that the $NaNbO_3$ crystal changes from a non-polar to a polar state by the application of an electric field and that the substances before and after the application of the field must have different, albeit closely related, structures with different space groups but nearly the same free energy. This wise hypothesis is remarkably close to the concept of antiferroelectricity and was proposed even before the famous publication of Kittel [8]. Megaw *et al.* [74] reexamined the space group of $NaNbO_3$ at room temperature and considered that the possible options were *Pbma* or the subgroups $Pb2_1a$ or $P2_12_12$. The structure of $NaNbO_3$ crystals subjected to a high electric field was studied by Cross in 1958 [75] and by Wood *et al.* in 1962 [76]. The ferroelectric phase induced by the application of the electric field was identified as the space group $P2_1ma$ by Wells and Megaw [77]. Disagreement over the polar or non-polar nature of $NaNbO_3$ called for a better understanding of its structure.

The crystallographic structures of the *Pbcm* and $P2_1ma$ phases of $NaNbO_3$ are shown in Figure 3.8(a) and Figure 3.8(b), which are also referred to as the *P* phase and the *Q* phase, respectively. Both structures exhibit orthorhombic symmetry with rhombic primitive cells ($a = b \neq c$, $\gamma \neq 90°$), i.e., the orthorhombic *a*- and *b*-axes are parallel to the face diagonals of the same pseudocubic cell. The way the successive primitive cells are arranged along the $[001]_{PC}$ axis is different for the *P* and *Q* phases. The unit cell of the *P* phase consists of 4 octahedral layers along the $[001]_{PC}$ direction, while the *Q* phase has only two, as shown by the black dashed lines in Figure 3.8. The tilting of the NbO_6 oxygen octahedra in the *P* phase is described by the Glazer notation $a^-a^-b^+/\ a^-a^-b^-/\ a^-a^-b^+$, while the *Q* phase is characterized by $a^-a^-b^+$ [71, 78]. In particular, the octahedra of layers 2 and 3 in the *P* phase are described by $a^-a^-b^-$, while the octahedra of layers 1 and 2, as well as layer 3 and 4 are described by $a^-a^-b^+$. The AFE order of the *Pbcm* structure arises from the antiparallel atomic displacements of Na and Nb in the top two layers (layer 1 and 2) and the bottom two layers (layer 3 and 4). The magnitude of the displacement of the Na(1) along the $[110]_{PC}$ direction is larger than that of Nb, while an Nb atom has more electric charges. In the FE *Q* phase, the spontaneous polarization is caused by the parallel displacements of Na and Nb atoms along the $[110]_{PC}$ direction. Since the primitive cell in the *P* and *Q* phases is multiplied by 4 and 2, respectively, in the $[001]_{PC}$ direction, the two phases are characterized by ¼ and ½ superlattice reflections, respectively [79].

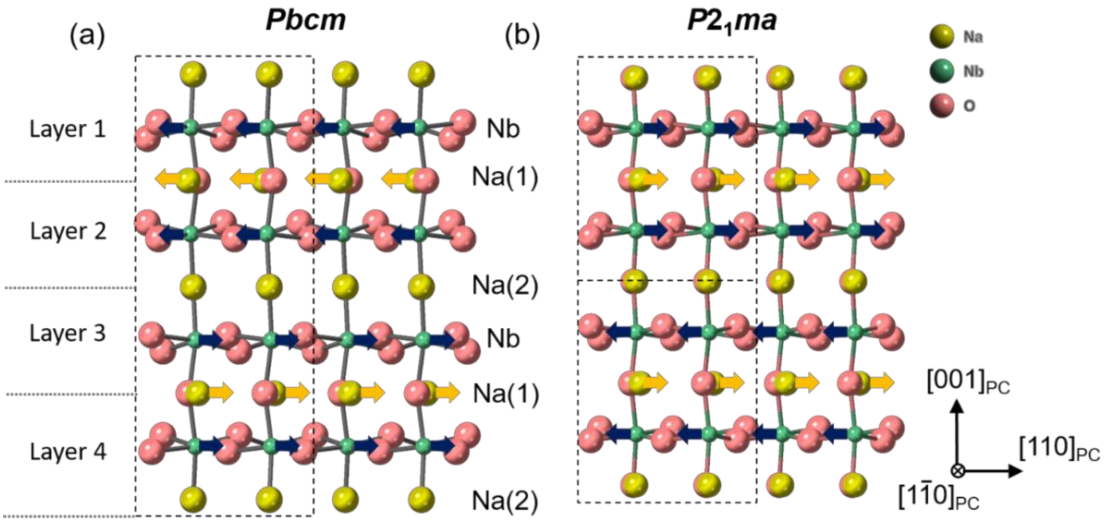

Figure 3.8: Crystallographic structures of the *Pbcm* and $P2_1ma$ phases of $NaNbO_3$, viewed along the $[1\bar{1}0]$ direction. The unit cells of the two phases are highlighted by black dashed lines. The atomic displacements of Na and Nb atoms are expressed by orange and dark blue arrows, respectively.

Jiang *et al.* [80] studied the local structure of $NaNbO_3$ using high-resolution neutron scattering and revealed that the Nb ion in the octahedral NbO_6 is off-centered by 0.15 Å or 7.7%, while the Na ion in NbO_8 is off-centered by 0.4 Å or 14%. The atomic displacements of both Na and Nb contribute to the local polarization in the *Pbcm* structure. Moreover, it was reported that despite the antiferroelectric *Pbcm* group symmetry over the long distance beyond 10 Å, the short-distance local structure (<10 Å) is always in the ferroelectric *R*3*c* space group. The *R*3*c* space group was considered to be the real ground state of $NaNbO_3$. The competition between the ferroelectric *R*3*c* and antiferroelectric *Pbcm* phases at room temperature and below was also reported by Mishra *et al.*[81]. Their theoretical lattice dynamical calculations pointed out that the free energies of the two phases are nearly identical over a wide temperature range.

3.3.2 Temperature dependence of the Phase Transitions

$NaNbO_3$ is characterized not only by a complex structure at room temperature, but also by a series of phase transitions as a function of temperature. Early temperature-dependent studies were performed using a combination of XRD and optical characterizations. In the 1950s, knowledge of the phase structures of $NaNbO_3$ at high temperatures was not uniform. Wood [82] and Shirane *et al.* [83] reported that a structural phase transition from orthorhombic to tetragonal occurs at 360 °C upon heating. Cross *et al.* [84] suggested that the symmetry above 360 °C is orthorhombic based on optical observations. Shirane *et al.* [83] showed that the tetragonal splitting decreases with increasing temperature and no clear line splitting was observed at temperatures above 430 °C. However, no significant changes were observed in their optical characterizations above 480 °C until the optically-isotropic state was reached at 640 °C. The discrepancies between the X-ray and optical observations were also reported by Wood [82]. Shirana *et al.* [83] believed that the optical measurements were more sensitive to slight lattice distortions than the X-ray technique at that time. Francombe [85] again carefully examined the high temperature structures of $NaNbO_3$. It was found that structures below 480 °C were considered pseudo-tetragonal (orthorhombic) and a true tetragonal structure appeared only above 560 °C. Detailed structural studies were subsequently carried out by Lefkowitz *et al.* [86], Glazer *et al.* [78] and Megaw [71] using higher resolution XRD. $NaNbO_3$ is now believed to have at least seven different phases at different temperatures, as shown in Figure 3.9. In particular, the structures differ in the off-centered Nb in the octahedron and tilting of oxygen octahedra [71].

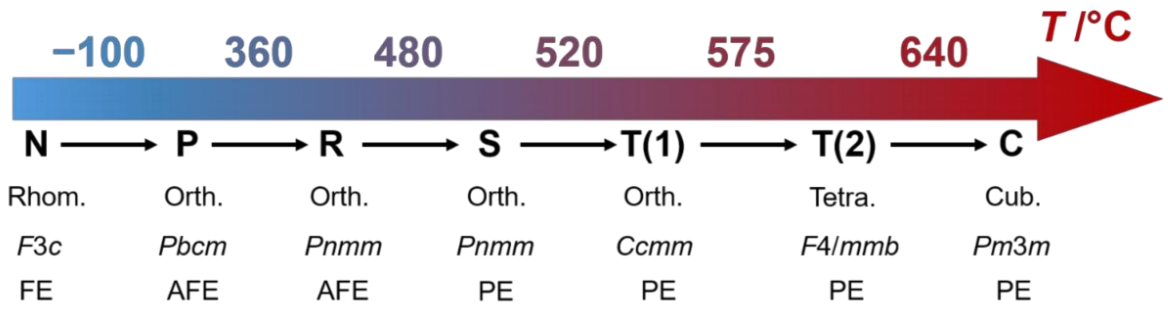

Figure 3.9: Sequence of the phase transitions of $NaNbO_3$ as a function of temperature, readpted from Ref. [71].

3.3.3 Field-Induced Phase Transitions in Crystals

Systematic electrical characterizations of $NaNbO_3$ crystals were first reported by Cross *et al.* [84]. Crystals were subjected to an electric field parallel or perpendicular to the orthorhombic *c*-axis at room temperature. Double polarization hysteresis loops could only be observed when the electric field was applied perpendicular to the *c*-axis, otherwise a linear relationship between polarization and field was maintained until dielectric breakdown. Anisotropy was also observed in the dielectric properties as a function of temperature. Later, Cross [75] reported that $NaNbO_3$ crystals modified by potassium, $(K_{0.005}Na_{0.095})NbO_3$, exhibited a double hysteresis loop in the first few cycles of electric field, while a ferroelectric loop was observed in the following cycles. The space group of $NaNbO_3$ before electric field application was determined as *Pbma* [74], while the state after field application was determined by Wells and Megaw [77] as space group $P2_1ma$, corresponding to an antiferroelectric to ferroelectric phase transition. The field-induced transition from the AFE state to the FE state has also been described by Miller *et al.* [87], Wood *et al.* [76], Zhelnova *et al.* [88] and Ulinzheev *et al.* [89]. Miller *et al.* [87] reported that a sufficiently high electric field can drive $NaNbO_3$ and $Na(Nb_{1-x}V_x)O_3$ crystals to the ferroelectric state and that some crystals can return to the non-ferroelectric state after the field is removed. Wood *et al.* [76] found that the AFE state of $NaNbO_3$ can be converted to the FE state by applying an electric field perpendicular to the orthorhombic *b*-axis with a field of 5 kV/mm. However, the structure induced by the field can coexist in a single crystal with the unchanged part that was not exposed to the field after the field was removed. Zhelnova *et al.* [88] also observed the coexistence of two phases, *Pbma* and $P2_1ma$, in $NaNbO_3$ crystals after the field-induced phase transition. It was found that the coexistence can be maintained for infinitely long periods of time and the sample can return to a single *Pbma* state either by heating to high temperatures or by applying a short electric pulse of opposite polarity to the crystal. Ulinzheev

et al. [89] systematically studied the dependence of the phase transitions on the crystallographic directions in a $NaNbO_3$ crystal by rotating the field vector within the (100) and (110) planes, and presented two electric field magnitude-direction phase diagrams. When the field vector is within the (100) plane, the *Pbma*−*P*2$_1$*ma* phase transition is thermodynamically irreversible when the angle between the field vector and the displacement of the Nb ions, φ, is between 0° and 57°; the observed behavior for φ>57° is characterized by a reorientation of the axes and a *Pbma*−*P*2$_1$*ma* phase transition. In the second case, no metastable states were observed, and the original orientation of the crystal lattice was not recovered after completion of the *Pbma*−*P*2$_1$*ma*−*Pbma* cycle. The phase transition characterizations of this work were based on observation of the amount of birefringence, the type of optical extinction, and the shape of the domain and twin boundaries using a polarized-light microscope, and no polarization hysteresis loops were reported.

3.3.4 Phase Stability of $NaNbO_3$ Ceramics

Since different properties such as antiferroelectricity [90], ferroelectricity [91], or a combination of both [92] have been found in $NaNbO_3$ ceramic materials, there is still a debate whether the ground state of $NaNbO_3$ ceramics in the virgin state is AFE or FE, or whether there it is a coexistence of both. According to first-principles calculations, the energy difference between the non-polar *Pbma* and polar *P*2$_1$*ma* structures is remarkably small (~1 meV/f.u.) [17, 93]. In contrast, the energy difference between the AFE and FE structures for $PbZrO_3$ was calculated to be 20 meV/f.u. [18]. The minimal energy difference between the two states of $NaNbO_3$ is likely responsible for the high sensitivity of phase stability to a variety of factors, including composition [11], starting chemical materials [12], externally applied hydrostatic stress [13], epitaxial stress [14, 15] and average grain size [16]. For example, Megaw and Wells [74] found that $NaNbO_3$ and $(Na_{0.995}K_{0.005})NbO_3$ have the same *Pbma* structure, in the sense that both the unit cell size and the atomic displacements of Nb are nearly the same. A later study by Wells and Megaw [77] revealed that the structure of $(Na_{0.975}K_{0.025})NbO_3$ turns out to be a *P*2$_1$*ma* space group. It is surprising that such a small difference in composition significantly alters the relative stability of the AFE and FE states. Li *et al.* [12] have shown that the relative contents of the AFE and FE phases of $NaNbO_3$ ceramics are sensitive to the Nb_2O_5 precursors used. Fan *et al.* [94] investigated the effects of A-site nonstoichiometry on the microstructure and electrical properties of $Na_{1+x}NbO_3$ ceramics. It was found that Na deficiency increases the average grain size, while Na excess decreases the average grain size. More importantly, the

electric field required to induce the transition from the AFE phase to the FE phase increased significantly from 10 kV/mm for pure $NaNbO_3$ to 17 kV/mm for the Na-deficient sample, indicating that the stability of the AFE phase increases with Na deficiency. It was found that the antiferroelectric state of $NaNbO_3$ can change to the ferroelectric and paraelectric states when the material is subjected to a hydrostatic pressure of 7 GPa and 12 GPa, respectively [13]. It has been found that epitaxial $NaNbO_3$ films under tensile stress exhibit FE properties instead of AFE properties [15]. Koruza *et al.* [16] studied the influence of grain size on the phase stability of $NaNbO_3$ ceramics. It was found that the FE order can be induced when the grain size is reduced to a critical value of 0.27 μm, above which the AFE order is preserved. The above controversies in the literature raise the following scientific questions to be addressed:

i. How to tailor the phase stability of $NaNbO_3$ and stabilize the antiferroelectric order of the sintered ceramic samples? This is the basis for the study of antiferroelectricity in $NaNbO_3$.

ii. Triggering the field-induced antiferroelectric to ferroelectric phase transition and understanding the phase transition behavior of $NaNbO_3$. In particular, how do the structure, microstructure, and macroscopic functional properties change with the phase transition?

iii. Exploring the irreversible nature of the field-induced phase transition.

3.4 $NaNbO_3$-Based Antiferroelectrics

Pure $NaNbO_3$ materials are characterized by an irreversible phase transition from the AFE state to the FE state, so that no stable double polarization hysteresis loops have been observed. To stabilize the AFE order, chemical compositional modifications have been used as one of the most common approaches. Most strategies aim at lowering the Goldschmidt tolerance factor *t*:

$$t = \frac{(R_A + R_O)}{\sqrt{2}(R_B + R_O)} \qquad 3\text{–}1$$

where R_A, R_B, and R_O are the ionic radii for the A- and B-site cations and the oxygen anion, respectively. Although the tolerance factor is usually considered as an empirical index to predict whether the AFE or the FE order is preferred [95], the first-principles calculations of Zhong and Vanderbilt [96] have shown that the tolerance factor is closely related to the antiferrodistortive (AFD) instability in cubic perovskites, which can profoundly modulate the

AFE stability of the materials. According to their calculations, $BaTiO_3$ and $KNbO_3$ are very stable to AFD distortions, while $CaTiO_3$, $PbZrO_3$ and $NaNbO_3$ exhibit strong AFD instability. It is known that $PbZrO_3$ and $NaNbO_3$ are antiferroelectric prototypes, while $BaTiO_3$ and $KNbO_3$ are typical ferroelectric systems. It has been found that a smaller *A* or a larger *B* atom tend to stabilize the AFE order, which provides the theoretical support for using the tolerance factor to develop new antiferroelectric compositions.

In order to stabilize the AFE order of $NaNbO_3$, Shimizu *et al.* [17] suggested that the selection of new compositions can be evaluated by considering a combination of tolerance factor, electronegativity difference and polarizability of the material. As shown in Figure 3.10, the tolerance factor can be divided into two regions: the ferroelectric distortive region (red) and the antiferroelectric distortive region (blue). For example, the tolerance factor increases when Na is substituted with K. The substitution is accompanied by an enhancement of the polar distortions and thus favors the FE order. In contrast, the substitution of Sr/Ca for Na in the A-site and the substitution of Hf/Zr for Nb in the B-site can decrease the tolerance factor, which is accompanied by an enhancement of antipolar distortions and thus favors the AFE order. Note that the simultaneous substitution of the A-site and the B-site can balance the charge neutrality.

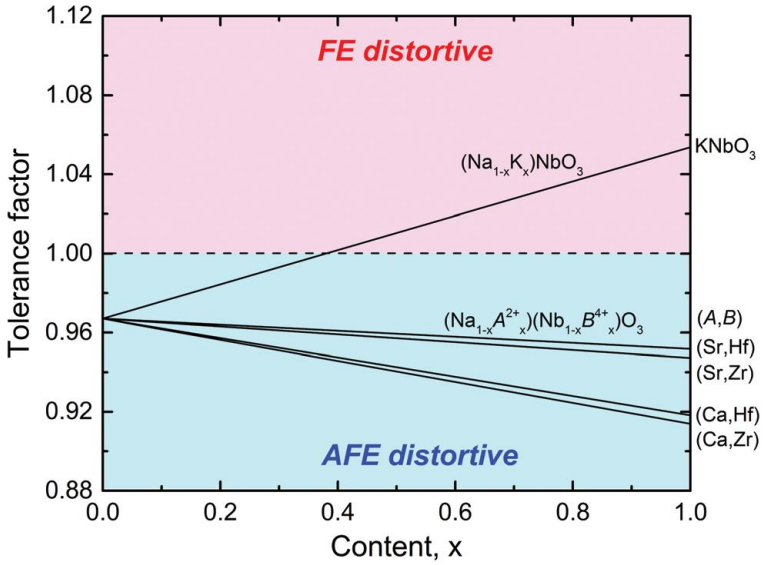

Figure 3.10: Plot of average tolerance factor versus dopant concentration x of $NaNbO_3$. Red and blue part represent ferroelectric and antiferroelectric distortive region, respectively. Reproduced from [17] with permission from the Royal Society of Chemistry.

In addition to the tolerance factor, the stability of perovskite compounds across different substitutions and solid solutions can be evaluated using a plot of tolerance factor and average

electronegativity, first constructed by Halliyal and Shrout [97]. The average electronegativity X is defined by:

$$X = \frac{X_{AO} + X_{BO}}{2} \qquad 3–2$$

where X_{AO} is the electronegativity difference between the A cation and the oxygen anion, and X_{BO} is the electronegativity difference between the B cation and the oxygen anion. The relationship between the tolerance factor t and the average electronegativity X for different perovskite compounds is summarized in Figure 3.11. For pure $NaNbO_3$, the tolerance factor t is slightly larger than 0.96 and its electronegativity is about 2.25. Shimizu *et al.* [17] suggested that decreasing the tolerance factor t while maintaining the electronegativity X around 2.25 can stabilize the AFE order in $NaNbO_3$. This means that $CaZrO_3$, $SrZrO_3$, $CaTiO_3$, and other compounds that meet the requirements are likely to stabilize the AFE order in $NaNbO_3$.

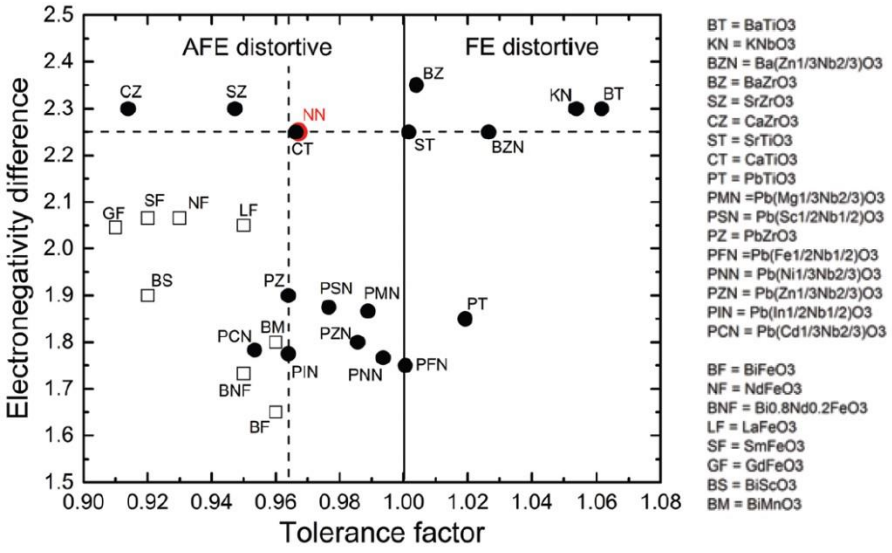

Figure 3.11: Tolerance factor versus averaged electronegativity difference for various perovskites. Reproduced from [17] with permission from the Royal Society of Chemistry.

Guo *et al.* substituted $NaNbO_3$ with $SrZrO_3$ [98, 99] and $CaZrO_3$ [100, 101] and characterized the electrical properties, microstructure, and crystallography of the new solid solutions. Although double polarization hysteresis loops were not present at room temperature, they could be observed at 120 °C [99]. The critical field, i.e. the field required to induce the phase transition, increases linearly with decreasing the tolerance factor [98]. This suggests that the introduction of $SrZrO_3$ and $CaZrO_3$ effectively stabilizes the AFE order. Gyan *et al.* [102] substituted $NaNbO_3$ with 3-5 mol% $CaTiO_3$. The XRD results showed that both the solid-solutions and the pure $NaNbO_3$ are characterized by the *Pbcm* structure, indicating the presence

of the AFE order. Although the polarization hysteresis loops of pure $NaNbO_3$ exhibited ferroelectric properties, the polarization loops of the solid-solutions could not be opened up to 20 kV/mm, indicating that the AFE order is stabilized. Gao *et al.* [103] substituted $NaNbO_3$ with $CaHfO_3$ and reported double hysteresis loops at room temperature. Although the loops were not fully opened and saturated, the transition is at least partially reversible. Dou *et al.* [104] substituted $NaNbO_3$ with $BaZrO_3$. The irreversible field-induced phase transition was accompanied by a giant strain of ~0.58%. Zuo *et al.* [105] substituted $NaNbO_3$ with both $BaZrO_3$ and $CaZrO_3$, and reported double polarization hysteresis loops at room temperature. To obtain new compositions exhibiting reversible field-induced phase transition, $SrTiO_3$ [106], $CaSnO_3$ [107], and $(Bi_{1/2}Na_{1/2})TiO_3$ [108], etc. were used to form new solid solutions.

To date, there are only a limited number of $NaNbO_3$-based systems that exhibit a reversible field-induced phase transition at ambient conditions. The prediction of new materials based on the empirical tolerance factor rule is not always successful. The reasons for the irreversible behavior of the field-induced phase transition are not well understood and appear to be related to the remarkably small difference in free energy between the antiferroelectric and ferroelectric states in $NaNbO_3$. New approaches to the development of new compositions exhibiting reversible field-induced antiferroelectric to ferroelectric phase transitions are required.

4 Materials and Methods

4.1 Materials

4.1.1 $NaNbO_3$

$NaNbO_3$ ceramic samples were prepared by the solid-state-reaction method. The chemicals Na_2CO_3 (99.95%, Alfa Aesar, Germany) and orthorhombic Nb_2O_5 (99.90%, Alfa Aesar, Germany) were dried at 200 °C for about 8 h due to the hygroscopic nature of alkali carbonates. They were then weighed in a stoichiometric ratio with 1 wt.% excess Na_2CO_3 to compensate for possible evaporation during the subsequent sintering process [109]. All chemicals were homogenized in ethanol by planetary ball milling with yttria-stabilized zirconia balls for 12 h at 250 rpm and then dried at 100 °C. The powder mixtures were calcined in alumina crucibles at 800 °C for 4 h and the calcined powders were then ball milled at 250 rpm for 12 h. The final powder products were pressed into discs with 10 mm in diameter and 1.5 mm in thickness and subjected to cold isostatic pressing with 200 MPa. A number of sintering conditions were tested. The optimized condition was sintering at 1355 °C for 3.5 h and packing powder of the same composition was used. The pellets were embedded in fresh packing powder, while the sintered packing powder from previous batches served as a "bed" at the bottom of the alumina crucible. The density of the sintered ceramic was determined to be 4.35 g/cm^3 by Archimedes method, which is 95.0% of the theoretical density (4.58 g/cm^3, calculated based on the cell volume determined by Rietveld refinement).

4.1.2 $(1-x)NaNbO_3$-$xSrSnO_3$

Ceramic samples $(1-x)NaNbO_3$-$xSrSnO_3$ (x = 0.03–0.06 with an interval of 0.01; abbreviated as NN100xSS) were prepared by the solid-state-reaction method used for $NaNbO_3$ samples. The chemicals were Na_2CO_3 (99.95%, Alfa Aesar, Germany), $SrCO_3$ (99.99%, Alfa Aesar, Germany), SnO_2 (99.90%, Alfa Aesar, Germany), and orthorhombic Nb_2O_5 (99.50%, Sinopharm, China). The orthorhombic Nb_2O_5 was purchased from Sinopharm in China, because there was a shortage of orthorhombic Nb_2O_5 in Germany. The preparation of the ceramic samples followed the same procedures as for $NaNbO_3$ described above. The differences and key conditions are highlighted below. Note that the chemicals were also weighed in a stoichiometric ratio with 1 wt.% excess Na_2CO_3. Calcination conditions were set at 800 °C for 4 h. The optimum sintering condition was 1320−1360 °C for 2 h, with lower temperatures

preferred for samples with high $SrSnO_3$ content. Similarly, packing powder of the same composition was used and the pellets were embedded in fresh packing powder with the sintered packing powder serving as a "bed" at the bottom of the alumina crucible.

4.1.3 Mn-Modified $0.95NaNbO_3$-$0.05SrSnO_3$

Mn-modified ceramic samples were prepared by the same solid-state-reaction method using the procedures described above for $(1-x)NaNbO_3$-$xSrSnO_3$. MnO_2 (99.9%, Alfa Aesar, Germany) was aded after the calcination process. Different amounts of MnO_2 by weight percent (0.1 wt.%, 0.5 wt.%, 1.0 wt.%, and 2.0 wt.%) were added to the calcined power and the powder mixture was ball milled and then dried, followed by the same treatment. Sintering conditions were set at 1320 °C for 2 h for all samples and packing powder was used.

4.1.4 Nb_2O_5 Precursor

It should be noted that Nb_2O_5 exhibits at least four different crystalline phases, namely, pseudohexagonal, orthorhombic, tetragonal, and monoclinic. XRD analysis of the used Nb_2O_5 revealed that they are essentially two different polymorphisms, orthorhombic and monoclinic Nb_2O_5, corresponding to the *Pbam* and *P*2 space groups, respective. Li *et al.* [12] reported that the proportion of ferroelectric phase with space group $P2_1ma$ in the sintered $NaNbO_3$ ceramic could be suppressed when an orthorhombic Nb_2O_5 precursor was used. In addition, a synthesis study on another niobate system, $K_{0.5}Na_{0.5}NbO_3$, revealed that the reaction of orthorhombic Nb_2O_5 with carbonates can form a homogeneous solid solution, while the monoclinic polymorph reacts with carbonates to form an inhomogeneous mixture of solid solutions [110]. Therefore, orthorhombic Nb_2O_5 (99.90%, Alfa Aesar, LOT: 61000279, produced in Karlsruhe, Germany) and orthorhombic Nb_2O_5 (99.50%, Sinopharm, China) were selected as the starting chemicals for the synthesis of $NaNbO_3$-based ceramics in this work.

4.2 Electrical Characterization

For all electrical measurements, the sintered specimens were ground and polished to a thickness of 0.20−0.30 mm and cut to rectangles of ca. 1.0−2.5 × 1.0−2.5 mm^2. The small thickness is important for the field-induced antiferroelectric to ferroelectric phase transition to be triggered

under conventional experimental conditions in the laboratory (limitations of the amplifier), since the critical field for antiferroelectrics is very high, 10−20 kV/mm for the $NaNbO_3$ materials in this work. The samples with the desired thickness were sputtered with platinum electrodes to cover the whole surface, allowing an effective field close to the applied electric field. They were then subjected to an annealing treatment to remove possible stresses generated during the grinding and polishing process.

4.2.1 Polarization and Strain Measurements

Polarization and strain hysteresis loops were obtained with a triangular field using a modified Sawyer-Tower circuit and an optical displacement sensor (D63, Philtec Inc., USA). A reference capacitor of 2.2 μF was used. A high voltage amplifier (20/20C, Trek, USA) was employed as the DC source. The field-induced longitudinal strain (S_{33}) and transverse strain (S_{11}) were additionally measured using linear variable differential transformers (WA/2mm, HBM, Germany) [111]. In general, a bipolar frequency of 1 Hz was used if not specified differently.

4.2.2 Temperature and Field Dependence of the Dielectric Properties

The temperature and frequency dependence of dielectric properties (dielectric constant and loss tangent) were measured using an LCR meter (4284A, Hewlett-Packard, USA). The probe AC voltage was 1 V. The data shown were recorded during the heating cycle at a heating rate of 2 °C/min and frequencies between 0.1 kHz and 1 MHz. The field dependence of the dielectric constant was measured by Dr. Lovro Fulanović using the LCR meter and a blocking circuit consisting of two 1 μF capacitors and a 100 kΩ resistor. A high voltage amplifier (20/20C, Trek, USA) was used as DC source.

4.2.3 Macroscopic Piezoelectricity d_{33}

Piezoelectric coefficient d_{33} was measured using a Berlincourt meter (Piezotest PM300, Singapore). An oscillating load of 0.25 N at a frequency of 110 Hz was applied, superimposed on a static force of 2 N.

4.2.4 TSDC Measurement

The thermally stimulated depolarization current (TSDC) of the $NaNbO_3$ sample that underwent the field-induced phase transition was recorded in two continuous cycles from room temperature to 700 °C. The measured sample was considered to be in the annealed state after the first cycle. The data were obtained using an electrometer (6517B, Keithly, USA) at a heating rate of 2 °C/min. The TSDC measurement was performed by Dr. Lovro Fulanović.

4.2.5 Latent Heat Measurement

The temperature change of the $NaNbO_3$ sample exposed to a linearly increasing electric field of 16 kV/mm within a period of 10 s was measured with a thermistor glued to the surface of the sample. The measurement was performed in silicone oil to prevent dielectric breakdown. A sample with a larger surface area (~4.0 × 4.0 ×0.25 mm^3) was specially prepared to detect the small temperature change. The latent heat measurement was indebted to Dr. Lovro Fulanović.

4.3 Scanning Electron Microscopy (SEM)

SEM (XL 30 FEG, Philips, Eindhoven, Netherlands) was used to examine the microstructure of the sintered samples. These samples were ground, polished with diamond paste to 1.0 μm particle size, thermally etched at temperatures 100−150 °C below the corresponding sintering temperatures for 30 min, and sputtered with Au to improve the conductivity of the sample surface. The average grain size for each sample was determined from the SEM images with more than 200 grains using a Labview-based image analysis program that identifies the area of the grains and calculates the diameter of circles with the equivalent area.

4.4 X-ray Diffraction

4.4.1 Conventional Laboratory XRD

The phase structures of the raw chemicals, calcined powder, and sintered pellets were examined using a conventional laboratory X-ray diffractometer (XRD, Bruker AXS D8 Advance, Germany) with Cu Kα radiation (wavelength $\lambda_{\alpha 1}$ = 1.5406 Å and $\lambda_{\alpha 2}$ = 1.5444 Å). The XRD patterns were recorded with a step size of 0.02° and a counting time per step of 10 s.

4.4.2 High-Energy XRD

The synchrotron XRD data of the $NaNbO_3$ ceramic sample were acquired at the DESY PETRA III P02.1 synchrotron beamline in transmission geometry with a Pilatus CdTe 2M area detector (Dectris Ltd., Switzerland). The beam energy and spot size were 60 keV (λ=0.20673 Å) and 0.3×0.3 mm^2, respectively. During the measurement, the samples were subjected to a unipolar electric field with a frequency of 0.05 Hz. The exposure time for each image was 415 ms. The synchrotron XRD data of the Mn-modified $NaNbO_3$-$SrSnO_3$ ceramic samples was collected using a Perkin-Elmer area detector (Perkin-Elmer, USA). The beam energy and spot sizes were 60 keV (λ=0.20727 Å) and 0.25×1.0 mm^2, respectively. For the field-dependent measurement of $0.95NaNbO_3$-$0.05SrSnO_3$ + 0.1 wt.% MnO_2 ceramic sample, a unipolar electric field of 18 kV/mm with a frequency of 0.2 Hz was applied. The exposure time for each image was 250 ms. The two-dimensional XRD patterns were converted to one-dimensional patterns by integrating the intensity in different azimuthal regions using Fit2D [112]. LeBail fitting was performed using the GSAS program [113]. The structural models, fitting parameters, and boundary conditions used in the fitting are given individually in the text.

4.5 Solid-State NMR Spectroscopy

NMR measurements were performed by Sonja Egert and Dr. B. Groszewicz was involved in the discussion and analysis of the data. ^{23}Na NMR spectra were recorded using a Bruker Avance III spectrometer with a 7.1 T magnet at a carrier frequency of 79.38 MHz. Two-dimensional Satellite Transition Magic Angle Spinning (STMAS) experiments were performed with a z-filtered sequence [114]. 2128 transients were averaged for each of the 110 increments with a relaxation delay of 1 s. Excitation, mixing, selective 90° and selective 180° pulse lengths were 1.4 µs, 2.1 µs, 21.75 µs, and 40.75 µs, respectively. The ^{23}Na chemical shift scale was referenced to the signal of $NaNO_3$(s) at −8.1 ppm [115]. To improve the signal-to-noise ratio, six $NaNbO_3$ ceramic pellets were cut into cuboids ($2.3 \times 2.3 \times 0.4$ mm^3), stacked, and packed into the central part of a 4 mm zirconia rotor. For $0.95NaNbO_3$-$0.05SrSnO_3$, four pellets with dimensions $2.3 \times 2.3 \times 0.6$ mm^3 were used [93]. TiO_2 was used as a filler material to enable magic angle spinning at 10 kHz. The quantitative amounts of the two phases are determined by fitting and integrating the projections along the indirect axis using Gaussian lines. Line shape simulations were performed using the program DMFit [116].

4.6 Transmission Electron Microscopy

TEM characterization was performed by Ding Hui and Prof. Dr. Hans-Joachim Kleebe and Dr. Leopoldo Molina-Luna contributed to the discussion and analysis of the data. To prepare the TEM specimens, thin cross sections of the sintered samples were polished down to a thickness of 15−20 μm using a MultiPrep polishing system (Allied High Tech Products Inc., USA) and diamond lapping films with grain sizes ranging from 15 μm to 0.1 μm. The samples were then annealed at 400 °C for 30 min to remove any mechanical stresses that may have arisen during the polishing process. Note that the $NaNbO_3$ sample, whose field-induced antiferroelectric−ferroelectric phase transition had already been triggered, was not annealed. The samples were then mounted on supporting molybdenum TEM grids (100 mesh; Plano, Germany) and milled with Ar ions using DuoMill 600 (Gatan, USA) until electron transparency was achieved. Finally, the TEM samples were lightly carbon-coated (Med 010, Liechtenstein) to minimize charging under the incident electron beam. The TEM studies were performed using a JEM 2100F microscope (JEOL, Tokyo, Japan) operated at 200 keV.

4.7 First-Principles Calculations

First-principles density functional theory (DFT) calculations were performed by Niloofar Hadaeghi and Prof. Dr. Hongbin Zhang contributed to the discussion of the results. Pure $NaNbO_3$ is substituted by 6.25 mol% $SrSnO_3$, and the nominal composition of the new system is $0.9375NaNbO_3$-$0.0625SrSnO_3$. To enable the calculation, supercells with 80 atoms were constructed for both the AFE and FE phases of the modified system. The 6.25 mol% $SrSnO_3$ corresponds to the substitution of Sr^{2+} and Sn^{4+} for one of the 16 possible A-site and B-site ions, respectively. Therefore, supercells containing 16 Na sites and 16 Nb sites are required, corresponding to supercells with 80 atoms. The *Pbcm* space group of $NaNbO_3$ of $NaNbO_3$ contains 40 atoms, while the $Pmc2_1$ space group contains 20 atoms. The initial lattice parameters are 5.504 Å, 5.570 Å, 15.517 Å for the former [117] and 7.8636 Å, 5.6306 Å, 5.5483 Å for the latter [118]. Therefore, the constructed structures with 80 atoms correspond to a $\sqrt{2}\times\sqrt{2}\times1$ supercell for the *Pbcm* space group and a $2\times\sqrt{2}\times\sqrt{2}$ supercell for the $Pmc2_1$ space group.

The AFE−FE transition in a real antiferroelectric $NaNbO_3$ system is of a displacive nature and therefore the boundary condition should be satisfied that the structures of the AFE and FE

phases have corresponding atomic shifts, so that the atomic configurations before and after the transition are consistent. This also means that despite the different local distortions, minor rotations, and atomic displacements of the substituted Sr or Sn ions in the constructed supercells, there is a one-to-one correspondence when we rotate the AFE structure to the FE structure and the atoms in one structure are mapped to the same atoms in the other structure. Note that the substitution of one Sr (Sn) atom for one Na (Nb) atom in the 80-atom supercells gives many different combinations. Based on the symmetry, Wyckoff position, distance between Sr and Sn atoms, and boundary condition, 10 representative geometries for each of the AFE and FE phases were considered and their energies after complete ionic relaxation were evaluated [93]. In particular, 3 scenarios were considered to compare the energies of the AFE and FE structures of the $0.9375NaNbO_3$-$0.0625SrSnO_3$ system. In this work, only scenario 1 is considered, which represents a simple comparison of the energies of the most stable AFE and FE structures. Detailed discussions about the other two scenarios are found elsewhere [93].

The calculations were performed using the projector augmented-wave method implemented in the VASP code [119, 120]. For both ferroelectric and antiferroelectric structures, supercells of 80 atoms were optimized with forces converged to be less than 0.0005 eV/Å. The cutoff energy for the plane wave basis was set to 520 eV for structural relaxation and total energy evaluation, with an effective k-mesh of 6 × 6 × 3 in the supercell geometry to ensure good convergence. The exchange-correlation functional was approximated using the generalized gradient approximation (GGA) parameterized by Perdew–Burke–Ernzerhof (PBE) [121]. The calculations started with the *Pbcm* (space group 57) and $Pmc2_1$ (space group 26) structures for the AFE and FE phases of pure $NaNbO_3$. The cell parameters of the structural models used were 5.504 Å, 5.570 Å, 15.517 Å [117] for the AFE phase and 7.8636 Å, 5.6306 Å, 5.5483 Å [118] for the FE phase. Supercells of 80 atoms correspond to a $\sqrt{2}\times\sqrt{2}\times1$ supercell for the AFE phase and a $2\times\sqrt{2}\times\sqrt{2}$ supercell for the FE phase. In the calculation of $0.9375NaNbO_3$-$0.0625SrSnO_3$, one Sr (Sn) atom replaced one Na (Nb) atom out of 16 possible positions, respectively, corresponding to a $SrSnO_3$ content of 6.25 mol%. Based on the symmetry, Wyckoff position, and the distance between Sr and Sn atoms, 10 representative geometries were created for each of the AFE and FE phases and the total energies of these structures were evaluated after full ionic relaxation. The AFE and FE structures with the lowest energies from each set of geometries were selected for discussion.

5 *Ex Situ* Study of the Field-Induced Transition in $NaNbO_3$

5.1 Electrical Properties

5.1.1 Field-Induced Phase Transition at Room Temperature

Antiferroelectric materials with reversible AFE to FE phase transition typically exhibit double polarization hysteresis loops under an applied electric field. To characterize the field-induced phase transition behavior of $NaNbO_3$, electroded $NaNbO_3$ samples were subjected to a bipolar electric field with a frequency of 1 Hz. The applied electric fields started at 3 kV/mm, and increased to 5 kV/mm, 8kV/mm, 10 kV/mm, and 12 kV/mm. Selected polarization and strain hysteresis loops are shown in Figure 5.1 (a-c) and Figure 5.1(d-f), respectively. The polarization hysteresis loop did not open at 8 kV/mm and 10 kV/mm, which resembles the loop of a linear dielectric material with leakage current contribution. The strain response under 8 kV/mm and 10 kV/mm is dominated by the electrostriction contribution, which is proportional to the square of the polarization, as featured in Figure 5.2. As a result, the strain values are small below 10 kV/mm. Surprisingly, the polarization suddenly exhibited a jump at 11.6 kV/mm, which is defined as the critical field E_F, namely the field required to trigger the phase transition. It should be noted that the significant electrical and mechanical changes at the critical field in this chapter are considered as a field-induced phase transition. However, we will show later (Chapter 6) that this behavior is nontrivial and in fact dominated by domain switching processes. The polarization saturated at 12 kV/mm, with a saturate polarization of 35 $\mu C/cm^2$. Meanwhile, a huge longitudinal strain of 0.64% was recorded simultaneously at 12 kV/mm. The large increase in polarization and strain at 11.6 kV/mm is due to an antiferroelectric−ferroelectric phase transition. The state after the phase transition is characterized by a large remanent polarization of 33 $\mu C/cm^2$ and a remanent strain of 0.53%, which are close to the values observed at 12 kV/mm. The material did not return to its original state, indicating irreversible phase transition behavior. A square-like polarization loop and a butterfly-shaped strain loop were observed as the electric field continued to decrease, which are typical characteristics of a ferroelectric material. The coercive field, defined as the electric field at which polarization is zero, is −3.1 kV/mm, much smaller than the critical field E_F. Once the phase transition, which involves enormous polarization and strain changes, has occurred, the $NaNbO_3$ sample behaves like an ordinary ferroelectric material, as shown in Figure 5.3. The phase transition is thought to break the original centrosymmetric structure of $NaNbO_3$ in the virgin state and gives rise to a non-centrosymmetric phase that exhibits piezoelectricity. This was confirmed by the

observation of a macroscopic d_{33} value of 35 pC/N after the electric field was removed. Note that no piezoelectricity was observed for the same $NaNbO_3$ sample in the virgin state.

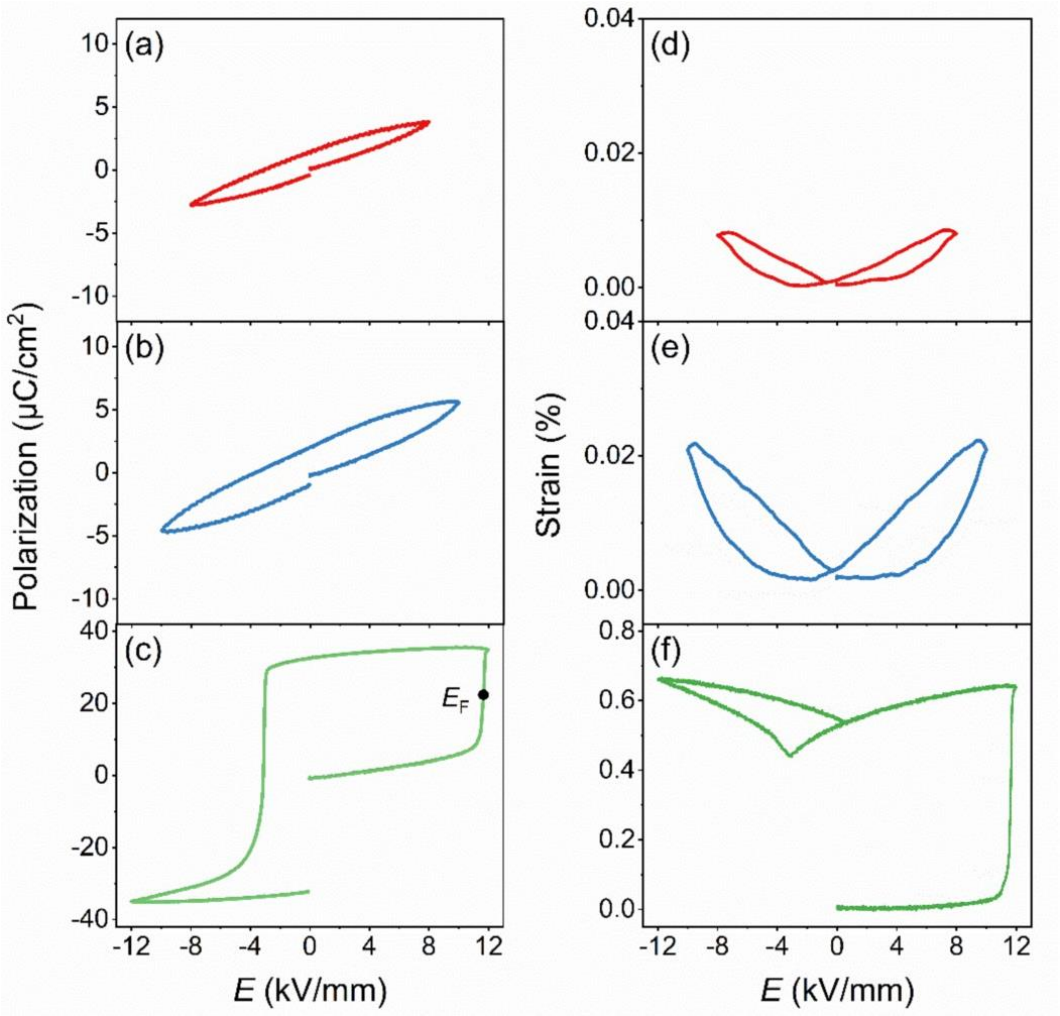

Figure 5.1: Large-signal (a-c) polarization and (d-f) strain hysteresis loops of $NaNbO_3$ ceramic samples under a bipolar electric field of 8 kV/mm, 10 kV/mm, and 12 kV/mm with a frequency of 1 Hz. The critical electric field, E_F, is defined as the electric field at which polarization reaches half of the saturate polarization value.

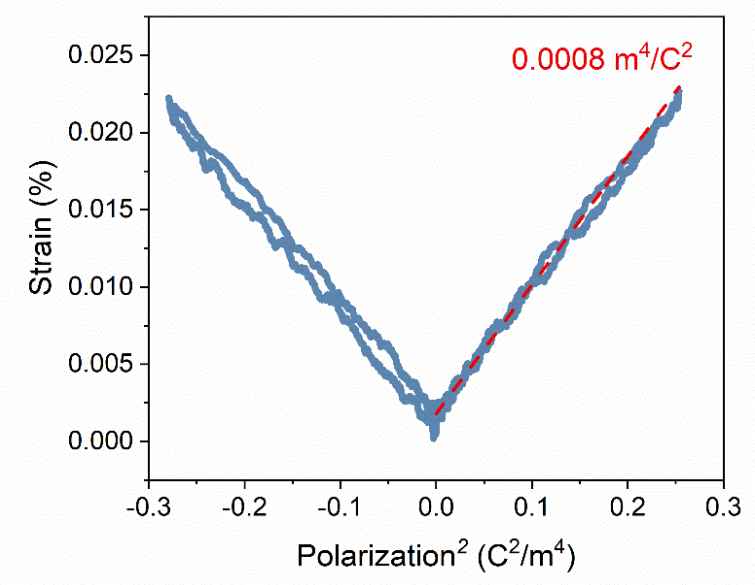

Figure 5.2: The strain-polarization^2 loop of $NaNbO_3$ ceramic sample. The fitted electrostrictive coefficient (0.0008 m^4/C^2) is highlighted.

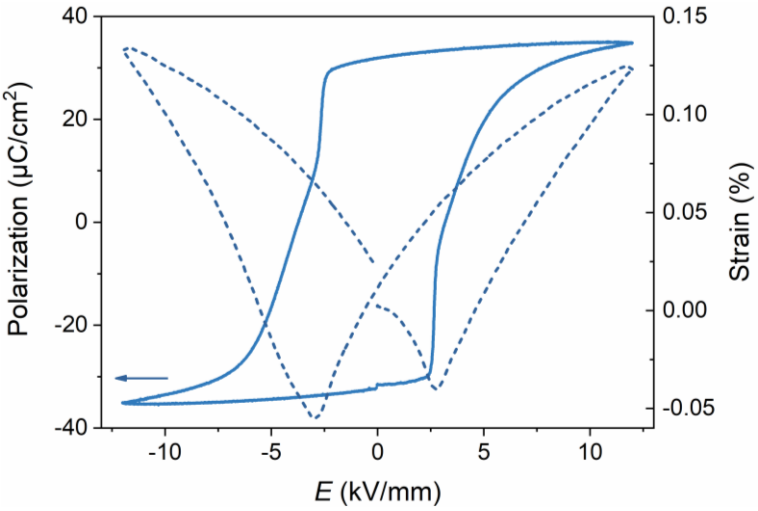

Figure 5.3: Large-signal polarization (solid line, left) and strain (dashed line, right) hysteresis loops of the $NaNbO_3$ sample that underwent the AFE−FE phase transition. A bipolar electric field of 12 kV/mm with a frequency of 1 Hz was applied.

5.1.2 Frequency Dependence of the Phase Transition

The field-induced phase transition behavior was examined at different frequencies, where the investigated $NaNbO_3$ samples were cut from the same ceramic pellet. Therefore, all samples were assumed to be the same in the virgin state. A bipolar electric field of 13 kV/mm was applied at various frequencies and the results are shown in Figure 5.4. The critical field E_F increases with increasing frequency, and the frequency dependence is described quantitatively

in Figure 5.5, where E_F increases linearly with increasing frequency on a logarithmic scale. This frequency dependence follows a simple power law relationship predicted by the modified Avrami model ($E_F \propto f^{\beta}$) [122, 123]. The value of the exponent β is fitted to be 0.032. A value of 0.038 was obtained for the frequency dependence of the coercive field in $Pb(Zr,Ti)O_3$ ceramics near the morphotropic phase boundary [124], and a value of 0.05 was obtained in a polycrystalline $Pb(Zr,Ti)O_3$ thin film [125]. It is surprising that the β value recorded for the phase transition in $NaNbO_3$ is so close to a value describing the domain switching process of $Pb(Zr,Ti)O_3$. This seems to indicate that the phase transition here is a domain switching process, which we will discuss in more detail in the next chapter. All polarization and strain loops except the one measured at 10 Hz are saturated. At such a high frequency of 10 Hz, a higher electric field is required for the polarization and strain to saturate. The remanent polarization and strain values show no significant differences for all loops, indicating that the remanent state is insensitive to the frequency of the applied field.

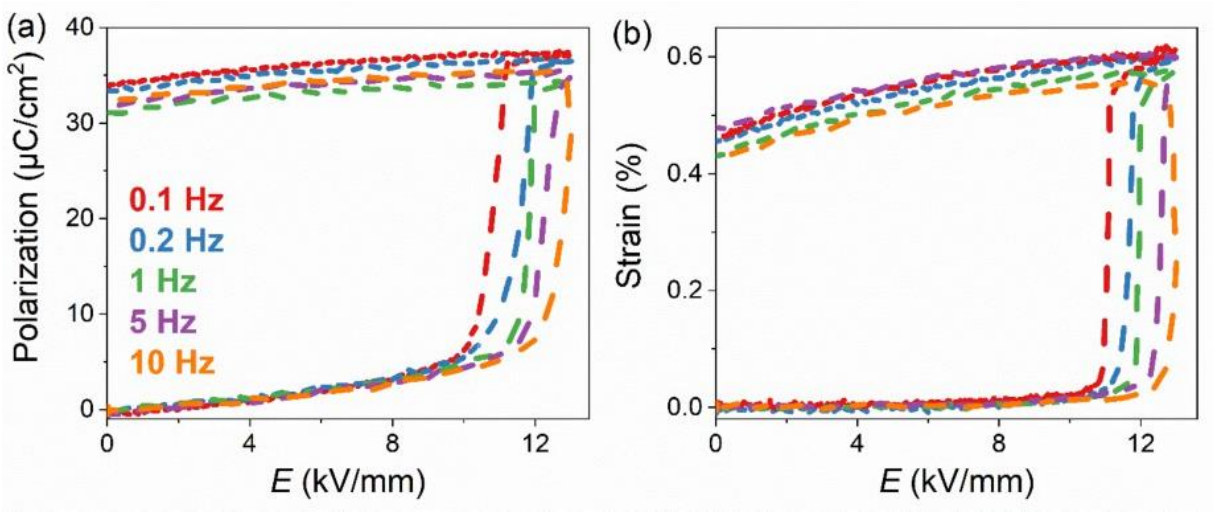

Figure 5.4: (a) Frequency dependence of the (a) polarization and (b) strain hysteresis loops of $NaNbO_3$ samples cut from the same ceramic pellet, so that the samples were assumed to be identical in the virgin state before a unipolar electric field of 13 kV/mm was applied.

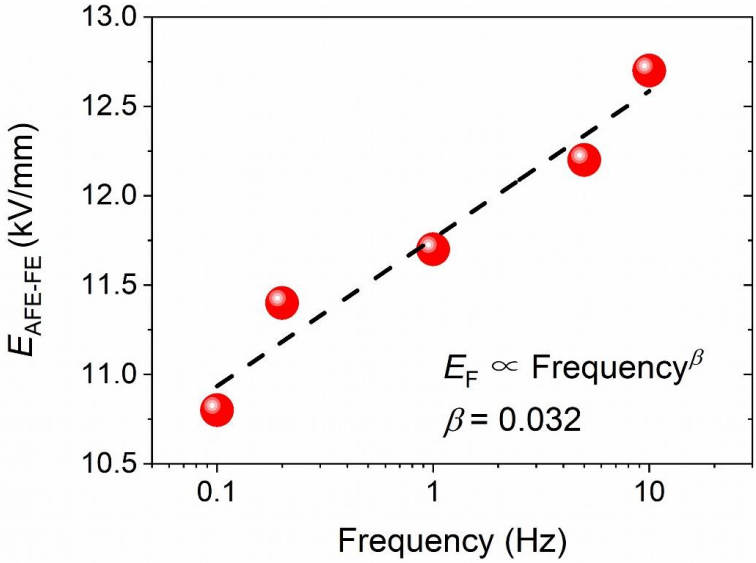

Figure 5.5: The scaling behavior of the critical field E_F versus frequency for the investigated $NaNbO_3$, based on the data obtained from Figure 5.4(a). The critical electric field, E_F, is defined as the electric field at which polarization reaches half of the saturate polarization value.

5.1.3 Temperature Dependence of the Phase Transition

The phase transition behavior was also investigated under different temperatures. Again, the $NaNbO_3$ samples were cut from the same ceramic pellet and were assumed to have the identical virgin state. A bipolar electric field of 12 kV/mm with a frequency of 1 Hz was applied. The temperature-dependent polarization and strain hysteresis loops are shown in Figure 5.6(a) and Figure 5.6(b), respectively. Note that a fresh sample was taken for each temperature. The critical field E_F decreases with increasing temperature. The temperature dependence is shown in Figure 5.7, where a linear decrease of E_F is obtained with a rate of $dE_F/dT = -0.039$ kV/mm·deg. Interestingly, a linear temperature dependence was found for $PbZrO_3$ ceramics, where a rate of $dE_F/dT = -0.17$ kV/mm·deg was obtained [126]. The different temperature dependences of $PbZrO_3$ and $NaNbO_3$ are attributed to their different origins, as will be discussed below. Although all the samples studied have similar maximum polarization and remanent polarization values, the maximum strain (at maximum field) and remanent strain values vary greatly from sample to sample. For the PLZST system, the field-induced polarization was found to be nearly constant with temperature, while the field-induced strain varied greatly with temperature [56]. Despite the different values for the remanent strain, a considerable value of more than 0.4% was observed for all the samples studied, indicating that the irreversible nature was not changed by the elevated temperatures. The unusual strain responses at 100 °C and 110 °C, i.e., the

remanent strain is larger than the strain at maximum field, is due to the thermal drift of the displacement sensor at high temperatures.

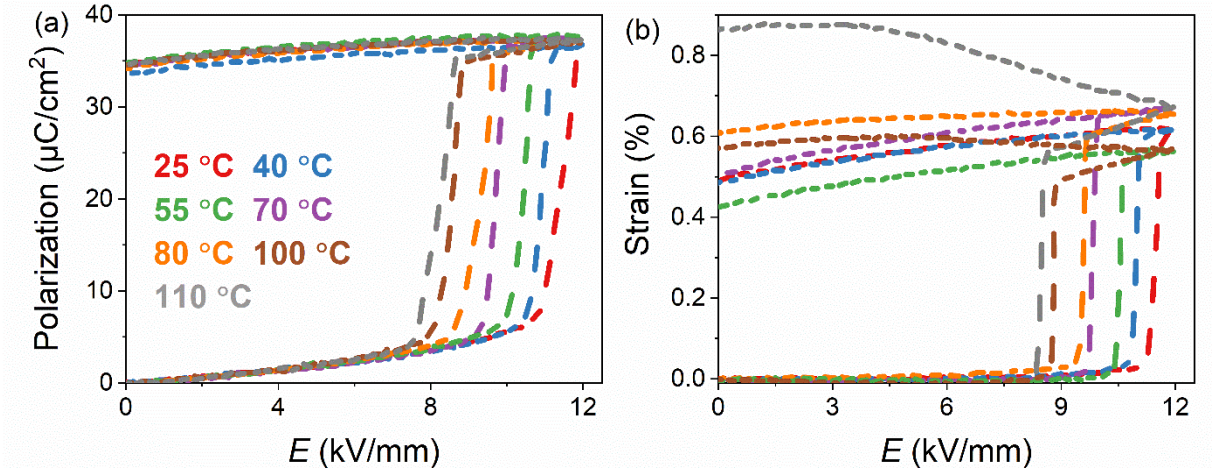

Figure 5.6: Temperature dependence of (a) polarization and (b) strain hysteresis loops of $NaNbO_3$ samples cut from the same ceramic pellet, so that the samples were assumed to be identical in the virgin state before a unipolar electric field of 12 kV/mm was applied.

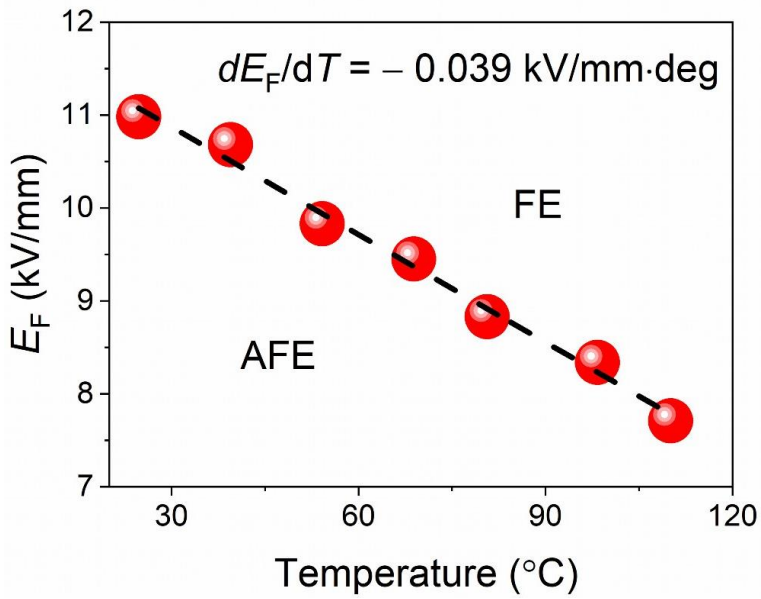

Figure 5.7: Decrease of the critical field E_F with temperature of the investigated $NaNbO_3$, based on the data obtained from Figure 5.6(a). The critical electric field, E_F, is defined as the electric field at which polarization reaches half of the saturate polarization value. Based on linear regression analysis of E_F as a function of temperature, a slope of $dE_F/dT = -0.039$ kV/mm·deg is obtained.

For the field-induced phase transition to occur, an energy barrier must be overcome, and the temperature dependence of the barrier is present in both $NaNbO_3$ and $PbZrO_3$ systems. However, it was found that not all antiferroelectric compositions exhibit a decrease in E_F with

increasing temperature. For example, the composition $Pb_{0.99}Nb_{0.02}[(Zr_{0.58}Sn_{0.43})_{0.92}Ti_{0.08}]_{0.98}O_3$ composition, which is a well-known lead-based antiferroelectric system, is characterized by an increase in the critical field with increasing temperature [7]. The mechanism has been attributed to the phase transition sequence as a function of temperature. In $PbZrO_3$, there is an intermediate ferroelectric phase that separates the antiferroelectric phase at low temperature and the paraelectric phase at high temperature [127, 128]. Therefore, the energy barrier required to trigger the AFE−FE phase transition is expected to decrease as one approaches the FE phase at higher temperatures. In contrast, the phase transition sequence in the $Pb_{0.99}Nb_{0.02}[(Zr_{0.58}Sn_{0.43})_{0.92}Ti_{0.08}]_{0.98}O_3$ system mentioned above is FE−AFE−PE upon heating. The phase composition lies deeper in the AFE region of the phase diagram with increasing temperature and therefore, the critical field increases instead of decreasing with increasing temperature.

Back to $NaNbO_3$, the phase transition sequence of $NaNbO_3$ is FE−AFE−PE upon heating [71]. Therefore, the phase transition sequence theory proposed for the $PbZrO_3$-based system cannot explain the observed phenomenon in $NaNbO_3$. However, it should be noted that not only a structural transition but also polarization switching could be involved in the $NaNbO_3$ system in our work. It has been demonstrated that the polarization switching is facilitated at higher temperatures [129, 130]. Therefore, the observed temperature dependence of the phase transition behavior of $NaNbO_3$, i.e., the critical E_F decreases with increasing temperature, is a result of the interaction of structural change and polarization switching. As will be shown in the next chapter, the macroscopic polarization and strain changes are essentially the result of polarization switching rather than a field-induced AFE−FE phase transition. Therefore, the observed temperature dependence of $NaNbO_3$ is justified.

From the above results, it can be seen that the remanent state (remanent polarization and remanent strain) is hardly affected by temperature and frequency, i.e., the irreversible behavior remains unchanged in the studied temperature and frequency range.

5.1.4 Temperature Dependence of the Dielectric Properties

To understand the effect of the field-induced AFE−FE phase transition on the dielectric properties and phase transition sequence as a function of temperature, the temperature dependence of the dielectric permittivity and loss for the sample before and after the phase transition is compared in Figure 5.8 and Figure 5.9. Both samples exhibited a frequency-

independent dielectric maximum at about 380 °C, which is generally attributed to the *P*–*R* phase transition [18, 44-46]. The dielectric anomaly at about 150 °C for the $NaNbO_3$ before the phase transition, which is associated with a significant frequency dispersion of the dielectric loss, has disappeared for the sample after the phase transition. The comparison can be seen even more clearly in Figure 5.9. A new dielectric anomaly at 270 °C was observed for the $NaNbO_3$ sample after the phase transition, as shown in Figure 5.8(b). This anomaly has been attributed to a temperature-induced phase transition from the FE *Q* phase to the AFE *P* phase [27, 42, 44]. Interestingly, a close examination of the *P*–*R* phase transition shows that the dielectric maximum is at 379 °C and 383 °C for the sample before and after the field-induced transition, respectively, as shown in Figure 5.9. Thus, it is possible that the AFE *P* phase was not fully recovered at 270 °C and some degree of ferroelectricity remained. This hypothesis is indirectly supported by the difference in dielectric permittivity and loss between the two samples between 270 °C and 380 °C (Figure 5.9). After 380 °C, both the dielectric permittivity and loss as a function of temperature look almost identical for the two samples.

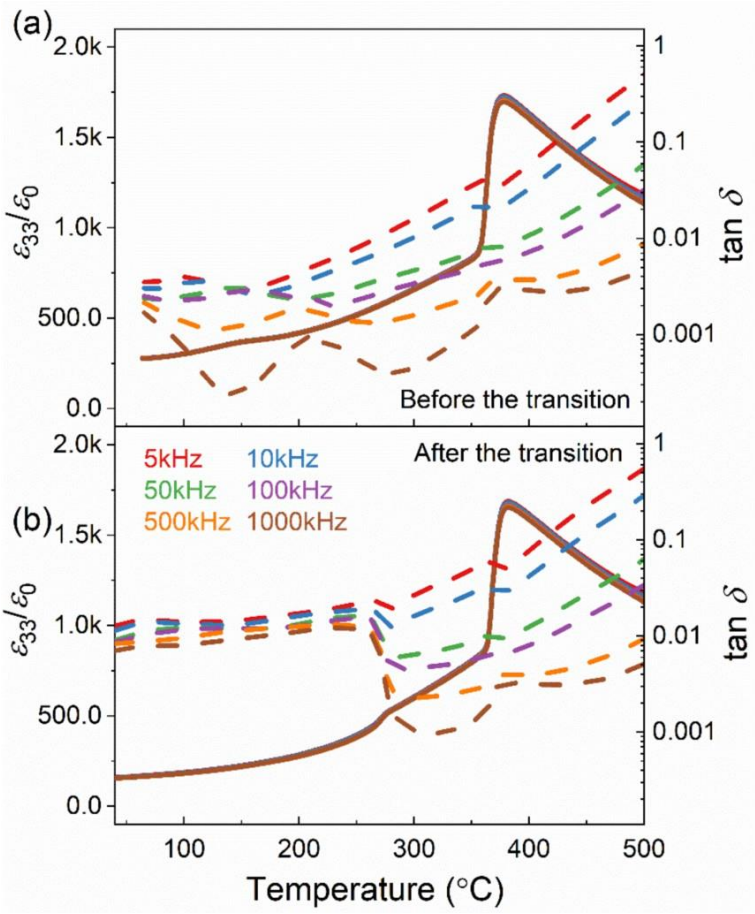

Figure 5.8: Temperature dependence of dielectric permittivity (solid lines) and dielectric loss (dashed lines) for the $NaNbO_3$ ceramic material (a) before and (b) after the field-induced phase transition in the frequency range from 5 kHz to 1 MHz.

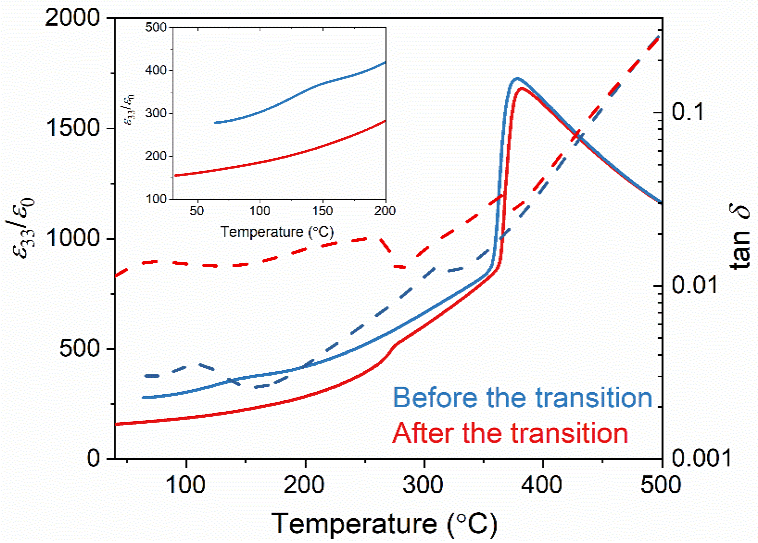

Figure 5.9: Comparison of the temperature dependence of dielectric permittivity (solid lines) and dielectric loss (dashed lines) for the $NaNbO_3$ ceramic material before and after the phase transition, measured at 10 kHz.

To further verify our hypothesis, thermally stimulated depolarization current (TSDC) analysis was performed, as shown in Figure 5.10. TSDC can capture the depolarization process that occurs during phase transitions and thermally activated release of currents due to the realignment of dipoles, trapped electrons or mobile ions. For the $NaNbO_3$ before the phase transition, no TSDC peak is observed, which is consistent with the non-polar nature of the AFE $NaNbO_3$ in the virgin state. Notably, no TSDC signal was observed at 150 °C, suggesting that the dielectric anomaly observed at this temperature is not due to mechanisms capable of inducing a pyroelectric current. The origin of the dielectric anomaly is still under debate. It was previously attributed to phase transition [131], incommensurate phase [132, 133] and dynamics of ferroelectric nanoregions [134]. A current density maximum was observed at 268 °C (Figure 5.10a), which agrees well with the depolarization process expected in the *Q–P* phase transition [27, 42, 44]. Moreover, a second current density peak was observed at 356 °C (Figure 5.10b), which is likely caused by a second depolarization process at higher temperatures, supporting the above hypothesis that the FE order did not completely disappear at 270 °C. Interestingly, the current density changed its sign from positive to negative at higher temperatures and showed a minimum at 490 °C. The exact origin is not clear and could have two reasons. First, it suggests the presence of different types of charge carriers with opposite signs [135]. Second, it could be related to the formation of an electret state with mutually compensated depolarization current and space charge motion [136]. It should be noted that such behavior did not occur in the $NaNbO_3$ sample without the application of large electric field. Therefore, the behavior is related to the change of state due to the phase transition. For example, microcracks are introduced into

the $NaNbO_3$ ceramic after the phase transition, as shown later in Figure 6.13. One possible hypothesis is that space charges accumulate at these microcracks and become mobile at higher temperatures.

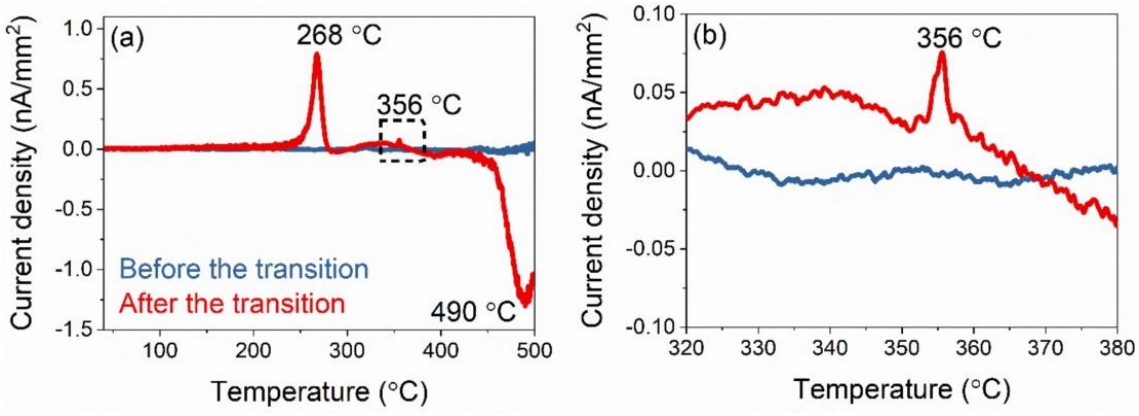

Figure 5.10: (a) TSDC measurements for the $NaNbO_3$ sample before (blue) and after (red) the field-induced AFE−FE phase transition. (b) An enlarged view of the current density peak at 356 °C.

5.1.5 Field Dependence of the Dielectric Properties

The field dependence of small-signal permittivity of a virgin-state $NaNbO_3$ that undergoes a field-induced phase transition is shown in Figure 5.11. The transition began at about 9.4 kV/mm, as indicated by a decrease in relative permittivity. The slightly smaller transition field is likely due to the low frequency (0.005 Hz) of the applied bipolar field. As demonstrated before, the critical field decreases with decreasing frequency, as shown in Figure 5.4. The permittivity drops from 226 to 172, which corresponds to a sharp drop of 24% in the field range of 0−12 kV/mm. This drop is due to a combination of the changed domain structures, dielectric anisotropy and the lower permittivity of the ferroelectric phase compared to its antiferroelectric modification [84]. After the phase transition, a permittivity maximum was observed at −2.3 kV/mm, close to the coercive field of −3.1 kV/mm. The permittivity maximum is observed at a field slightly smaller than the critical field for the PZT-PIC151 sample [137], which is commonly used as a standard piezoelectric sample. The exact mechanism is not yet fully understood, but it is probably due to the movement of domain walls, and the sequence of 180° and non-180° switching events. The similar field dependence of the permittivity behavior of $NaNbO_3$ and PZT-PIC151 suggests that $NaNbO_3$ is of ferroelectric nature after the transition.

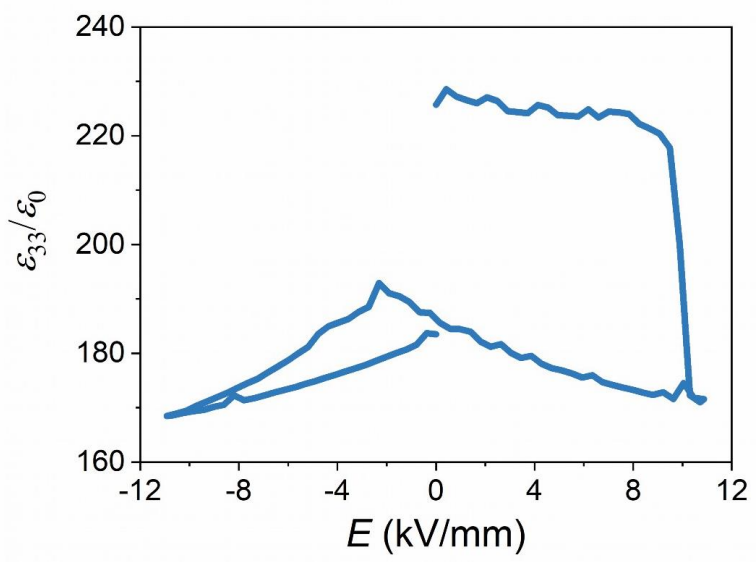

Figure 5.11: Field dependence of small-signal permittivity of $NaNbO_3$ in the virgin state. A small-signal AC voltage of 1 V at 10 kHz was applied, superimposed on a large-signal bipolar electric field of 12 kV/mm with a frequency of 0.005 Hz.

The field dependence of the permittivity of $NaNbO_3$ is reminiscent of the behavior of the lead-based $(Pb_{0.97}La_{0.02})(Zr_{0.75}Sn_{0.13}Ti_{0.12})O_3$ system, which also exhibits an irreversible AFE−FE phase transition at RT, as depicted in Figure 5.12. The irreversible behavior is evident in the differences in the polarization hysteresis loops and the field dependence of the permittivity between the first and subsequent electrical cycles. In the first cycle, the permittivity drops sharply from 839 at 0 kV/mm to 395 at 1.5 kV/mm. Moreover, the critical field of 1.1 kV/mm is higher than the coercive field of 0.8 kV/mm in the following cycles, and the square-like polarization hysteresis loops indicate that the material is in the ferroelectric state. All these properties are very similar to those of $NaNbO_3$. Interestingly, the $(Pb_{0.97}La_{0.02})(Zr_{0.75}Sn_{0.13}Ti_{0.12})O_3$ composition shows hysteresis-free double polarization loops at 180 °C, which is a feature of reversible AFE−FE phase transition. Moreover, the permittivity shows a high sensitivity to the applied field, increasing from 5560 at zero field to 11180 at about 1 kV/mm. This type of field dependence of permittivity has been previously recognized as a characteristic feature of antiferroelectric materials [138].

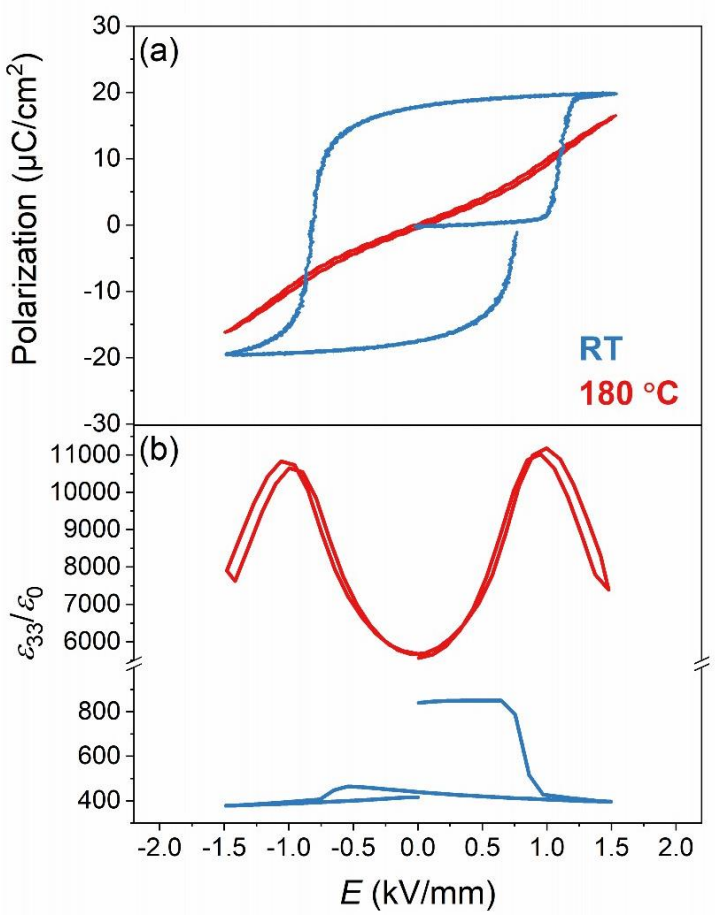

Figure 5.12: (a) Polarization hysteresis loops and (b) field dependence of small-signal permittivity of $(Pb_{0.97}La_{0.02})(Zr_{0.75}Sn_{0.13}Ti_{0.12})O_3$ at RT and 180 °C. The polarization loops were measured at 0.1 Hz. A small-signal AC voltage of 1 V at 10 kHz was applied, superimposed on a large-signal bipolar electric field of 1.5 kV/mm with a frequency of 0.005 Hz.

In summary, the above macroscopic electrical properties have shown that the AFE−FE phase transition of $NaNbO_3$ is accompanied by the appearance of macroscopic piezoelectricity, characteristic ferroelectric hysteresis loops, a decrease in dielectric permittivity, and the appearance of new dielectric anomalies at higher temperatures. All observations point to an irreversible phase transition behavior that is unaffected by both frequency and elevated temperature up to 110 °C. It is interesting to note that the $(Pb_{0.97}La_{0.02})(Zr_{0.75}Sn_{0.13}Ti_{0.12})O_3$ composition exhibits very similar irreversible phase transition behavior as $NaNbO_3$ at RT. More importantly, the irreversibility of the $(Pb_{0.97}La_{0.02})(Zr_{0.75}Sn_{0.13}Ti_{0.12})O_3$ system can be modified by temperature. Well-defined double polarization hysteresis loops indicative of reversible AFE−FE phase transition are observed at higher temperatures, which can be attributed to the temperature-induced FE−AFE phase change. However, from the temperature dependent dielectric curve of $NaNbO_3$ (Figure 5.9), it is evident that no phase transition occurs in the

temperature range studied. Approaching the *P*−*R* phase transition temperature at 380 °C may make a difference, but this temperature is too high and beyond the capabilities of current experimental measurement setups. Furthermore, the significantly increased loss tangent above 300 °C is likely to prevent such a measurement. In the next section, the structural change before and after the phase transition will be investigated.

5.2 Structure and Microstructure

5.2.1 XRD Characterization

The XRD profiles of a $NaNbO_3$ sample in the virgin state and after the field-induced phase transition by applying a bipolar electric field are compared, as demonstrated in Figure 5.13. Both profiles exhibit the typical orthorhombic perovskite structure. Although the two XRD profiles do not differ much in terms of the 2theta values of the main reflections, a close look reveals slight differences in both the main and superlattice reflections. The intensity ratios of some main reflections are altered. For example, the main reflections at a 2theta value of 32.5°, 52.5°, and 58°. The analysis shows that the XRD pattern before the transition is consistent with the *Pbcm* structure, while the pattern after the transition is close to the $P2_1ma$ structure. This is evident from the superlattice reflections in the 2theta regions of 35.5−37.5°, 42.5−44.2°, and 54.0−56.0°, as shown in Figure 5.13(b-d). In particular, (201) and (102), characteristic reflections of the $P2_1ma$ space group, are absent from the pattern before the phase transition, as shown in Figure 5.13(b). In addition, (221) and (122), also characteristic reflections of the $P2_1ma$ space group, are absent in the pattern before the transition, as shown in Figure 5.13(c). The XRD results show that $NaNbO_3$ in this work was in pure AFE phase and no $P2_1ma$ signal was detected. However, the coexistence of *Pbcm* and $P2_1ma$ structures in $NaNbO_3$ ceramics has been reported elsewhere [12]. There are two possible reasons for this. First, Li *et al.* [12] reported that the *Pbcm* space group is preferred when an orthorhombic Nb_2O_5 precursor is used, which is the case in this work. Secondly, Koruza *et al.* [16] reported that the *Pbcm* space group can be stabilized when the grain size of $NaNbO_3$ is above a critical value of 0.27 μm. The average grain size of $NaNbO_3$ ceramics in this work is 8.9 μm. Therefore, an AFE *Pbcm* structure is preferred.

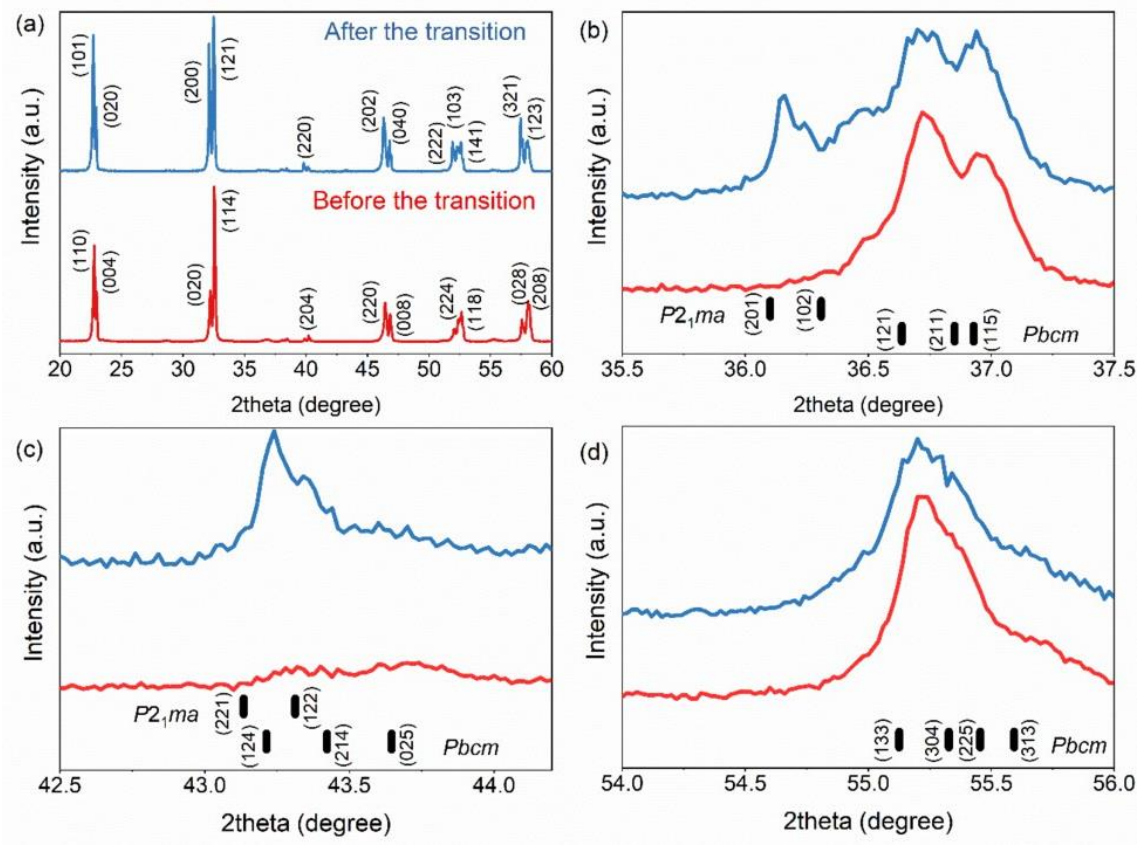

Figure 5.13: (a) XRD patterns of $NaNbO_3$ before (red lines) and after (blue lines) the field-induced phase transition. Detailed XRD scans of the 2theta regions of (b) 35.5−37.5°, (c) 42.5−44.2°, and (d) 54.0−56.0°. Two groups of labels represent the reflections associated with the AFE *Pbcm* and FE $P2_1ma$ space groups (for labels, please refer to the PDF-ICDD database). The XRD signal was obtained from the surface of the same pellet sample in reflection mode. A conductive silver paste that can be dissolved in acetone was used as the electrode, so that the XRD measurement could be performed immediately after the phase transition.

The appearance of the characteristic reflections of the $P2_1ma$ space group in the *ex situ* XRD characterization suggests that ferroelectric order is induced and maintained after electric field application, supporting the macroscopic electrical characterizations. Interestingly, characteristic reflections of the *Pbcm* space group can still be observed in the XRD pattern after the transition, which can be seen in the 2theta regions of 35.5−37.5° and 54.0−56.0°. This indicates a possible coexistence of AFE and FE phases in the $NaNbO_3$ ceramic sample after the phase transition.

5.2.2 TEM Study[1]

Conventional TEM was used to study the microstructural and local structural changes before and after the phase transition, which was triggered by applying a bipolar electric field. Selected area electron diffraction (SAED) of $NaNbO_3$ before the phase transition showed the characteristic ¼ type superlattice reflections of the AFE *Pbcm* structure, which arise due to the quadrupling of the primitive cell along the $[001]_{PC}$ direction, as highlighted in Figure 5.14(a). Note that the ¼ superlattice reflection spots are characterized by a distinct striation feature. When imaging one of the ¼ superlattice reflections using centered dark field imaging, domain blocks were observed, as depicted in Figure 5.14(b). The width of the domain blocks was reported to range from 0.5 μm to 0.9 μm [139]. The parallel straight lines with dark contrast within the domain blocks were referred to as translational domain walls in $NaNbO_3$ in an early TEM study [79]. Gao *et al.* [140] believed that the streaking features in the electron diffraction patterns are related to the incommensurate structure, as also reported in $PbZrO_3$-based AFE systems [63]. Recently, Ding *et al.*[139] showed that antiphase boundaries (APBs) are present in the $NaNbO_3$ ceramics studied and that the streaking features of the ¼ superlattice reflections are due to the irregular periodicity of the APBs. They defined APBs as interfaces of finite thickness separating the translational domains on both sides [139, 141]. Early studies of APBs in AFE crystals date back to Chang *et al.* [142], who attributed the parallel striation observed in AFE domains accompanied by streaking satellite spots in the SAED patterns to one-dimensional regular arrays of APBs. Similar features were also observed in lead-containing AFE materials [141, 143]. Due to the non-polar nature of the unit cell in AFE crystals, the antiparallel configurations of polarizations in AFE crystals would cancel each other out, so that no electrostatic interaction occurs during the formation of AFE domain structures during cooling from the high-temperature paraelectric phase. In contrast, the formation of FE domains is attributed to the reduction of both electrostatic and mechanical energy. After examining more than 15 grains, only the ¼ superlattice reflections, the characteristic domain blocks, and APBs were found in the grains of $NaNbO_3$ before the application of the electric field, indicating they are typical microstructural features of the AFE phase of $NaNbO_3$ ceramics. The TEM observation of the pure *Pbcm* structure for the sample before the phase transition is consistent

[1] My colleague, Ms. Ding Hui, is acknowledged for the characterization and processing of the TEM data. The discussion and analysis of the results was supported by Prof. Dr. Hans-Joachim Kleebe and Dr. Leopoldo Molina-Luna.

with the XRD results. More detailed interpretations of the microstructural features of the AFE phase of $NaNbO_3$ ceramics can be found elsewhere in Ding *et al.* [139].

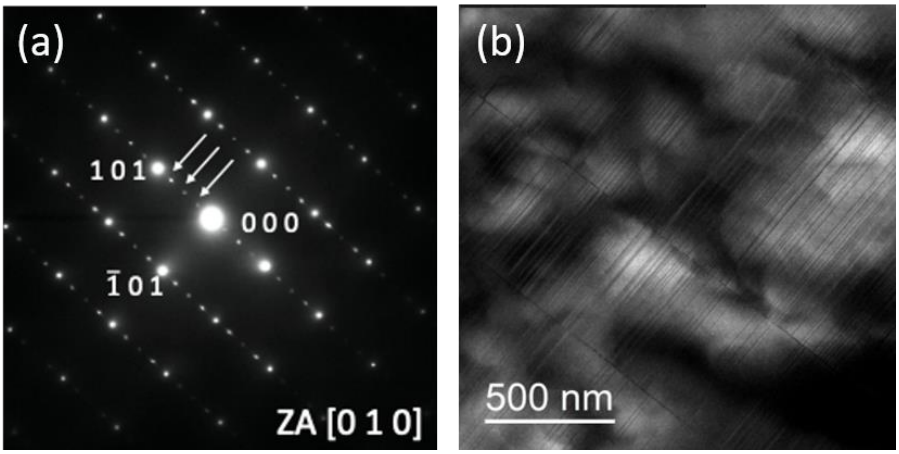

Figure 5.14: (a) SAED pattern of the $NaNbO_3$ before the electric-field-induced phase transition. (b) The corresponding dark field image obtained by imaging one of the ¼ superlattice spots highlighted by the arrows in (a).

The TEM study of the $NaNbO_3$ sample, which underwent the AFE−FE phase transition, showed the coexistence of AFE and FE phases in different grains. About 20 grains were examined and about 50% of them showed ¼ superlattice reflections in the SAED patterns, characteristic of the *P* phase. Moreover, the remaining 50% showed ½ superlattice reflections characteristic of the $P2_1ma$ structure. The phase coexistence suggested by the XRD analysis was confirmed by the TEM studies. Note that no phase coexistence was observed within one individual grain, i.e. all grains studied were exclusively in either *P* phase or *Q* phase. Pure $NaNbO_3$ with coexisting *P* and *Q* phases within a grain has been reported previously [100], where the sample was poled at an electric field of 10 kV/mm for 10 min. However, the sample in this work was only subjected to a bipolar electric field to trigger the phase transition, suggesting that exposing $NaNbO_3$ to an electric field for an extended period of time helps stabilize the FE order within a grain. In addition, AFE and FE phases have been reported to coexist within a single grain in lead-based AFE materials [53]. Two types of SAED patterns and domain morphology were found for the $NaNbO_3$ after the phase transition. Selected SAED patterns of the two structures are shown in Figure 5.15(a) and Figure 5.15(c). The corresponding domain morphology was obtained by imaging one of the ¼ superlattice spots highlighted by the arrows and the circled diffraction spot, as shown in Figure 5.15(b) and Figure 5.15(d), respectively. Domain blocks and arrays of APBs were still observed in the AFE regions for the $NaNbO_3$ after the transition. Moreover, a new domain morphology, i.e., wedge-shaped domains, was observed in the newly

formed ferroelectric regions. To obtain a better representation of the new domains, a zone axis (ZA) of [1 2 10] was used. A similar domain morphology was observed in ferroelectric $K_{0.15}Na_{0.85}NbO_3$ single crystals [144]. Although the exact space group of the crystal was not given, the observed ferroelectric properties suggest the phase structure is *Q* phase or at least a coexistence of *P* and *Q* phases. Based on the macroscopic piezoelectricity of the $NaNbO_3$ that underwent the phase transition, the newly formed wedge-shaped domains are expected to be not only ferroelastic but also ferroelectric in nature.

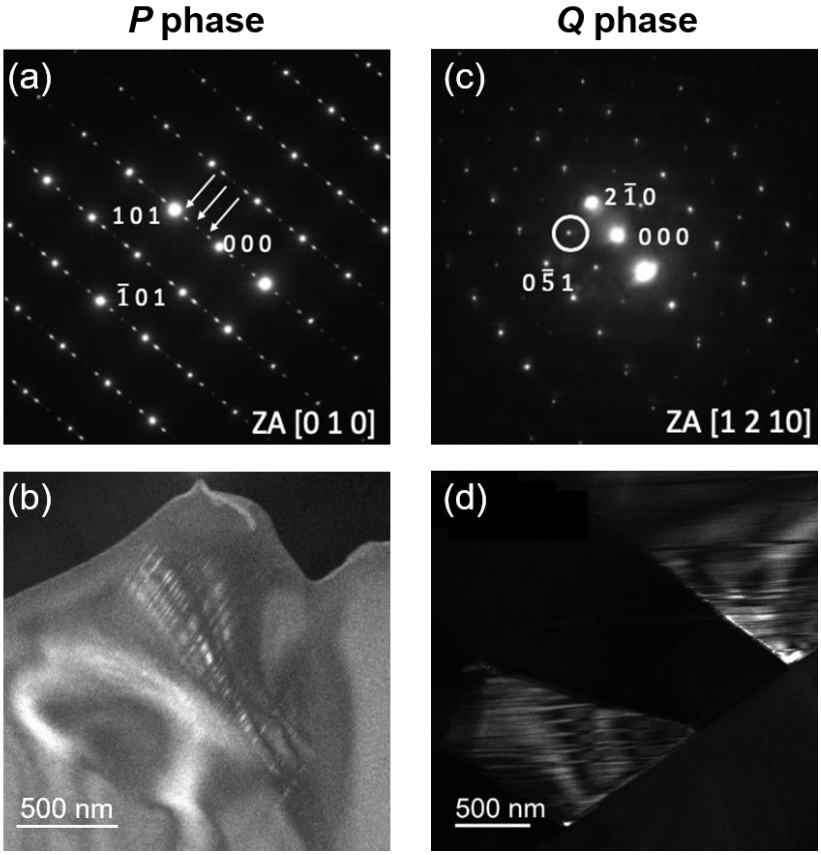

Figure 5.15: (a) SAED pattern and (b) the corresponding dark field image of the AFE region of the $NaNbO_3$ after the field-induced phase transition. (c) SAED pattern and (c) the corresponding dark field image of the FE region of the $NaNbO_3$ after the transition.

5.2.3 NMR Study[1]

XRD analysis reflects the global structure of $NaNbO_3$ ceramics before and after the field-induced phase transition. Although the local structural and microstructural changes due to the transition have been characterized by the TEM study, a statistical analysis of the field-induced

[1] My colleague, Ms. Sonja Egert, is acknowledged for the measurement and analysis of the NMR data. Dr. Pedro B. Groszewicz is acknowledged for helping with interpretation of the results.

FE order is not available. The rough estimate of a 50:50 ratio of AFE and FE phases was based only on the results obtained from about 20 grains. From a local structural point of view, the phase transition from the *Pbcm* structure to the $P2_1ma$ structure is accompanied by the breaking of the axial or 4-fold rotational symmetry. The two sodium sites in the *Pbcm* structure, Na(1) and Na(2), have different local chemical environments. Na(1) is on a symmetry rotation axis, while Na(2) is in a non-axial symmetric environment that deviates from the center of the NaO_{12} cuboctahedron [145]. Solid-state nuclear magnetic resonance (NMR) spectroscopy is particularly sensitive to minimal distortions of the local structure [117]. More importantly, ^{23}Na is a sensitive NMR nucleus with a spin number of 1/2, a gyromagnetic ratio of 7.0761×10^7 rad/(T·s) [146], and a natural abundance of 100% [145]. This makes NMR a suitable probe for the study of phase heterogeneity, namely the coexistence of *Pbcm* and $P2_1ma$ phases in $NaNbO_3$. Detailed descriptions of the basic concepts of NMR and its applications to perovskite oxides can be found elsewhere [145, 147].

Satellite Transition Magic Angle Spinning (STMAS) is a two-dimensional NMR pulse sequence similar to triple-quantum magic angle spinning (3QMAS), both of which enable high-resolution NMR spectroscopy of quadrupolar nuclei, e.g., ^{23}Na [145]. Ashbrook *et al.* [148] applied the 3QMAS technique to study the structure of $NaNbO_3$ and identified a mixture of two polymorphs, believed to be *Pbcm* and $P2_1ma$, in a $NaNbO_3$ sample. The two space groups were subsequently confirmed by Johnston *et al.* [117] using a combination of NMR, XRD, second harmonic generation measurements, and DFT calculations. Compared to 3QMAS, Egert *et al.* [147] have shown that STMAS can improve the resolution of Na(1) signals in the *P* and *Q* phases at lower magnetic fields, allowing more accurate quantification of their relative amounts.

The ^{23}Na STMAS spectra of $NaNbO_3$ ceramic pellets before and after the phase transition are shown in Figure 5.16. The field-induced phase transition was realized by applying a bipolar electric field. It can be seen that there are two signals in the two-dimensional spectrum, which can be separated in the indirect dimension. Previous XRD and TEM characterizations have shown that $NaNbO_3$ in the virgin state is characterized by pure AFE *P* phase. The lower signal with two maxima is attributed to the Na(1) site, while the upper signal with one maximum corresponds to the Na(2) signal. An additional signal at δ_1 = 12.1 ppm with a single maximum appears after the phase transition, while the Na(2) signal remains almost unchanged. The newly induced Na(1) signal at δ_1 = 12.1 ppm should be attributed to the field-induced FE *Q* phase. Although the two Na(1) signals of the *P* and *Q* phases are not completely separated, they are sufficiently resolved to quantify their relative amounts. A clear view is obtained by projecting

the two-dimensional data along the indirect axis, as shown in Figure 5.16(c). The profile of the Na(1) signal before the phase transition centers at δ_1 = 9.7 ppm and is symmetric, indicating the presence of a pure AFE *P* phase. The newly induced Na(1) signal at δ_1 = 12.1 ppm indicates the coexistence of *P* and *Q* phases after the application of an electric field. This agrees well with the new superlattice reflections in the XRD pattern and satellite spots in the SAED pattern, as well as the appearance of wedge-shaped domains. Deconvolution of the lines with two Gaussian functions allows quantification of the phase coexistence by simple integration of the signal area. The relative proportion is determined as 50 ± 5% of the *P* phase and 50 ± 5% of the *Q* phase after the phase transition.

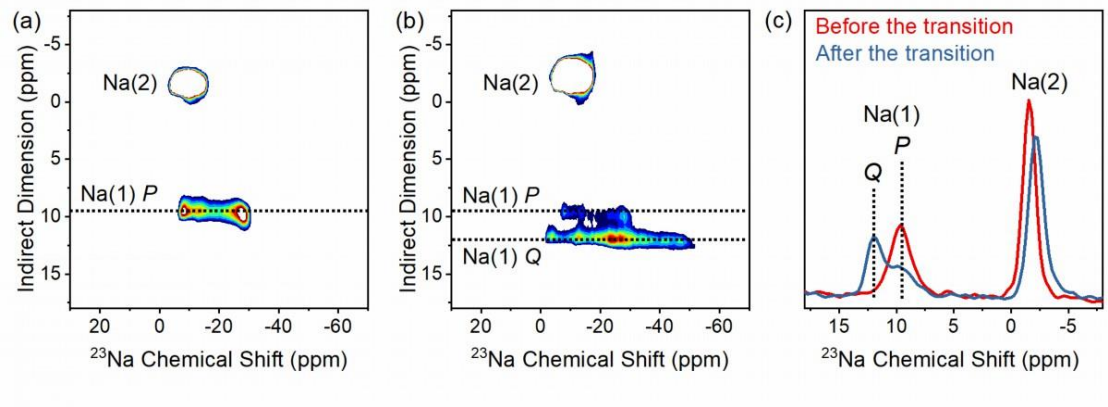

Figure 5.16: Two-dimensional ^{23}Na STMAS spectra of $NaNbO_3$ sample (a) before and (b) after the phase transition by applying a bipolar electric field of 12 kV/mm. (c) Projection of both spectra along the indirect dimension illustrating the profiles of the signals. The signal of the Na(2) site is located at −1.8 ppm and that of the Na(1) site is between 9 and 13 ppm. Only the signature line shape of the *P* phase is observed before the transition, while the signals corresponding to the *P* and *Q* phases are resolved after the phase transition. Note that the Na(2) signal in (a) and (b) are cut to increase the visibility of the Na(1) signal.

5.3 Summary

In summary, a series of structural and microstructural characterizations, including *ex situ* XRD, TEM, and NMR, have shown that the $NaNbO_3$ ceramic prepared in this work is a pure antiferroelectric phase with the *Pbcm* space group in the initial states prior to the application of an electric field. The use of orthorhombic Nb_2O_5 precursors and an average grain size of 8.9 µm of the sintered ceramic are probably two important conditions to obtain the phase-pure *Pbcm* structure. The presence of ferroelectric order was first confirmed by the appearance of superlattice reflections characteristic of the polar space group $P2_1ma$ after the application of an electric field. This indicates that the global structure of $NaNbO_3$ has been altered by the field application and a nonzero macroscopic polarization is present at the unit cell level. The local

electron diffraction study revealed the coexistence of ¼ and ½ satellite spots in the SAED pattern after the phase transition, while only the ¼ type was observed in the virgin state. Moreover, a change in domain morphology was observed from the characteristic domain blocks and APBs in the grains with antiferroelectric nature to the wedge-shaped domains in the grains with ferroelectric nature. Numerical estimation of the studied grains (~20) revealed that 50% of them are in the antiferroelectric phase and the rest 50% in the ferroelectric phase, which is in agreement with the subsequent NMR study. Since the measured NMR data contain all the information about the local chemical environment of the Na(1) and Na(2) atoms, NMR can quantify the phase coexistence in a more statistical way and is more reliable.

Regarding the interesting results related to the antiferroelectric-ferroelectric phase transition in $NaNbO_3$, some questions naturally arise. For example, is the 50:50 phase coexistence due to 50% of the material being unable to transform from the *Pbcm* structure to the $P2_1ma$ structure, or is it due to 100% of the material having transformed but 50% returning to the *Pbcm* structure after the electric field is removed or reversed? Since the AFE−FE phase transition in $NaNbO_3$ shows irreversible behavior, is it possible to make it reversible? The above questions have led us to an *in situ* structural investigation of $NaNbO_3$ ceramics by high-energy X-ray diffraction, which we discuss in the next section.

6 *In Situ* Study of the Field-Induced Transition in $NaNbO_3$

6.1 Refinement of the Structure at Zero Field[1]

The structure of the investigated $NaNbO_3$ ceramic sample was studied by high-energy XRD. The Rietveld refinement of the XRD data obtained from the sample in the virgin state (without any electrical history), was performed based on the centrosymmetric *Pbcm* space group. The atomic positions of Na, Nb, and O ions and their corresponding thermal parameters U_{iso} were refined. It was assumed that the atoms on the A-site, B-site, and oxygen-site each have the same thermal parameters U_{iso}. The results of the refinement are shown in Figure 6.1. The full pattern can be satisfactorily refined to a reasonable R_w value of 0.0521. The goodness of fit is illustrated by representative superlattice reflections in Figure 6.1(b) and high-angle main reflections in Figure 6.1(c-d), which show excellent agreement between the observed and calculated patterns. No reflections characteristic of the non-centrosymmetric $P2_1ma$ structure were found. The refined cell parameters are a = 5.50346(10) Å, b = 5.56652(10) Å, c = 15.53871(24) Å and the cell volume is 476.031(10) $Å^3$. The refined atomic positions are given in Table 6.1.

Table 6.1: Rietveld refinement data for $NaNbO_3$ on the basis of the space group *Pbcm*.

	Atomic position			
	x	*y*	*z*	U_{iso}
Na(1)	0.23133	0.25	0.0	0.0099
Na(2)	0.23133	0.2172	0.25	0.0099
Nb	0.25221	0.7308	0.12499	0.00183
O(1)	0.67739	0.25	0	0.0021
O(2)	0.21284	0.76055	0.25	0.0021
O(3)	0.47334	0.4543	0.14918	0.0021
O(4)	0.03175	0.02979	0.11323	0.0021

[1] Dr. Changhao Zhao is acknowledged for helping with refinement of the synchrotron data.

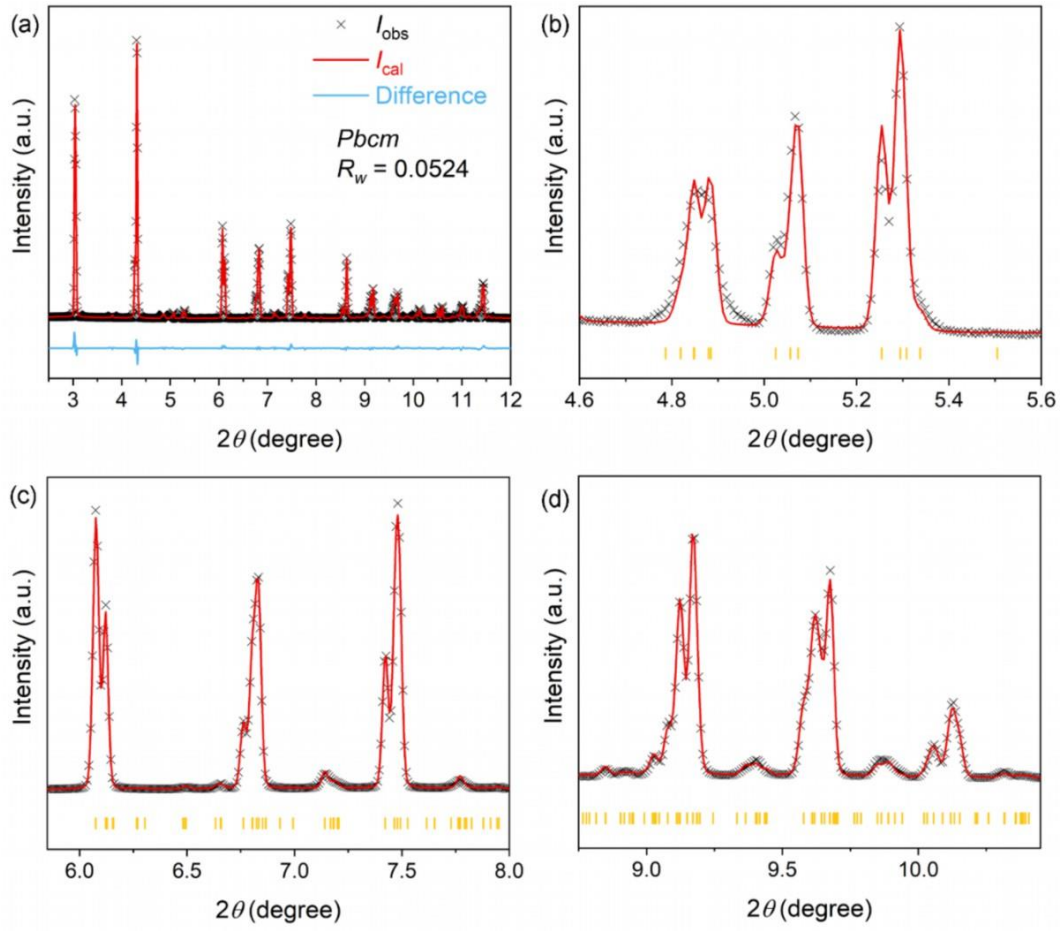

Figure 6.1: (a) Rietveld refinement of the high-energy XRD pattern of $NaNbO_3$ in the virgin state using the *Pbcm* space group. Magnified views of (b) representative superlattice reflections and (c-d) high-angle main reflections. The reflections associated with the *Pbcm* space group are shown by the yellow tick marks. The starting parameters of the *Pbcm* model for the refinement were taken from the X-ray and powder diffraction data refinements of Mishchuk *et al.* [149].

6.2 High-Energy XRD with Field

The one-dimensional XRD patterns of the $NaNbO_3$ sample as a function of increasing electric field from zero to 16 kV/mm are shown in Figure 6.2. At zero field, the sample in pure AFE phase showed only ¼ superlattice reflections characteristic of the *P* phase, including $¼403_{PC}$, $¼843_{PC}$, and the latter is highlighted by the black arrows. No superlattice reflections belonging to the FE *Q* phase were observed. Above a critical field, all ¼ superlattice reflections highlighted in the dashed boxes suddenly disappeared. The patterns below the critical field did not seem to be affected. The disappearance of the ¼ superlattice reflections was accompanied by changes in the main reflections and some other superlattice reflections highlighted in the largest dashed box. Unfortunately, the changes are not well visible in the one-dimensional XRD patterns. Simultaneously with the disappearance of all ¼ superlattice reflections, a new

reflection appeared in the 2theta range of 5.5−6.0 degree, which can be attributed to the ½312$_{PC}$ reflection characteristic of the field-induced *Q* phase.

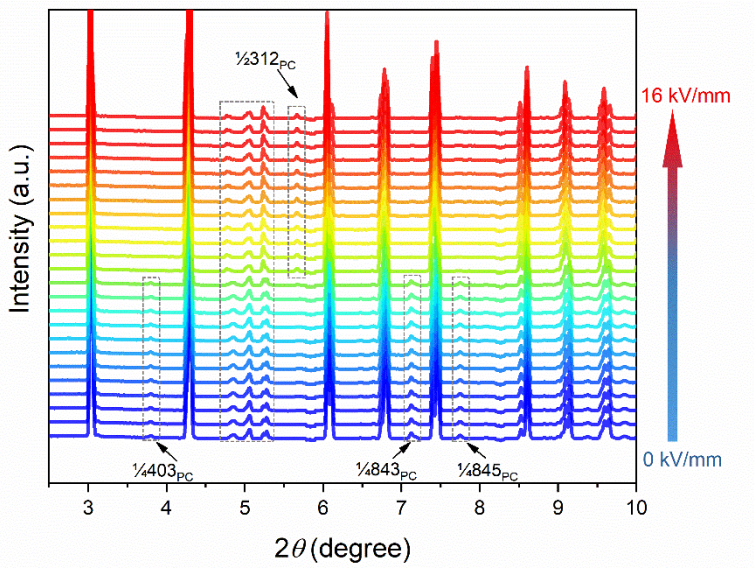

Figure 6.2: One-dimensional XRD patterns of $NaNbO_3$ ceramics as a function of increasing electric field from 0 kV/mm to 16 kV/mm. The patterns were integrated from the 45° sectors at different electric field amplitudes. Typical ¼ superlattice reflections characteristic of the AFE *P* phase were identified for the $NaNbO_3$ before applying the electric field. The superlattice reflections most affected by the field application are highlighted in the dashed boxes.

To capture further details of the field-induced phase transition, the evolution of selected primary and superlattice reflections is shown in Figure 6.3 and Figure 6.4, respectively. Overall, the whole pattern can be divided into three distinct stages. At stage 1, no changes were observed in the primary and superlattice reflections, indicating that the initial *P* phase remained unaffected up to 8 kV/mm. No structural or microstructural changes were observed at this stage. The transition from stage 1 to stage 2 was marked by changes in the 2theta values of the main reflections and the clear disappearance of the ¼ superlattice reflections. The simultaneous appearance of the ½312$_{PC}$ reflections suggests that the FE *Q* phase was induced at the stage 2 (~8kV/mm). No significant changes were observed in the field range of 8−12 kV/mm for both the main and superlattice reflections. The transition from stage 2 to stage 3 was marked by the changes in the intensities and positions of the main reflections at 12 kV/mm. The intensity of the 100$_{PC}$ and 200$_{PC}$ reflections suddenly decreased, while the intensity of the 110$_{PC}$ increased during the transition from stage 2 to stage 3. However, only minor changes were observed in all superlattice reflections, suggesting that the space group remained unchanged during the transition from stage 2 to stage 3 and that the change was mainly due to microstructural changes, i.e., polarization switching, as explained below.

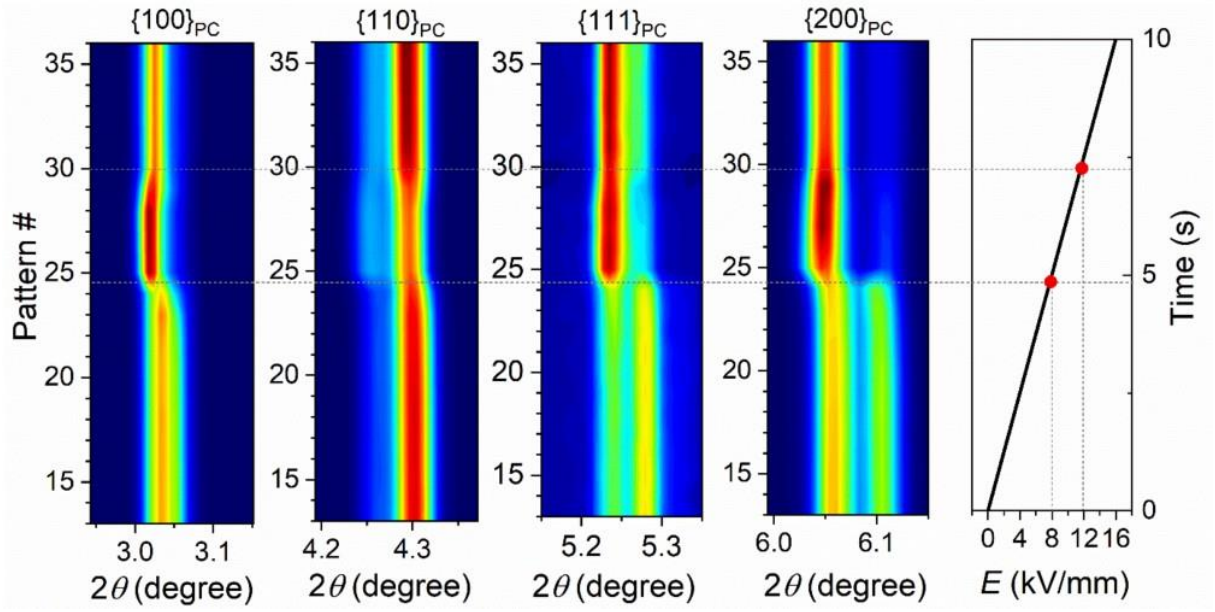

Figure 6.3: Evolution of selected primary reflections from the 45° sectors with increasing electric field from 0 kV/mm to 16 kV/mm in a period of 10 s. The patterns from the bottom to the top were recorded every 415 ms, which corresponds to a field range of ~0.6 kV/mm.

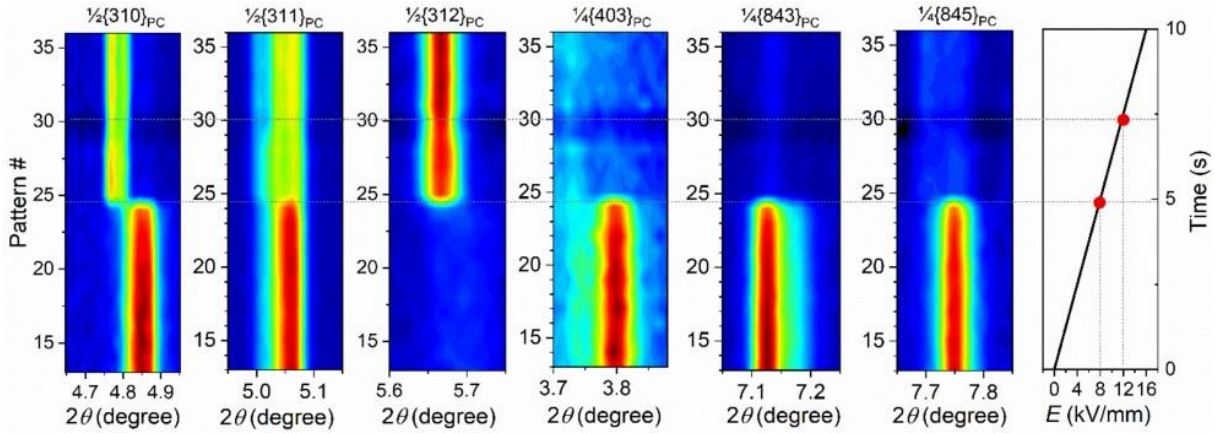

Figure 6.4: Evolution of selected superlattice reflections from the 45° sectors with increasing electric field from 0 kV/mm to 16 kV/mm in a period of 10 s.

6.3 *In Situ* Characterization of Macroscopic Properties

Since the AFE *P* phase is the only phase present in the virgin state, the ¼ superlattice reflections can be used as a measure to quantify the evolution of the phase fraction of the *P* phase as a function of increasing electric field. The ¼843$_{PC}$ reflection is selected because it has the highest intensity among all ¼ superlattice reflections. The one-dimensional XRD patterns of the ¼843$_{PC}$ and ½312$_{PC}$ reflections as a function of increasing electric field are shown in Figure 6.5(a) and Figure 6.5(b), respectively. The integrated area of the ¼843$_{PC}$ reflection at zero field

is defined as a benchmark representing 100% *P* phase. The phase fraction of the *P* phase as a function of increasing electric field is plotted in Figure 6.5(c). In addition, the macroscopic polarization and longitudinal strain S_{33} were recorded simultaneously while the synchrotron data were measured, as shown in Figure 6.5(c). Note that the dramatic decrease of the *P* phase fraction at 8 kV/mm (80% → 10%) indicated that the phase transition from the AFE *P* phase to the FE *Q* phase was triggered, which was accompanied by the appearance of the $½312_{PC}$ reflection. After the significant decrease at 8 kV/mm, the fraction of the *P* phase remained close to zero until the maximum field. Surprisingly, the macroscopic polarization and strain showed a jump only at 13 kV/mm, which was obviously decoupled from the field-induced phase transition at 8 kV/mm. It should be noted that the small increase in polarization after 6 kV/mm was not due to the phase transition, but could be related to the dielectric displacement and a small contribution from the leakage current, since a low frequency of 0.05 Hz was chosen. The postponed macroscopic changes were counterintuitive since dramatic mechanical and electrical changes are expected to occur simultaneously with the transition [64].

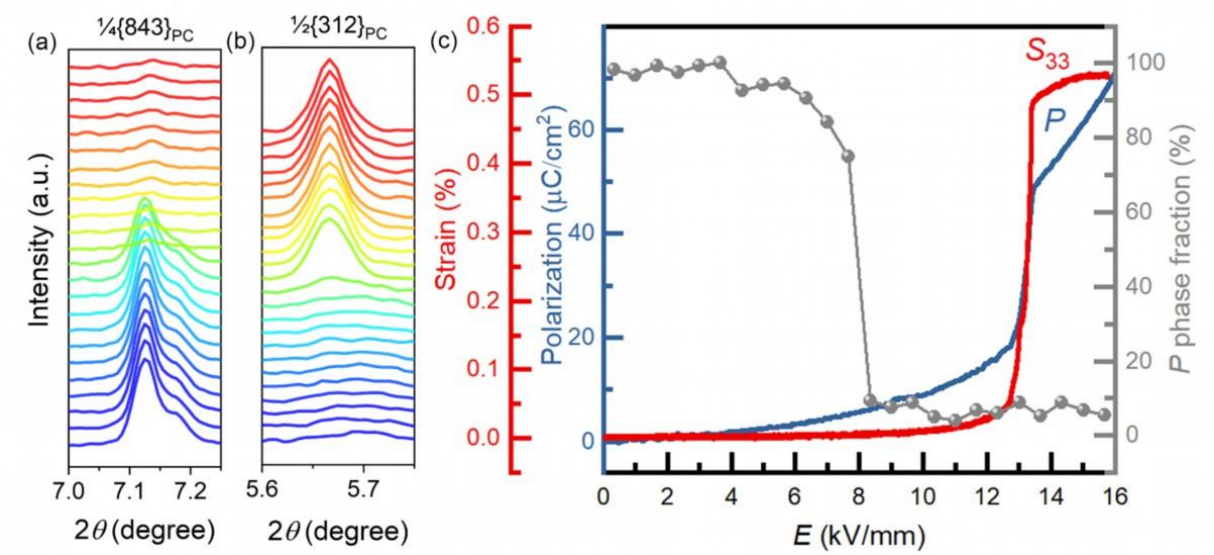

Figure 6.5: One-dimensional XRD patterns of the superlattice reflections (a) $¼843_{PC}$ and (b) $½312_{PC}$ reflections as a function of increasing electric field from 0 kV/mm and 16 kV/mm. The patterns were integrated from the 45° sectors. The integrated area of the $¼843_{PC}$ at 0 kV/mm is taken as a reference, representing 100% of the AFE *P* phase. (c) *P* phase fraction determined by the integrated area of the $¼843_{PC}$ reflections as a function of increasing field and the *in situ* macroscopic polarization (*P*) and longitudinal strain (S_{33}).

6.4 Latent Heat Measurement[1]

To confirm that the changes in the XRD patterns at 8 kV/mm were indeed caused by a structural phase transition, the temperature change of a virgin $NaNbO_3$ sample was recorded when it was subjected to the same electric field load of 16 kV/mm with a unipolar frequency of 0.05 Hz. No significant temperature change was observed below 5 kV/mm, as shown in Figure 6.6. A cooling effect was observed in the field range of 5−12 kV/mm, indicating an absorption of the latent heat. The observed latent heat indicates the presence of a first-order phase transition in the corresponding field region, which is consistent with the changes observed in the superlattice reflections during the diffraction measurements. Note that the field-induced phase transition from the *P* phase to the *Q* phase in $NaNbO_3$ crystals has been shown to be of first order [88]. An evident heating effect was observed at 12 kV/mm, at which field the large macroscopic changes the polarization and strains were observed. Therefore, it is assumed that the heating effect is a consequence of ferroelectric switching.

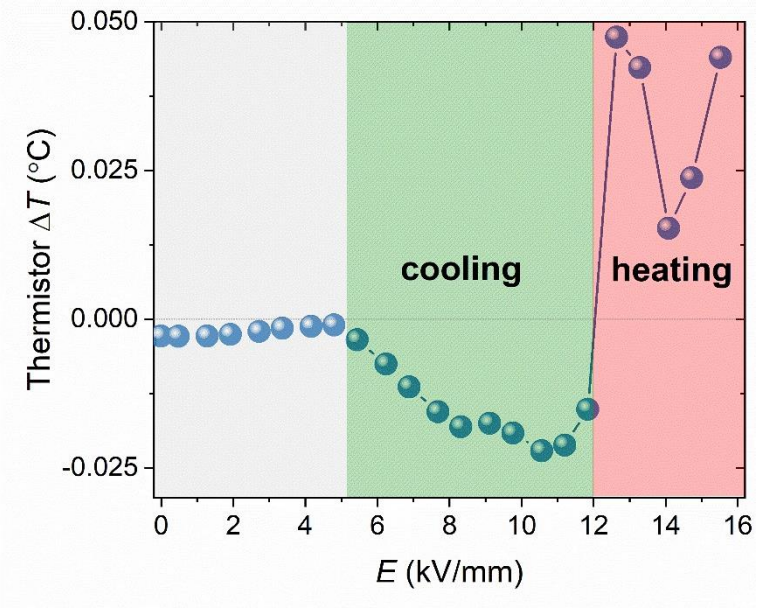

Figure 6.6: Temperature change of $NaNbO_3$ sample when subjected to an increasing electric field from 0 kV/mm and 16 kV/mm with a unipolar frequency of 0.05 Hz. The temperature was measured with a thermistor glued to the surface of the sample. To prevent dielectric breakdown, the measurement was carried out in silicone oil.

6.5 Cell Parameter Change

The combination of the high-energy XRD and the complementary latent heat measurements clearly confirmed that the *P*−*Q* phase transition could be triggered at 8 kV/mm. Since the

[1] My colleague, Dr. Lovro Fulanović, is acknowledged for measuring the latent heat.

structure of the sample does not conform to the isotropic assumption when the electric field is applied, which is required for Rietveld refinement, the LeBail fitting [150] was used to track the evolution of the cell parameters as a function of increasing electric field, as shown in Figure 6.7. The LeBail fitting was based on single-phase models with the *Pbcm* and $P2_1ma$ space groups. The one-dimensional XRD data represent the average structure as they were integrated over the entire azimuthal range. At stage 1, no significant changes were observed in the cell parameters a_{PC}, b_{PC}, c_{PC}, and γ_{PC}. The cell volume seemed to show a very slight increase at the end of this stage, which might be related to the volume expansion as a consequence of the electrostrictive effect. The transition from stage 1 to the stage 2 was marked by changes in the cell parameters. In particular, the cell parameters a_{PC}, b_{PC}, and γ_{PC} increased, whereas c_{PC} slightly decreased. An obvious increase in the cell volume from 59.43 $Å^3$ to 59.64 $Å^3$ was observed, corresponding to a volume strain of 0.35%.

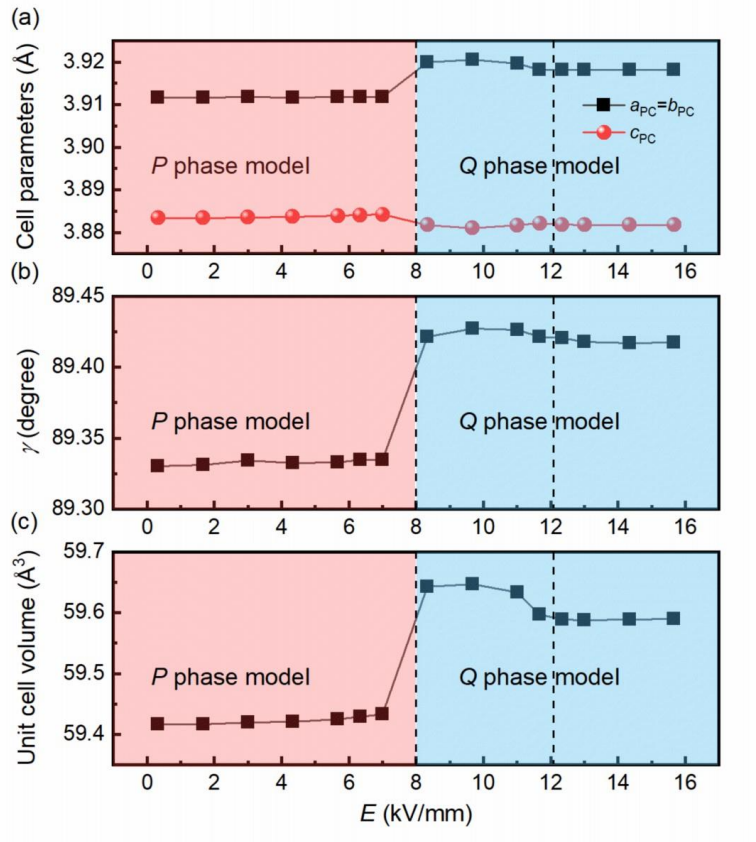

Figure 6.7: Pseudocubic lattice parameters (a) a_{PC}, b_{PC}, c_{PC}, (b) γ_{PC}, and (c) primitive cell volume as a function of increasing electric field from 0 kV/mm to 16 kV/mm. All parameters were obtained from LeBail fitting using single-phase models. The one-dimensional XRD patterns for the LeBail fitting were integrated over the entire azimuthal range and represent the average structure.

A schematic representation of the crystallographic structure of $NaNbO_3$ in the *P* and *Q* phases is given in Figure 6.8. The antiparallel displacement of the Na and Nb ions in the AFE *P* phase is along the *y* direction, which is the same direction of the spontaneous polarization in the FE *Q* phase. One can imagine that the change of the unit cell during the *P*−*Q* transition corresponds to a stretching of the unit cell along the *y* direction. It can be expected that a_{PC}, b_{PC}, and γ are larger in the *Q* phase. In addition, the cell volume is larger in the *Q* phase than in the *P* phase. Therefore, an increase in a_{PC}, b_{PC}, γ, and cell volume occurs when the field-induced *P*−*Q* phase transition is triggered. Interestingly, such volume expansion (at ~8 kV/mm) was not visible in the macroscopic strain measurement at the corresponding stage. Only at 12 kV/mm a dramatic longitudinal strain was observed. However, at the same time, no significant changes of the cell parameters a_{PC}, b_{PC}, c_{PC}, and γ_{PC} were observed. And only a slight decrease in the cell volume was observed. Between the initial state (0 kV/mm) and the final state (16 kV/mm), there was a volume strain of 0.27%.

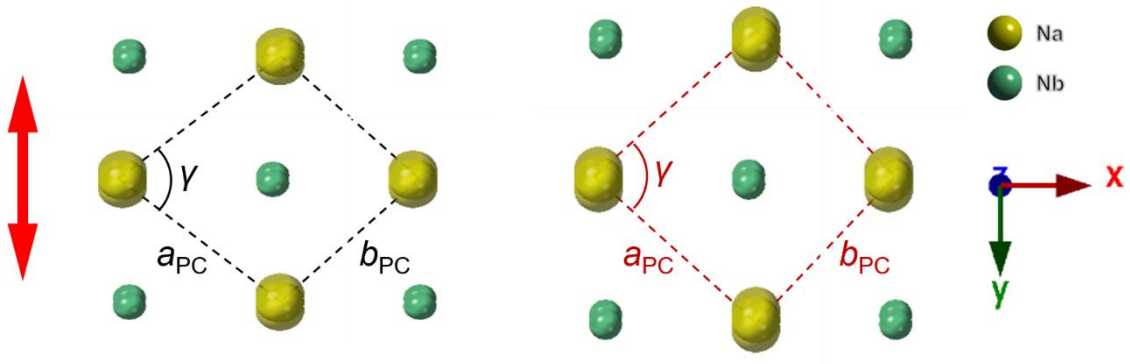

Figure 6.8: A schematic representation of the crystallographic structure of $NaNbO_3$ in the *P* phase (left) and the *Q* phase (right), viewed along the 001_{PC} direction. The orientation of the double arrow represents the direction of antiparallel atomic displacement of Na and Nb atoms.

6.6 Macroscopic Volume Change

To gain further insight into the macroscopic volume change, both the longitudinal strain S_{33} and the transverse strain S_{11} were recorded simultaneously using a homemade setup based on linear variable differential transformers. Thus, the volumetric strain S_V could be calculated ($S_V = S_{33} + 2S_{11}$). The strains S_{33}, S_{11}, and S_V of $NaNbO_3$ as a function of increasing field are shown in Figure 6.9(a). Below 12 kV/mm, no S_{33} and S_{11} responses of $NaNbO_3$ were observed. A large increase of 0.49% in strain S_{33} and a decrease of −0.25% in strain S_{11} were recorded simultaneously at about 13 kV/mm, resulting in an immediate increase in strain S_V. The strain S_V was characterized by a pulse-like behavior, i.e., a small decrease and increase just before

and after the large strain change. A volumetric strain of 0.25% was recorded between the initial zero field and 16 kV/mm, which is very close to the value of 0.27% calculated from the XRD data. Note that the AFE−FE phase transition in lead-based antiferroelectrics is characterized by auxetic behavior, i.e., simultaneous expansion in the longitudinal and transverse directions [59, 60, 151]. An example of $(Pb_{0.97}La_{0.02})(Zr_{0.75}Sn_{0.13}Ti_{0.12})O_3$ exhibiting an irreversible AFE−FE phase transition (Figure 5.12) is shown in Figure 6.9(b), where both the longitudinal strain S_{33} and the transverse strain S_{11} increase when the phase transition occurs. Such auxetic behavior is not present in the $NaNbO_3$ ceramics, suggesting that the macroscopic volumetric expansion observed at 13 kV/mm is of a different nature than that of the $(Pb_{0.97}La_{0.02})(Zr_{0.75}Sn_{0.13}Ti_{0.12})O_3$ composition. Since no evidence of a structural phase transition was observed in the synchrotron measurements, the macroscopic mechanical and electrical change observed at stage 3 are mainly due to a microstructural change, i.e., ferroelectric switching.

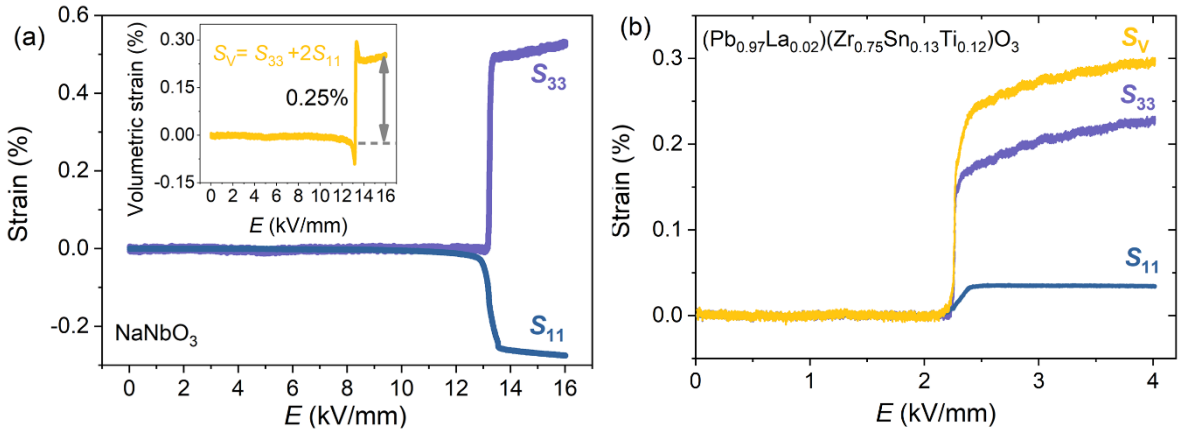

Figure 6.9: Longitudinal strain S_{33}, transverse strain S_{11}, and volume strain $S_{33}+2S_{11}$ as a function of externally applied electric field for (a) $NaNbO_3$ and (b) $(Pb_{0.97}La_{0.02})(Zr_{0.75}Sn_{0.13}Ti_{0.12})O_3$ during the very first cycle of application. A volumetric strain of 0.25% was recorded for $NaNbO_3$ between the initial and the final states.

6.7 Discussion of the Decoupling Behavior

The total macroscopic volume change calculated from the XRD data (0.27%) agrees well with that obtained from the macroscopic measurement (0.25%), suggesting that both the macroscopic and synchrotron characterization of the state change of $NaNbO_3$ between the initial state and the final state (at 16 kV/mm) are in good agreement. However, it is unclear why the phase transition (at 8 kV/mm) and the macroscopic mechanical and electrical signals were not synchronized. Based on the obtained data, a possible scenario of stage 2, which links the structural phase transition (stage 1) and the subsequent microstructural change (stage 3), is proposed. Due to the first-order nature of the field-induced $P-Q$ phase transition, both phases

are expected to coexist over a period of time or an excursion of electric field as the field increases with time. Although the phase boundary between the AFE and FE phases is not directly visible during the phase transition in our studies, the process of an AFE−FE phase transition of $PbZrO_3$ [152], which is also a first-order transition, was filmed with an infrared camera [153]. As can be seen in Figure 6.10, the phase transition nucleated from right side and the phase boundary swept across from the right end to the left end, accompanied by a decrease in temperature. The cooling effect was due to the absorbed latent heat as a result of the first-order phase transition, which was also found in the phase transition of $NaNbO_3$ studied (Figure 6.6). It is therefore expected that a process similar to that for $PbZrO_3$ will also occur for $NaNbO_3$. Note that this is a dynamic process that depends on temperature and the externally applied field, and should be different for different material systems. In the case of $PbZrO_3$, it took about 30 ms for the phase boundary to pass through the sample at a high temperature of 216 °C. In the case of $NaNbO_3$, such a process may take longer time when it takes place at room temperature.

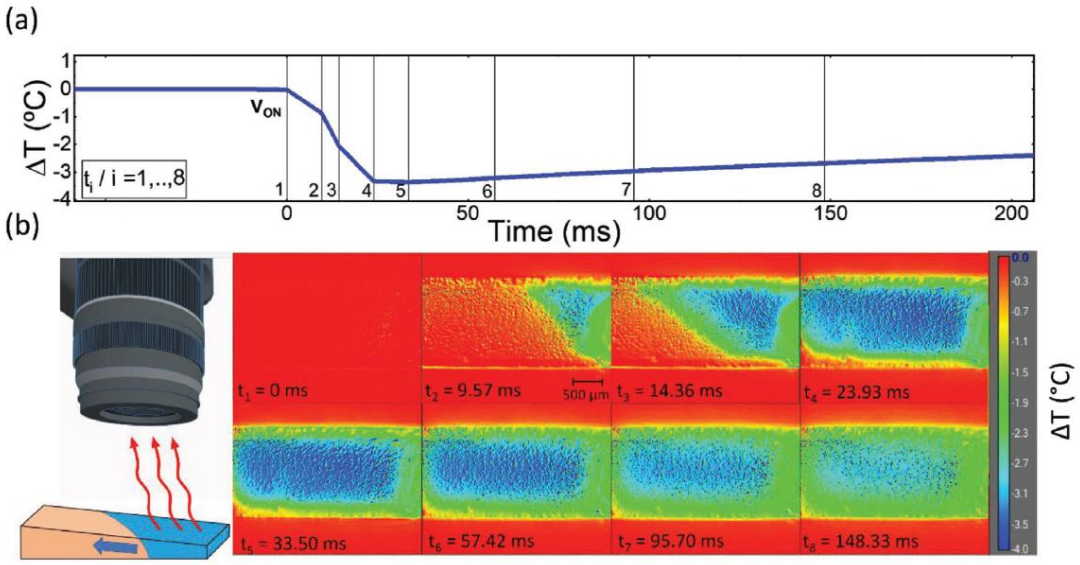

Figure 6.10: Temperature profile of $PbZrO_3$ ceramic at T = 216 °C when an average electric field of E = 3.5 kV/mm was applied. (b) AFE–FE phase boundary propagating across the sample. The phase transition was accompanied with the negative electrocaloric effect. Thickness gradients were introduced to concentrate the nucleation at one side of the sample and thus a sideways propagation of the phase boundary. Each frame has dimensions of 3.2 mm × 2.55 mm. Reprinted with permission from [153]. Copyright © John Wiley & Sons, Inc.

At the end of stage 1, the electric field was strong enough to break the *Pbcm* symmetry of the sample and triggered the phase transition from the *P* phase to the *Q* phase, leading to the disappearance of ¼ superlattice reflections at about 8 kV/mm. In a polycrystalline ceramic

material, the grains are randomly oriented, while the externally applied field is oriented along a specific direction. A field-induced phase transition is favored in certain grains with preferential crystallographic orientation [154]. Therefore, in a polycrystalline sample, a distribution of critical fields is expected at which a phase transition can be triggered [155, 156]. The formation of nucleation sites occurs in the favored grains, followed by propagation of the AFE−FE phase boundary in these grains. As the phase boundary sweeps across the sample, the two sets of lattices at the interface must conform to each other due to the larger volume of the primitive cell of the *Q* phase, leading to mechanical stress near the phase boundary [157, 158]. Therefore, an increase in volume at the intragranular level is expected. However, this microscopic volume change can be compensated by grain boundaries, pores, and domain twinning, leading to a buildup of internal mechanical stresses. The compensation temporarily postpones the macroscopic volume change that should be occurring. At this stage, a temporary equilibrium is established between the electric field driving the macroscopic mechanical/electrical changes and the internal mechanical stress caused by the polycrystallinity. As the applied field continued to increase, the electric field was strong enough to overcome the internal mechanical stress at the end of stage 2. As a result, a significant increase in macroscopic polarization and strain was observed and the mechanical stress was released.

The presence of mechanical stress at stage 2 is reflected by the evolution of the *d*-spacing values as a function of increasing electric field, which shows a particularly different behavior at this stage. The evolution of the *d*-spacings of the 220_{PC} reflections in the directions parallel and perpendicular to the applied electric field is shown in Figure 6.11(a) and two significant changes are observed. The first change observed at ~8 kV/mm corresponds to the field-induced phase transition, while the second at ~10 kV/mm corresponds to the microstructural change. At stage 2, the *d*-spacing of 220 reflection exhibited a maximum in the direction parallel to the electric field and a minimum in the direction perpendicular to the electric field. This can be explained by the hypothesis that the cells with 220 orientation were subjected to tensile stress in the direction parallel to the electric field and compressive stress in the direction perpendicular to the electric field, as shown in Figure 6.11(b). The green and red arrows represent the tensile stress and compressive stress, respectively. Similarly, the cells with 202 orientation suffered tensile stress in the direction parallel to the electric field and compressive stress in the direction perpendicular to the electric field. But the magnitude of the stress of the 202-oriented cells was

much smaller than that of the 220-oriented cells, which is due to the insignificant changes in the *d*-spacing at stage 2.

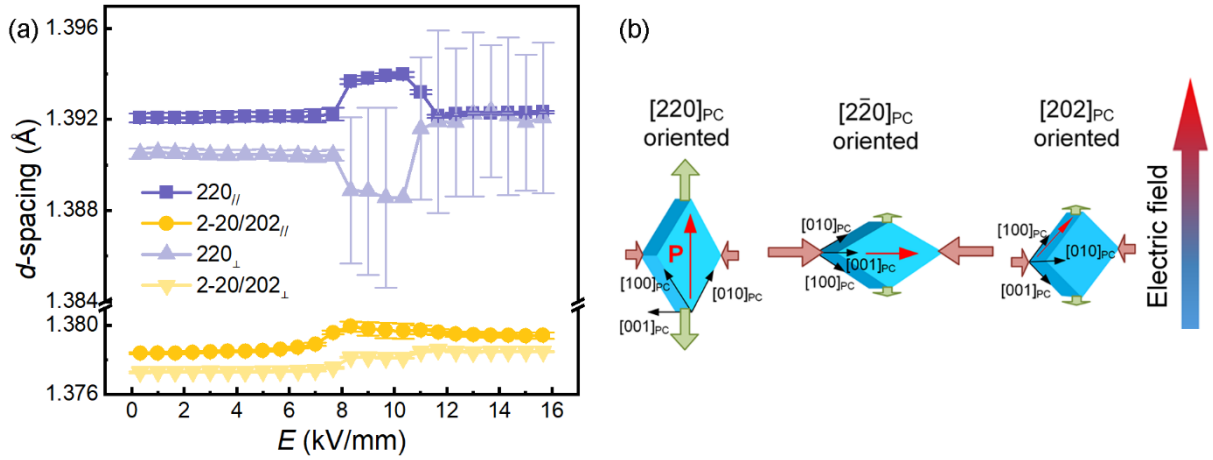

Figure 6.11: Evolution of the *d*-spacings of (a) 220_{PC} reflections in the directions parallel and perpendicular to the applied electric field. The 2theta positions of the 2−20 and 202 reflections are too close to each other to be resolved in the diffraction patterns. Therefore, the *d*-spacings of the two reflections are assumed to be equal. (b) Illustration of the differently oriented cells being subjected to tensile stress and compressive stress. The thin arrows (red) on the surfaces of the cells represent the direction of spontaneous polarization. The bold arrows represent the mechanical stress and their magnitude indicates the strength.

The evolution of the *d*-spacings of the 200_{PC} reflections in directions parallel and perpendicular to the applied electric field is shown in Figure 6.12(a). The most significant changes are observed for the 200/020 and 002 reflections parallel to the electric field. The larger *d*-spacing at stage 2 indicated that the cells with orientation 200/020 and 002 were subjected to tensile stress in the direction parallel to the electric field at this stage, as illustrated in Figure 6.12(b).

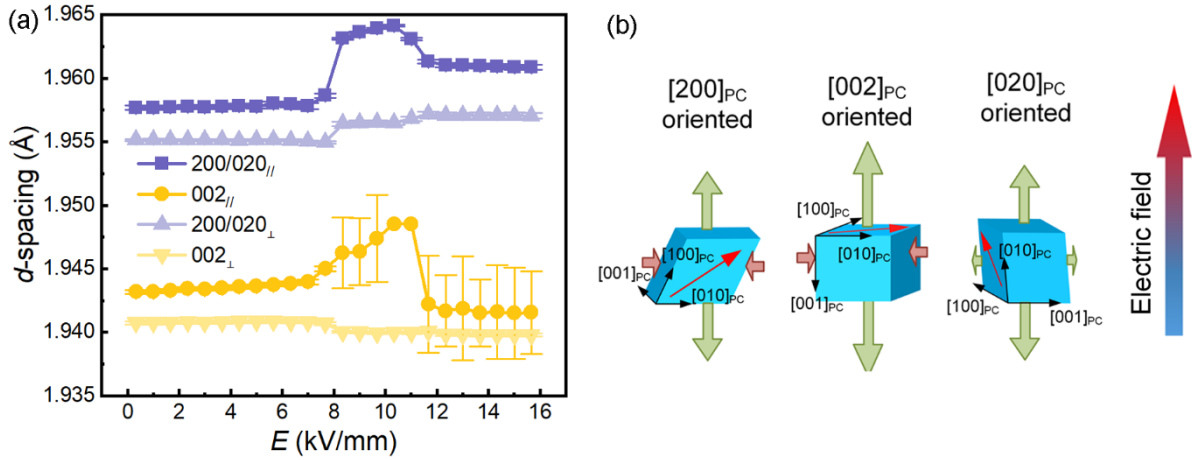

Figure 6.12: Evolution of the *d*-spacings of (a) 200_{PC} reflections in the directions parallel and perpendicular to the applied electric field. (b) Illustration of the differently oriented cells being subjected to tensile stress and compressive stress. The thin arrows (red) on the surfaces of the cells represent the direction of spontaneous polarization. The bold arrows represent the mechanical stress and their magnitude indicates the strength.

A comparison of the microstructure of the same $NaNbO_3$ sample before and after the field-induced phase transition revealed the presence of microcracks in the sample exposed to the electric field, as shown in Figure 6.13. The formation of microcracks was probably due to the release of mechanical stress at stage 3. The *d*-spacings of the 220 and 200/020 reflections parallel to the electric field increased with increasing field at the stage 2, so the tensile stress increased with increasing field. At the end of the stage 2, the tensile stress was strong enough to initiate the propagation of microcracks. The polarization hysteresis loops of $NaNbO_3$ with microcracks that have undergone the transition are shown in Figure 6.14. The loops become more slanted during cycling because the local effective field drops across microcracks [159], resulting in a broader distribution of switching fields.

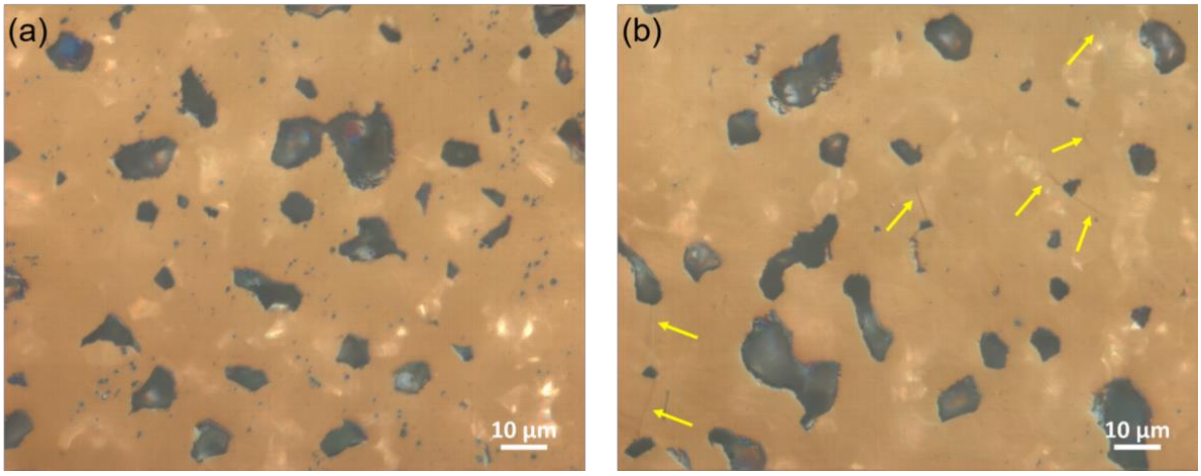

Figure 6.13: Micrographs of polished $NaNbO_3$ samples (a) before and (b) after the field-induced phase transition. Microcracks are highlighted using yellow arrows. The crack length is about 5–10 µm. The images were taken in the circular polarized light-differential interference contrast (C–DIC) mode, using the Axio Imager 2 microscope (Zeiss, Germany).

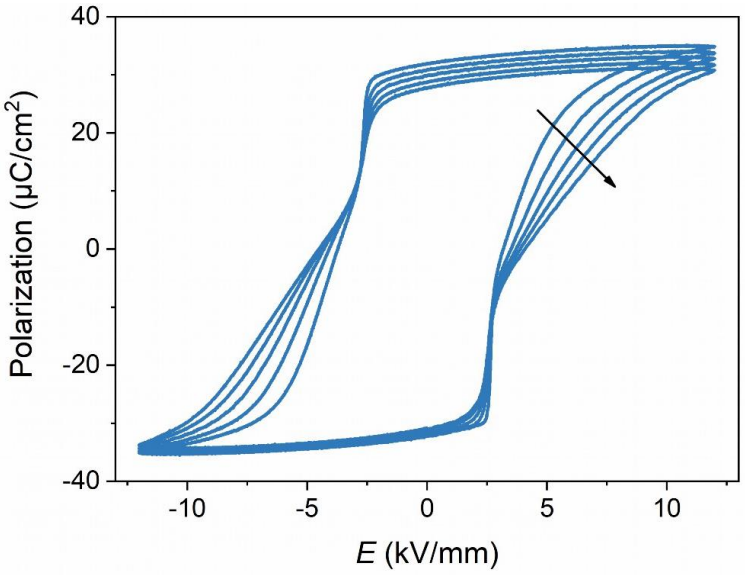

Figure 6.14: Cycling behavior of the polarization hysteresis loops of $NaNbO_3$ with microcracks.

6.8 Summary

In situ high-energy diffraction measurements were employed to investigate the structural and microstructural changes during the antiferroelectric−ferroelectric phase transition in $NaNbO_3$ ceramic samples, complemented by simultaneous recording of the macroscopic polarization and strain responses. The decoupling of structural phase transition and microstructural ferroelectric switching is attributed to the buildup of intragranular stress and compensation of microscopic volume expansion due to polycrystallinity. The internal mechanical stress is released by the propagation of microcracks when the applied field is strong enough at the stage 3 to trigger the macroscopic volume increase. The three-step AFE−FE phase transition behavior of $NaNbO_3$ differs distinctly from $PbZrO_3$-based antiferroelectric materials.

With the synchrotron measurement, we have demonstrated that almost 100% of the *P* phase can be transformed to the *Q* phase by a unipolar electric field. It is unclear whether applying an electric field can completely convert the AFE order to the FE order in other AFE systems that exhibit a reversible field-induced phase transition, e.g., $PbZrO_3$, $PbZrO_3$-derived materials (PNZST, PLZST), and $AgNbO_3$ (AN). Intuitively, it is assumed that in the materials exhibiting a reversible AFE−FE phase transition, some degree of AFE order is preserved, which likely contributes to the recovery of the AFE phase when a reverse electric field is applied. Therefore, the nearly 100% conversion from the *P* phase to the *Q* phase makes it very difficult for a reversible FE−AFE phase transition to occur in $NaNbO_3$, resulting in an irreversible AFE−FE phase transition. The 50-50 coexistence of the *P* and *Q* phases after the application of a bipolar electric field suggests that some fraction of the *Q* phase transforms back to the *P* phase after the

application of a reversed electric field, which has already been reported for a $NaNbO_3$-based ceramic material [160]. The application of a reverse electric field can help to return the displaced Na and Nb ions to their original positions (Figure 6.8) and recover the *P* phase. However, it has been reported that in the PLZST system the activation energy for the field-induced AFE−FE phase transition (~15−20 kV/mm) is much higher than that of the domain switching (0.5−1.0 kV/mm) [56], and therefore the domain switching is also likely to occur. The two competing mechanisms can coexist in $NaNbO_3$ but domain switching dominates. As a result, a square-like polarization hysteresis loop (Figure 5.1c) was observed in $NaNbO_3$ ceramics, which is characteristic of the domain switching behavior. However, the domain switching is accompanied by changes in the phase fractions of the *P* and *Q* phases, as shown by the XRD, TEM and NMR characterizations. Therefore, it would be interesting to study the structural and microstructural changes of $NaNbO_3$ under a bipolar electric field using *in situ* high-energy XRD in the future. Overall, the irreversible behavior of the AFE−FE phase transition of pure $NaNbO_3$ prevents its implementation in practical applications. The development of new $NaNbO_3$-based compositions exhibiting a reversible AFE−FE transition is addressed in the next section.

7 Design of New $NaNbO_3$-Based Antiferroelectric Compositions

7.1 Energy Difference Calculated by DFT[1]

Antiferroelectric materials are characterized by a small difference in free energy between the AFE and the FE structures [1, 38], which allows the AFE−FE phase transition to be triggered, for example, by the application of an electric field. Using first-principles calculations, the energy of the AFE structure in the prototypical $PbZrO_3$ system was calculated to be 20 meV per formula unit (f.u.) lower than that of the FE structure at 250 K [18]. The free energies of the AFE and FE structures in $NaNbO_3$ were calculated. The energy of the FE structure (space group $P2_1ma$) is 2.3 meV/f.u. lower than that of the AFE structure (space group *Pbcm*), indicating that the FE phase is energetically more stable, as listed in Table 7.1. Our calculation agrees well with a previous study by Shimizu *et al.* [17], in which the polar $P2_1ma$ structure is energetically favored by 2.4 meV/f.u..

To find a new composition that has a reversible AFE-FE phase transition, the AFE order should be slightly energetically favored so that the AFE state is restored from the field-induced FE state. Sn is an essential element in PLZST and PNZST systems, both of which are the most studied $PbZrO_3$-based AFE materials and exhibit a reversible field-induced AFE−FE phase transition. As described in the previous sections, Sn acts as an AFE stabilizer when it replaces the B-site ions in $PbZrO_3$ [54]. In $PbZrO_3$, the substitution of Sr^{2+} for the A-site cation also allows the stabilization of the AFE order [161]. The Goldschmidt tolerance factor of $NaNbO_3$ and $SrSnO_3$ is 0.9672 and 0.9610, respectively, thus alloying $NaNbO_3$ with $SrSnO_3$ can reduce the tolerance factor of the system and thus stabilize the AFE order. Therefore, first-principles calculations were performed to examine the stability of the AFE and FE phases of a $SrSnO_3$ modified $NaNbO_3$ system using first-principles calculations. Supercells with the nominal composition $0.9375NaNbO_3$-$0.0625SrSnO_3$ were constructed, as illustrated in Figure 7.1. For more details on how the calculation was performed, see the methods in Chapter 3.

Our calculation showed that the energy of the AFE structure is 1.4 meV/f.u. lower than that of the FE modification in the modified system (Table 7.1) and is thus energetically more stable. This suggests that the introduction of $SrSnO_3$ leads to a more stable AFE structure than the corresponding FE modification. Previous studies predicted that a stable AFE state and the

[1] My colleague, Mr. Niloofar Hadaeghi, is acknowledged for performing the DFT calculations. The interpretation of the results was supported by Prof. Dr. Hongbin Zhang.

simultaneous presence of a FE state with slightly higher energy are necessary conditions for the existence of a reversible AFE−FE phase transition [1, 38].

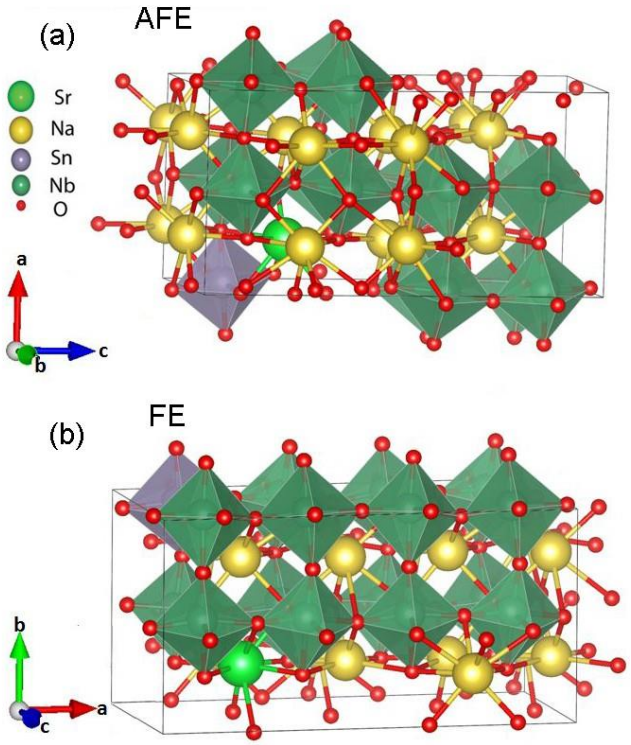

Figure 7.1: Calculated structures of the most stable AFE structure of $0.9375NaNbO_3$-$0.0625SrSnO_3$ and the corresponding FE modification.

Table 7.1: DFT calculated energies and structural parameters for the *Pbcm* and *Pmc*2_1 structures of pure and $SrSnO_3$-substituted $NaNbO_3$, on a per formula unit (f.u.) basis[1].

		$NaNbO_3$	$0.9375NaNbO_3$-$0.0625SrSnO_3$
AFE phase	E [eV]	−39.08240	−38.60406
	a [Å]	5.564	5.597
	b [Å]	5.641	5.600
	c [Å]	15.586	15.760
	V [Å^3]	489.22	493.94
FE phase	E [eV]	−39.08470	−38.60267
	a [Å]	7.798	7.850
	b [Å]	5.585	5.612
	c [Å]	5.649	5.625
	V [Å^3]	246.02	247.78
Difference	ΔE [meV]	2.3	1.4
Ground state		FE	AFE

[1] Here we only compare the energies of the most stable AFE and FE structures. Other scenarios please refer to [92]. In all scenarios, the energy of the AFE structure is 1.4 meV/f.u. lower than that of the FE modification and is thus energetically more stable.

7.2 Global Structure

Based on our first-principles calculations, a series of $SrSnO_3$-substituted $NaNbO_3$ ceramic samples containing 3-6 mol% $SrSnO_3$ were prepared by the conventional solid-state reaction method. The nominal compositions $(1-x)NaNbO_3$-$xSrSnO_3$ (x = 0.03−0.06 with an interval of 0.01) are abbreviated as NN100xSS in the following. All $SrSnO_3$-substituted samples exhibit a perovskite structure, as depicted in Figure 7.2. A close examination of the 2theta regions of 35.5−37.5°, 42.5−44.2°, and 54.0−56.0° shows that they are characterized by superlattice reflections that belonging to the *Pbcm* structure, as highlighted in Figure 7.2(c-d). This suggests that the AFE order is preserved after the substitution of $SrSnO_3$. A small amount of a non-perovskite secondary phase was detected in the $SrSnO_3$-substituted samples, and the composition of the impurity phase is close to SnO_2. Note that SnO_2 is a refractory material with a melting point of 1630 °C and the sintering temperature of unmodified SnO_2 is over 1300 °C [162]. It was found that the mass-transport mechanism during sintering of SnO_2 is controlled by surface diffusion below 1000 °C and evaporation-condensation above 1300 °C. Sn^{4+} (0.69 Å; coordination number (CN) = 6) is larger than Nb^{5+} (0.64 Å, CN = 6). The presence of SnO_2 secondary phase could be due to the slow lattice diffusion rate of Sn^{4+} in $NaNbO_3$. In addition, the high volatility of Na during sintering may reduce the solubility of Sn due to charge neutrality. The amount of secondary phase can be slightly reduced by a second calcination treatment, but the effect is not significant. In the final sintering stage, the amount of impurity phase can be significantly reduced but not completely removed. Based on the high-energy XRD data (energy ~60 keV) recorded in transmission geometry, the refined phase fraction of SnO_2 secondary phase in the NN5SS sample is 0.83%, corresponding to a Sn deficiency of 14.3%. Thus, the actual composition of the NN5SS sample with the nominal composition of $0.95NaNbO_3$-$0.05SrSnO_3$ is estimated to be $0.957NaNbO_3$-$0.043SrSnO_3$.

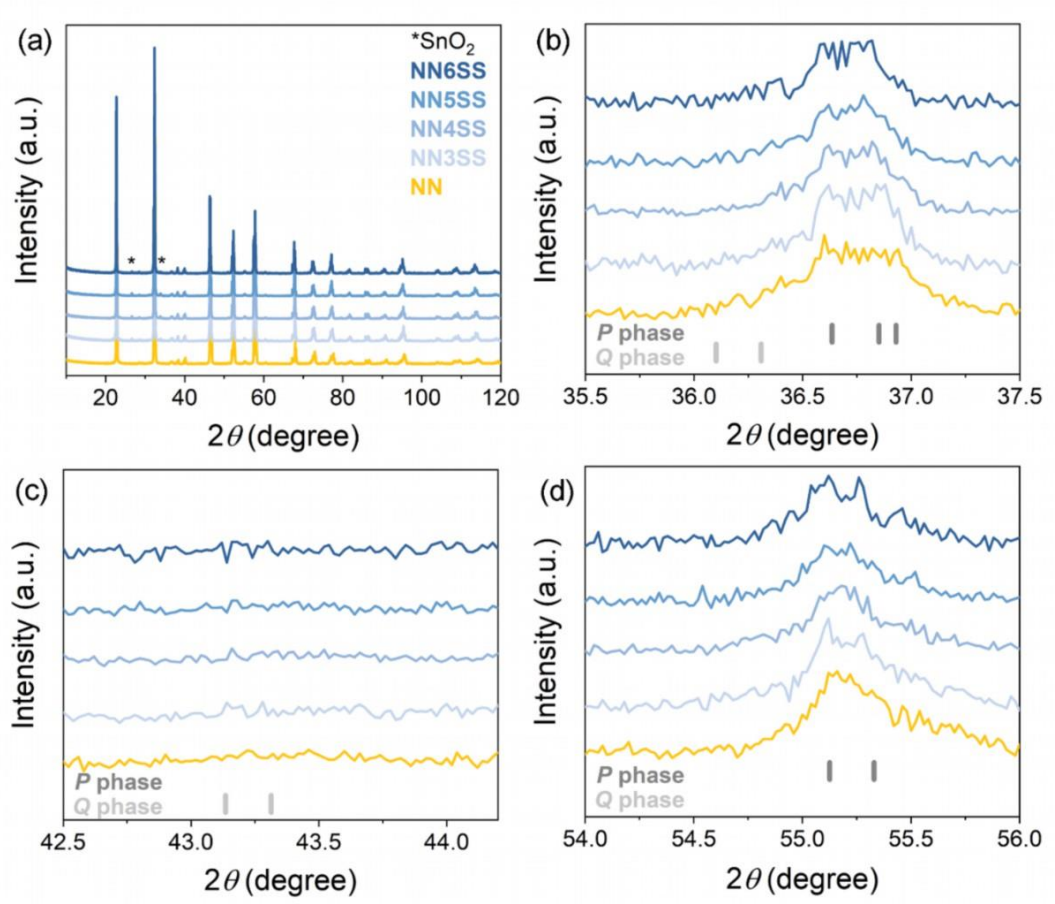

Figure 7.2: (a) Full XRD patterns of pure $NaNbO_3$ and $SrSnO_3$-substituted samples and superlattice reflections in the 2theta regions of (b) 35.5−37.5°, (c) 42.5−44.2°, and (d) 54.0−56.0°. Two sets of markers represent the reflections associated with the *P* phase (dark grey) and the *Q* phase (light grey). The reflection geometry XRD signal was obtained from the crushed powder of the sintered pellets.

The cell parameters of the $SrSnO_3$-substituted samples were determined using Rietveld refinement, as demonstrated in Figure 7.3. The cell parameters *a*, *c*, and the unit cell volume increase with increasing $SrSnO_3$ content, while the cell parameter *b* decreases with increasing $SrSnO_3$ content. The cell parameters calculated by DFT are listed in Table 7.1 and also highlighted in Figure 7.3. The cell parameters *a*, *c*, and unit cell volume are larger in the $SrSnO_3$-substituted system, while the cell parameter *b* is smaller, which agrees well with the results obtained using Rietveld refinement. The overall increase in the unit cell volume of the $SrSnO_3$-substituted samples can be justified by the larger ionic radii of Sr^{2+} (1.44 Å, coordination number (CN) = 12) and Sn^{4+} (0.69 Å, CN = 6) than those of Na^{+} (1.39 Å, CN = 12) and Nb^{5+} (0.64 Å; CN = 6). Accordingly, the tolerance factor decreases from 0.9672 for $NaNbO_3$ to 0.9641 for NN5SS, indicating that the AFE order is stabilized after the introduction of $SrSnO_3$.

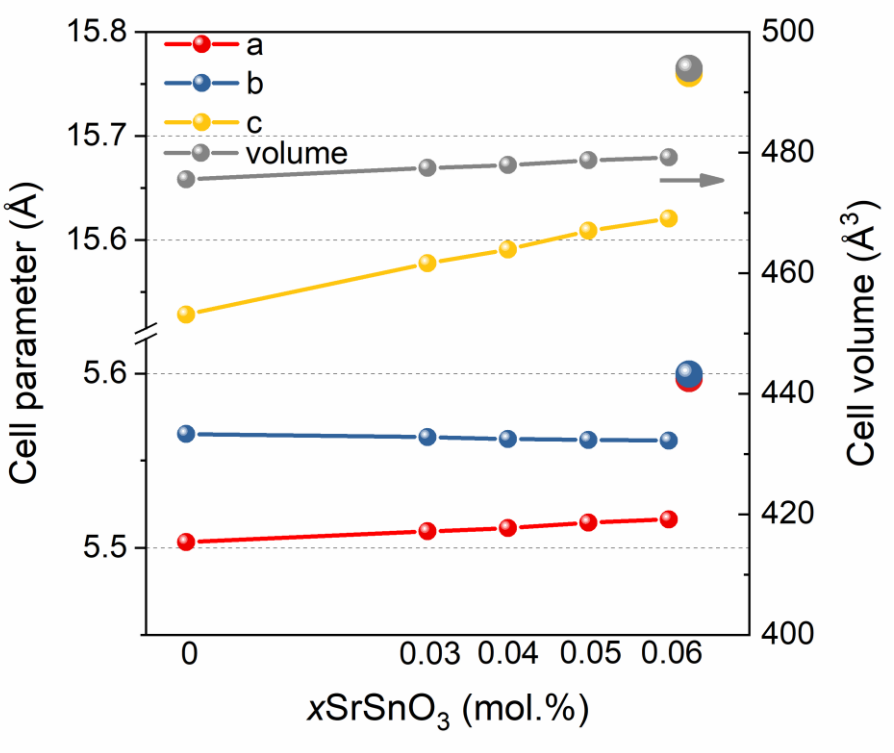

Figure 7.3: Cell parameters of pure $NaNbO_3$ and $SrSnO_3$-substituted $NaNbO_3$ samples, determined from Rietveld refinements. The bigger symbols represent the cell parameters calculated by DFT.

To gain further insight into the influence of $SrSnO_3$ on $NaNbO_3$, the structure of NN5SS was studied using high-energy XRD recorded in transmission geometry. Rietveld refinement of the XRD data obtained from the sample in the virgin state (without electrical history) was performed based on the centrosymmetric *Pbcm* space and the results are shown in Figure 7.4. The positions of Na, Nb, and O ions and their corresponding thermal parameters U_{iso} were refined. Sr and Sn atoms were assumed to occupy the Na(1) and Nb sites, respectively. It was assumed that the atoms on the A-site, B-site, and oxygen-site each have the same thermal parameters U_{iso}. The full pattern could be satisfactorily refined to a reasonable R_w value of 0.0892. The good agreement is illustrated by the superlattice reflections in Figure 7.4(b) and high-angle main reflections in Figure 7.4(c-d), which show excellent agreement between the observed and calculated patterns. No reflections characteristic of the $P2_1ma$ structure were found. The refined cell parameters are a = 5.51535(7) Å, b = 5.56344(10) Å, c = 15.61913(21) Å, and a cell volume of 479.263(7) Å^3. The refined atomic positions are listed in Table 7.2. A comparison of the atomic positions of $NaNbO_3$ (Table 6.1) and NN5SS shows that the atomic shift of Na(1) and Na(2) along the x-axis is larger in $NaNbO_3$, while the atomic positions of Nb are almost the same in both systems, as depicted in Figure 7.5. The calculated

atomic displacements of the Na(1) ions relative to the symmetric centers in the cubic phase are 0.10 Å and 0.03 Å in $NaNbO_3$ and NN5SS, respectively. The antiparallel atomic displacements of both Na and Nb contribute to the local polarization of the *Pbcm* structure. Since the atomic positions of the oxygen sites in the two systems are slightly different, the magnitude of the local polarization contributed by the Nb ions is slightly different in the two systems. In particular, the contribution of Na ions to the local polarization in NN5SS is much smaller than that in pure $NaNbO_3$, which may affect the macroscopic polarization and even the reversibility of the field-induced AFE−FE phase transition and will be discussed later. Despite the different local structures, the overall global structures of $NaNbO_3$ and NN5SS are close to each other, as they are well described by the *Pbcm* space group.

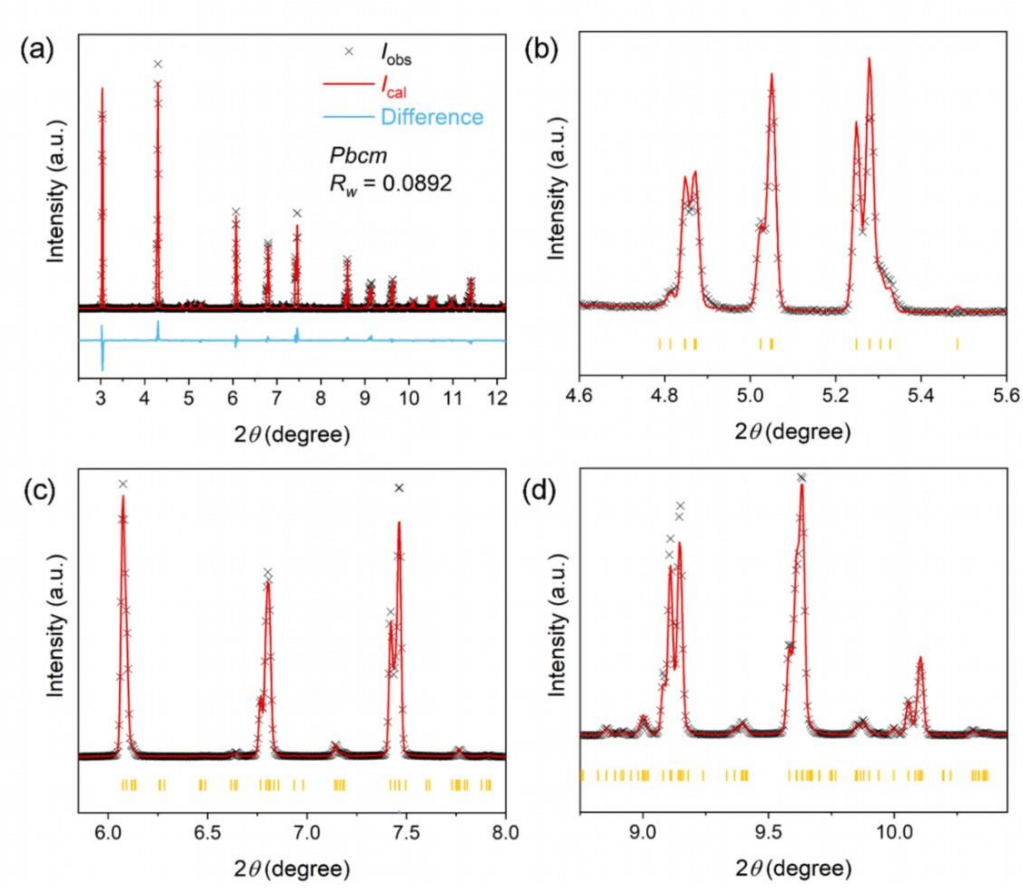

Figure 7.4: (a) Rietveld refinement of the high-energy XRD data of the virgin-state NN5SS system using the *Pbcm* space group. Magnified views of (b) representative superlattice reflections and (c-d) high-angle main reflections. Reflections associated with the *Pbcm* structure are shown by the yellow tick marks. The starting parameters of the *Pbcm* model for the refinement were taken from the refinements of pure $NaNbO_3$ in this work.

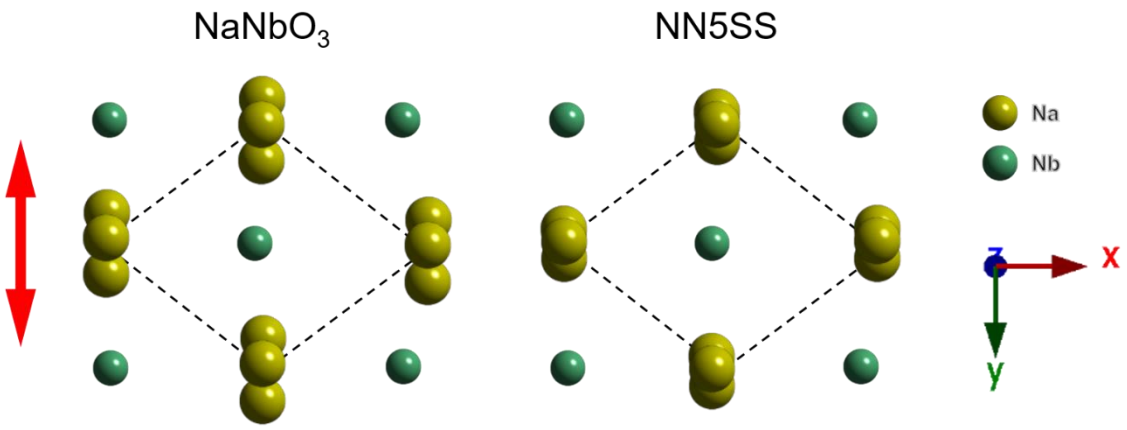

Figure 7.5: A schematic representation of the atomic displacements of Na in $NaNbO_3$ (left) and NN5SS (right) systems, both of which have *Pbcm* space group in the virgin state, viewed along the 001_{PC} direction. The atomic displacements are exaggerated to highlight the small differences in atomic displacements. The orientation of the double arrow represents the direction of the antiparallel atomic displacement of the Na and Nb atoms.

Table 7.2: Rietveld refinement data for NN5SS on the basis of the space group *Pbcm*.

	Atomic positions			
	x	*y*	*z*	U_{iso}
Na(1)	0.24478	0.25	0.0	0.00274
Na(2)	0.24478	0.2172	0.25	0.00274
Sr	0.24478	0.25	0	0.00274
Nb	0.25221	0.7308	0.12489	0.00313
Sn	0.25211	0.73431	0.12489	0.00314
O(1)	0.66807	0.25	0	0.00062
O(2)	0.20858	0.7652	0.25	0.00062
O(3)	0.46615	0.46233	0.14925	0.00062
O(4)	0.03338	0.04012	0.11252	0.00062

7.3 Local Structure[1]

Solid-state ^{23}Na NMR spectroscopy was employed to investigate the effects of $SrSnO_3$ substitution on the local structure of $NaNbO_3$. The ^{23}Na STMAS spectra of $NaNbO_3$ and NN5SS samples in the virgin state are compared and shown in Figure 7.6. In the two-dimensional spectrum, two NMR signals corresponding to the Na(1) and Na(2) sodium sites of the *Pbcm* structure can be seen, as revealed in Figure 7.6(a). The two signals are distinguishable in pure $NaNbO_3$ the NN5SS sample, indicating that both sodium sites are still present in the structure after the substitution of 5 mol% $SrSnO_3$. Projecting the two signals along the indirect dimension (δ_1), a continuous shape of the signal trace is obtained, as shown in Figure 7.6(e).

[1] My colleague, Ms. Sonja Egert, is acknowledged for the measurement and analysis of the NMR data. Dr. Pedro B. Groszewicz is acknowledged for helping with interpretation of the results.

Since the presence of the $P2_1ma$ structure would appear as a shoulder of the Na(1) signal [148], the continuous profile seems to indicate the absence of the *Q* phase, similar to the case of $NaNbO_3$, as shown in Figure 7.6(b). This agrees well with the fact that the structure of the NN5SS sample can be well described by the *Pbcm* space group (Figure 7.4). Moreover, no significant changes in the positions of the two signals were observed. The position of the NMR lines contains important information about the local structure of a particular ion and is often understood as a "fingerprint" of the local environment [145, 163]. The retention of both signals and their positions indicates that the global structure is preserved after the substitution of 5 mol% $SrSnO_3$, which is consistent with the XRD results shown above.

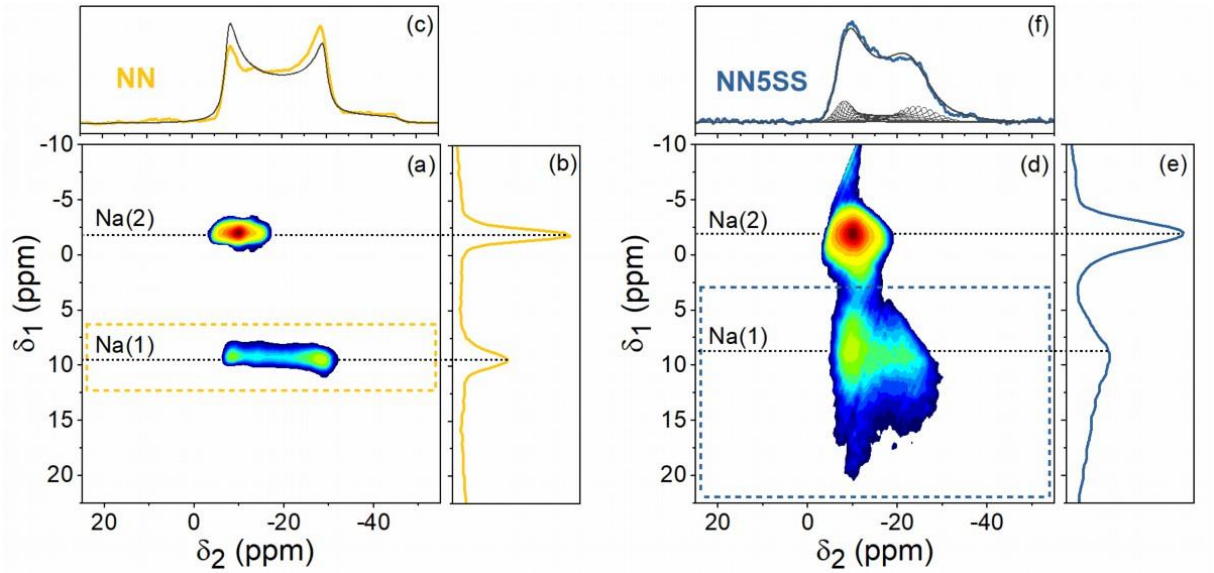

Figure 7.6: Two-dimensional ^{23}Na STMAS spectra of (a) pure $NaNbO_3$ and (b) NN5SS systems in the virgin state. Summation of the signals along the indirect dimension (δ_1) for (b) $NaNbO_3$ and (e) NN5SS. Projections of the Na(1) signals (area within the dashed rectangles) along the direct dimension (δ_2) for (c) $NaNbO_3$ (in yellow) and (f) NN5SS (in blue) with the best achieved line shape simulations (in gray), from which NMR parameters and distributions thereof are extracted as described in [93].

Despite the similarities, it is evident that both the shape and the width of the two signals are affected by the substitution of $SrSnO_3$. Both the Na(1) and Na(2) signals, are broadened along the indirect dimension (δ_1) compared to the spectra of $NaNbO_3$, with the effect being more pronounced for the Na(1) site, as shown in Figure 7.6(e). Moreover, the shape of the Na(1) signal also changes significantly along the direct dimension (δ_2), which is well seen by projecting the Na(1) signal along the δ_2 dimension, as shown in Figure 7.6(c) and Figure 7.6(f). The line shape of $NaNbO_3$ is characterized by a well-defined profile with two maxima at −9 ppm and −29 ppm, which is consistent with the previously reported NMR parameters [117].

In the case of NN5SS, the maximum at −9 ppm is preserved, while the maximum at −29 ppm is less significant. A detailed analysis of the line shape of NN5SS has been published elsewhere [93]. The observed changes in the Na(1) signal indicate the following two differences after $SrSnO_3$ is introduced into the system: (1) the quadrupolar coupling constant, which represents the degree of structural distortion of the NaO_{12} cubooctahedral cages, decreases; (2) the distribution of the chemical shift, which represents the distribution of average Na-O distances, increases. In other words, from the NMR perspective, the formation of NN5SS solid solution results in a more disordered, albeit less distorted, local structure of the Na(1) site. As shown by the Rietveld refinement, the atomic displacement of Na ions in NN5SS is 70% smaller than in pure $NaNbO_3$ (Figure 7.5), implying that the local structure of the Na(1) is less distorted by the formation of the NN5SS solid solution. The increased disorder is expected to result from the introduction of new elements into the system and hence, a broader variation in the local environments of the Na sites. After all, in the new solid solution the Na ion is exposed to a more complicated chemical environment.

7.4 Electrical Properties

7.4.1 Field-Induced Phase Transition

The $SrSnO_3$-substituted samples in the virgin state were subjected to large electric fields to study the field-induced phase transition behavior. The polarization and strain hysteresis loops are shown in Figure 7.7. Although $NaNbO_3$ exhibits an irreversible AFE−FE phase transition, double polarization hysteresis loops were observed in all $SrSnO_3$-substituted samples, indicating that the transition became reversible. The remanent polarization, which characterizes the ability to maintain ferroelectricity after removal of the electric field, decreases with increasing $SrSnO_3$ content. The measured macroscopic piezoelectric charge coefficient d_{33} decreases from 35 pC/N for $NaNbO_3$ to 8 pC/N, 4 pC/N, and 2 pC/N for NN3SS, NN4SS, and NN5SS samples, respectively. The loss of macroscopic piezoelectricity in the $SrSnO_3$-substituted samples suggests that the reversibility of the field-induced AFE−FE increases with increasing $SrSnO_3$ content, i.e., the centrosymmetric *Pbcm* structure can be restored to a higher extent after the electric field is removed. This means that the ferroelectric order is suppressed and the AFE order is stabilized after the introduction of $SrSnO_3$. The suppression of the ferroelectric order is also reflected in the change of the strain hysteresis loops with increasing $SrSnO_3$ content, which changes from a butterfly shape to a sprout shape, characteristic of antiferroelectrics. The negative strain of the strain loops, defined as the difference between the

zero strain and the minimum strain in the second electric field cycle, represents a combination of the non-180° domain switching and the converse piezoelectric effect. The negative strain decreases with increasing $SrSnO_3$ content, which is in good agreement with the suppressed FE order, as shown in Figure 7.7(d). The critical field, E_F, increases from 11.6 kV/mm for $NaNbO_3$ to 12.4 kV/mm, 12.8 kV/mm, and 15.0 kV/mm for NN3SS, NN4SS, and NN5SS, respectively. The increased critical fields are expected to result mainly from the enhanced antiferroelectric order, since the average grain size is comparable for $NaNbO_3$ (8.9 μm), NN3SS (10.7 μm), NN4SS (11.5 μm), and NN5SS (8.1 μm), as revealed in Figure 7.8. $SrSrO_3$-content samples.

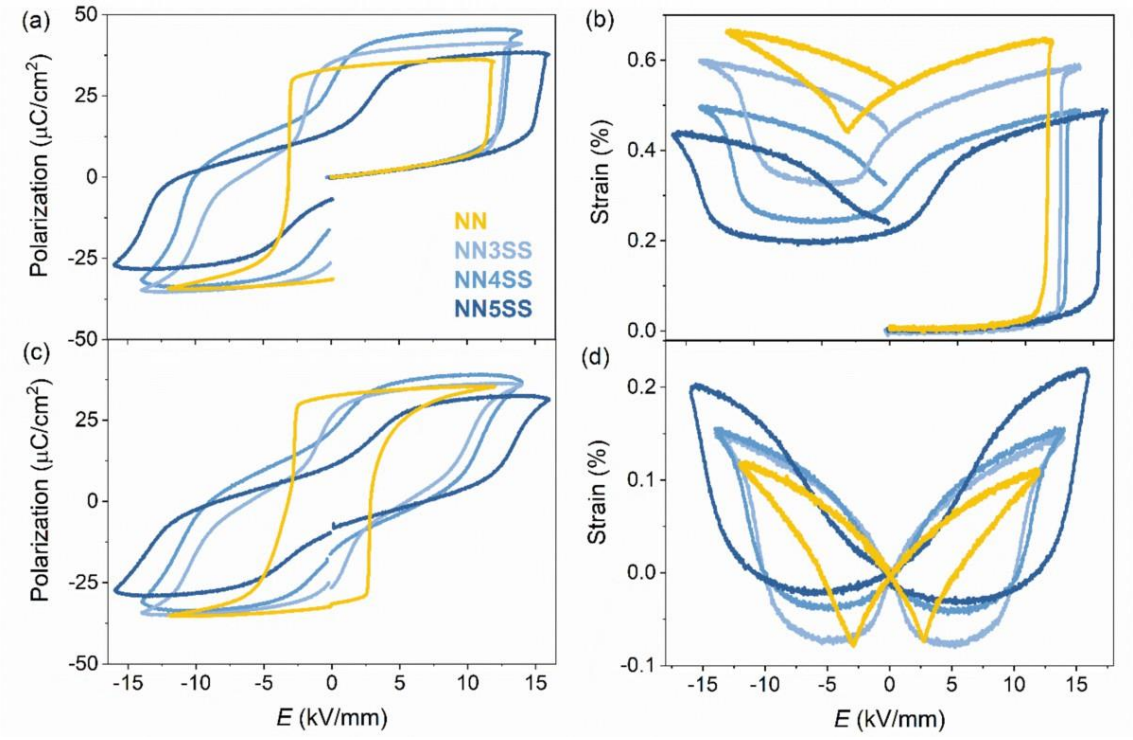

Figure 7.7: (a) Polarization and (b) strain hysteresis loops of $NaNbO_3$, NN3SS, NN4SS, and NN5SS ceramic samples in the first electric cycle, measured at 1 Hz and room temperature. (c) Polarization and (d) strain hysteresis loops in the second electric field cycle.

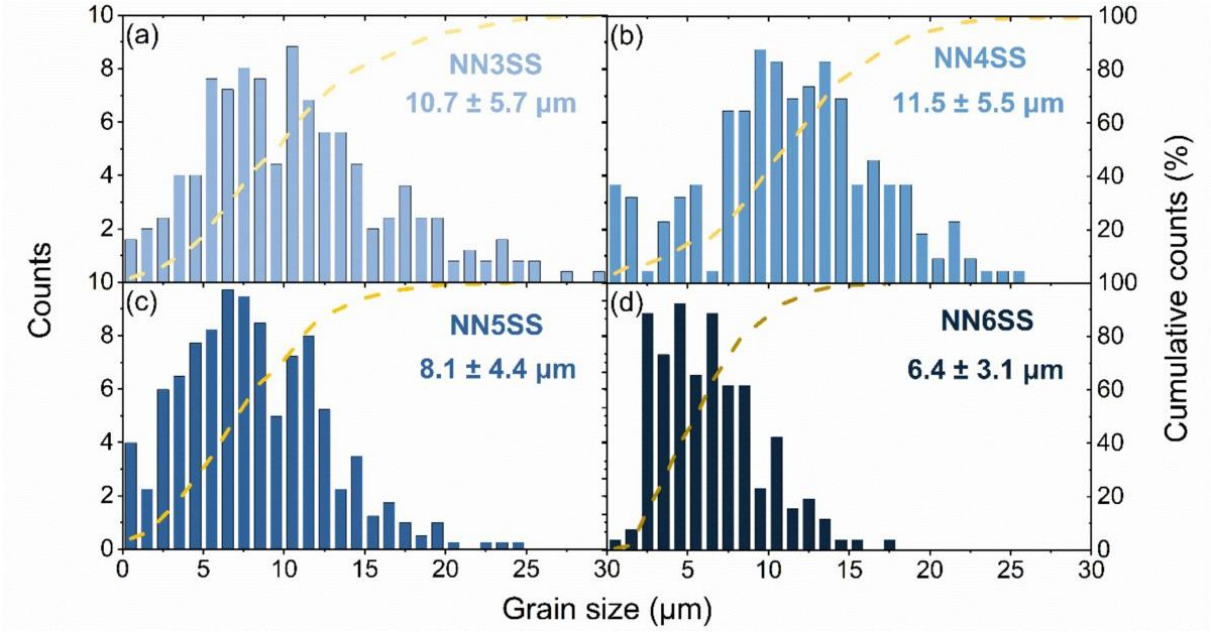

Figure 7.8: Grain size distributions of (a) NN3SS, (b) NN4SS, (c) NN5SS, and (d) NN6SS ceramic samples.

The increased reversibility of the field-induced AFE−FE phase transition in the $SrSnO_3$-substituted samples may be related to the less distorted structure after the formation of the solid solution, as demonstrated by both the global and local characterizations of the structure. In the AFE state, both the $NaNbO_3$ and NN5SS samples exhibit the antiparallel atomic displacements of the Na ions, since both materials have the *Pbcm* space group. Since the atomic positions of the Nb ions in $NaNbO_3$ and NN5SS are very close (see Table 6.1 and Table 7.2), we mainly consider the contribution of the Na ions here. The atomic displacement of Na ions in NN5SS (0.03 Å) is calculated to be almost 70% smaller than that in $NaNbO_3$ (0.10 Å), as previously illustrated in Figure 7.5. Although there are no detailed Rietveld refinements of the atomic positions of the NN3SS and NN4SS samples, it is reasonable to assume that the magnitude of the atomic displacement of Na decreases with increasing $SrSnO_3$ content. In the field-induced FE state, the antiparallel atomic configurations of both Na and Nb ions are switched by the application of an electric field, resulting in the macroscopic polarization. A similar process was observed in pure $NaNbO_3$ (Figure 6.7). It appears that as the $SrSnO_3$ content increases, it becomes increasingly difficult to switch the Na ions, and this has two consequences. First, realization of the field-induced AFE−FE phase transition requires a higher driving field, as shown by the increase in E_F with increasing $SrSnO_3$ content. Alternatively, the field-induced polarization decreases with increasing $SrSnO_3$ content at the same electric field, see, for example, the polarization at 10 kV/mm in Figure 7.7c. Second, the switched ions in the field-

induced FE state are likely to return to their original position after the electric field is removed. As a result, lower remanent polarization and macroscopic piezoelectricity were observed with increasing $SrSnO_3$, as depicted in Figure 7.7. *In situ* high-energy XRD characterizations are required to confirm the above hypotheses.

Due to the reversible field-induced AFE−FE phase transition in the $SrSnO_3$-substituted samples, the energy storage properties are improved. The energy storage density increases from 0.12 J/cm^3 for $NaNbO_3$ to 0.30 J/cm^3, 0.49 J/cm^3, and 0.90 J/cm^3 for NN3SS, NN4SS, and NN5SS, respectively. More detailed data on the electrical properties are given in Table 7.3.

Table 7.3: Electrical properties of $NaNbO_3$, NN3SS, NN4SS, and NN5SS ceramic samples. P_r is the remanent polarization, E_F is the critical field, S_{neg} is the negative strain, d_{33} is the macroscopic piezoelectricity, ω_{stor} is the storage energy density, ω_{rec} is the recoverable energy density, and η is the energy storage efficiency (ω_{rec}/ ω_{stor}).

	$NaNbO_3$	NN3SS	NN4SS	NN5SS
P_r (μC/cm^2)	32.4	26.3	21.7	11.0
E_F (kV/mm)	11.6	12.4	12.8	15.0
S_{neg} (%)	−0.077	−0.080	−0.043	−0.033
d_{33} (pC/N)	35 ± 1	8 ± 1	4 ± 1	2 ± 1
ω_{stor} (J/cm^3)	/	0.52	3.98	4.23
ω_{rec} (J/cm^3)	0.12	0.30	0.49	0.90
η (%)	/	8.5	12.2	21.4

7.4.2 Dielectric Properties

The impact of $SrSnO_3$ substitution on the dielectric properties is shown in Figure 7.9. $NaNbO_3$ exhibits a dielectric maximum at about 380 °C, where the *P* phase changes to the *R* phase upon heating. The *P*−*R* phase transition temperature $T_{P–R}$ is 312 °C, 288 °C, and 236 °C for NN3SS, NN4SS, and NN5SS, respectively. It is assumed that the decrease of $T_{P–R}$ with increasing $SrSnO_3$ content is due to the reduced orthorhombic lattice distortion within the *ab* plane (cell parameter ratio *b*/*a*), which decreases with increasing $SrSnO_3$ content, as indicated in Table 7.4. It has been reported that the structures of the *P* and *R* phases show strong similarities and the atomic displacements in the *R* phase are smaller compared to those in the *P* phase [71, 164]. Since the orthorhombic lattice distortion is mainly caused by the atomic displacements within the *ab* plane, it essentially reflects the magnitude of the atomic displacement. As the $SrSnO_3$ content increases, the *P* phase structures become more similar to those of the *R* phase in the sense that the lattice distortion decreases, bringing the *P*−*R* phase transition temperature $T_{P–R}$ closer to room temperature. The correlation between the *P*−*R* phase transition temperature $T_{P–R}$ and the orthorhombic lattice distortion is nicely illustrated in Figure 7.10.

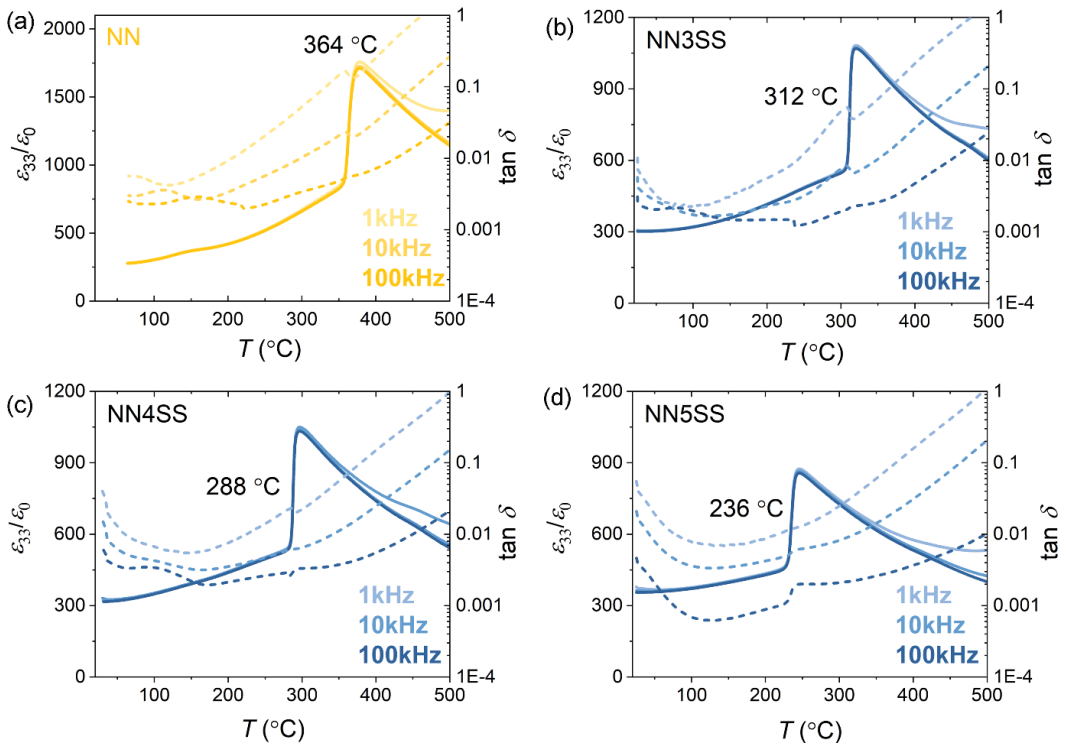

Figure 7.9: Temperature dependence of (a) dielectric constant and (b) loss tangent for $NaNbO_3$, NN3SS, NN4SS, NN5SS, and NN6SS ceramic samples in the virgin state, measured at 1−100 kHz.

Table 7.4: Orthorhombic lattice distortion (*b*/*a*) calculated from the refined lattice constants of $NaNbO_3$, NN3SS, NN4SS, and NN5SS ceramic samples.

	NN	NN3SS	NN4SS	NN5SS
b (Å)	5.5653	5.5635	5.5624	5.5618
a (Å)	5.5031	5.5094	5.5112	5.5144
b/*a*	1.0113	1.0098	1.0093	1.0086

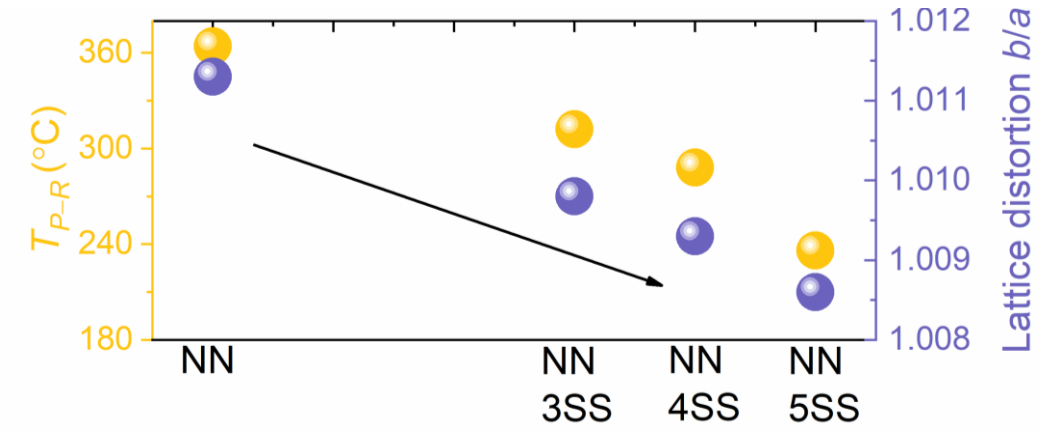

Figure 7.10: The *P*−*R* phase transition temperature T_{P-R} and the orthorhombic lattice distortion *b*/*a* within the *ab* plane of $NaNbO_3$, NN3SS, NN4SS, and NN5SS ceramic samples. The arrow highlights the trend that both parameters decrease with increasing $SrSnO_3$.

In addition to the change in T_{P-R}, the permittivity maximum at the *P*−*R* phase transition (at 10 kHz) decreases significantly from about 1726 for $NaNbO_3$ to 1073 for NN3SS, a decrease of 38%. Moreover, the permittivity maximum of the $SrSnO_3$-substituted samples decreases with increasing $SrSnO_3$ content. However, the permittivity value at 60 °C (at 10 kHz) increases from 277 for $NaNbO_3$ to 304 for NN3SS (the permittivity value of $NaNbO_3$ at room temperature was not recorded). Moreover, the room temperature permittivity value increases with increasing $SrSnO_3$ content, as shown in Figure 7.9. The increased room temperature permittivity value in the solid solutions could be related to the reduced lattice distortions, as reported for ferroelectric niobates [165]. The dielectric anomaly observed at about 150 °C for $NaNbO_3$ (Figure 7.9a) vanishes for the $SrSnO_3$-substituted samples. However, the frequency dispersion is evident for NN3SS and can still be observed for NN4SS. For NN5SS, the frequency dispersion disappears completely. The frequency dispersion in pure $NaNbO_3$ is associated with the dielectric anomaly (Figure 5.8), the origin of which has already been discussed in Chapter 5. Koruza *et al.* [134] suggested that this anomaly is related to the dynamics of ferroelectric nanoregions. However, since both pure $NaNbO_3$ and solid solutions have the centrosymmetric *Pbcm* structure in the virgin state, it is unclear whether ferroelectric nanoregions are present in these materials and needs further investigation. However, it cannot be ruled out that the frequency dispersion is due to the polarization mechanism related to the thermally activated conduction of mobile ions and/or other defects. Ding *et al.* [139] found that the density of APBs decreases with increasing $SrSnO_3$ content. Note that APBs are a type of planar defects reported in ferroelectrics [142], but whether and how the APBs can affect the dielectric properties needs further research. In addition, Ding *et al.* [139] also investigated the domain morphology of pure $NaNbO_3$ and a series of $SrSnO_3$-substituted $NaNbO_3$ ceramics. It was found that the domain structures in the solid solutions are significantly different from those of $NaNbO_3$. The domain blocks with obvious streaking features in $NaNbO_3$ disappear after the introduction of $SrSnO_3$. NN5SS exhibits a well-defined domain structure with sharp domain boundaries. The dielectric properties may also depend on the microstructural changes in the solid solutions, which requires further systematic studies and is beyond the scope of this work.

7.5 Mn-Modified NN5SS Composition

7.5.1 Field-Induced Phase Transition at Room Temperature

Despite the reversible AFE−FE phase transition observed in the $SrSnO_3$-substituted samples, the double polarization hysteresis loops are characterized by a large remanent polarization. As a result, the energy storage density and efficiency are low, making them unsuitable for high-energy storage applications. Moreover, the best composition, NN5SS, cannot withstand high and/or long-term electric field exposure to electric fields. For example, the ceramic samples break easily after a few electric field cycles when the AFE−FE phase transition is triggered. This makes it difficult to study the frequency and temperature dependence of the field-induced phase transitions. In addition, the weak samples are very likely to break when exposed to an electric field under X-ray irradiations, making *in situ* characterization of the structure impossible. The origins of the dielectric breakdowns are unclear, but may be related to the large remanence reflected in the polarization hysteresis loops and related to leakage current and/or mobile defects. For this reason, the NN5SS composition was further modified by Mn. In alkali niobates, it has been demonstrated that the addition of Mn can suppress the leakage current by 3~4 orders of magnitude [166, 167] and tune the defect chemistry in the system due to the multi-valence states of Mn [166-168].

Different amounts of MnO_2 (0.1 wt.%, 0.5 wt.%, 1.0 wt.%, and 2.0 wt.%) were added to the powder mixture after the calcination process and these compositions are abbreviated as NN5SS_0.1Mn, NN5SS_0.5Mn, NN5SS_1.0Mn, and NN5SS_2.0Mn, respectively. Well-defined double polarization hysteresis loops with minimal remanent polarization are observed for the Mn-modified NN5SS samples, as featured in Figure 7.11. The remanent polarization decreases significantly from 13.9 $\mu C/cm^2$ for NN5SS to about 3.5 $\mu C/cm^2$ for the Mn-modified NN5SS samples, which corresponds to a 75% decrease. The remanent polarization of 3.5 $\mu C/cm^2$ is close to that of $AgNbO_3$ [169, 170] and the model $(Pb,La)(Zr,Ti,Sn)O_3$ system (~4 $\mu C/cm^2$) [171]. The asymmetric strain hysteresis loop of NN5SS is not present in the Mn-modified samples, which exhibit symmetric loops. Moreover, the negative strain decreases from −0.027% for NN5SS to −0.010% for NN5SS_0.1Mn, indicating that the contribution of non-180° domain switching and converse piezoelectricity is suppressed in the Mn-modified materials.

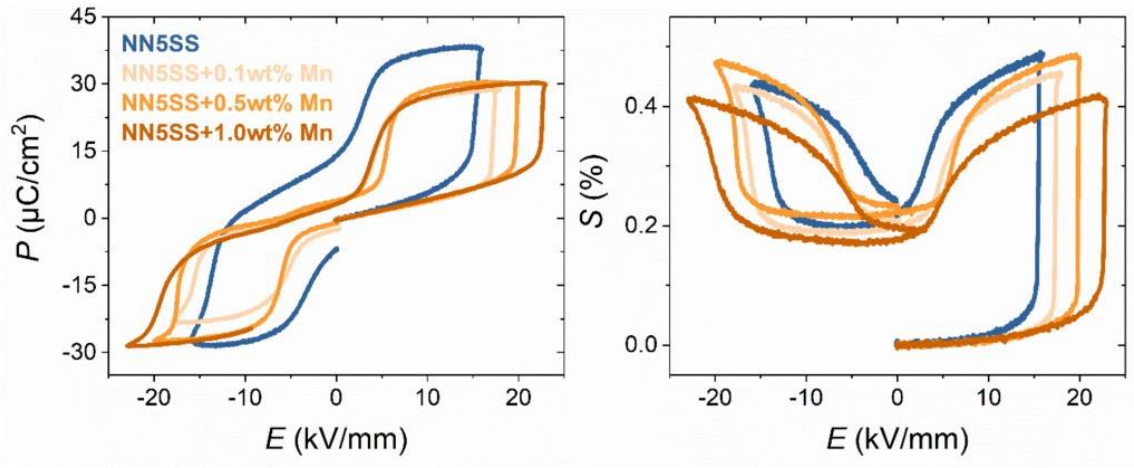

Figure 7.11: (a) Polarization and (b) strain hysteresis loops of NN5SS ceramic samples modified with different amounts of Mn (0.1 wt.%, 0.5 wt.%, and 1.0 wt.%) in the first electric cycle, measured at 1 Hz and room temperature.

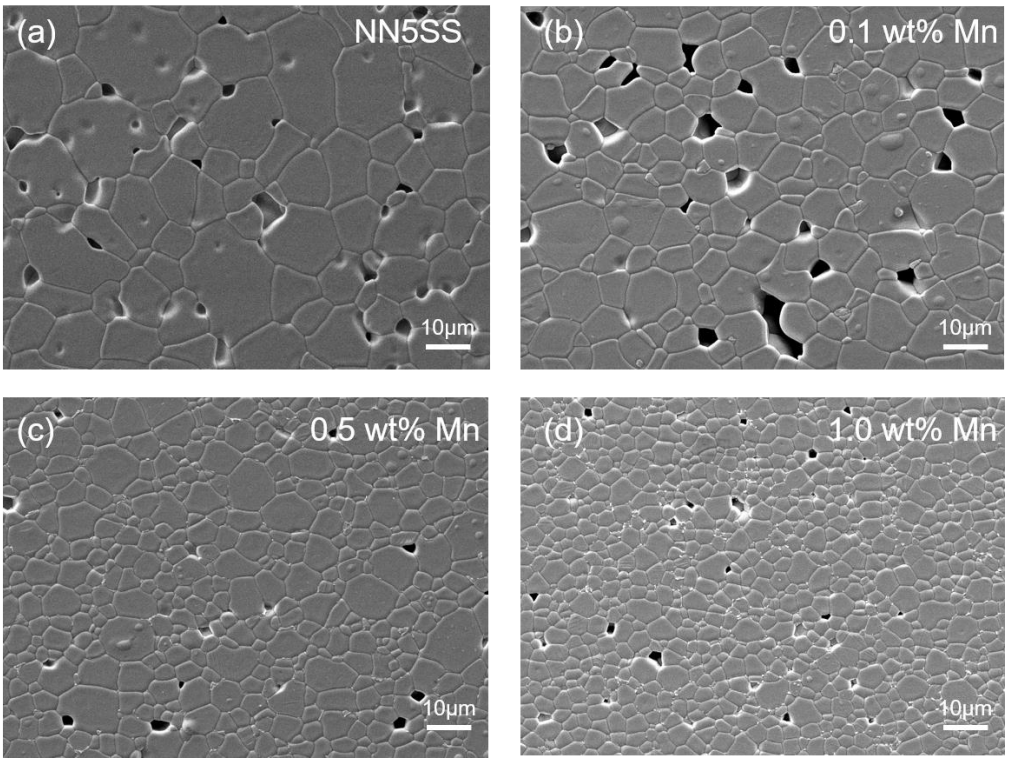

Figure 7.12: SEM images of the thermally etched surfaces of (a) NN5SS and the NN5SS samples modified with (b) 0.1 wt.%, (c) 0.5 wt.%, and (d) 1.0 wt.% Mn.

The critical field E_F of the Mn-modified samples is higher than that of NN5SS and E_F increases with increasing Mn content. Considering the minor changes in compositions due to the addition of Mn, the increased critical fields are attributed to the decreased average grain sizes in the Mn-modified samples, as has been reported for other antiferroelectric niobates [172]. The average

grain size decreases with increasing Mn content, as demonstrated in Figure 7.12. Similar effects have been reported for $BaTiO_3$ [173], $BiFeO_3$ [174], and $SrTiO_3$ [175] systems. It is hypothesized that the addition of Mn alters the defect chemistry, which in turn affects the mass-transport mechanism and hence the grain growth processes in the system.

In addition to the differences in E_F, the FE−AFE phase transition for NN5SS_1.0Mn occurs at a lower electric field than for the other two compositions. In $PbZrO_3$-based antiferroelectrics, it has been demonstrated that the FE−AFE transition field can be considered as a driving force for the restoration of the AFE state [67]. Despite the reversible AFE−FE phase transition, the slightly decreased FE−AFE phase transition field in the NN5SS_1.0Mn composition suggests that a small amount of Mn addition is helpful for observing double polarization hysteresis loops, while excessive Mn addition can stabilize the FE order. The NN5SS_2.0Mn sample exhibits polarization hysteresis loops characteristic of ferroelectric properties, as shown in Figure 7.13. Detailed Rietveld refinement analyses show that the average structure of NN5SS_1.0Mn is well described by the *Pbcm* space group, while that of NN5SS_2.0Mn is better described by the $P2_1ma$ space group. The representative high-angle reflections of all Mn-modified NN5SS ceramic samples are highlighted in Figure 7.14. It can be seen that NN5SS_0.1Mn, NN5SS_0.5Mn, and NN5SS_1.0Mn display the same peak splittings characteristic of the *Pbcm* space group. However, no peak splittings are observed for NN5SS_2.0Mn. Therefore, the critical amount of Mn modification that can convert NN5SS from the AFE state to the FE state is between 1.0 wt.% and 2.0 wt.%. Overall, the behavior of the field-induced phase transition is similar for all Mn-modified compositions except NN5SS_2.0Mn. More importantly, all Mn-modified samples can withstand stronger electric fields but are less likely to fail, even when subjected to very high electric fields exceeding 20 kV/mm (Figure 7.11).

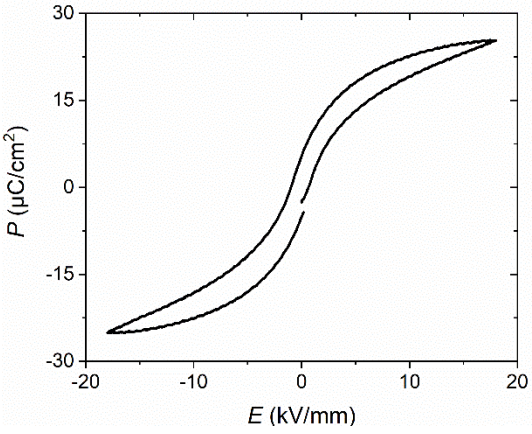

Figure 7.13: Polarization and (b) strain hysteresis loops of NN5SS ceramic samples modified with 2.0 wt.% Mn, measured at 1 Hz and room temperature.

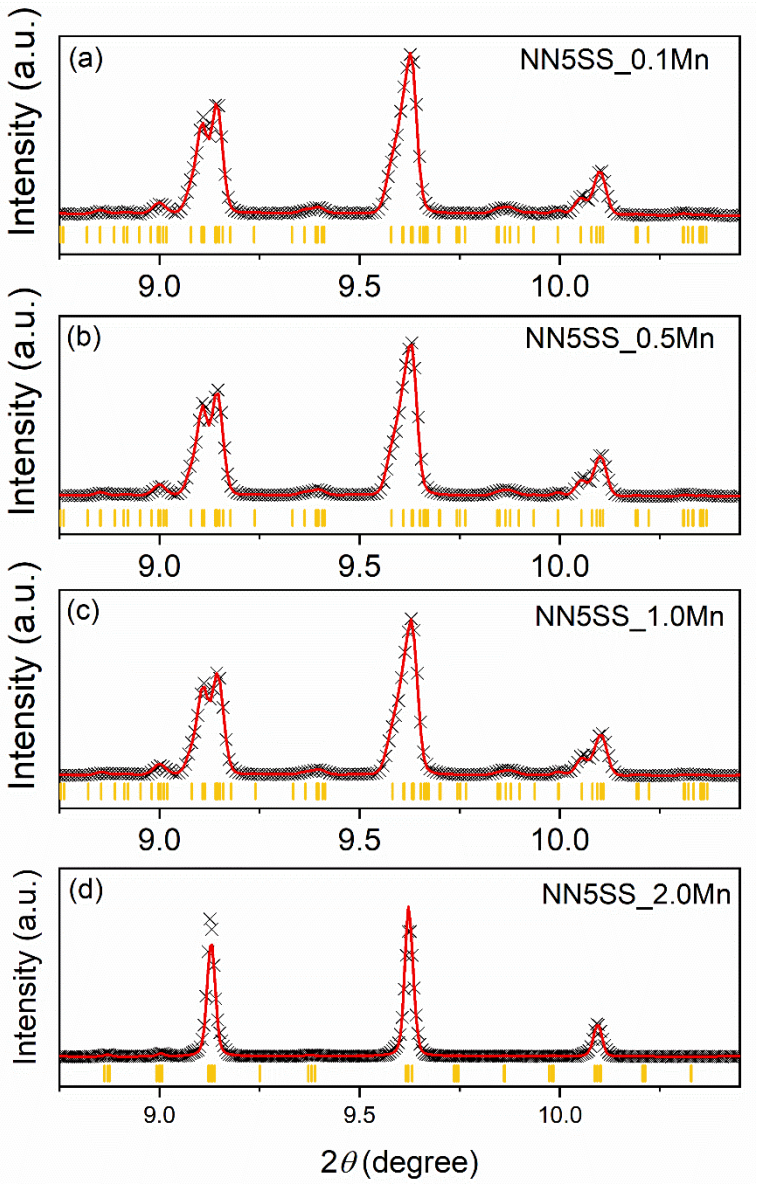

Figure 7.14: Magnified views of representative high-angle main reflections of (a) NN5SS_0.1Mn, (b) NN5SS_0.5Mn, (c) NN5SS_1.0Mn, and (d) NN5SS_2.0Mn ceramic samples in the virgin state. The structure of the first three compositions is well described by the *Pbcm* space group, while the structure of the last composition is better described by the $P2_1ma$ space group. The reflections associated with the two structures are indicated by the yellow tick marks.

7.5.2 *In situ* Synchrotron XRD Characterization of the Phase Transition

In Chapter 6, it has been demonstrated that the macroscopic mechanical and electrical changes observed in stage 3 in pure $NaNbO_3$ are mainly due to ferroelectric switching rather than a field-induced phase transition (Figure 6.5). To determine whether the double polarization hysteresis loops observed for the Mn-modified compositions are caused by a field-induced AFE−FE phase transition, the NN5SS_0.1Mn composition was selected for detailed *in situ* high-energy XRD

characterizations. The patterns of the samples before they were exposed to an electric field can be satisfactorily refined to reasonable R_w values of about 0.06, as displayed in Figure 7.15. The good agreement is illustrated by the representative superlattice reflections and high-angle main reflections, which show excellent agreement between the observed and calculated patterns. This implies that the *Pbcm* space group and the average structure of NN5SS are preserved in NN5SS_0.1Mn. The calculated orthorhombic lattice distortion of NN5SS_0.1Mn (1.0087) is very close to that of NN5SS (1.0086), as listed in Table 7.5.

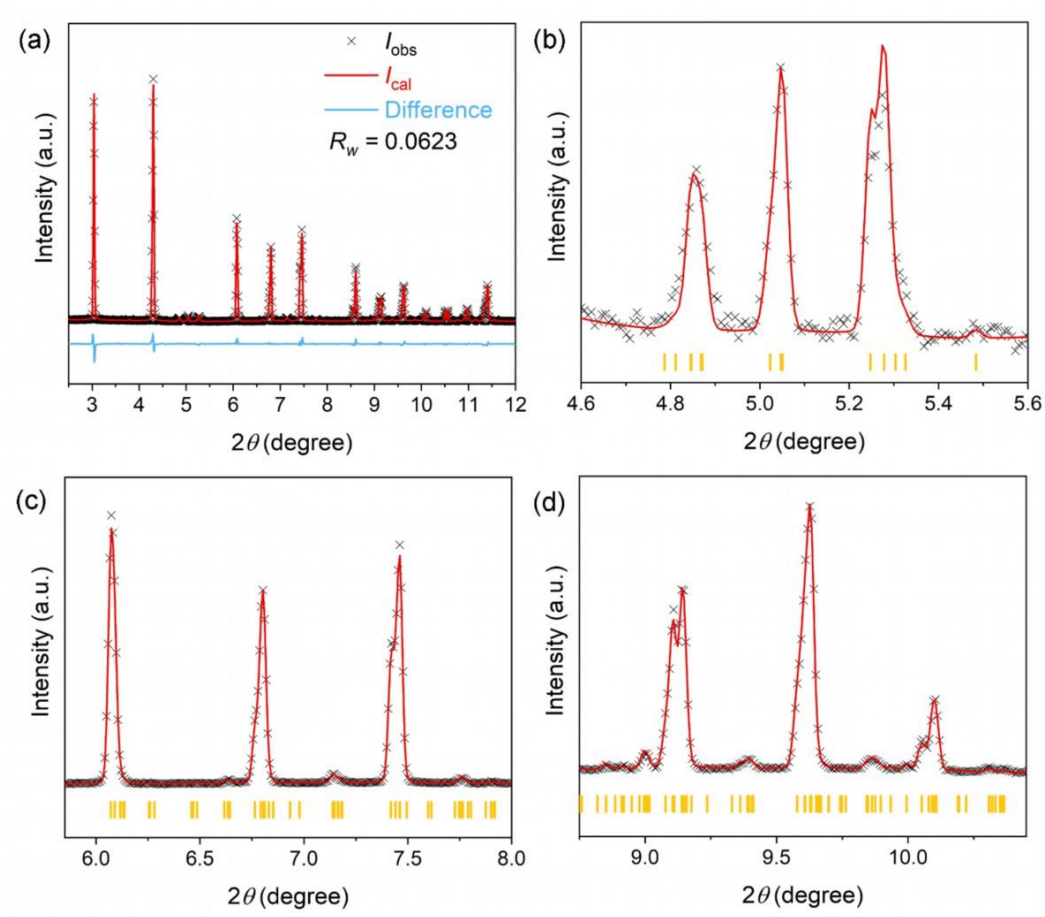

Figure 7.15: (a) Rietveld refinement of the high-energy XRD pattern of the NN5SS sample modified with 0.1 wt.% Mn in the virgin state using the *Pbcm* space group. Magnified views of (b) representative superlattice reflections and (c-d) high-angle main reflections. Reflections associated with the *Pbcm* structure are shown by the yellow tick marks. The starting parameters of the *Pbcm* model for the refinement were taken from the refinements of the NN5SS ceramic sample in this work.

Table 7.5: Lattice constants and orthorhombic lattice distortion (b/a) calculated from the refined lattice constants of $NaNbO_3$, NN5SS, NN5SS_0.1Mn, NN5SS_0.5Mn, and NN5SS_1.0Mn ceramic samples.

	NN	NN5SS	NN5SS_0.1 Mn	NN5SS_0.5 Mn	NN5SS_1.0 Mn
a (Å)	5.5031	5.5144	5.5151	5.5144	5.5135
b (Å)	5.5653	5.5618	5.5633	5.5625	5.5614
c (Å)	15.5387	15.6191	15.6168	15.6166	15.6151
b/a	1.0113	1.0086	1.0087	1.0087	1.0087

Selected main reflections and superlattice reflections as a function of electric field increasing from 0 to 18 kV/mm are provided in Figure 7.16. Below ~16.5 kV/mm, no obvious changes were observed in either type of reflections, indicating that no structural or microstructural changes were induced at this stage by the application of an electric field. Therefore, the cell parameters do not show significant changes, as revealed in Figure 7.17. Thereafter, the field-induced AFE−FE phase transition occurred, which was accompanied by significant changes in both the main reflections and superlattice reflections. In particular, the $¼843_{PC}$ reflection representing the AFE order became weaker, while the intensity of the $½312_{PC}$ reflection increased. The latter is a reflection characteristic of the FE Q phase [50] and therefore represents the FE order. The AFE−FE phase transition was associated with a large increase in a_{PC} (b_{PC}), γ angle, and cell volume, and a slight decrease in c_{PC}. The cell volume increases from 59.89 $Å^3$ to 60.05 $Å^3$, corresponding to a volume strain of 0.27%. A schematic representation of the crystallographic structures in the virgin AFE state and in the field-induced FE state can be found in Figure 7.17c. Both Na and Nb exhibit antiparallel atomic shifts along the y-direction. In the field-induced FE state, both ions need to have a larger atomic displacement along this direction, i.e., the primitive cells will expand along this direction. As a result, an increase in a_{PC} (b_{PC}) and γ is expected.

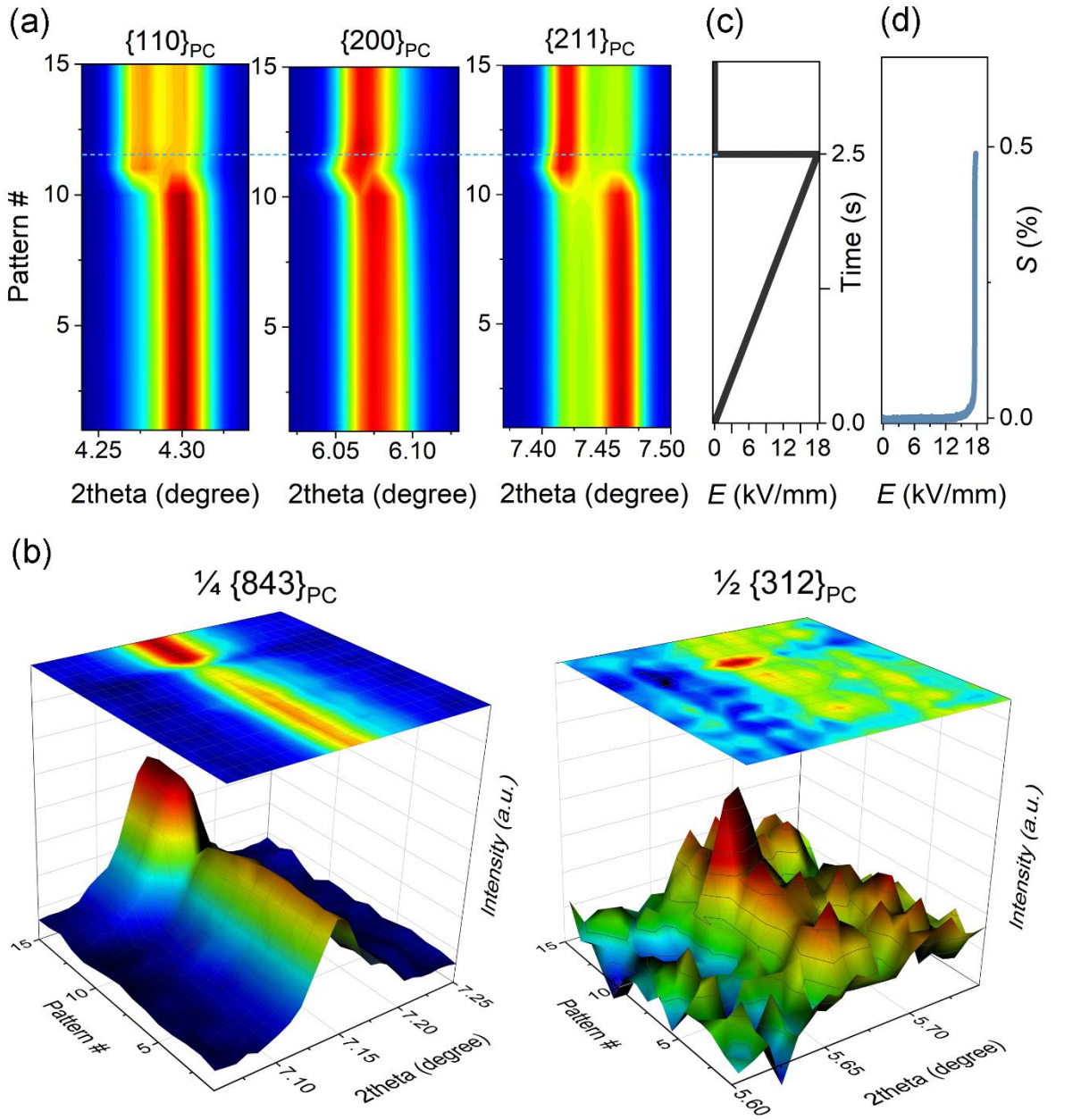

Figure 7.16: Contour plots of (a) primary reflections and (b) three-dimensional surface maps of superlattice reflections of the NN5SS_0.1Mn ceramic sample during the field-induced phase transition. (c) A unipolar electric field of 18 kV/mm was applied within 2.5 s. (d) Longitudinal strain (S_{33}) recorded simultaneously with the *in situ* synchrotron measurement.

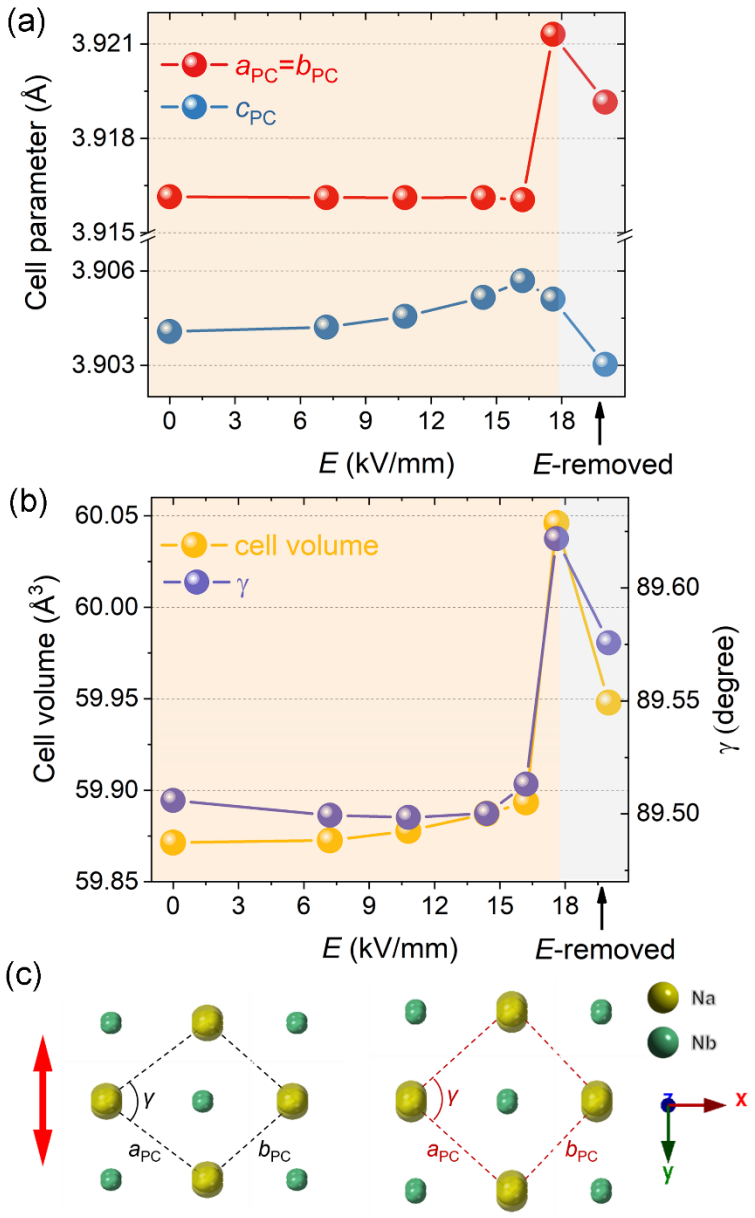

Figure 7.17: (a) Pseudocubic lattice parameters and primitive cell volume as a function of electric field during the field-induced phase transition and after removal of the field, determined by LeBail fitting using a single-phase model. (b) Schematic representation of the crystallographic structure of the studied material in the virgin state (black dashed lines) and in the field-induced FE state (red dashed lines), viewed along the $[001]_{PC}$ direction. The orientation of the double-headed arrow represents the direction of antiparallel atomic displacement of Na and Nb atoms.

The presence of a phase transition was complemented by the longitudinal strain recorded simultaneously with the measurement of synchrotron data and a large strain of 0.5% was observed. The above results undoubtedly confirm that the double polarization hysteresis loops observed for the NN5SS_0.1Mn composition are caused by the field-induced AFE−FE phase transition. More importantly, the intensity of the $¼843_{PC}$ reflection increases, while that of the $½312_{PC}$ reflection decreases after the electric field is removed, as revealed in Figure 7.16b. This

indicates that the AFE order is stabilized again and the FE order is suppressed after the electric field is removed, which establishes the structural basis of the reversible phase transition. Although none of the cell parameters return to their original values, it is very clear that the remanent state after removal of the electric field is different from the field-induced FE state, as feature in Figure 7.17. The calculated orthorhombic lattice distortions of the NN5SS_0.1Mn sample are given in Table 7.6. The lattice distortion decreases from 1.0087 in the AFE state to 1.0066 in the field-induced FE state, which increases to 1.0074 in the remanent state. The smaller lattice distortion in the field-induced FE state is due to the larger atomic displacements of the Na ions along the *y* direction. However, the detailed atomic positions in the FE state are missing because the Rietveld refinement cannot be applied. Instead, the reduced lattice distortion can be justified by the increased γ angle, which is closer to 90° in the FE state. Due to the larger atomic displacements of the Na ions in the FE state, the two in-plane orthorhombic lattice constants are closer, leading to a smaller lattice distortion. In pure $NaNbO_3$, the lattice distortion decreases from 1.0115 in the AFE state to 1.0101 in the FE state (Table 7.6), but it remains the same after the electric field is removed (Figure 6.7), providing the structural basis for the irreversible phase transition. Interestingly, the intensity of the ¼843$_{PC}$ reflection is even stronger in the remanent state compared to the virgin state, which is attributed to the textured state of the sample after exposure to the electric field. The slightly larger a_{PC} and γ angle in the remanent state compared to those in the virgin state also indicate that the ceramic sample develops macroscopic polarization due to the oriented atomic displacements within the *ab* plane and is therefore no longer isotropic. Note that the remanent polarization determined from the double polarization hysteresis loops is also a nonzero value (~3.5 μC/cm^2).

Table 7.6: Orthorhombic lattice distortion (*b*/*a*) calculated from the refined lattice constants of $NaNbO_3$ in the AFE and FE states, and NN5SS_0.1Mn in the AFE, FE, and remanent states. The results of the AFE state are based on Rietveld refinement, while those of the FE and remanent states are based on Lebail fitting, as the ceramic sample is not isotropic after exposure to the electric field.

	NN (AFE)	NN (FE)	NN5SS_0.1Mn (AFE)	NN5SS_0.1Mn (FE)	NN5SS_0.1Mn (remanent)
b (Å)	5.5035	5.5155	5.5633	5.5272	5.5220
a (Å)	5.5665	5.5715	5.5151	5.5638	5.5630
b/*a*	1.0115	1.0101	1.0087	1.0066	1.0074

7.5.3 Discussion of the Effect of Mn

Given the volatilization of alkali species during high temperature sintering [176], alkali vacancies at the perovskite *A* site are created inevitably in alkaline niobates. First-principles calculations have shown that the formation energy of the Na vacancy in $NaNbO_3$ is the lowest among all point defects [177]. The presence of alkali vacancies has been experimentally demonstrated in $NaNbO_3$ and $(K,Na)NbO_3$ bulk ceramics [178, 179], single crystals [180, 181], and thin films [182]. The formation of sodium vacancies is expressed by the following equation in Kröger-Vink notation:

$$Na_{Na}^{X} \rightarrow V_{Na}' + h^{\bullet} \qquad 7\text{–}1$$

where the hole is represented by $h^{\bullet}$. In addition, oxygen vacancies [183, 184] and the multiple oxidation states of the B-site Nb ions [180] are expected in the ceramic materials:

$$O_O \rightarrow V_O^{\bullet\bullet} + \frac{1}{2}O_2 + 2e' \qquad 7\text{–}2$$

$$Nb(IV) \xrightarrow{Nb(V)} Nb(IV)_{Nb}' + h^{\bullet} \qquad 7\text{–}3$$

Therefore, the high remanence of the NN5SS ceramic sample (Figure 7.7) can be attributed to two reasons: (1) a high leakage current; (2) the presence of defects and/or defect dipoles that become mobile upon application of an electric field, resulting in an increased polarization. However, the polarization hysteresis loops of NN5SS appear to consist of a limited contribution of leakage current, otherwise such a high electric field of ~15 kV/mm could hardly be applied. The frequency dependence of the dielectric loss of NN5SS and all Mn-modified NN5SS ceramic samples is revealed in Figure 7.18. The loss tangent of the NN5SS sample increases significantly from 0.011 at 1 Hz to 0.19 at 0.01 Hz, which is a 17-fold increase. Although the dielectric loss of the Mn-modified samples increases with decreasing frequency, they exhibit much smaller loss tangent values compared to the NN5SS sample. It has been shown that dielectric relaxations in ferroelectrics usually occur at low frequencies due to ionic space-charge carriers, such as the oxygen vacancies and defects generated during high temperature sintering, as well as interfacial polarizations located at the grain boundary or at the sample-electrode interface [185]. The observed differences cannot be attributed to the interfacial polarizations, since the average grain sizes are comparable and the electrode is the same for all ceramic samples studied. Since metal vacancies are tend to be immobile, the dielectric relaxation observed at low frequencies is much more likely to be due to the movement of oxygen vacancies

[186]. More importantly, it has been demonstrated in ferroelectrics that the addition of Mn can help to consume oxygen vacancies [187]:

$$Mn^{2+} + V_O^{\bullet\bullet} \rightarrow Mn^{4+} \qquad 7\text{–}4$$

Moreover, the effective drift mobility of oxygen vacancies would decrease with the increasing probability of encountering Mn-modified unit cells during their transport [187]. Therefore, the presence of mobile oxygen vacancies is thought to be responsible for the strong dielectric relaxation observed in the NN5SS sample at low frequencies. After Mn modification, the concentration of oxygen vacancies is expected to be reduced, as evidenced by the reduced loss tangent at low frequencies for the Mn-modified samples. As a result, the Mn-modified samples can be exposed to high and/or long-term electric fields.

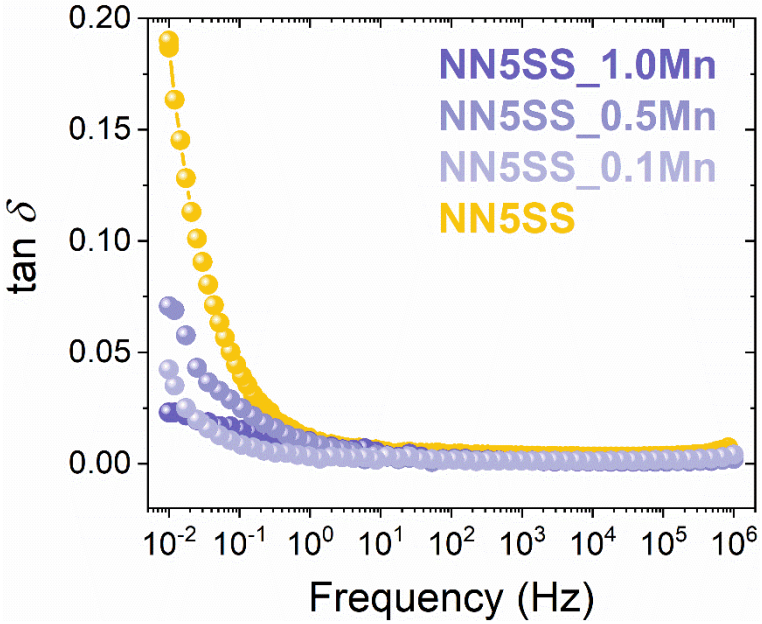

Figure 7.18: Frequency dependence of (a) dielectric permittivity and (b) loss tangent of NN5SS, NN5SS_0.1Mn, NN5SS_0.5Mn, and NN5SS_1.0 ceramic samples.

The frequency dependence of the polarization and strain hysteresis loops of the NN5SS_0.1Mn sample is shown in Figure 7.19. It can be seen that the polarization hysteresis loops measured at a frequency of 0.5−20 Hz are almost frequency independent, while the loop measured at 0.1 Hz is characterized by a much larger hysteresis and a much higher remanent polarization value. It should be noted that the lossy part can be observed only in the field-induced FE state and not in the AFE state, i.e., the polarization loop at 0.1 Hz follows the linear regime part like other loops and starts to show a deviation after the AFE−FE phase transition is triggered. This behavior agrees well with the observations in ferroelectrics that the polarization contribution of defect dipoles is activated at low frequencies [185, 188]. The antiparallel polarizations are

expected to cancel each other out in the AFE state (although this may be not perfectly the case in reality), leading to a much lower interaction between the AFE domains and defects, which are less likely to migrate when the field-induced phase transition is not triggered. The field-induced strain decreases slightly with increasing frequency, which was also observed for pure $NaNbO_3$ (Figure 5.4b). The exposure time to the applied electric field decreases with increasing frequency, and thus the field-induced FE state is less saturated at the maximum field at a high frequency than at a low frequency, leading to the slightly decreased strain values. Note that the decrease in maximum polarization with increasing frequency is less significant compared to the decrease in strain. The different frequency dependences of polarization and strain suggest that the two properties have a different origin. Forst *et al.* [66] suggested that the polarization response is mainly caused by the field-induced phase transition, while the strain is closely related to the domain switching.

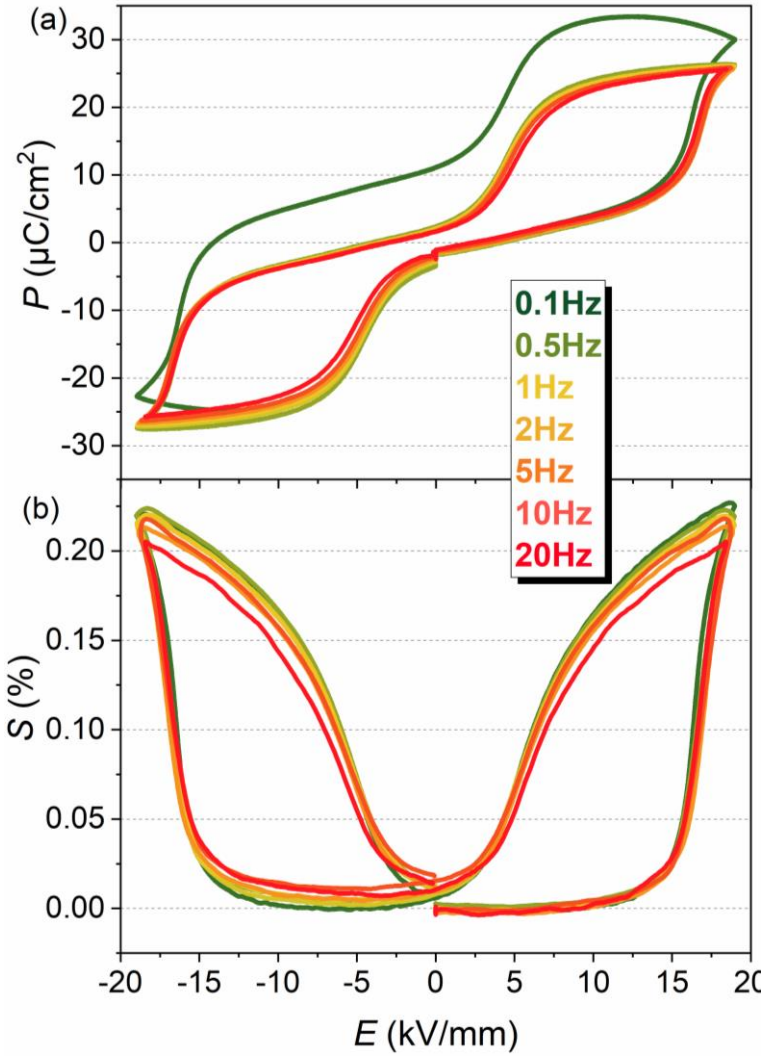

Figure 7.19: Frequency dependence of (a) polarization and (b) strain hysteresis loops of the NN5SS_0.1Mn ceramic sample.

7.5.4 Temperature Dependence of the Phase Transition

The NN5SS_0.5Mn ceramic sample was selected to study the temperature dependence of the field-induced AFE−FE phase transition. The temperature dependence of the polarization hysteresis loops is shown in Figure 7.20(a). Well-defined double polarization hysteresis loops were observed over a wide temperature range of 25−150 °C, with minimal change in the values of maximum and remanent polarization. Interestingly, the maximum and remanent polarization of $NaNbO_3$ are also insensitive to temperature changes (Figure 5.6). The critical field decreases with increasing temperature at a rate of dE_F/dT = −0.020 kV/mm·deg, as featured in Figure 7.20(b). The rate is about half that of $NaNbO_3$ (−0.039 kV/mm·deg) and much lower than that of $PbZrO_3$ (−0.17 kV/mm·deg). It has been demonstrated that the sharp increase in polarization in $NaNbO_3$ at the critical field is caused by domain switching (Figure 6.5), which is facilitated at elevated temperatures. However, the changes at the critical field of both $PbZrO_3$ and Mn-modified NN5SS samples are attributed to a field-induced AFE−FE phase transition. The different temperature dependences of the critical field can be explained by the different temperature dependences of the energy barrier in the two systems, which must be overcome for the phase transition to occur. The field-induced phase transition of $PbZrO_3$ could only be triggered in a narrow temperature range close to the Curie point (~235 °C) and should therefore be more temperature sensitive. As a result, the rate of temperature dependence of $PbZrO_3$ is much higher than that of the Mn-modified NN5SS material.

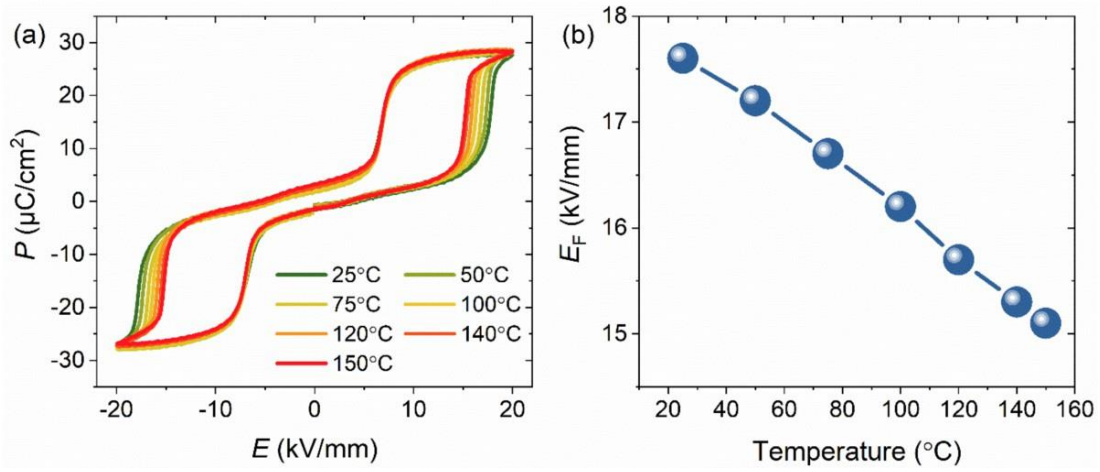

Figure 7.20: (a) Temperature dependence of the polarization hysteresis loops of the NN5SS_0.5Mn ceramic sample. (b) The scaling behavior of the critical field E_F versus temperature, based on the data obtained from (a). The critical electric field, E_F, is defined as the electric field at which polarization reaches half of the maximum polarization value. Based on the linear regression analysis of the E_F as a function of temperature, a slope of dE_F/dT = −0.020 kV/mm·deg is determined.

7.5.5 Energy Storage Properties

The energy storage density and efficiency data for $NaNbO_3$, NN5SS, and selected Mn-modified NN5SS materials (NN5SS_0.5Mn) are highlighted in Figure 7.21. The energy storage density increases from 0.12 J/cm^3 for $NaNbO_3$ to 0.90 J/cm^3 for NN5SS because the irreversible AFE−FE phase transition for $NaNbO_3$ changes to a reversible one for NN5SS. However, the energy storage efficiency of NN5SS is only 21.4% due to the large remanent polarization and hysteresis. The energy storage density increases from 0.90 J/cm^3 for NN5SS to 1.82 J/cm^3 for NN5SS_0.5Mn, which is a 2-fold increase. The efficiency of the NN5SS_0.5Mn sample increases to 41%, because the remanent polarization is significantly reduced from 13.9 μC/cm^2 for NN5SS to about 3.5 μC/cm^2 for the Mn-modified sample. As a result of the temperature stable polarization hysteresis loops (Figure 7.20), both the density and efficiency are temperature independent and maintain high and stable values over a wide temperature range from room temperature to 150 °C.

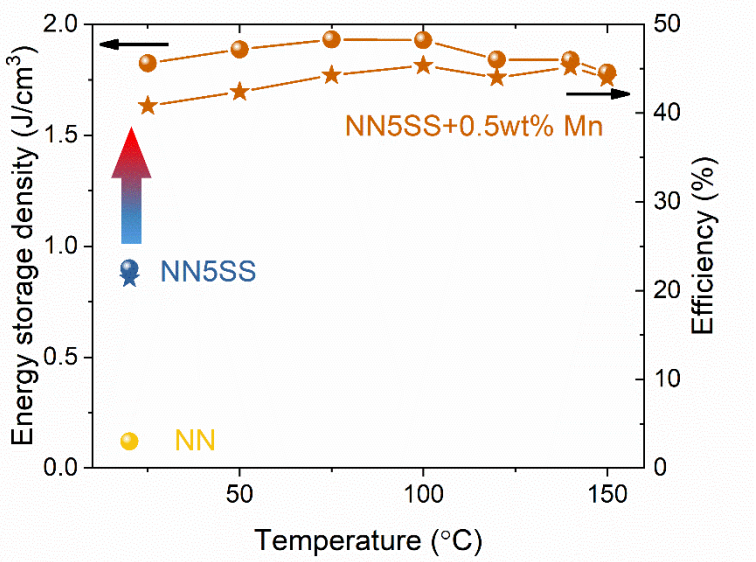

Figure 7.21: Energy storage density and efficiency of $NaNbO_3$, NN5SS, and NN5SS_0.5Mn ceramic samples, determined from the bipolar polarization hysteresis loops.

7.6 Summary

Our first-principles calculations show that the introduction of 6.25 mol% $SrSnO_3$ stabilizes the antiferroelectric order by 1.4 meV/f.u. in the new system, while the ferroelectric order is energetically more favored in $NaNbO_3$. A series of $SrSnO_3$-substituted ceramic samples were prepared and their structure, microstructure, and electrical properties were investigated. The

irreversible nature of the AFE−FE phase transition of $NaNbO_3$ is successfully adapted to be reversible after the substitution of $SrSnO_3$. The stabilization of the AFE order (alternatively the suppression the of FE order) in the newly developed $(1-x)NaNbO_3$-$xSrSnO_3$ materials was evidenced by the appearance of double polarization hysteresis loops and a significantly suppressed macroscopic piezoelectricity d_{33} after the removal of the electric field. The global structure of the new compositions is close to that of $NaNbO_3$ and can be well described by the *Pbcm* structure. A less distorted local structure of the Na(1) site and a lower orthorhombic lattice distortion were revealed, and their influence on the reversibility of the field-induced phase transition is discussed.

Due to its large remanence and poor dielectric breakdown strength, NN5SS was further modified by Mn. Well-defined double loops with a minimum remanent polarization of ~3.5 $\mu C/cm^2$ were obtained. A selected Mn-modified composition was chosen to study the field-induced AFE−FE phase transition using *in situ* synchrotron XRD. The structural basis of the reversible phase transition was clarified and compared with the irreversible phase transition in $NaNbO_3$. The rigid structures of the Mn-modified NN5SS, where the atomic displacements of Na ions are nearly 70% smaller, are expected to provide a restoring force for the reversible phase transition. It is assumed that the addition of Mn suppresses the formation of oxygen vacancies and their mobility under the electric field. As a result, a high energy storage density of 1.82 J/cm^3 is achieved, which a 15-fold increase over that of pure $NaNbO_3$. More importantly, the high energy storage property is stable over a wide temperature range, making it a promising candidate for high temperature capacitor applications.

8 Conclusion and Outlook

The present work started with a benchmark study of the field-induced phase transition in pure $NaNbO_3$. A huge strain of 0.65% and a large macroscopic polarization were recorded only above a critical electric field, indicating a phase transition from AFE to FE. The significant state change was accompanied by an irreversible change in average structure, local chemical environment of the sodium site, and domain morphology. However, a detailed *in situ* synchrotron XRD study revealed that the large volume change corresponds to a domain switching process that is decoupled from the field-induced AFE−FE phase transition process. Such decoupling phenomenon differs from the decoupling behavior previously reported for lead-based antiferroelectrics, i.e., the polarization and strain responses are not synchronized.

To achieve a reversible phase transition, a compound, $SrSnO_3$, was proposed to be alloyed with $NaNbO_3$, and its functionality in stabilizing the AFE order was validated by first-principles calculations. As a result, a new type of $NaNbO_3$-based antiferroelectric polycrystalline ceramic materials with a reversible field-induced AFE to FE phase transition was developed and further modified by Mn to tune the defect chemistry. The reversibility of the phase transition was evidenced by characteristic double polarization hysteresis loops and *in situ* synchrotron XRD characterization of the reversible structural changes. The attending reversible phase transition differs from the irreversible phase transition in the prototype antiferroelectric $NaNbO_3$, where the ferroelectric order is preserved upon being induced by the electric field. As a result, the newly developed material has a high energy storage density of 1.82 J/cm^3, which is 15 times higher than that of pure $NaNbO_3$. The structural basis for the reversibility of the phase transition is attributed to the rigid structure of the antiferroelectric phase, which can be associated with a 70% lower atomic displacement of the new material compared to that of pure $NaNbO_3$.

From an experimental point of view, there are several questions regarding the field-induced AFE−FE phase transition and its associated functionalities that remain to be understood and clarified. First, if the decoupling phenomenon observed in pure $NaNbO_3$ is the result of polycrystallinity and first-order nature of the phase transition, it would be interesting to study the field-induced phase transition at different frequencies. Vales-Castro *et al.* recorded a AFE−FE phase boundary moving across the sample during a field-induced phase transition in $PbZrO_3$ [153]. The hypothesis is that if the phase boundaries are given sufficient time to relax during the phase transition, the buildup of internal mechanical stresses and thus the decoupling behavior can be alleviated.

Second, it has been demonstrated for $PbZrO_3$-based [3] and $AgNbO_3$ [170] antiferroelectrics that the dielectric permittivity increases with increasing electric field up to the critical field. This functionality is not present in ferroelectrics and makes antiferroelectrics highly desirable for high density power electronic systems. However, such behavior is not observed for the materials studied in this work. Moreover, to our knowledge, it has not yet been reported for any $NaNbO_3$-based antiferroelectric materials. Our studies (Figure 5.12) have shown that such behavior is not always observed even for $PbZrO_3$-based antiferroelectrics. The hypothesis is that the compositions of the material should be tuned to meet certain criteria, e.g., the phase compositions should be tuned to be close to a tricritical point where the metastable ferroelectric, antiferroelectric, and paraelectric phases merge [7].

For the design of next-generation antiferroelectric materials, existing approaches are mainly based on empirical rules, and a systematic understanding of the delicate competition between the AFE and the FE order needs to be further explored. In this work, it has been shown that a complete picture of the composition, defect chemistry, local chemical environment, average crystallographic structure, and microstructure are important parameters that define the functional properties of antiferroelectrics. With the advent of advanced first-principles methods, the electronic structures should be better understood in order to select relevant elements that can help to establish the delicate balance between the ferroic and antiferroic order.

Acknowledgement

Spring is here in Darmstadt as I approach the end of this wonderful journey, which would not have been so meaningful without the presence of many people who have supported and helped me over the years.

First and foremost, I would like to thank my mentor Prof. Dr. Jürgen Rödel for giving me the opportunity to join the team at NAW and to work with him and all the other dear colleagues. I greatly appreciate his great wisdom, insightful opinions and the art of leading a strong and dynamic team that he demonstrated and I learned a lot. The great opportunities he provided me and his encouragements also trained and shaped me a lot. In addition, I am grateful to him for choosing the best supervisor for me.

I would like to express my sincere gratitude to my supervisor Jurij Koruza. I thank you for always providing me with insightful advice, for your cooperative attitude, for thoughtful scientific contributions during our collaborative meetings, for your rigorous academic attitude, for the relaxed and pleasant working atmosphere, and for carefully revising and proofreading my papers and my dissertation with always constructive feedback. Without your presence, my doctoral experience would not have been so great.

I would like to address my gratitude to Prof. Dr. Wolfgang Donner for being the second reviewer of this dissertation and he happens to be my second supervisor in the FLAME project.

I would like to acknowledge the LOEWE project FLAME, which brings together so many great colleagues I have had pleasure to work with over the past 3 years: Lovro Fulanović, Sonja Egert, Hui Ding, Niloofar Hadaeghi, Binxiang Huang, Leif Carstensen, Lorenzo Villa, Thorsten Schneider, Nicole Bein, Julian Moxter, Zhen Liu, Pedro Groszewicz, Prof. Dr. Hongbin Zhang, Prof. Dr. Leopoldo Molina-Luna, Prof. Dr. Hans-Joachim Kleebe, Prof. Dr. Bai-Xiang Xu, Prof. Dr. Karsten Albe, and Prof. Dr. Andreas Klein. And many thanks to Jessica Bagnoli for taking good care of the organization and administration in this FLAME family.

My doctoral life would not have been so pleasant and memorable without the company of my dear NAW colleagues. My special thanks to Daniel Isaia and Patrick Breckner for their prompt response and technical support, and to our able secretary Gila Völzke for taking care of the group. An-Phuc Hoang and Mihail Slabki are acknowledged, I miss the nice experience we had together in our 107 office before the pandemic. I thank Jan Schultheiß for setting a good example for me at the beginning of my PhD study. I would like to thank all Chinese colleagues and friends (Fangping Zhuo, Kuan Ding, Shuang Gao, Xufei Fang, and many others) in the

group, I had a great time with all of you here in a foreign country far from home. In particular, I would like to thank Changhao Zhao for introducing me to the interesting world of *in situ* synchrotron characterization of materials and for the inspiration and ideas that came out of the after-work meetings. I have had the pleasure to supervise two great students here, Bohan Xu and Umair Saeed. My sincere gratitude goes to all other members of the NAW family, including those who have left the group.

Deutsches Elektronen-Synchrotron, DESY, is acknowledged, for the provision of experimental facilities for the synchrotron study. Parts of this research were carried out at PETRA III using beamline P02.1. Beamtime was allocated for proposal (I-20210563).

I would like to take this opportunity to sincerely thank my mentor Prof. Ke Wang, who opened the door to the beautiful world of functional ceramics for a confused and lost undergraduate student. I am very grateful for the valuable opportunities you provided me in the early stage of my research career to meet the best scientists in the world. Without your strong support, I would not have come this far. In addition, I would like to thank Prof. Jing-Feng Li for his kind support and encouragement. The pandemic did not break my connections with my peer friends at Tsinghua. With Hao-Cheng Thong, Yixuan Liu and many others, we had frequent fruitful and interesting discussions.

I was fortunate to meet so many good friends in Darmstadt, and we went through an unforgettable time together. I would like to thank Zhenghao Wu and Tianhang Zhou for the enjoyable experiences we had together in our Doppelhaus at Evenaristraße 2, Darmstadt. My encounters with Chen Shen, Ying Zhan and many other little fellows brighten my colorful memories of this three-year stay in Germany. I have always been lucky to cultivate good friendships on the soccer field and I cherish the time and experiences I spent with Ran Huang, Di Xiao and many others.

Last but not least, please allow me to express my deepest and most sincere gratitude to my parents for their great love, unwavering support, never-ending inspiration and encouragement, and to my girlfriend Liangqi for her love, everlasting motivation and continued understanding during the special time of the pandemic. It has been a difficult time for all families like us, and let us continue to hope that this pandemic will end soon.

Maohua Zhang（张茂华）
Darmstadt, March 2022

List of Tables

Table 2.1: Overview of 32 point groups. Crystallographic classification according to their crystal systems, centrosymmetry and polarity [19]. Piezoelectrics are highlighted in bold. 9

Table 2.2: Summary of representative thermodynamic potential functions of elastic dielectrics. 13

Table 2.3: Summary of representative thermodynamic potential functions in the differential form..... 14

Table 6.1: Rietveld refinement data for $NaNbO_3$ on the basis of the space group *Pbcm*..... 77

Table 7.1: DFT calculated energies and structural parameters for the *Pbcm* and $Pmc2_1$ structures of pure and $SrSnO_3$-substituted $NaNbO_3$, on a per formula unit (f.u.) basis. 94

Table 7.2: Rietveld refinement data for NN5SS on the basis of the space group *Pbcm*. 99

Table 7.3: Electrical properties of $NaNbO_3$, NN3SS, NN4SS, and NN5SS ceramic samples. P_r is the remanent polarization, E_F is the critical field, S_{neg} is the negative strain, d_{33} is the macroscopic piezoelectricity, ω_{stor} is the storage energy density, ω_{rec} is the recoverable energy density, and η is the energy storage efficiency ($\omega_{rec}/\omega_{stor}$)..... 104

Table 7.4: Orthorhombic lattice distortion (b/a) calculated from the refined lattice constants of $NaNbO_3$, NN3SS, NN4SS, and NN5SS ceramic samples..... 105

Table 7.5: Lattice constants and orthorhombic lattice distortion (b/a) calculated from the refined lattice constants of $NaNbO_3$, NN5SS, NN5SS_0.1Mn, NN5SS_0.5Mn, and NN5SS_1.0Mn ceramic samples. 112

Table 7.6: Orthorhombic lattice distortion (b/a) calculated from the refined lattice constants of $NaNbO_3$ in the AFE and FE states, and NN5SS_0.1Mn in the AFE, FE, and remanent states. The results of the AFE state are based on Rietveld refinement, while those of the FE and remanent states are based on Lebail fitting, as the ceramic sample is not isotropic after exposure to the electric field. 115

List of figures

Figure 2.1: Representative electric field dependence of small-signal permittivity of linear dielectrics, ferroelectrics, and antiferroelectrics. 5

Figure 2.2: Four main polarization mechanisms under the application of an electric field: electronic polarization, ionic polarization, orientation polarization, and space charge polarization. 6

Figure 2.3: Real part $\varepsilon r'$ and imaginary part $\varepsilon r''$ of the dielectric permittivity as a function of frequency. Space charge and orientation polarizations are relaxation processes and are strongly temperature dependent. Ionic and electronic polarizations are resonance processes and almost temperature independent. 7

Figure 2.4: Piezoelectrics, pyroelectrics, and ferroelectrics are subgroups of dielectrics. 8

Figure 2.5: Schematic illustrations of the orientations of dipoles in neighboring unit cells of (a) pyroelectrics, (b) ferroelectrics, and (c-d) two cases of antiferroelectrics. The unit cells of antiferroelectrics are highlighted by dashed rectangle. 11

Figure 2.6: A schematic plot of the elastic Gibbs function G_1 of the second-order phase transition as a function of polarization at $T < T_0$, $T = T_0$, and $T > T_0$ 16

Figure 2.7: A schematic plot of the elastic Gibbs function G_1 of the first-order phase transition as a function of polarization at i. $T < T_0$, ii. $T_0 < T < T_c$, iii. $T = T_c$, iv. $T > T_c$, and v. $T > T_c$. 18

Figure 2.8: Theoretical temperature-electric field (T-E) phase diagram associated with the free energy given by equation 2–50 for $\beta > 0$ and $\delta > 0$. Hatched and hatched-dotted curves represent, respectively, second-order transition and limit of stability curves. Reprinted figure with permission from [35]. Copyright (2016) by the American Physical Society. 23

Figure 3.1: Schematic projection of the structure of $PbZrO_3$ on orthorhombic (001) plane. The black arrows represent the antiparallel atomic displacements of the Pb ions. The dashed lines delineate the pseudocubic subcells and the solid line shows the orthorhombic unit cell. Reprinted figure with permission from [9]. Copyright (1951) by the American Physical Society. 28

Figure 3.2: Phase diagram of $(Pb_{0.98}La_{0.02})(Zr, Ti, Sn)O_3$ systems. Copyright © 1966 IEEE, reprinted with permission from [49]. The compositions near the phase boundary

between the antiferroelectric (AFE_T) and ferroelectric (F_R) phases are the most studied. 31

Figure 3.3: Phase diagram of (Pb,La)(Zr,Ti)O_3 system at room temperature, reprinted with permission from [51]. Copyright © John Wiley & Sons, Inc. 32

Figure 3.4: Temperature dependence of dielectric permittivity of Sn-modified PNZST ceramics as a function of Sn contents, measured at 10^5 Hz. Reprinted from [55], with the permission of AIP Publishing. 33

Figure 3.5: (200) and (002) reflection peaks of the PLZST sample at room temperature and zero field for (a) the ceramic sample to which an electric field was applied and (b) the same ceramic sample after it was ground to a powder. Reprinted from [68], with the permission of AIP Publishing. 37

Figure 3.6: (111) reflection peaks of the PLZST ceramic sample at (a) zero field and (b) an applied electric field of 2.6 kV/mm. The profiles at zero field and 2.6 kV/mm can be fitted with a single tetragonal structure and a single rhombohedral structure, respectively. Reprinted from [68], with the permission of AIP Publishing. 37

Figure 3.7: Schematic diagram of the AFE-FE phase transition procedure of the PLZST ceramic sample. Reprinted from [62], with the permission of AIP Publishing. 38

Figure 3.8: Crystallographic structures of the *Pbcm* and $P2_1ma$ phases of $NaNbO_3$, viewed along the 110 direction. The unit cells of the two phases are highlighted by black dashed lines. The atomic displacements of Na and Nb atoms are expressed by orange and dark blue arrows, respectively. 40

Figure 3.9: Sequence of the phase transitions of $NaNbO_3$ as a function of temperature, readpted from Ref. [71]. 42

Figure 3.10: Plot of average tolerance factor versus dopant concentration x of NaNbO3. Red and blue part represent ferroelectric and antiferroelectric distortive region, respectively. Reproduced from [17] with permission from the Royal Society of Chemistry. 45

Figure 3.11: Tolerance factor versus averaged electronegativity difference for various perovskites. Reproduced from [17] with permission from the Royal Society of Chemistry. 46

Figure 5.1: Large-signal (a-c) polarization and (d-f) strain hysteresis loops of $NaNbO_3$ ceramic samples under a bipolar electric field of 8 kV/mm, 10 kV/mm, and 12 kV/mm with a

frequency of 1 Hz. The critical electric field, E_F, is defined as the electric field at which polarization reaches half of the saturate polarization value. 58

Figure 5.2: The strain-polarization^2 loop of $NaNbO_3$ ceramic sample. The fitted electrostrictive coefficient (0.0008 m^4/C^2) is highlighted. 59

Figure 5.3: Large-signal polarization (solid line, left) and strain (dashed line, right) hysteresis loops of the $NaNbO_3$ sample that underwent the AFE−FE phase transition. A bipolar electric field of 12 kV/mm with a frequency of 1 Hz was applied. 59

Figure 5.4: (a) Frequency dependence of the (a) polarization and (b) strain hysteresis loops of $NaNbO_3$ samples cut from the same ceramic pellet, so that the samples were assumed to be identical in the virgin state before a unipolar electric field of 13 kV/mm was applied. 60

Figure 5.5: The scaling behavior of the critical field E_F versus frequency for the investigated $NaNbO_3$, based on the data obtained from Figure 5.4(a). The critical electric field, E_F, is defined as the electric field at which polarization reaches half of the saturate polarization value. 61

Figure 5.6: Temperature dependence of (a) polarization and (b) strain hysteresis loops of $NaNbO_3$ samples cut from the same ceramic pellet, so that the samples were assumed to be identical in the virgin state before a unipolar electric field of 12 kV/mm was applied. 62

Figure 5.7: Decrease of the critical field E_F with temperature of the investigated $NaNbO_3$, based on the data obtained from Figure 5.6(a). The critical electric field, E_F, is defined as the electric field at which polarization reaches half of the saturate polarization value. Based on linear regression analysis of E_F as a function of temperature, a slope of dE_F/dT = −0.039 kV/mm·deg is obtained. 62

Figure 5.8: Temperature dependence of dielectric permittivity (solid lines) and dielectric loss (dashed lines) for the $NaNbO_3$ ceramic material (a) before and (b) after the field-induced phase transition in the frequency range from 5 kHz to 1 MHz. 64

Figure 5.9: Comparison of the temperature dependence of dielectric permittivity (solid lines) and dielectric loss (dashed lines) for the $NaNbO_3$ ceramic material before and after the phase transition, measured at 10 kHz. 65

Figure 5.10: (a) TSDC measurements for the $NaNbO_3$ sample before (blue) and after (red) the field-induced AFE−FE phase transition. (b) An enlarged view of the current density peak at 356 °C. 66

Figure 5.11: Field dependence of small-signal permittivity of $NaNbO_3$ in the virgin state. A small-signal AC voltage of 1 V at 10 kHz was applied, superimposed on a large-signal bipolar electric field of 12 kV/mm with a frequency of 0.005 Hz. 67

Figure 5.12: (a) Polarization hysteresis loops and (b) field dependence of small-signal permittivity of $(Pb_{0.97}La_{0.02})(Zr_{0.75}Sn_{0.13}Ti_{0.12})O_3$ at RT and 180 °C. The polarization loops were measured at 0.1 Hz. A small-signal AC voltage of 1 V at 10 kHz was applied, superimposed on a large-signal bipolar electric field of 1.5 kV/mm with a frequency of 0.005 Hz. 68

Figure 5.13: (a) XRD patterns of $NaNbO_3$ before (red lines) and after (blue lines) the field-induced phase transition. Detailed XRD scans of the 2theta regions of (b) 35.5−37.5°, (c) 42.5−44.2°, and (d) 54.0−56.0°. Two groups of labels represent the reflections associated with the AFE *Pbcm* and FE $P2_1ma$ space groups (for labels, please refer to the PDF-ICDD database). The XRD signal was obtained from the surface of the same pellet sample in reflection mode. A conductive silver paste that can be dissolved in acetone was used as the electrode, so that the XRD measurement could be performed immediately after the phase transition. 70

Figure 5.14: (a) SAED pattern of the $NaNbO_3$ before the electric-field-induced phase transition. (b) The corresponding dark field image obtained by imaging one of the ¼ superlattice spots highlighted by the arrows in (a). 72

Figure 5.15: (a) SAED pattern and (b) the corresponding dark field image of the AFE region of the $NaNbO_3$ after the field-induced phase transition. (c) SAED pattern and (c) the corresponding dark field image of the FE region of the $NaNbO_3$ after the transition. .73

Figure 5.16: Two-dimensional ^{23}Na STMAS spectra of $NaNbO_3$ sample (a) before and (b) after the phase transition by applying a bipolar electric field of 12 kV/mm. (c) Projection of both spectra along the indirect dimension illustrating the profiles of the signals. The signal of the Na(2) site is located at −1.8 ppm and that of the Na(1) site is between 9 and 13 ppm. Only the signature line shape of the *P* phase is observed before the transition, while the signals corresponding to the *P* and *Q* phases are resolved after the phase transition. Note that the Na(2) signal in (a) and (b) are cut to increase the visibility of the Na(1) signal. 75

Figure 6.1: (a) Rietveld refinement of the high-energy XRD pattern of $NaNbO_3$ in the virgin state using the *Pbcm* space group. Magnified views of (b) representative superlattice reflections and (c-d) high-angle main reflections. The reflections associated with the

Pbcm space group are shown by the yellow tick marks. The starting parameters of the *Pbcm* model for the refinement were taken from the X-ray and powder diffraction data refinements of Mishchuk *et al.* [149]. 78

Figure 6.2: One-dimensional XRD patterns of $NaNbO_3$ ceramics as a function of increasing electric field from 0 kV/mm to 16 kV/mm. The patterns were integrated from the 45° sectors at different electric field amplitudes. Typical ¼ superlattice reflections characteristic of the AFE *P* phase were identified for the $NaNbO_3$ before applying the electric field. The superlattice reflections most affected by the field application are highlighted in the dashed boxes. 79

Figure 6.3: Evolution of selected primary reflections from the 45° sectors with increasing electric field from 0 kV/mm to 16 kV/mm in a period of 10 s. The patterns from the bottom to the top were recorded every 415 ms, which corresponds to a field range of ~0.6 kV/mm. 80

Figure 6.4: Evolution of selected superlattice reflections from the 45° sectors with increasing electric field from 0 kV/mm to 16 kV/mm in a period of 10 s. 80

Figure 6.5: One-dimensional XRD patterns of the superlattice reflections (a) $¼843_{PC}$ and (b) $½312_{PC}$ reflections as a function of increasing electric field from 0 kV/mm and 16 kV/mm. The patterns were integrated from the 45° sectors. The integrated area of the $¼843_{PC}$ at 0 kV/mm is taken as a reference, representing 100% of the AFE *P* phase. (c) *P* phase fraction determined by the integrated area of the $¼843_{PC}$ reflections as a function of increasing field and the *in situ* macroscopic polarization (*P*) and longitudinal strain (S_{33}). 81

Figure 6.6: Temperature change of $NaNbO_3$ sample when subjected to an increasing electric field from 0 kV/mm and 16 kV/mm with a unipolar frequency of 0.05 Hz. The temperature was measured with a thermistor glued to the surface of the sample. To prevent dielectric breakdown, the measurement was carried out in silicone oil. 82

Figure 6.7: Pseudocubic lattice parameters (a) a_{PC}, b_{PC}, c_{PC}, (b) γ_{PC}, and (c) primitive cell volume as a function of increasing electric field from 0 kV/mm to 16 kV/mm. All parameters were obtained from LeBail fitting using single-phase models. The one-dimensional XRD patterns for the LeBail fitting were integrated over the entire azimuthal range and represent the average structure. 83

Figure 6.8: A schematic representation of the crystallographic structure of $NaNbO_3$ in the *P* phase (left) and the *Q* phase (right), viewed along the 001_{PC} direction. The orientation

of the double arrow represents the direction of antiparallel atomic displacement of Na and Nb atoms.....84

Figure 6.9: Longitudinal strain S_{33}, transverse strain S_{11}, and volume strain $S_{33}+2S_{11}$ as a function of externally applied electric field for (a) $NaNbO_3$ and (b) $(Pb_{0.97}La_{0.02})(Zr_{0.75}Sn_{0.13}Ti_{0.12})O_3$ during the very first cycle of application. A volumetric strain of 0.25% was recorded for $NaNbO_3$ between the initial and the final states. 85

Figure 6.10: Temperature profile of $PbZrO_3$ ceramic at T = 216 °C when an average electric field of E = 3.5 kV/mm was applied. (b) AFE–FE phase boundary propagating across the sample. The phase transition was accompanied with the negative electrocaloric effect. Thickness gradients were introduced to concentrate the nucleation at one side of the sample and thus a sideways propagation of the phase boundary. Each frame has dimensions of 3.2 mm × 2.55 mm. Reprinted with permission from [153]. Copyright © John Wiley & Sons, Inc.....86

Figure 6.11: Evolution of the *d*-spacings of (a) 220_{PC} reflections in the directions parallel and perpendicular to the applied electric field. The 2theta positions of the 2−20 and 202 reflections are too close to each other to be resolved in the diffraction patterns. Therefore, the *d*-spacings of the two reflections are assumed to be equal. (b) Illustration of the differently oriented cells being subjected to tensile stress and compressive stress. The thin arrows (red) on the surfaces of the cells represent the direction of spontaneous polarization. The bold arrows represent the mechanical stress and their magnitude indicates the strength. 88

Figure 6.12: Evolution of the *d*-spacings of (a) 200_{PC} reflections in the directions parallel and perpendicular to the applied electric field. (b) Illustration of the differently oriented cells being subjected to tensile stress and compressive stress. The thin arrows (red) on the surfaces of the cells represent the direction of spontaneous polarization. The bold arrows represent the mechanical stress and their magnitude indicates the strength. 88

Figure 6.13: Micrographs of polished $NaNbO_3$ samples (a) before and (b) after the field-induced phase transition. Microcracks are highlighted using yellow arrows. The crack length is about 5–10 μm. The images were taken in the circular polarized light-differential interference contrast (C–DIC) mode, using the Axio Imager 2 microscope (Zeiss, Germany).....89

Figure 6.14: Cycling behavior of the polarization hysteresis loops of $NaNbO_3$ with microcracks. 90

Figure 7.1: Calculated structures of the most stable AFE structure of 0.9375$NaNbO_3$-0.0625$SrSnO_3$ and the corresponding FE modification. 94

Figure 7.2: (a) Full XRD patterns of pure $NaNbO_3$ and $SrSnO_3$-substituted samples and superlattice reflections in the 2theta regions of (b) 35.5−37.5°, (c) 42.5−44.2°, and (d) 54.0−56.0°. Two sets of markers represent the reflections associated with the *P* phase (dark grey) and the *Q* phase (light grey). The reflection geometry XRD signal was obtained from the crushed powder of the sintered pellets. 96

Figure 7.3: Cell parameters of pure $NaNbO_3$ and $SrSnO_3$-substituted $NaNbO_3$ samples, determined from Rietveld refinements. The bigger symbols represent the cell parameters calculated by DFT. 97

Figure 7.4: (a) Rietveld refinement of the high-energy XRD data of the virgin-state NN5SS system using the *Pbcm* space group. Magnified views of (b) representative superlattice reflections and (c-d) high-angle main reflections. Reflections associated with the *Pbcm* structure are shown by the yellow tick marks. The starting parameters of the *Pbcm* model for the refinement were taken from the refinements of pure $NaNbO_3$ in this work. 98

Figure 7.5: A schematic representation of the atomic displacements of Na in $NaNbO_3$ (left) and NN5SS (right) systems, both of which have *Pbcm* space group in the virgin state, viewed along the 001_{PC} direction. The atomic displacements are exaggerated to highlight the small differences in atomic displacements. The orientation of the double arrow represents the direction of the antiparallel atomic displacement of the Na and Nb atoms. 99

Figure 7.6: Two-dimensional ^{23}Na STMAS spectra of (a) pure $NaNbO_3$ and (b) NN5SS systems in the virgin state. Summation of the signals along the indirect dimension (δ_1) for (b) $NaNbO_3$ and (e) NN5SS. Projections of the Na(1) signals (area within the dashed rectangles) along the direct dimension (δ_2) for (c) $NaNbO_3$ (in yellow) and (f) NN5SS (in blue) with the best achieved line shape simulations (in gray), from which NMR parameters and distributions thereof are extracted as described in [93]. 100

Figure 7.7: (a) Polarization and (b) strain hysteresis loops of $NaNbO_3$, NN3SS, NN4SS, and NN5SS ceramic samples in the first electric cycle, measured at 1 Hz and room temperature. (c) Polarization and (d) strain hysteresis loops in the second electric field cycle. 102

Figure 7.8: Grain size distributions of (a) NN3SS, (b) NN4SS, (c) NN5SS, and (d) NN6SS ceramic samples. 103

Figure 7.9: Temperature dependence of (a) dielectric constant and (b) loss tangent for $NaNbO_3$, NN3SS, NN4SS, NN5SS, and NN6SS ceramic samples in the virgin state, measured at 1−100 kHz. 105

Figure 7.10: The *P*−*R* phase transition temperature T_{P-R} and the orthorhombic lattice distortion *b*/*a* within the *ab* plane of $NaNbO_3$, NN3SS, NN4SS, and NN5SS ceramic samples. The arrow highlights the trend that both parameters decrease with increasing $SrSnO_3$. ...105

Figure 7.11: (a) Polarization and (b) strain hysteresis loops of NN5SS ceramic samples modified with different amounts of Mn (0.1 wt.%, 0.5 wt.%, and 1.0 wt.%) in the first electric cycle, measured at 1 Hz and room temperature. 108

Figure 7.12: SEM images of the thermally etched surfaces of (a) NN5SS and the NN5SS...108

Figure 7.13: Polarization and (b) strain hysteresis loops of NN5SS ceramic samples modified with 2.0 wt.% Mn, measured at 1 Hz and room temperature.....109

Figure 7.14: Magnified views of representative high-angle main reflections of (a) NN5SS_0.1Mn, (b) NN5SS_0.5Mn, (c) NN5SS_1.0Mn, and (d) NN5SS_2.0Mn ceramic samples in the virgin state. The structure of the first three compositions is well described by the *Pbcm* space group, while the structure of the last composition is better described by the $P2_1ma$ space group. The reflections associated with the two structures are indicated by the yellow tick marks.....110

Figure 7.15: (a) Rietveld refinement of the high-energy XRD pattern of the NN5SS sample modified with 0.1 wt.% Mn in the virgin state using the *Pbcm* space group. Magnified views of (b) representative superlattice reflections and (c-d) high-angle main reflections. Reflections associated with the *Pbcm* structure are shown by the yellow tick marks. The starting parameters of the *Pbcm* model for the refinement were taken from the refinements of the NN5SS ceramic sample in this work. 111

Figure 7.16: Contour plots of (a) primary reflections and (b) three-dimensional surface maps of superlattice reflections of the NN5SS_0.1Mn ceramic sample during the field-induced phase transition. (c) A unipolar electric field of 18 kV/mm was applied within 2.5 s. (d) Longitudinal strain (S_{33}) recorded simultaneously with the *in situ* synchrotron measurement.....113

Figure 7.17: (a) Pseudocubic lattice parameters and primitive cell volume as a function of electric field during the field-induced phase transition and after removal of the field, determined by LeBail fitting using a single-phase model. (b) Schematic representation of the crystallographic structure of the studied material in the virgin state (black dashed lines) and in the field-induced FE state (red dashed lines), viewed along the $[001]_{PC}$ direction. The orientation of the double-headed arrow represents the direction of antiparallel atomic displacement of Na and Nb atoms. 114

Figure 7.18: Frequency dependence of (a) dielectric permittivity and (b) loss tangent of NN5SS, NN5SS_0.1Mn, NN5SS_0.5Mn, and NN5SS_1.0 ceramic samples. 117

Figure 7.19: Frequency dependence of (a) polarization and (b) strain hysteresis loops of the NN5SS_0.1Mn ceramic sample..... 118

Figure 7.20: (a) Temperature dependence of the polarization hysteresis loops of the NN5SS_0.5Mn ceramic sample. (b) The scaling behavior of the critical field E_F versus temperature, based on the data obtained from (a). The critical electric field, E_F, is defined as the electric field at which polarization reaches half of the maximum polarization value. Based on the linear regression analysis of the E_F as a function of temperature, a slope of $dE_F/dT = -0.020$ kV/mm·deg is determined. 119

Figure 7.21: Energy storage density and efficiency of $NaNbO_3$, NN5SS, and NN5SS_0.5Mn ceramic samples, determined from the bipolar polarization hysteresis loops. 120

Bibliography

[1] K.M. Rabe, Antiferroelectricity in Oxides: A Reexamination, Functional Metal Oxides 2013, pp. 221-244.

[2] C.A. Randall, Z. Fan, I. Reaney, L.-Q. Chen, S. Trolier-McKinstry, Antiferroelectrics: History, fundamentals, crystal chemistry, crystal structures, size effects, and applications, J. Am. Ceram. Soc. 104(8) (2021) 3775-3810.

[3] G.F. Engel, Design and Materials of Antiferroelectric Capacitors for High Density Power Electronic Applications, CIPS 2016; 9th International Conference on Integrated Power Electronics Systems, 2016, pp. 1-7.

[4] Z. Liu, T. Lu, J. Ye, G. Wang, X. Dong, R. Withers, Y. Liu, Antiferroelectrics for Energy Storage Applications: a Review, Adv. Mater. Technol. 3(9) (2018) 1800111.

[5] D. Yang, J. Gao, L. Shu, Y.-X. Liu, J. Yu, Y. Zhang, X. Wang, B.-P. Zhang, J.-F. Li, Lead-free antiferroelectric niobates $AgNbO_3$ and $NaNbO_3$ for energy storage applications, J. Mater. Chem. A 8(45) (2020) 23724-23737.

[6] A.S. Mischenko, Q. Zhang, J.F. Scott, R.W. Whatmore, N.D. Mathur, Giant Electrocaloric Effect in Thin-Film $PbZr_{0.95}Ti_{0.05}O_3$, Science 311(5765) (2006) 1270.

[7] N. Novak, F. Weyland, S. Patel, H. Guo, X. Tan, J. Rödel, J. Koruza, Interplay of conventional with inverse electrocaloric response in $(Pb,Nb)(Zr,Sn,Ti)O_3$ antiferroelectric materials, Phys. Rev. B 97(9) (2018) 094113.

[8] C. Kittel, Theory of Antiferroelectric Crystals, Phys. Rev. 82(5) (1951) 729-732.

[9] E. Sawaguchi, H. Maniwa, S. Hoshino, Antiferroelectric Structure of Lead Zirconate, Phys. Rev. 83(5) (1951) 1078-1078.

[10] M.E. Lines, A.M. Glass, Principles and Applications of Ferroelectrics and Related Materials, OUP Oxford 2001.

[11] R.H. Dungan, R.D. Golding, Metastable Ferroelectric Sodium Niobate, J. Am. Ceram. Soc. 47(2) (1964) 73-76.

[12] W. Li, X. Xia, J. Zeng, L. Zheng, G. Li, Significant differences in $NaNbO_3$ ceramics fabricated using Nb_2O_5 precursors with various crystal structures, Ceram. Int. 46(3) (2020) 3759-3766.

[13] Z.X. Shen, X.B. Wang, S.H. Tang, M.H. Kuok, R. Malekfar, High-pressure Raman study and pressure-induced phase transitions of sodium niobate $NaNbO_3$, J. Raman Spectrosc. 31(5) (2000) 439-443.

[14] J. Schwarzkopf, M. Schmidbauer, T. Remmele, A. Duk, A. Kwasniewski, S. Bin Anooz, A. Devi, R. Fornari, Strain-induced phase transitions in epitaxial $NaNbO_3$ thin films grown by metal–organic chemical vapour deposition, J. Appl. Crystallogr. 45(5) (2012) 1015-1023.
[15] Y.I. Yuzyuk, R.A. Shakhovoy, S.I. Raevskaya, I.P. Raevski, M.E. Marssi, M.G. Karkut, P. Simon, Ferroelectric Q-phase in a $NaNbO_3$ epitaxial thin film, Appl. Phys. Lett. 96(22) (2010) 222904.
[16] J. Koruza, P. Groszewicz, H. Breitzke, G. Buntkowsky, T. Rojac, B. Malič, Grain-size-induced ferroelectricity in $NaNbO_3$, Acta Mater. 126 (2017) 77-85.
[17] H. Shimizu, H. Guo, S.E. Reyes-Lillo, Y. Mizuno, K.M. Rabe, C.A. Randall, Lead-free antiferroelectric: $xCaZrO_3$-$(1-x)NaNbO_3$ system ($0 \leqslant x \leqslant 0.10$), Dalton Trans. 44(23) (2015) 10763-10772.
[18] D.J. Singh, Structure and energetics of antiferroelectric $PbZrO_3$, Phys. Rev. B 52(17) (1995) 12559-12563.
[19] K. Uchino, Ferroelectric devices, CRC press 2018.
[20] A.J. Moulson, J.M. Herbert, Electroceramics: materials, properties, applications, John Wiley & Sons2003.
[21] R.E. Cohen, Origin of ferroelectricity in perovskite oxides, Nature 358(6382) (1992) 136-138.
[22] A. Xie, J. Fu, R. Zuo, C. Zhou, Z. Qiao, T. Li, S. Zhang, $NaNbO_3$-$CaTiO_3$ lead-free relaxor antiferroelectric ceramics featuring giant energy density, high energy efficiency and power density, Chem. Eng. J. 429 (2022) 132534.
[23] W. Kanzig, J. Seitz, D. Turnbull, Solid state physics, vol. 4, Academic Press, Inc., New York 1957.
[24] G. Goldsmith, J. White, Ferroelectric behavior of thiourea, J. Chem. Phys. 31(5) (1959) 1175-1187.
[25] N. Setter, What is a ferroelectric–a materials designer perspective, Ferroelectrics 500(1) (2016) 164-182.
[26] Z. Wang, K.G. Webber, J.M. Hudspeth, M. Hinterstein, J.E. Daniels, Electric-field-induced paraelectric to ferroelectric phase transformation in prototypical polycrystalline $BaTiO_3$, Appl. Phys. Lett. 105(16) (2014) 161903.
[27] H. Mueller, Properties of Rochelle Salt, Phys. Rev. 57(9) (1940) 829-839.
[28] L.D. Landau, E.M. Lifshitz, Course of theoretical physics, Elsevier 2013.
[29] A.F. Devonshire, Theory of barium titanate, Lond. Edinb. Dubl. Phil. Mag. 40(309) (1949) 1040-1063.

[30] L.E. Cross, Antiferroelectric-Ferroelectric Switching in a Simple "Kittel" Antiferroelectric, J. Phys. Soc. Jpn. 23(1) (1967) 77-82.

[31] K. Okada, Phenomenological Theory of Antiferroelectric Transition. I. Second-Order Transition, J. Phys. Soc. Jpn. 27(2) (1969) 420-428.

[32] M.J. Haun, T.J. Harvin, M.T. Lanagan, Z.Q. Zhuang, S.J. Jang, L.E. Cross, Thermodynamic theory of $PbZrO_3$, J. Appl. Phys. 65(8) (1989) 3173-3180.

[33] E.A. Eliseev, M.D. Glinchuk, A.N. Morozovska, Antiferroelectric thin films phase diagrams, Ph. Transit. 80(1-2) (2007) 47-54.

[34] E.A. Eliseev, M.D. Glinchuk, Size-induced appearance of ferroelectricity in thin antiferroelectric films, Phys. B: Condens. Matter 400(1) (2007) 106-113.

[35] P. Tolédano, M. Guennou, Theory of antiferroelectric phase transitions, Phys. Rev. B 94(1) (2016) 014107.

[36] G. Shirane, A. Takeda, Phase Transitions in Solid Solutions of $PbZrO_3$ and $PbTiO_3$ (I) Small Concentrations of $PbTiO_3$, J. Phys. Soc. Jpn. 7(1) (1952) 5-11.

[37] S. Roberts, Dielectric Properties of Lead Zirconate and Barium-Lead Zirconate, J. Am. Ceram. Soc. 33(2) (1950) 63-66.

[38] G. Shirane, E. Sawaguchi, Y. Takagi, Dielectric Properties of Lead Zirconate, Phys. Rev. 84(3) (1951) 476-481.

[39] H.D. Megaw, Crystal structure of double oxides of the perovskite type, Proc. Phys. Soc. 58(2) (1946) 133.

[40] H. Fujishita, Y. Shiozaki, N. Achiwa, E. Sawaguchi, Crystal Structure Determination of Antiferroelectric $PbZrO_3$-Application of Profile Analysis Method to Powder Method of X-ray and Neutron Diffraction, J. Phys. Soc. Jpn. 51(11) (1982) 3583-3591.

[41] F. Jona, G. Shirane, F. Mazzi, R. Pepinsky, X-Ray and Neutron Diffraction Study of Antiferroelectric Lead Zirconate, $PbZrO_3$, Phys. Rev. 105(3) (1957) 849-856.

[42] M. Tanaka, R. Saito, K. Tsuzuki, Determinations of Space Group and Oxygen Coordinates in the Antiferroelectric Phase of Lead Zirconate by Conventional and Convergent-Beam Electron Diffraction, J. Phys. Soc. Jpn. 51(8) (1982) 2635-2640.

[43] A. Glazer, K. Roleder, J. Dec, Structure and disorder in single-crystal lead zirconate, $PbZrO_3$, Acta Crystallogr., Sect. B: Struct. Sci., Cryst. Eng. Mater. 49(5) (1993) 846-852.

[44] D. Corker, A. Glazer, J. Dec, K. Roleder, R.J.A.C.S.B.S.S. Whatmore, A re-investigation of the crystal structure of the perovskite $PbZrO_3$ by X-ray and neutron diffraction, Acta Crystallogr., Sect. B: Struct. Sci., Cryst. Eng. Mater. 53(1) (1997) 135-142.

[45] S. Teslic, T. Egami, Atomic structure of $PbZrO_3$ determined by pulsed neutron diffraction, Acta Crystallogr., Sect. B: Struct. Sci., Cryst. Eng. Mater. 54(6) (1998) 750-765.

[46] B. Jaffe, Antiferroelectric Ceramics with Field-Enforced Transitions: A New Nonlinear Circuit Element, Proc. IRE 49(8) (1961) 1264-1267.

[47] D. Berlincourt, H. Jaffe, H.H.A. Krueger, B. Jaffe, Release of electric energy in $PbNb(Zr,Ti,Sn)O_3$ by temperature- and by pressure-enforced phase transitions, Appl. Phys. Lett. 3(5) (1963) 90-92.

[48] D. Berlincourt, Transducer using the electric field-forced antiferroelectric-ferroelectric transition, Ultrasonics 6(1) (1968) 48-51.

[49] D. Berlincourt, Transducers Using Forced Transitions Between Ferroelectric and Antiferroelectric States, IEEE Trans. Son. Ultrason. 13(4) (1966) 116-124.

[50] M.-H. Zhang, C. Zhao, L. Fulanović, J. Rödel, N. Novak, A. Schökel, J. Koruza, Revealing the mechanism of electric-field-induced phase transition in antiferroelectric $NaNbO_3$ by in situ high-energy x-ray diffraction, Appl. Phys. Lett. 118(13) (2021) 132903.

[51] G.H. Haertling, C.E. Land, Hot-Pressed $(Pb,La)(Zr,Ti)O_3$ Ferroelectric Ceramics for Electrooptic Applications, J. Am. Ceram. Soc. 54(1) (1971) 1-11.

[52] X. Dai, A. DiGiovanni, D. Viehland, Dielectric properties of tetragonal lanthanum modified lead zirconate titanate ceramics, J. Appl. Phys. 74(5) (1993) 3399-3405.

[53] D. Viehland, Z. Xu, D.A. Payne, Origin of F spots and stress sensitivity in lanthanum lead zirconate titanate, J. Appl. Phys. 74(12) (1993) 7454-7460.

[54] K. Markowski, S.-E. Park, S. Yoshikawa, L.E. Cross, Effect of Compositional Variations in the Lead Lanthanum Zirconate Stannate Titanate System on Electrical Properties, J. Am. Ceram. Soc. 79(12) (1996) 3297-3304.

[55] D. Viehland, D. Forst, J.F. Li, Compositional heterogeneity and the origins of the multicell cubic state in Sn ‐ doped lead zirconate titanate ceramics, J. Appl. Phys. 75(8) (1994) 4137-4143.

[56] W.Y. Pan, C.Q. Dam, Q.M. Zhang, L.E. Cross, Large displacement transducers based on electric field forced phase transitions in the tetragonal $(Pb_{0.97}La_{0.02})$ $(Ti,Zr,Sn)O_3$ family of ceramics, J. Appl. Phys. 66(12) (1989) 6014-6023.

[57] W. Pan, Q. Zhang, A. Bhalla, L.E. Cross, Field-Forced Antiferroelectric-to-Ferroelectric Switching in Modified Lead Zirconate Titanate Stannate Ceramics, J. Am. Ceram. Soc. 72(4) (1989) 571-578.

[58] X. Tan, J. Frederick, C. Ma, E. Aulbach, M. Marsilius, W. Hong, T. Granzow, W. Jo, J. Rödel, Electric-field-induced antiferroelectric to ferroelectric phase transition in mechanically confined $Pb_{0.99}Nb_{0.02}[(Zr_{0.57}Sn_{0.43})_{0.94}Ti_{0.06}]_{0.98}O_3$, Phys. Rev. B 81(1) (2010) 014103.

[59] X. Tan, W. Jo, T. Granzow, J. Frederick, E. Aulbach, J. Rödel, Auxetic behavior under electrical loads in an induced ferroelectric phase, Appl. Phys. Lett. 94(4) (2009) 042909.

[60] J. Frederick, X. Tan, W. Jo, Strains and Polarization During Antiferroelectric–Ferroelectric Phase Switching in $Pb_{0.99}Nb_{0.02}[(Zr_{0.57}Sn_{0.43})_{1-y}Ti_y]_{0.98}O_3$ Ceramics, J. Am. Ceram. Soc. 94(4) (2011) 1149-1155.

[61] D. Forst, J.-F. Li, D. Viehland, Observation of multiple electrically induced phase transitions and a decoupling of the induced strain and polarization in Sn-modified lead zirconate titanate, Appl. Phys. Lett. 71(11) (1997) 1472-1474.

[62] S.-E. Park, M.-J. Pan, K. Markowski, S. Yoshikawa, L.E. Cross, Electric field induced phase transition of antiferroelectric lead lanthanum zirconate titanate stannate ceramics, J. Appl. Phys. 82(4) (1997) 1798-1803.

[63] D. Viehland, D. Forst, Z. Xu, J.-F. Li, Incommensurately Modulated Polar Structures in Antiferroelectric Sn-Modified Lead Zirconate Titanate: The Modulated Structure and Its Influences on Electrically Induced Polarizations and Strains, J. Am. Ceram. Soc. 78(8) (1995) 2101-2112.

[64] M.E. Lines, A.M. Glass, Principles and applications of ferroelectrics and related materials, Oxford university press2001.

[65] M.-J. Pan, S.-E. Park, K.A. Markowski, W.S. Hackenberger, S. Yoshikawa, L.E. Cross, Electric field induced phase transition in lead lanthanum stannate zirconate titanate (PLSnZT) antiferroelectrics: tailoring properties through compositional modification, Ferroelectrics 215(1) (1998) 153-167.

[66] R.P. Brodeur, K. wa Gachigi, P.M. Pruna, T.R. Shrout, Ultra-High Strain Ceramics with Multiple Field-Induced Phase Transitions, J. Am. Ceram. Soc. 77(11) (1994) 3042-3044.

[67] W.Y. Pan, W.Y. Gu, L.E. Cross, Transition speed on switching from a field-induced ferroelectric to an antiferroelectric upon the release of the applied electric field in (Pb,La) (Zr, Ti,Sn)O_3 antiferroelectric ceramics, Ferroelectrics 99(1) (1989) 185-194.

[68] C.T. Blue, J.C. Hicks, S.E. Park, S. Yoshikawa, L.E. Cross, In situ x‐ray diffraction study of the antiferroelectric‐ferroelectric phase transition in PLSnZT, Appl. Phys. Lett. 68(21) (1996) 2942-2944.

[69] B.T. Matthias, New Ferroelectric Crystals, Phys. Rev. 75(11) (1949) 1771-1771.

[70] B.T. Matthias, J.P. Remeika, Dielectric Properties of Sodium and Potassium Niobates, Phys. Rev. 82(5) (1951) 727-729.

[71] H.D. Megaw, The seven phases of sodium niobate, Ferroelectrics 7(1) (1974) 87-89.

[72] P. Vousden, The structure of ferroelectric sodium niobate at room temperature, Acta Crystallogr. 4(6) (1951) 545-551.

[73] P. Vousden, The non-polarity of sodium niobate, Acta Crystallogr. 5(5) (1952) 690-690.

[74] H. Megaw, M.J. Wells, The space group of $NaNbO_3$ and $(Na_{0.995}K_{0.005})NbO_3$, Acta Crystallogr. 11(12) (1958) 858-862.

[75] L. Cross, Electric double hysteresis in $(K_xNa_{1-x})NbO_3$ single crystals, Nature 181(4603) (1958) 178-179.

[76] E. Wood, R. Miller, J. Remeika, The field-induced ferroelectric phase of sodium niobate, Acta Crystallogr. 15(12) (1962) 1273-1279.

[77] M. Wells, H.D. Megaw, The Structures of $NaNbO_3$ and $Na_{0.975}K_{0.025}NbO_3$, Proc. Phys. Soc. 78(6) (1961) 1258-1259.

[78] A. Glazer, H. Megaw, Studies of the lattice parameters and domains in the phase transitions of $NaNbO_3$, Acta Crystallogr., A, Found. Crystallogr. 29(5) (1973) 489-495.

[79] J. Chen, F. Duan, TEM Studies of Phase and Domains in $NaNbO_3$ at Room Temperature, Phys. Status Solidi A 109(1) (1988) 171-185.

[80] L. Jiang, D.C. Mitchell, W. Dmowski, T. Egami, Local structure of $NaNbO_3$: A neutron scattering study, Phys. Rev. B 88(1) (2013) 014105.

[81] S.K. Mishra, N. Choudhury, S.L. Chaplot, P.S.R. Krishna, R. Mittal, Competing antiferroelectric and ferroelectric interactions in $NaNbO_3$: Neutron diffraction and theoretical studies, Phys. Rev. B 76(2) (2007) 024110.

[82] E.A. Wood, Polymorphism in potassium niobate, sodium niobate, and other ABO_3 compounds, Acta Crystallogr. 4(4) (1951) 353-362.

[83] G. Shirane, R. Newnham, R. Pepinsky, Dielectric Properties and Phase Transitions of $NaNbO_3$ and $(Na,K)NbO_3$, Phys. Rev. 96(3) (1954) 581-588.

[84] L.E. Cross, B.J. Nicholson, The optical and electrical properties of single crystals of sodium niobate, Lond. Edinb. Dubl. Phil. Mag. 46(376) (1955) 453-466.

[85] M. Francombe, High-temperature structure transitions in sodium niobate, Acta Crystallogr. 9(3) (1956) 256-259.

[86] I. Lefkowitz, K. Łukaszewicz, H.D. Megaw, The high-temperature phases of sodium niobate and the nature of transitions in pseudosymmetric structures, Acta Crystallogr. 20(5) (1966) 670-683.

[87] R.C. Miller, E.A. Wood, J.P. Remeika, A. Savage, $Na(Nb_{1-x}V_x)O_3$ System and ``Ferrielectricity", J. Appl. Phys. 33(5) (1962) 1623-1630.

[88] O.A. Zhelnova, O.E. Fesenko, Phase transitions and twinning in $NaNbO_3$ crystals, Ferroelectrics 75(1) (1987) 469-475.

[89] A.V. Ulinzheev, A.V. Leiderman, V.G. Smotrakov, V.Y. Topolov, O.E. Fesenko, Phase transitions induced in $NaNbO_3$ crystals by varying the direction of an external electric field, Phys. Solid State 39(6) (1997) 972-974.

[90] L. Chao, Y. Hou, M. Zheng, M. Zhu, High dense structure boosts stability of antiferroelectric phase of $NaNbO_3$ polycrystalline ceramics, Appl. Phys. Lett. 108(21) (2016) 212902.

[91] L. Chao, Y. Hou, M. Zheng, Y. Yue, M. Zhu, Macroscopic ferroelectricity and piezoelectricity in nanostructured $NaNbO_3$ ceramics, Appl. Phys. Lett. 110(12) (2017) 122901.

[92] H. Zhang, B. Yang, H. Yan, I. Abrahams, Isolation of a ferroelectric intermediate phase in antiferroelectric dense sodium niobate ceramics, Acta Mater. 179 (2019) 255-261.

[93] M.-H. Zhang, N. Hadaeghi, S. Egert, H. Ding, H. Zhang, P.B. Groszewicz, G. Buntkowsky, A. Klein, J. Koruza, Design of New Lead-Free Antiferroelectric (1-x)$NaNbO_3$-x$SrSnO_3$ Composi-tions Guided by First-Principles Calculations, Chem. Mater. 33(1) (2021) 266-274.

[94] Y. Fan, Z. Zhou, R. Liang, M. Zhou, X. Dong, The effect of A-site nonstoichiometry on the microstructure, electric properties, and phase stability of $NaNbO_3$ polycrystalline ceramics, J. Eur. Ceram. Soc. 39(15) (2019) 4712-4718.

[95] V. Goldschmidt, Die Gesetze Der Krystallochemie (The laws of crystal chemistry), Naturwissenschaften 14(21) (1926) 477-485.

[96] W. Zhong, D. Vanderbilt, Competing Structural Instabilities in Cubic Perovskites, Phys. Rev. Lett. 74(13) (1995) 2587-2590.

[97] A. Halliyal, T.R. Shrout, American Ceramics Conference (Regional) (1987) New Orleans.

[98] H. Guo, H. Shimizu, Y. Mizuno, C.A. Randall, Strategy for stabilization of the antiferroelectric phase (Pbma) over the metastable ferroelectric phase ($P2_1ma$) to establish double loop hysteresis in lead-free (1−x)$NaNbO_3$-x$SrZrO_3$ solid solution, J. Appl. Phys. 117(21) (2015) 214103.

[99] H. Guo, H. Shimizu, C.A. Randall, Direct evidence of an incommensurate phase in $NaNbO_3$ and its implication in $NaNbO_3$-based lead-free antiferroelectrics, Appl. Phys. Lett. 107(11) (2015) 112904.

[100] H. Guo, H. Shimizu, Y. Mizuno, C.A. Randall, Domain configuration changes under electric field-induced antiferroelectric-ferroelectric phase transitions in $NaNbO_3$-based ceramics, J. Appl. Phys. 118(5) (2015) 054102.

[101] H. Guo, H. Shimizu, C.A. Randall, Microstructural evolution in $NaNbO_3$-based antiferroelectrics, J. Appl. Phys. 118(17) (2015) 174107.

[102] D. Sri Gyan, A.A. Goyal, Y. Tamrakar, A. Dwivedi, Stabilization of anti-ferroelectric Pbcm phase over ferroelectric $P2_1ma$ phase in intermittent ferroelectric $NaNbO_3$ by incorporating $CaTiO_3$, J. Phys. D: Appl. Phys. 52(16) (2019) 165304.

[103] L. Gao, H. Guo, S. Zhang, C.A. Randall, A perovskite lead-free antiferroelectric $xCaHfO_3$-(1-x) $NaNbO_3$ with induced double hysteresis loops at room temperature, J. Appl. Phys. 120(20) (2016) 204102.

[104] M. Dou, J. Fu, R. Zuo, Electric field induced phase transition and accompanying giant poling strain in lead-free $NaNbO_3$-$BaZrO_3$ ceramics, J. Eur. Ceram. Soc. 38(9) (2018) 3104-3110.

[105] R. Zuo, J. Fu, H. Qi, Stable antiferroelectricity with incompletely reversible phase transition and low volume-strain contribution in $BaZrO_3$ and $CaZrO_3$ substituted $NaNbO_3$ ceramics, Acta Mater. 161 (2018) 352-359.

[106] A. Xie, H. Qi, R. Zuo, A. Tian, J. Chen, S. Zhang, An environmentally-benign $NaNbO_3$ based perovskite antiferroelectric alternative to traditional lead-based counterparts, J. Mater. Chem. C 7(48) (2019) 15153-15161.

[107] J. Ye, G. Wang, X. Chen, F. Cao, X. Dong, Enhanced antiferroelectricity and double hysteresis loop observed in lead-free $(1-x)NaNbO_3$-$xCaSnO_3$ ceramics, Appl. Phys. Lett. 114(12) (2019) 122901.

[108] H. Qi, A. Xie, J. Fu, R. Zuo, Emerging antiferroelectric phases with fascinating dielectric, polarization and strain response in $NaNbO_3$-$(Bi_{0.5}Na_{0.5})TiO_3$ lead-free binary system, Acta Mater. 208 (2021) 116710.

[109] A. Popovič, L. Bencze, J. Koruza, B. Malič, Vapour pressure and mixing thermodynamic properties of the $KNbO_3$–$NaNbO_3$ system, RSC Adv. 5(93) (2015) 76249-76256.

[110] J. Hreščak, A. Bencan, T. Rojac, B. Malič, The influence of different niobium pentoxide precursors on the solid-state synthesis of potassium sodium niobate, J. Eur. Ceram. Soc. 33(15) (2013) 3065-3075.

[111] W. Jo, T. Granzow, E. Aulbach, J. Rödel, D. Damjanovic, Origin of the large strain response in $(K_{0.5}Na_{0.5})NbO_3$-modified $(Bi_{0.5}Na_{0.5})TiO_3$–$BaTiO_3$ lead-free piezoceramics, J. Appl. Phys. 105(9) (2009) 094102.

[112] A. Hammersley, FIT2D: an introduction and overview, J European Synchrotron Radiation Facility Internal Report ESRF97HA02T 68 (1997) 58.

[113] B.H. Toby, EXPGUI, a graphical user interface for GSAS, J. Appl. Crystallogr. 34(2) (2001) 210-213.

[114] H.-T. Kwak, Z. Gan, Double-quantum filtered STMAS, J. Magn. Reson. 164(2) (2003) 369-372.

[115] J. Skibsted, N.C. Nielsen, H. Bildsøe, H.J. Jakobsen, Satellite transitions in MAS NMR spectra of quadrupolar nuclei, J. Magn. Reson. 95(1) (1991) 88-117.

[116] D. Massiot, F. Fayon, M. Capron, I. King, S. Le Calvé, B. Alonso, J.-O. Durand, B. Bujoli, Z. Gan, G. Hoatson, Modelling one- and two-dimensional solid-state NMR spectra, Magn. Reson. Chem. 40(1) (2002) 70-76.

[117] K.E. Johnston, C.C. Tang, J.E. Parker, K.S. Knight, P. Lightfoot, S.E. Ashbrook, The Polar Phase of $NaNbO_3$: A Combined Study by Powder Diffraction, Solid-State NMR, and First-Principles Calculations, J. Am. Chem. Soc. 132(25) (2010) 8732-8746.

[118] V. Shanker, S.L. Samal, G.K. Pradhan, C. Narayana, A.K. Ganguli, Nanocrystalline $NaNbO_3$ and $NaTaO_3$: Rietveld studies, Raman spectroscopy and dielectric properties, Solid State Sci. 11(2) (2009) 562-569.

[119] G. Kresse, J. Furthmüller, Efficiency of ab-initio total energy calculations for metals and semiconductors using a plane-wave basis set, Comput. Mater. Sci. 6(1) (1996) 15-50.

[120] G. Kresse, J. Furthmüller, Efficient iterative schemes for ab initio total-energy calculations using a plane-wave basis set, Phys. Rev. B 54(16) (1996) 11169-11186.

[121] J.P. Perdew, K. Burke, M. Ernzerhof, Generalized Gradient Approximation Made Simple, Phys. Rev. Lett. 77(18) (1996) 3865-3868.

[122] H. Orihara, S. Hashimoto, Y. Ishibashi, A Theory of D-E Hysteresis Loop Based on the Avrami Model, J. Phys. Soc. Jpn. 63(3) (1994) 1031-1035.

[123] Y. Ishibashi, H. Orihara, A theory of D-E hysteresis loop, Integr. Ferroelectr. 9(1-3) (1995) 57-61.

[124] X. Chen, X. Dong, H. Zhang, F. Cao, G. Wang, Y. Gu, H. He, Y. Liu, Frequency Dependence of Coercive Field in Soft $Pb(Zr_{1-x}Ti_x)O_3$ ($0.20 \leqslant x \leqslant 0.60$) Bulk Ceramics, J. Am. Ceram. Soc. 94(12) (2011) 4165-4168.

[125] J.F. Scott, Models for the frequency dependence of coercive field and the size dependence of remanent polarization in ferroelectric thin films, Integr. Ferroelectr. 12(2-4) (1996) 71-81.

[126] E. Sawaguchi, T. Kittaka, Antiferroelectricity and Ferroelectricity in Lead Zirconate, J. Phys. Soc. Jpn. 7(3) (1952) 336-337.

[127] B.A. Scott, G. Burns, Crystal Growth and Observation of the Ferroelectric Phase of $PbZrO_3$, J. Am. Ceram. Soc. 55(7) (1972) 331-333.
[128] V.J. Tennery, High-Temperature Phase Transitions in $PbZrO_3$, J. Am. Ceram. Soc. 49(9) (1966) 483-486.
[129] E.K.H. Salje, X. Ding, Z. Zhao, T. Lookman, A. Saxena, Thermally activated avalanches: Jamming and the progression of needle domains, Phys. Rev. B 83(10) (2011) 104109.
[130] J.Y. Jo, S.M. Yang, T.H. Kim, H.N. Lee, J.G. Yoon, S. Park, Y. Jo, M.H. Jung, T.W. Noh, Nonlinear Dynamics of Domain-Wall Propagation in Epitaxial Ferroelectric Thin Films, Phys. Rev. Lett. 102(4) (2009) 045701.
[131] I.P. Raevskii, L.A. Reznichenko, V.G. Smotrakov, V.V. Eremkin, M.A. Malitskaya, E.M. Kuznetsova, L.A. Shilkina, A new phase transition in sodium niobate, Tech. Phys. Lett. 26(8) (2000) 744-746.
[132] Y.I. Yuzyuk, P. Simon, E. Gagarina, L. Hennet, D. Thiaudière, V.I. Torgashev, S.I. Raevskaya, I.P. Raevskii, L.A. Reznitchenko, J.L. Sauvajol, Modulated phases in $NaNbO_3$: Raman scattering, synchrotron x-ray diffraction, and dielectric investigations, J. Phys.: Condens. Matter 17(33) (2005) 4977-4990.
[133] L.A. Reznichenko, L.A. Shilkina, E.S. Gagarina, I.P. Raevskii, E.A. Dul'kin, E.M. Kuznetsova, V.V. Akhnazarova, Structural instabilities, incommensurate modulations and P and Q phases in sodium niobate in the temperature range 300–500 K, Crystallogr. Rep. 48(3) (2003) 448-456.
[134] J. Koruza, J. Tellier, B. Malič, V. Bobnar, M. Kosec, Phase transitions of sodium niobate powder and ceramics, prepared by solid state synthesis, J. Appl. Phys. 108(11) (2010) 113509.
[135] J. Castellon, J. Bouquart, J.P. Reboul, A. Toureille, A new tool to study the ageing of the winding insulation of electrical machines, IEEE 1997 Annual Report Conference on Electrical Insulation and Dielectric Phenomena, Minneapolis, MN, USA, 1997, pp. 447-450 vol.2.
[136] J. Vanderschueren, J. Gasiot, Field-induced thermally stimulated currents, in: P. Bräunlich (Ed.), Thermally Stimulated Relaxation in Solids, Springer Berlin Heidelberg, Berlin, Heidelberg, 1979, pp. 135-223.
[137] J. Schultheiß, L. Liu, H. Kungl, M. Weber, L. Kodumudi Venkataraman, S. Checchia, D. Damjanovic, J.E. Daniels, J. Koruza, Revealing the sequence of switching mechanisms in polycrystalline ferroelectric/ferroelastic materials, Acta Mater. 157 (2018) 355-363.
[138] J. Íñiguez, M. Stengel, S. Prosandeev, L. Bellaiche, First-principles study of the multimode antiferroelectric transition in $PbZrO_3$, Phys. Rev. B 90(22) (2014) 220103.

[139] H. Ding, M.-H. Zhang, J. Koruza, L. Molina-Luna, H.-J. Kleebe, Domain morphology of newly designed lead-free antiferroelectric $NaNbO_3$-$SrSnO_3$ ceramics, J. Am. Ceram. Soc. 104 (2021) 3715-3725.

[140] L. Gao, H. Guo, S. Zhang, C.A. Randall, Stabilized antiferroelectricity in xBiScO3-(1-x)NaNbO3 lead-free ceramics with established double hysteresis loops, Appl. Phys. Lett. 112(9) (2018) 092905.

[141] X.-K. Wei, A.K. Tagantsev, A. Kvasov, K. Roleder, C.-L. Jia, N. Setter, Ferroelectric translational antiphase boundaries in nonpolar materials, Nat. Commun. 5(1) (2014) 3031.

[142] Y.-J. Chang, J.-Y. Lian, Y.-l.J.A.P.A. Wang, One-dimensional regular arrays of antiphase domain boundaries in anti-ferroelectric tin-substituted lead zirconate titanate (PZT) ceramics, Appl. Phys. A 36(4) (1985) 221-227.

[143] K. Baba-Kishi, D. Barber, Transmission electron microscope studies of phase transitions in single crystals and ceramics of ferroelectric $Pb(Sc_{1/2}Ta_{1/2})O_3$, J. Appl. Crystallogr. 23(1) (1990) 43-54.

[144] Y. Chen, C.-M. Wong, H. Deng, H.-M. Yau, D. Wang, Z. Yan, H. Luo, H.L.W. Chan, J. Dai, Ferroelectric domain structures in <001>-oriented $K_{0.15}Na_{0.85}NbO_3$ lead-free single crystal, AIP Adv. 5(3) (2015) 037117.

[145] P.B. Groszewicz, NMR spectroscopy of electroceramics – Applications to lead-free perovskite oxides, Open Ceram. 5 (2021) 100083.

[146] N. Stone, Table of nuclear magnetic dipole and electric quadrupole moments, At. Data Nucl. Data Tables 90(1) (2005) 75-176.

[147] S. Egert, M.-H. Zhang, J. Koruza, P.B. Groszewicz, G. Buntkowsky, ^{23}Na NMR Spectroscopic Quantification of the Antiferroelectric–Ferroelectric Phase Coexistence in Sodium Niobate, J. Phys. Chem. C 124(43) (2020) 23852-23858.

[148] S.E. Ashbrook, L. Le Pollès, R. Gautier, C.J. Pickard, R.I. Walton, ^{23}Na multiple-quantum MAS NMR of the perovskites $NaNbO_3$ and $NaTaO_3$, Phys. Chem. Chem. Phys. 8(29) (2006) 3423-3431.

[149] D.O. Mishchuk, O.I. V'yunov, O.V. Ovchar, A.G. Belous, Structural and dielectric properties of solid solutions of sodium niobate in lanthanum and neodymium niobates, Inorg. Mater. 40(12) (2004) 1324-1330.

[150] A. Le Bail, Whole powder pattern decomposition methods and applications: A retrospection, Powder Diffr. 20(4) (2005) 316-326.

[151] K. Uchino, Digital Displacement Transducer Using Antiferroelectrics, Jpn. J. App. Phys. 24(S2) (1985) 460.

[152] O.E. Fesenko, R.V. Kolesova, Y.G. Sindeyev, The structural phase transitions in lead zirconate in super-high electric fields, Ferroelectrics 20(1) (1978) 177-178.
[153] P. Vales-Castro, M. Vellvehi, X. Perpiñà, J.M. Caicedo, X. Jordà, R. Faye, K. Roleder, D. Kajewski, A. Perez-Tomas, E. Defay, G. Catalan, Direct Visualization of Anti-Ferroelectric Switching Dynamics via Electrocaloric Imaging, Adv. Electron. Mater. 7(12) (2021) 2100380.
[154] J. Zhao, S.D. Funni, E.R. Molina, E.C. Dickey, J.L. Jones, Inhomogeneous electric field-induced structural changes in soft lead zirconate titanate ferroelectric ceramics, Acta Mater. 226 (2022) 117682.
[155] F. Weyland, M. Acosta, J. Koruza, P. Breckner, J. Rödel, N. Novak, Criticality: Concept to Enhance the Piezoelectric and Electrocaloric Properties of Ferroelectrics, Adv. Funct. Mater. 26(40) (2016) 7326-7333.
[156] N. Novak, R. Pirc, Z. Kutnjak, Diffuse critical point in PLZT ceramics, EPL (Europhysics Letters) 102(1) (2013) 17003.
[157] J. Dec, Phase boundary kinetics at the antiferroelectric transformation in $NaNbO_3$ crystals and the ferroelectric transformation in $PbTiO_3$ crystals, Ferroelectrics 69(1) (1986) 187-200.
[158] B. Liu, X. Tian, L. Zhou, X. Tan, Motion of phase boundary during antiferroelectric--ferroelectric transition in a $PbZrO_3$-based ceramic, Phys. Rev. Mater. 4(10) (2020) 104417.
[159] D.E. Dausch, Ferroelectric Polarization Fatigue in PZT-Based RAINBOWs and Bulk Ceramics, J. Am. Ceram. Soc. 80(9) (1997) 2355-2360.
[160] Y. Xu, W. Hong, Y. Feng, X. Tan, Antiferroelectricity induced by electric field in $NaNbO_3$-based lead-free ceramics, Appl. Phys. Lett. 104(5) (2014) 052903.
[161] S.-E. Park, K. Markowski, S. Yoshikawa, L.E. Cross, Effect on Electrical Properties of Barium and Strontium Additions in the Lead Lanthanum Zirconate Stannate Titanate System, J. Am. Ceram. Soc. 80(2) (1997) 407-412.
[162] E.R. Leite, J.A. Cerri, E. Longo, J.A. Varela, C.A. Paskocima, Sintering of ultrafine undoped SnO_2 powder, J. Eur. Ceram. Soc. 21(5) (2001) 669-675.
[163] S.F. Dec, M.F. Davis, G.E. Maciel, C.E. Bronnimann, J.J. Fitzgerald, S.S. Han, Solid-state multinuclear NMR studies of ferroelectric, piezoelectric, and related materials, Inorg. Chem. 32(6) (1993) 955-959.
[164] M.D. Peel, S.P. Thompson, A. Daoud-Aladine, S.E. Ashbrook, P. Lightfoot, New Twists on the Perovskite Theme: Crystal Structures of the Elusive Phases R and S of $NaNbO_3$, Inorg. Chem. 51(12) (2012) 6876-6889.

[165] M.-H. Zhang, Y.-X. Liu, K. Wang, J. Koruza, J. Schultheiß, Origin of high electromechanical properties in (K,Na)NbO_3-based lead-free piezoelectrics modified with $BaZrO_3$, Phys. Rev. Mater. 4(6) (2020) 064407.

[166] L. Wang, W. Ren, P. Shi, X. Chen, X. Wu, X. Yao, Enhanced ferroelectric properties in Mn-doped $K_{0.5}Na_{0.5}NbO_3$ thin films derived from chemical solution deposition, Appl. Phys. Lett. 97(7) (2010) 072902.

[167] M. Abazari, E.K. Akdoğan, A. Safari, Effect of manganese doping on remnant polarization and leakage current in $(K_{0.44},Na_{0.52},Li_{0.04})(Nb_{0.84},Ta_{0.10},Sb_{0.06})O_3$ epitaxial thin films on $SrTiO_3$, Appl. Phys. Lett. 92(21) (2008) 212903.

[168] L. Wang, W. Ren, W. Ma, M. Liu, P. Shi, X. Wu, Improved electrical properties for Mn-doped lead-free piezoelectric potassium sodium niobate ceramics, AIP Adv. 5(9) (2015) 097120.

[169] M.-H. Zhang, L. Carstensen, C. Zhao, L. Fulanović, W. Donner, J. Koruza, Revealing the solid-state processing mechanisms of antiferroelectric $AgNbO_3$ for energy storage, J. Am. Ceram. Soc. 105(1) (2022) 451-460.

[170] J. Gao, L. Zhao, Q. Liu, X. Wang, S. Zhang, J.-F. Li, Antiferroelectric-ferroelectric phase transition in lead-free $AgNbO_3$ ceramics for energy storage applications, J. Am. Ceram. Soc. 101(12) (2018) 5443-5450.

[171] Z. Fu, X. Chen, Z. Li, T. Hu, L. Zhang, P. Lu, S. Zhang, G. Wang, X. Dong, F. Xu, Unveiling the ferrielectric nature of $PbZrO_3$-based antiferroelectric materials, Nat. Commun. 11(1) (2020) 3809.

[172] N. Luo, K. Han, F. Zhuo, L. Liu, X. Chen, B. Peng, X. Wang, Q. Feng, Y. Wei, Design for high energy storage density and temperature-insensitive lead-free antiferroelectric ceramics, J. Mater. Chem. C 7(17) (2019) 4999-5008.

[173] W. Chen, X. Zhao, J. Sun, L. Zhang, L. Zhong, Effect of the Mn doping concentration on the dielectric and ferroelectric properties of different-routes-fabricated $BaTiO_3$-based ceramics, J. Alloys Compd. 670 (2016) 48-54.

[174] Z. Wen, G. Hu, S. Fan, C. Yang, W. Wu, Y. Zhou, X. Chen, S. Cui, Effects of annealing process and Mn substitution on structure and ferroelectric properties of $BiFeO_3$ films, Thin Solid Films 517(16) (2009) 4497-4501.

[175] A. Tkach, P.M. Vilarinho, A. Kholkin, Structural and Dielectric Properties of Mn-Doped Strontium Titanate Ceramics, Ferroelectrics 304(1) (2004) 87-90.

[176] R.H. Lamoreaux, D.L. Hildenbrand, High Temperature Vaporization Behavior of Oxides. I. Alkali Metal Binary Oxides, J. Phys. Chem. Ref. Data 13(1) (1984) 151-173.

[177] A. Shigemi, T. Wada, Enthalpy of Formation of Various Phases and Formation Energy of Point Defects in Perovskite-Type $NaNbO_3$ by First-Principles Calculation, Jpn. J. App. Phys. 43(9B) (2004) 6793-6798.

[178] H. Shimizu, K. Kobayashi, Y. Mizuno, C.A. Randall, Advantages of Low Partial Pressure of Oxygen Processing of Alkali Niobate: $NaNbO_3$, J. Am. Ceram. Soc. 97(6) (2014) 1791-1796.

[179] M. Zhou, R. Liang, Z. Zhou, X. Dong, Superior energy storage properties and excellent stability of novel $NaNbO_3$-based lead-free ceramics with A-site vacancy obtained via a Bi_2O_3 substitution strategy, J. Mater. Chem. A 6(37) (2018) 17896-17904.

[180] Y. Kizaki, Y. Noguchi, M. Miyayama, Defect control for low leakage current in $K_{0.5}Na_{0.5}NbO_3$ single crystals, Appl. Phys. Lett. 89(14) (2006) 142910.

[181] H. Liu, P. Veber, J. Rödel, D. Rytz, P.B. Fabritchnyi, M.I. Afanasov, E.A. Patterson, T. Frömling, M. Maglione, J. Koruza, High-performance piezoelectric (K,Na,Li)(Nb,Ta,Sb)O_3 single crystals by oxygen annealing, Acta Mater. 148 (2018) 499-507.

[182] J. Sellmann, J. Schwarzkopf, A. Kwasniewski, M. Schmidbauer, D. Braun, A. Duk, Strained ferroelectric $NaNbO_3$ thin films: Impact of pulsed laser deposition growth conditions on structural properties, Thin Solid Films 570 (2014) 107-113.

[183] M. Maglione, G. Philippot, D. Levasseur, S. Payan, C. Aymonier, C. Elissalde, Defect chemistry in ferroelectric perovskites: long standing issues and recent advances, Dalton Trans. 44(30) (2015) 13411-13418.

[184] A. Pramanick, A.D. Prewitt, J.S. Forrester, J.L. Jones, Domains, Domain Walls and Defects in Perovskite Ferroelectric Oxides: A Review of Present Understanding and Recent Contributions, Crit. Rev. Solid State Mater. Sci. 37(4) (2012) 243-275.

[185] S.-J. Lee, K.-Y. Kang, S.-K. Han, Low-frequency dielectric relaxation of $BaTiO_3$ thin-film capacitors, Appl. Phys. Lett. 75(12) (1999) 1784-1786.

[186] Y.A. Genenko, J. Glaum, M.J. Hoffmann, K. Albe, Mechanisms of aging and fatigue in ferroelectrics, Mater. Sci. Eng., B 192 (2015) 52-82.

[187] Q. Zhang, R.W. Whatmore, Improved ferroelectric and pyroelectric properties in Mn-doped lead zirconate titanate thin films, J. Appl. Phys. 94(8) (2003) 5228-5233.

[188] C. Long, H. Fan, M. Li, A ferroelectric polarization contribution from defect dipoles in acceptor Aurivillius oxide, $(Na,Bi)_{0.47}(Li,Ce)_{0.03}Bi_2Ta_{1.97}Sc_{0.03}O_{8.97}$, Appl. Phys. Lett. 103(19) (2013) 192908.

Curriculum Vitae

Personal data

Name	Mao-Hua Zhang

Education

10/2018−present	Technical University of Darmstadt
08/2016−07/2018	Tsinghua University
07/2012−07/2016	Tsinghua University

Publications

Mao-Hua Zhang, Leif Carstensen, Changhao Zhao, *et al.*; Revealing the solid-state processing mechanisms of Antiferroelectric $AgNbO_3$ for energy storage; J. Amer. Ceram. Soc., 105, 451-460 (2022)

Mao-Hua Zhang, Niloofar Hadaeghi, Sonja Egert, *et al.*; Design of Lead-Free Antiferroelectric $(1–x)NaNbO_3–xSrSnO_3$ Compositions Guided by First-Principles Calculations; Chem. Mater., 33, 266-274 (2021)

Mao-Hua Zhang, Changhao Zhao, Lovro Fulanović, *et al.*; Revealing the mechanism of electric-field-induced phase transition in antiferroelectric $NaNbO_3$ by in situ high-energy x-ray diffraction, Appl. Phys. Lett., 118, 132903 (2021)

Mao-Hua Zhang, Qinghua Zhang, Tingting Yu, *et al.*; Enhanced electric-field-induced strains in $(K,Na)NbO_3$ piezoelectrics from heterogeneous structures, Mater. Today, 46, 44-53 (2021)

Yuri Genenko, **Mao-Hua Zhang**, Ivan Vorotiahin, *et al.*; Multistep stochastic mechanism of polarization reversal in orthorhombic ferroelectrics, Phys. Rev. B, 104, 184106 (2021)

Lovro Fulanović, **Mao-Hua Zhang**, Yuping Fu, *et al.*; $NaNbO_3$-based Antiferroelectric Multilayer Ceramic Capacitors for Energy Storage *Applications*, J. Eur. Ceram. Soc., 41, 5519-5525 (2021)

Hui Ding, **Mao-Hua Zhang**, Jurij Koruza, *et al.*, Domain morphology of newly designed lead-free antiferroelectric $NaNbO_3$-$SrSnO_3$ *ceramics*, J. Amer. Ceram. Soc., 104, 3715-3725 (2021)

Zhao Pan, **Mao-Hua Zhang**, Takumi Nishikubo, *et al.* Polarization Rotation at Morphotropic Phase Boundary in New Lead-Free $Na_{1/2}Bi_{1/2}V_{1-x}TixO_3$ Piezoceramics, ACS Appl. Mater. Interfaces, 13, 5208-5215 (2021)

Mao-Hua Zhang, Lovro Fulanović, Sonja Egert, *et al.*; Electric-field-induced antiferroelectric to ferroelectric phase transition in polycrystalline $NaNbO_3$, Acta Mater., 200, 127-135 (2020)

Mao-Hua Zhang, Patrick Breckner, Till Frömling, *et al.*; Role of thermal gradients on the depolarization and conductivity in quenched $Na_{1/2}Bi_{1/2}TiO_3$-$BaTiO_3$, Appl. Phys. Lett., 116, 262902 (2020)

Mao-Hua Zhang, Yi-Xuan Liu, Ke Wang, *et al.*; Origin of high electromechanical properties in (K,Na)NbO_3-based lead-free piezoelectrics modified with $BaZrO_3$, Phys. Rev. Mater., 4, 064407 (2020)

Mao-Hua Zhang, Chengpeng Hu, Zhen Zhou, Determination of polarization states in (K,Na)NbO_3 lead-free piezoelectric crystal, J. Adv. Ceram., 9, 204-209 (2020)

Sonja Egert, **Mao-Hua Zhang**, Jurij Koruza, *et al.*; ^{23}Na NMR Spectroscopic Quantification of the Antiferroelectric–Ferroelectric Phase Coexistence in Sodium Niobate, J. Phys. Chem., 124, 23852-23858 (2020)

Conference Contributions

M.-H. Zhang, H. Ding, S. Egert, L. Fulanović, J. Koruza; $NaNbO_3$-based antiferroelectric ceramics for energy storage; Keramik 2022, 97th DKG Annual Meeting; Karlsruhe, Germany (online); 03/2022; oral presentation

M.-H. Zhang, C. Zhao, L. Fulanović, H. Ding, N. Hadaeghi, S. Egert, H. Zhang, P. Groszewicz, J. Koruza; Reversibility of the electric-field-induced phase transition in lead-free antiferroelectrics; The 6th International Conference on Advanced Electromaterials; Jeju, Korea (hybrid); 11/2021; oral presentation

M.-H. Zhang, L. Fulanović, L. Carstensen, J. Koruza; Solid-State Synthesis of $AgNbO_3$ in Air and Oxygen Atmospheres and the Influence on the Antiferroelectric Properties; 2021 Joint ISAF-ISIF-PFM Virtual Conference; 05/2021; oral presentation

M.-H. Zhang, N. Hadaeghi, S. Egert, H. Ding, H. Zhang, P. Groszewicz, G. Buntkowsky, A. Klein, J. Koruza; Design of New Lead-Free Antiferroelectric $(1-x)NaNbO_3$-$xSrSnO_3$ Compositions Guided by First-Principles Calculations; Electronic Materials and Applications 2021 Virtual; 01/2021; oral presentation

M.-H. Zhang, L. Fulanović, S. Egert, H. Ding, P. Groszewicz, H.-J. Kleebe, L. Molina-Luna, J. Koruza, Electric Field-Induced Antiferroelectric to Ferroelectric Phase Transition in Polycrystalline $NaNbO_3$; Virtual Electroceramics XVII; 08/2020; oral presentation